MICROWAVE OBSERVATIONS PROVIDE CLUES TO THE ORIGIN OF SATURN'S MAIN RINGS

A Dissertation

Presented to the Faculty of the Graduate School

of Cornell University

In Partial Fulfillment of the Requirements for the Degree of

Doctor of Philosophy

by

Zhimeng Zhang

January 2017

MICROWAVE OBSERVATIONS PROVIDE CLUES TO THE ORIGIN OF SATURN'S MAIN RINGS

Zhimeng Zhang, Ph. D.

Cornell University 2017

Despite considerable study, Saturn's rings continue to challenge current theories for their provenance. Water ice comprises the bulk of Saturn's rings, yet it is the small fraction of non-icy material that is more valuable in revealing clues about the system's origin and age. Herein, we present new measurements of the non-icy material fraction in Saturn's main rings, determined from microwave radiometry observations acquired by the Cassini spacecraft at 2.2 cm and multi-wavelength VLA interferometer. We find the C ring particles to be 70%-75% porous. Our results also show that most regions in the C ring contain about 1-2% silicates together with an enhanced abundance in the middle C ring reaching 6%-11% when assumed to be mixed volumetrically ("intramixed") with water ice. As opposed to an intramixure model, we also consider a silicate-core, icy-mantle model to address the fact that silicates may be present in chunks instead of fine powder in the ring particles, which naturally explains the opacity distribution. Our most preferred model is that the C ring has been continuously polluted by meteoroid bombardment since it first formed 15-90 million years ago, while the middle C ring was further contaminated by an disrupted Centaur 10-20 million years ago.

We derive the silicates fractions in the B ring, which has a significant dependence on the assumed porosity, but the radial distribution follows the same trend as the optical depth. Owing to the B

ring's high opacity (i.e. high optical depth but low surface density), its particles are likely to have 85%-90% porosity, with corresponding silicates fractions of ~ 0.3% - 0.5% in the inner and outer B ring, and ~0.1% - 0.2% in the middle regions. For the A ring interior to the Encke gap, the derived silicate fraction is ~0.2% - 0.3% everywhere for porosities ranging from 55% - 90%. Finally, our results for the Cassini Division indicate a silicates fraction of ~1% - 2% similar to most regions in the C ring, except that the Cassini Division particles are more likely to contain $\gtrsim$ 90% porosity due to its high opacity. We find that the overall pollution exposure time for the A and B rings and the Cassini Division ranges from ~40 - 150 Myr, which is in line with the ~15 – 90 Myr in the C ring. Our results support the idea that Saturn's rings may be $\lesssim$ 150 Myr old suggesting an origin scenario in which the rings are derived from the relatively recent breakup of an icy moon.

The multi-wavelength VLA observations confirm the high porosity in the C ring particles and the presence of a "hot band" in the middle C ring. In the intramixure model, our multi-wavelength study suggests a corresponding decrease in the imaginary part of the silicates dielectric constant at higher frequencies. However, we do not see evidence for such decrease in the B ring particles. The results support the idea that the silicates in middle C ring has different origin source from meteoroid flux or that the middle C ring particles are more likely to be described by the core-mantle model which naturally matches observations at all wavelengths. Finally, the silicates fraction in the B ring is consistent with that derived from Cassini observations, less than 1%. We confirm that the B ring particles are likely to be over 80% porous, which at the same time explains the high opacity in the B ring measured by density waves.

BIOGRAPHICAL SKETCH

Zhimeng Zhang was born on a snowy winter day in Shanghai, China on December 4th, 1988, where she began her predestined relationship with the frozen world. She spent her formative years in Shanghai and moved to Beijing to attend Peking University in 2006. In 2011, she received a Bachelor's degrees in Physics from Peking University after which she bravely ventured off to a strange and foreign land called Ithaca, New York to begin a doctorate program in Astronomy where she renewed her direct acquaintance with the frozen world. Indeed, Zhimeng found Ithaca to be a place favored by winter and snow, and at many times during her graduate career even felt it was a place where she would be doomed to stay. But with the perseverance and a lot of hard work that has marked the completion of her doctoral thesis, she can now finally bid farewell to this land of icy winters, to replace it with the much more forgiving climate of Southern California where the next chapter of her story, yet to unfold, will come to pass.

Dedicated to

My beloved parents Jinfu Zhang and Yuejun Sun, grandparents Yisong Gao and Huizhen Hu, who stand by me, support me and love me no matter what.

献给我最亲爱的父亲张金福，母亲孙跃君，外祖父高意松，外祖母胡惠珍。

In memory of

My lovely grandpa, Qifu Zhang

纪念我敬爱的祖父张启富。

ACKNOWLEDGMENTS

There are many people without whom this thesis would not have been possible. First and foremost, I would like to thank my PhD advisor, my mentor, Alexander Hayes, who has been encouraging, supporting and guiding me for all these years. As I first started graduate school, I found the conversion from physics to astronomy and indeed from an undergrad to a graduate student more difficult than I had anticipated. Then come along Alex! He guided me and helped me to find my own way. He taught me not only the knowledge and wisdom, but also the attitude towards science, towards life which I needed for which I will be forever grateful. Looking back at the past few years, without his guidance, I would never become the person I am now, to become more matured as a scientist. Alex will always be one of the people that I trust most.

I also greatly appreciate the substantial contributions and mentorship from my collaborators: Dr. Michael Janssen, who collected the Cassini data presented in this work, offered me the chance to work with him every summer and taught me patiently even though he is actually always super busy; Professor Philip Nicholson, who knows everything like a walking encyclopedia, always has an answer to my questions and kept me motivated even when we were the only few people working in the department late at night; Dr. Jeffrey Cuzzi, who always listens to my naive ideas patiently, encourages me, and always gives me the most valuable insights and brings his light during those times when my path seems shrouded in darkness; Professor Imke de Pater, who taught me the secret art of calibrating interferometer observations and with her husband invited me to dinner at their warm house when I missed home most; Professor Matthew Hedman, who is one of the smartest and nicest people on the planet, and who always comes up with great ideas when I encountered obstacles in my research; Dr. David Dunn who spent a lot of time during the summers

with me, teaching me the skills of modeling and calibrating VLA data; and Dr. Paul Estrada, who helped to produce the complicated viscous spreading simulation in explaining the radially-varying silicate fraction in the middle C ring, helped me review my papers and contributed a lot to the length of our papers.

I would like to thank many professors at Cornell in astronomy whose knowledge and guidance I have benefited from. In particular, I am lucky to have several outstanding professors on my special committee: Professor Philip Nicholson, Professor Saul Teukolsky, and Professor Dominik Riechers who have all contributed invaluably to my graduate education. I would especially like to thank Professor Joseph Burns who inspires and motivates me; Professor Donald Campbell, whom I bugged a lot on the subject of material dielectric constants; and Professor Peter Gierasch, who helped me a lot in the modeling of the particle scattering process. Finally I would like to thank the lifelong friends I've made while at Cornell, who worked with me, studied for physics class exams with me, played with me, got frozen in the snow with me and made fun of me, in particular Lyann Lau, Joyce Byun and Paul Corlies.

I would like to thank the NASA Outer Planets Research Program (Grant Number NNX14AR27G) for funding the work on the Cassini data. I also thank the NASA SSW Program (Grant Number NNX15AJ95G) for funding the work on the VLA data. Finally, I gratefully acknowledge those who designed, developed and operate the Cassini/Huygens mission, which is a joint endeavor of NASA, the European Space Agency (ESA), and the Italian Space Agency (ASI) and is managed by JPL/Caltech under a contract with NASA, and those at NRAO who designed, developed and operate the VLA interferometer.

TABLE OF CONTENTS

LIST OF FIGURES

LIST OF TABLES

LIST OF ABBREVIATIONS

CDA	Cosmic Dust Analyzer
CMB	Cosmic microwave background
DDA	Discrete Dipole Approximation
EMT	Effective Medium Theory
EVLA	Expanded Very Large Array
FWHM	Full width at half maximum
RSS	Radio Science Subsystem
RFI	Radio Frequency Interference
SNR	Signal-to-noise ratio
UVIS	Ultraviolet Imaging Spectrograph
VLA	Very Large Array

LIST OF SYMBOLS

R_S	Saturn's radius
B	Ring opening angle
G	Gain pattern of Cassini RADAR antenna
G_{mb}	Gain pattern of Cassini RADAR antenna in the main beam
G_{sl}	Gain pattern of Cassini RADAR antenna in the sidelobes
N_{sky}	Normal counts on the empty sky obtained by Cassini RADAR
T_{sys}	Cassini RADAR system baseline offset
A	Cassini RADAR receiver gain
F_{corr}	Cassini RADAR gain correction factor
t	Time in years since the start of September 2005
T_a	Antenna temperature obtained by Cassini RADAR
T_{acorr}	Antenna temperature corrected for baseline and gain drift with time
T_a'	Relative antenna temperature obtained by Cassini RADAR with respect to the cold sky
T_{zero}	Cold sky baseline obtained by Cassini RADAR
T_b	Brightness temperature
$\bar{T}_{mb}$	Mean brightness temperature in the main beam
$\bar{T}_{sl}$	Mean brightness temperature in the sidelobes
a	Ring particle radius in cm
$a_{\min}$	Minimum particle size of ring particle power law size distribution
$a_{\max}$	Minimum particle size of ring particle power law size distribution
q	Power law index of ring particle power law size dsitribution
ε_{ice}	Complex dielectric constant of water ice
$\varepsilon_{non\text{-}ice}$	Complex dielectric constant of non-icy material
$\varepsilon_{silicate}$	Complex dielectric constant of silicate
ε_{iron}	Complex dielectric constant of un-oxidized iron

ε_{eff}	Effective complex dielectric constant of ring particle
ε_i	Imaginary component of dielectric constant
ε_r	Real part of dielectric constant
f_p	Particle porosity
f_v	Non-icy material volume fraction
n	Complex refractive index
n_r	Real part of the complex refractive index
n_i	Imaginary part of the complex refractive index
λ	Observed wavelength
α_λ	Absorption coefficient at wavelength λ
$\alpha_{H_2O_{ice}}$	Absorption coefficient of water ice
T_{ring}	Physical temperature of the rings
$n(a)$	The areal number density of ring particles with radius a
κ	Ring opacity
σ	Ring surface mass density
τ	Normal optical depth
$\tau_{geometry}$	Geometric normal optical depth
τ_{abs}	Absorption optical depth
$\overline{\rho}$	Mean particle density
Q_{sca}	Efficiency factor for scattering
Q_{abs}	Efficiency factors for absorption
Q_{ext}	Efficiency factors for extinction
Q_{RSS}	Efficiency factors for extinction for the RSS occultation
Q_{UVIS}	Efficiency factors for extinction for the UVIS stellar occultation
I	Incident light intensity
β	Incidence angle
μ	Cosine of the incidence angle β
τ_{eff}	Effective optical depth in the main beam
$T_{simulate}$	Simulated brightness temperature
$T_{scatter}(T_{scat})$	Simulated scattered effective Saturn thermal emission

$T_{thermal}(T_{th})$	Simulated intrinsic thermal emission from the rings particles
$T_{direct}(T_{dir})$	Simulated directly transmitted Saturn radiation
τ_{wake}	Normal optical depth in the wakes
τ_{gap}	Normal optical depth in the gaps
W	Wake width of wake structures
S	Gap width of wake structures
L	Wavelength of wake structures
H	Ring layer thickness
ϕ_{wake}	Wake alignment direction relative to the local radial direction
x	Particle size parameter
$P(\theta)$	Particle single scattering phase function
$P_{mie}(\theta)$	Particle Mie scattering phase function
f_{iso}	The fraction of isotropic scattering in the hybrid phase function
M	Empirical constant in the semi-empirical phase function
x_0	Critical size parameter, beyond which particle non-sphericity becomes important
F	Fresnel number
L_s	Extension of the near-field (shadow zone) in the forward scattering direction
$\dot{\sigma}_\infty$	Micrometeoroid flux at infinity
$\dot{\sigma}_e$	Two-sided incident flux of micrometeoroid flux crossing the ring plane at a ring radius r
$\dot{\sigma}_{im}$	Local impacting flux
$\dot{\sigma}_{ej}$	Ejected mass flux
F	Gravitational focusing factor
$\subsetneq$	Impact probability
δ	Throw distance of ejecta
v_{ej}	Velocity of the bulk of ejecta
t_g	Gross erosion time
t_{BT}	Ballistic transport time scale
Y_0	Mass ejecta yield
a_{crit}	Critical size for the population that includes large silicate chunks in the core-mantle model

f_r	The ratio of silicate core radius to particle radius in the core-containing particles
g_{eff}	Effective anisotropy factor
t_{visc}	Viscous timescale
ν	Viscosity
ν_L	Viscosity from particle random motions (local shear stress component)
ν_{NL}	Viscosity from physical collisions
ν_{grav}	Viscosity from gravitational scattering due to the presence of self-gravity wakes
Q_T	Tommre parameter
M_S	Mass of Saturn
c	Velocity dispersion
T_{Saturn}	Saturn radiation relative to CMB
T_0	Uniform Saturn disk brightness
T_1	Limb darkening factor
η_{flux}	Uncertainty in flux measurements

1 Introduction

The rings of Saturn have continued to attract great interest from astronomers since Galileo Galilei discovered them with his telescope in 1610. With each advance in observations of the rings over the last four centuries, new structure has been revealed, starting with the recognition that the rings are a disk by Huygens in 1655, through discoveries of the broad organization of the main rings and their constituent gaps and ringlets, to Cassini observations that indirectly reveal individual clumps of particles tens of meters in size (Colwell et al., 2009). There are billions of ring particles in the entire ring system, mostly mm- to m- size, and apparently made almost entirely of water ice. The main rings are, working outward from the planet, known as the C, B and A rings (see Figure 1,1). The Cassini Division is the largest gap in the rings that separates the B and A rings. But the Cassini Division is by no means empty, and in fact is itself composed of interesting and complex structure. In addition, a number of fainter rings were discovered once observational techniques allowed for it. The D ring is exceedingly faint and closest to the planet, yet displays similar spiral structures, seen more commonly throughout the more dense portions of the rings, which apparently have been evolving on relatively short (since Voyager) time scales. The F ring, shepherded by Saturn's small moons Prometheus and Pandora, is a dynamic narrow ring just outside the A ring and on the outskirts of Saturn's Roche zone which demonstrates constantly changing structure with clumps forming and breaking apart on time scales of hours to days. Beyond that are two far fainter rings named G and E. The G ring is a faint arc of material whose origin and maintenance remains uncertain, but its proximity to Mimas may indicate that that moon plays a role in its dynamics. The E ring on the other hand is thought to be produced from icy debris ejected from

plumes of Saturn's extremely active mid-sized moon, Enceladus. Indeed, all the rings show a tremendous amount of structure on all scales with some of this structure being related indirectly or directly to interactions with Saturn's many moons, but much of the structures across the rings remains unexplained. In this work, we focus on the main rings - the C, B, A rings and the Cassini Division.

Figure 1.1: Structures of Saturn's rings and satellites system (figure from NASA imaging)

Saturn's rings are the most massive, extensive and diverse ring system in the Solar System, yet despite decades of ground and spacecraft-based observations (Dougherty et al., 2009; Grossman, 1990; de Pater and Dickel, 1991; van der Tak et al., 1999; Dunn et al., 2002, 2005; Poulet et al., 2003; Nicholson et al., 2008), their origin and age continue to be a subject of debate. Although water ice has long been accepted as the most prominent component of ring composition (Cuzzi et al. 1984, Esposito et al. 1984), it is the small fraction of non-icy material that is crucial in understanding their origin and age through source composition and exposure time to extrinsic micrometeoroid bombardment (Cuzzi and Estrada, 1998). However, these still remain poorly

understood. It is the specific goal of this work to determine the fraction and composition of the rings' non-icy material and what that can tell us about their origin.

At first, astronomers predominantly agreed Saturn's rings were primordial (Harris et al., 1984) until observations from the Voyager spacecraft suggested that dynamical considerations necessitated a short (~10^8 yrs) lifetime (Harris et al., 1984; Dones et al., 1991; Goldreich and Tremaine, 1982). A more recent post-Cassini view returns to an ancient origin (Esposito, 2008), but invokes a much more massive pure-ice primordial ring formed via tidal disruption of a Titan-sized, differentiated satellite (Canup, 2010). Yet another recently revisited scenario (Charnoz et al., 2009a) suggests that the cometary flux was so high during the Late Heavy Bombardment (LHB) that several tens of Mimas masses of cometary material may have been brought into Saturn's Hill sphere, and that a fraction of it could have ended in Saturn's Roche zone. In this 'destroyed satellite scenario', it has been recently shown (Charnoz et al., 2009b) that a Mimas-mass moon located 10^5 km from Saturn can be disrupted during a LHB type event (Tsiganis et al., 2005) about 700 Myr after the planet's birth (though possibly even later, see Sec. 5.2.2). The probability for disruption is model dependent, but can be > 95% (see Table 3, Charnoz et al., 2009b, and references therein). Indeed, there are several formation scenarios all of which apply to primordial or old ring systems. It has not been until recently that formation scenarios for a young ring system have begun to be explored. The abundance and character of non-icy material in Saturn's present-day ring system can help distinguish between these origin scenarios by constraining the composition of source material and, for a given initial composition, estimate the rings' exposure age due to micrometeoroid bombardment (Cuzzi and Estrada, 1998).

The exact composition of Saturn's ring particles remains unclear. As mentioned above, water ice

has long been known as the most prominent component (Cuzzi et al., 1984; Esposito et al., 1984), but the single scattering albedos of ring particles are much too low for them to be pure water ice. The rings' spectrum in the visible and near-IR shows strong absorption at near-UV and blue wavelengths leading to a decrease in reflectivity at wavelengths shorter than 0.6 μm. Yet, little is known about the specific makeup of the non-icy, absorbing material that accounts for this observation, the presence of which apparently gives the rings their slightly non-gray, very pale tan or salmon color (Estrada and Cuzzi, 1996). Several investigators have considered a variety of potential UV absorber candidates such as tholins, PAHs, nanophase iron and nanophase hematite in order to match the observed color. Despite the range of materials considered, all of these studies have generally constrained the non-icy fraction to be less than a few percent by mass (Cuzzi and Estrada, 1998; Cruikshank et al., 2005; Morris et al., 1985; Clark et al., 2008). Furthermore, ring photometry has shown that the optically thin C ring and Cassini Division have darker and less red particles than the optically thick A and B rings (Estrada and Cuzzi, 1996), which indicates the presence of varying amounts of unidentified darkening non-icy material with a spectrally neutral color (Smith et al., 1982; Cuzzi et al., 1984; Dones et al., 1993; Poulet et al., 2003; Nicholson et al., 2008). In this work we will show that the very small amount of reddening material required to give the rings their apparent color in the visible and near IR wouldn't contribute significantly to the microwave observation (Sec. 5.2.4), and thus it is the presence of some other non-icy material, besides these reddening materials, that determines the intrinsic thermal emission at the wavelength of our interest.

The C ring and Cassini Division are the darkest of all the main rings. The reason for this is fairly straightforward if one considers that the rings have been continuously darkened by incoming micrometeoroids. In optically thin regions like the C ring and Cassini Division, ring particles are

sparse and only a fraction of incoming meteoroids actually hit the rings as opposed to merely passing through them. Nevertheless, these thin rings become dark relatively quickly owing to their low surface densities. As the rings become optically thicker, a larger fraction of the meteoroids are absorbed by the ring particles until reaching a level of saturation, where none of the incoming meteoroids can pass through. Saturation is reached for an optical depth $\tau \gtrsim 1$, while the mass of material to be darkened continues to increase with τ, so the time needed to significantly darken the rings increases. Thus, the optically thin C ring and Cassini Division are initially easier to darken than the optically thicker A and B rings.

It should be noted that many of the structures we see in the C ring lack a satisfactory explanation. Apart from having a profound darkening effect on the rings, micrometeoroid bombardment and transport of their impact ejecta has been shown to explain many aspects of C ring structure (see Estrada et al., 2015), but much of the structure, especially the plateaus, remain enigmatic. A great deal of the mystery of the C ring revolves around the measured ring opacity (see Sec. 5.2) which can be associated with the particle size distribution. A complete radial profile of the C ring opacity is lacking, but observations suggest that the particle size distribution in the C ring differs across the ring and within different ring regions (e.g., Marouf et al., 2008; Cuzzi et al., 2009; Colwell et al., 2011, 2012) which further complicates efforts to explain the observed structure. Though our analyses are not meant to address the specifics of C ring structure, we do advance a compelling model to explain one particular C ring enigma, that of the anomalously low opacity (and thus structure) in the middle C ring (Sec. 5.2.2).

Microwave observations at mm- to cm- wavelengths provide an ideal window through which to study the non-icy material fraction in Saturn's main rings, as it operates at a wavelength where the

absorptivity of water ice is negligible compared to that of most non-icy material, and thus the intrinsic thermal radiation from the ring layer is dominated by the non-icy components. Moreover, whereas visible and near-IR spectra are only sensitive to the top millimeter or less of ring particle surfaces, microwave observations are able to sample the bulk of the ring mass. For solid pure water ice particles, radiation from Saturn at microwave wavelengths can penetrate as deep as almost 100 m, while the largest particles in the rings are no larger than 10 m (Marouf et al., 2008). Furthermore, microwave measurements at mm- to cm- wavelengths are most sensitive to mm- and cm- scale particles, which has known to be the most dominant sizes of the ring particles.

There are currently three classes of microwave observations of Saturn's rings: radio occultations such as the Voyager and Cassini RSS, active RADAR such as Arecibo, and passive radiometry such as the Cassini RADAR (see below) and specifically, another source of the dataset we obtained, the VLA. Radio occultations provide measurements of optical depth and the moments of the particle size distribution (e.g., Marouf et al., 2008) while active RADAR provides information regarding the zero phase backscatter cross-section and circular polarization ratio (e.g., Nicholson et al., 2005). Passive microwave observations (e.g., Cuzzi et al., 1980; van der Tak et al. 1999; Dunn et al., 2002) incorporate scattered light across a range of geometries (forward, side, and back scattering) and fill in the gaps between the forward scattering provided by occultation experiments and backscattering provided by active measurements.

The onboard Cassini RADAR instrument is a 13.8 Ghz (~2.2 cm wavelength) Ku-band 5-beam sensor that can operate in several different modes. These modes include altimeter, scatterometer, imaging (synthetic aperture radar, or SAR) and radiometer modes. Although specifically designed to use all modes to map the surface of Titan over many fly-bys, Saturn's atmosphere and rings

were planned targets to be scanned in the radiometer mode only. Unlike the other modes where the spacecraft bounces pulses of microwave energy off the target and measures the time it takes for the pulses to return, in the radiometer mode the instrument operates passively (i.e. simply "listens"). In the radiometer mode, the Cassini RADAR collects brightness temperature maps, and thus of specific interest for this work the microwave flux due to the thermal emission of ring particles as well as due to scattering of emission from Saturn's atmosphere by the ring particles. A full description of the Cassini RADAR instrument can be found in Elachi et al. (2004).

The Cassini RADAR scanned Saturn and its rings at 2.2 cm wavelength on twelve occasions during its prime mission between Dec 2004 and Oct 2008, at distance range of 5~20 Saturn radii (Saturn's equatorial radius is 60330 km). It provides us with unprecedented resolutions and for the first time reveals detailed C ring particle compositions. All radiant power observed in the Saturn system is thermal in origin, which is described in terms of the temperature (in units of Kelvin) of a blackbody that emits the equivalent power. In particular, the power collected by the antenna is called the "antenna temperature." For an ideal antenna with a pencil beam and no sidelobes, the antenna temperature is the same as the "brightness temperature," or equivalent blackbody temperature, of the source observed in the beam of the antenna. In practice, and particularly for Cassini, the process of obtaining calibrated brightness temperatures from antenna temperature measurements is not straightforward (Cassini Radar Users Guide), and a cautious sidelobe removal process is required. On the other hand, as for the VLA observations, its very advantage is its multi-wavelength coverage from 0.62 cm to 15.04 cm that can help to unravel the effects of composition and geometrical scattering. Based on the analysis results from Cassini passive radiometry observations, we also present a combined analysis of both short and long wavelengths using VLA data to disentangle brightness temperature variations from changes in the particle size distribution and the

non-icy material abundance in the C and B rings. More importantly, with these multi-wavelength VLA observations, we are able to provide an important test of our Cassini analyses for the C and B rings by constraining ring particle properties through their behavior at various wavelengths and provide more insights at the same time.

The observed brightness temperature of the rings has four components: directly transmitted light, scattered component, intrinsic thermal emission and the cosmic microwave background (2.7K). The directly transmitted light is only present when the rings are occulting Saturn, and depends on the local optical depth and ring opening angle. The scattered component is the scattered Saturn radiation by the ring particles, which is determined by the local optical depth and ring particle scattering properties. In most parts of the main ring, the incident Saturn radiation is scattered multiple times before escaping the ring layer. We employ a photon counting Monte Carlo Code, *"Simrings"*, to deal with this multiple scattering process which was originally developed to simulate ground-based VLA observations of Saturn and its rings, though with a lower resolution and narrower frequency coverage than our data.

Specifically, *Simrings* uses a Monte Carlo approach which makes use of realistic particle compositions, size and spatial distributions and ring particle scattering properties (phase functions) to model radiative transfer in a layer of ring particles (Dunn et al., 2002). Once given the scattering properties of individual ring particles, *Simrings* tracks the fate of virtual photons impinging on a plane-parallel slab containing an ensemble of particles characterized by some size distribution, layer height and normal optical depth at a specific wavelength which are either scattered or absorbed by the ring particle material. Tracking the fate of virtual photons requires the

determination of random events such as, for example, how far the photon travels, the particle size encountered, the scattering phase angle (if scattering occurs) or whether they are absorbed (Dunn et al., 2002).

Simrings is ideal for simulating our VLA observations and we further adopted it for the Cassini RADAR observation geometry. Moreover, the code lends itself well to computation of physically realistic structures such as wakes such as those found in the A and B rings. We model the ring particles as porous water ice particles with non-icy material embedded in the particle matrix in the form of very small inclusions; a volumetric mixture that is referred to as an "intramixed" model. The composite particles' effective macroscopic dielectric properties can then be calculated with Effective Medium Theory (EMT). The intrinsic thermal emission from the ring particles is then determined from their intramixed non-icy material fraction.

Advances in observational techniques and instrument sensitivity over the last few decades have led to vast improvements in resolution for observations of Saturn at microwave wavelengths which has been instrumental in allowing for the development of more sophisticated and complete ring layer radiative transfer models. Goldstein and Morris (1973) conducted the very first high resolution radar observational measurements of the rings that provided the opportunity to conduct the first significant modeling efforts of the rings (Cuzzi and Van Blerkom, 1974; Cuzzi and Dent, 1975). For example, Cuzzi and Van Blerkom (1974) developed a detailed radiative transfer ring model which consisted of a plane-parallel layer of identical particles of constant optical thickness typical of the B ring to investigate the Pollack et al. (1973) multiple-scattering model in order to constrain ring parameters using a Monte Carlo approach. Cuzzi and Dent (1975) modeled the B

and A ring separately and computed visibility curves to fit the radar data and determined a lower limit on the ring brightness temperature of 15 K in agreement with Cuzzi and Van Blerkom (1974).

Later, multi-wavelength radar observations (Goldstein *et al.* 1977) would lead to new and more sophisticated models that would incorporate other ring particle properties not considered before. For example, using the radiative transfer doubling method, Cuzzi and Pollack (1978) constructed models that included a ring particle size distribution as well as consideration of the effects of ring particle nonsphericity. Using a model similar to Cuzzi and Van Blerkom (1974), Cuzzi, Pollack, and Summers (1980) also included a particle size distribution, but in addition took into account radial structure in the rings. These workers considered several wavelengths to compare with the data, but found that they could not resolve the azimuthal brightness variations despite constructing higher resolution models. Much higher quality data with high resolution would later be obtained using the VLA (de Pater and Dickel 1982, 1983; de Pater 1985; Grossman, Muhleman and Berge 1989) allowing for more sophisticated model comparisons. In his thesis, Grossman (1990) presented an analysis of microwave images of Saturn's atmosphere and rings at multiple wavelengths. In particular, he modeled the emission, scattering and extinction in the rings in an effort to constrain ring particle composition, sizes and shape using Mie theory for a distribution of spherical, dirty ice particles, but neglected the effects of multiple scattering. Grossman (1990) found that Mie theory didn't account for the observed orientation of the polarized emission and instead suggested a semi-empirical alternative to Mie scattering. However, he provided no quantitative comparisons. In this work, we employ the most recent photon-counting Monte Carlo Code *Simrings* developed by Dunn et al. (2002), which takes into account the multiple scattering process, non-sphericity effects on the particle scattering phase function, particle size distributions and a more complete resolved Saturn radiation model.

In this thesis, we first employ the microwave radiometry observations acquired by the Cassini spacecraft at 2.2 cm in order to investigate the non-icy material fraction in the C ring, B ring, Cassini Division and A ring. In Chapter 2 we give an overview of Cassini Radiometry observations of the rings and describe the calibration process and the resulting brightness temperature map. In Chapter 3 we present the method we use to model the microwave scattering and emission in the rings. We also list the ring parameters that determine the simulated brightness temperature. In Chapter 4, we compare the simulated brightness temperatures from the model with Cassini observations in the C ring, B ring, Cassini Division and A ring. We vary the ring properties and search for the best-fit parameters. In Chapter 5, we discuss the implication of our results and suggest possible ring origin scenarios that could explain our findings. In Chapter 6, we present the VLA multi-wavelength observations, briefly describe the calibration process and the final observational results. We describe how we generate the synthetic model map to compare with the observations and all the ring parameters required to conduct our simulations. We applied our previous analysis results from Cassini observations at 2.2 cm in the model, compare the simulation results with the VLA observations, and investigate the derived ring particle properties. In Section 7, we summarize our conclusions and their implications for the rings' origin and age. Finally, in Section 8, we discuss the exciting future observations planned for the Cassini end of mission finale.

2 Cassini Passive Radiometry Observations at 2.2 cm

Portion of this work is published in: Zhang Z., Hayes A.G., Janssen M.A., Nicholson P.D., Cuzzi J.N., de Pater I., Dunn D.E., Estrada P.R., Hedman M., 2017a. Cassini microwave observations provide clues to the origin of Saturn's C ring. Icarus.

Portion of this work is published in: Zhang Z., Hayes A.G., Janssen M.A., Nicholson P.D., Cuzzi J.N., de Pater I., Dunn D.E., 2017b. Exposure age of Saturn's A and B rings, and Cassini Division as suggested by their non-icy material content. Submitted to Icarus.

2.1 Observation Overview

The Cassini RADAR instrument (Elachi et al., 2004) scanned Saturn and its rings at 2.2 cm wavelength on twelve occasions during its prime mission between Dec 2004 and Oct 2008. There are two categories of radiometric observations of Saturn's rings: low-resolution map scans from a distance of ~ 20 R_S (where R_S = 60330 km is Saturn's radius) and high-resolution "spoke scans" (not related to the fuzzy features seen in the B ring) from a distance of ~ 5 - 8 R_S. The map scan "footprints" (**Figure 2.1 upper panel**, red circles) cover all of the main rings at all azimuthal angles. The projection of the line connecting Saturn center and the spacecraft onto the ring plane lies at zero degree azimuth, and the azimuthal angle increases anti-clockwise in the ring plane. At small azimuthal angles, the observed ring regions occult Saturn. These observations are comparable to stellar and radio occultations except that the light source is due to the planet's radiation. On the other hand, high-resolution spoke scan footprints (**Figure 2.1 lower panel**, red circles) only cover the main rings at five distinct azimuthal angles where the rings are not occulting Saturn. While map scans reveal the complete angular scattering profile, spoke scans show finer radial structures. Five of these occasions (four low-resolution maps and one set of high-resolution spoke scans) were collected when the ring plane had the largest ring opening angle of about -20° and thus they have the best resolution. In this work, we investigate these five datasets as listed in **Table 2.1**.

The Cassini Radar has a main beam size of 0.36^{o} in angular diameter (full width at half maximum [FWHM] power). As the main-beam projects onto the ring plane, the resolution in the direction perpendicular to the line-of sight equals the angular diameter multiplied by the observer-target distance, while the resolution along the line-of-sight is elongated by a factor $(\sin |B|)^{-1}$, where B is the opening angle. In high and low resolution cases with a ~-20° ring opening angle, the radial resolution is about ~2,000 km and ~8,000 km, respectively, in the direction perpendicular to Cassini's line-of-sight, and ~6,000 km and ~24,000 km, respectively in the direction parallel to Cassini's line-of-sight. For each occasion, the data are collected at three different linear polarization orientations: polarization 1, horizontal to the ring plane; polarization 3, $\sim 20^{o}$ to the ring plane normal; and polarization 2, which lies in between polarizations 1 and 3. As described below, each polarization is calibrated independently.

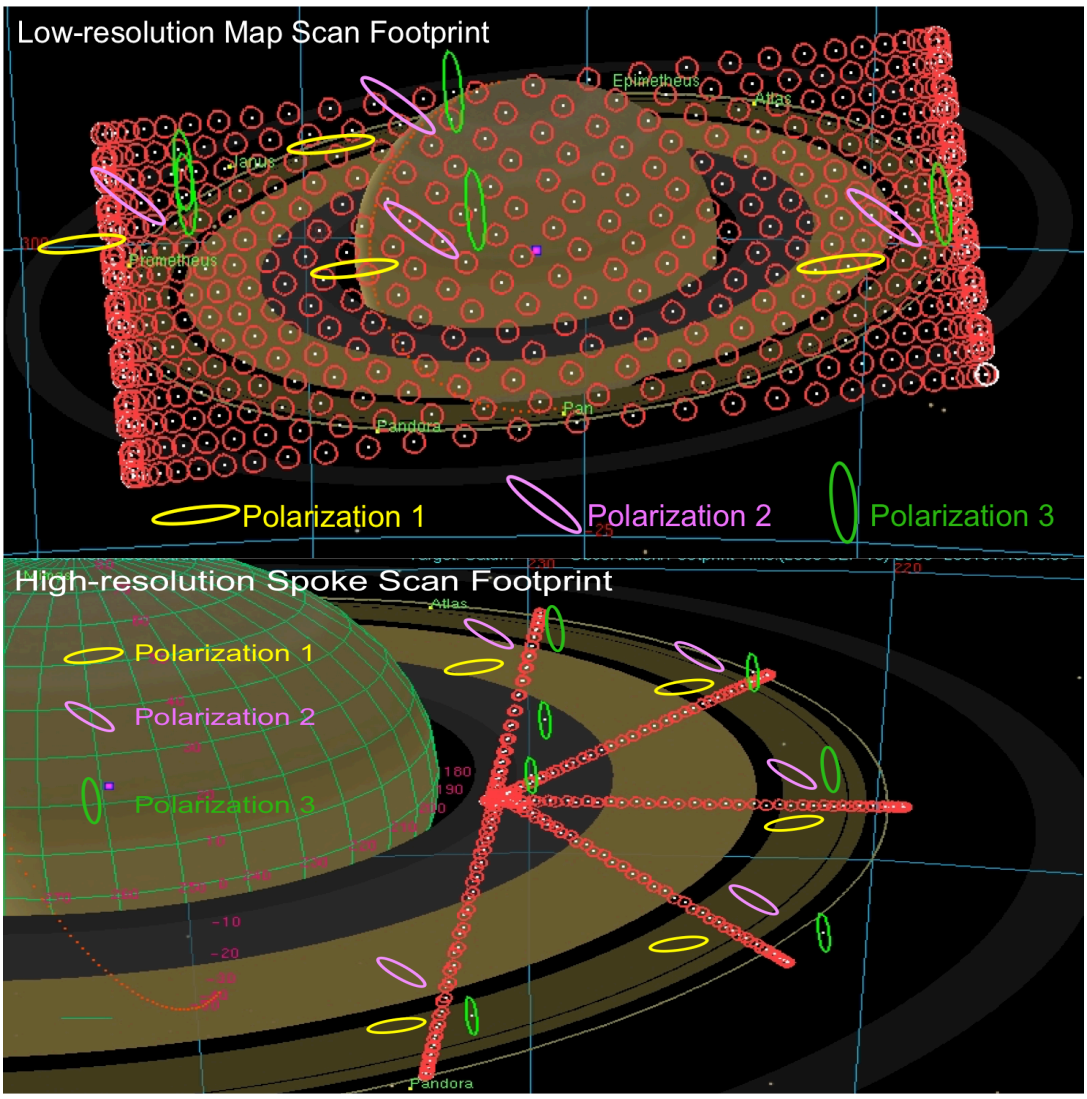

Figure 2.1: Footprint of Cassini Radar on the rings during low-resolution map scan (upper panel) and high-resolution spoke scan (lower panel) [figures from the Cassini RADAR team page]. Small red circles represent the half-power beam width of the Cassini Radar Beam 3 and show the observation footprints on the rings. Beam 3 is the central Radar beam used for radiometry. The major axes of the ellipses show the linear polarization orientations; polarization 1 (yellow), horizontal to the ring plane; polarization 3 (green), ~20o to the ring plane normal, roughly aligned with the projection of the ring plane normal in the figure; and polarization 2 (purple), which lies in between polarizations 1 and 3.

Table 2.1: Cassini Radiometry Data Set

Occasion	Request Name	Scan Type	Calendar Date	Distance (R_S)	Opening Angle (degree)
Rev028_ HIGH	RADAR_028RI_PO1 RINGS002_PRIME	High-resolution spoke scan	2006-253T01:00:00-2006-253T06:00:00	6.7	-24.5~-23.3
Rev028_ LOW	RADAR_028RI_045 MATCH001_PRIME	Low-resolution map scan	2006-254T08:00:00-2006-254T11:30:00	19.2	-22.2~-21.9
Rev038_ 1_LOW	RADAR_038RI_038 MATCH1001_PRIME	Low-resolution map scan	2007-027T16:36:00-2007-028T02:36:00	24.4	-22.5~-18.3
Rev038_ 2_LOW	RADAR_038RI_038 MATCH2001_PRIME	Low-resolution map scan	2007-035T20:52:00-2007-036T05:22:00	21.9	-20.8~-15.5
Rev039_ LOW	RADAR_039RI_39R1 MATCH001_PRIME	Low-resolution map scan	2007-054T13:11:00-2007-054T19:22:00	24.1	-24.5~-21.7

2.2 De-convolution process

While this data set presents several advantages, such as the low microwave absorptivity of water ice and a wavelength comparable to the size of the most abundant ring particles, it is also very challenging to process. This is because Saturn and its rings are extended targets that require combining a large number of measurements to obtain full coverage. More importantly, each measurement of antenna temperature is the convolution of the radiometer's broad gain pattern and the brightness temperature of all targets in the field of view (Janssen et al., 2009). The antenna temperature T_a is given by

$$T_a = \int_0^{2\pi} \int_0^{\pi} T_b(\theta, \phi) G(\theta, \phi) sin\theta d\theta d\phi \quad . \tag{2.1}$$

where (θ, ϕ) is the angular deviation from the beam center, $T_b(\theta, \phi)$ is the brightness

temperature in the direction of the solid angle element $\sin\theta d\theta d\phi$, and $G(\theta,\phi)$ is the gain of the antenna. The gain pattern of the Cassini RADAR was measured in-flight by Janssen et al. (2009), and consists of an asymmetric near-Gaussian main beam (FWHM of 0.36°) with extensive sidelobes that, on average, drop to -35 dB ($10^{-3.5}$) within ~2° of beam center. The sidelobes outside 2°, which extended as far as 60°, were never measured in the ground calibrations, but were solved for as a byproduct of mapping Titan (Janssen et al., 2016). The gain is normalized such that:

$$\int_0^{2\pi}\int_0^{\pi} G(\theta,\phi) sin\theta d\theta d\phi = 1 \quad . \tag{2.2}$$

Radiometer processing requires two primary tasks: (1) relate the normalized counts obtained by the radiometer to antenna temperature, and (2) remove beam sidelobe contributions to convert measured antenna temperature to target brightness temperature in the direction of the beam axis. In order to obtain values of T_b, the contribution to the signal from the sidelobes must be removed from each observation. To remove the sidelobe contributions from measurements of Saturn's rings, we developed an iterative adaptation of the successful calibration and sidelobe removal algorithms developed for Titan (Janssen et al., 2009, 2016) and Saturn (Janssen et al., 2013). Because Saturn is an order of magnitude brighter than the rings and always sits in the sidelobes, a more complex processing scheme was required to handle the sidelobes for ring observations.

The observed antenna temperature T_a is derived from the response to hot and cold reference targets observed by the antenna, while a reference load tracks relative gain variations. The conversion from normalized counts on the sky N_{sky} to T_a is given by (Janssen et al., 2009)

$$T_a = \left(N_{sky}/A\right) - T_{sys} \quad . \tag{2.3}$$

where T_{sys} is the system baseline offset due to the receiver noise temperature and the physical

temperature of the reference load, and A is the receiver gain. Both the baseline and gain drift with time due to the aging of receiver components. We use the gain calibration and drift factors described in Janssen et al. (2013), which include a time-dependent component allowing for linear gain drift

$$T_{acorr} = T_a \cdot (1 - 0.004t) \cdot F_{corr} \quad . \tag{2.4}$$

where t is the time in years since the start of September 2005. F_{corr} is the gain correction accounting for two factors: 1) gain calibration adjustment for converting original Titan calibration (Janssen et al., 2009) to September 2005 Saturn calibration (Janssen et al., 2013); 2) the reduction in reference Titan brightness of 92K by a factor of 0.994 at the top of the atmosphere (Janssen et al., 2016).

After deriving calibrated measurements of T_a, it remains to obtain the brightness temperature T_b in the direction of the beam center. The main objective of this task is to remove contributions that are distant from the beam axis in order to obtain a best estimate of the on-axis brightness. We begin by separating the antenna temperature into the cold sky baseline T_{zero} and the relative antenna temperature T_a' with respect to the cold sky:

$$T_a = T_{zero} + T_a' \quad . \tag{2.5}$$

The cold sky baseline T_{zero} is determined from excursions off-source at the end of every scan. By linearly interpolating baseline estimates with time between adjacent cold sky observations, we obtain the offset for each point.

The antenna gain pattern can be written as the sum of a main beam and a sidelobe pattern (Janssen

et al., 2009):

$$G(\theta,\phi) = G_{mb}(\theta,\phi) + G_{sl}(\theta,\phi) \quad . \tag{2.6}$$

Therefore, the antenna temperature T_a in Eqn.(2.1) can now be written as:

$$T_a = T_{zero} + \int_0^{2\pi}\int_0^{\pi}(T_b(\theta,\phi) - 2.7K)\cdot(G_{mb}(\theta,\phi) + G_{sl}(\theta,\phi))sin\theta d\theta d\phi. \tag{2.7}$$

where 2.7 K is the CMB brightness temperature when looking at cold sky. Our desired result is the average brightness in the main beam:

$$\bar{T}_{mb} = \frac{\int_0^{2\pi}\int_0^{\pi} T_b(\theta,\phi)G_{mb}(\theta,\phi)sin\theta d\theta d\phi}{\int_0^{2\pi}\int_0^{\pi} G_{mb}(\theta,\phi)sin\theta d\theta d\phi} \quad . \tag{2.8}$$

On the other hand, the average brightness in the sidelobes is given by

$$\bar{T}_{sl} = \frac{\int_0^{2\pi}\int_0^{\pi} T_b(\theta,\phi)G_{sl}(\theta,\phi)sin\theta d\theta d\phi}{\int_0^{2\pi}\int_0^{\pi} G_{sl}(\theta,\phi)sin\theta d\theta d\phi} \quad . \tag{2.9}$$

Combining Eq. (2.7) with (2.8) and (2.9) yields the mean brightness temperature in the main beam:

$$\bar{T}_{mb} = \frac{1}{1-b}[T_a - T_{zero} - b(\bar{T}_{sl} - 2.7K)] + 2.7K \quad . \tag{2.10}$$

where $b = \int_0^{2\pi}\int_0^{\pi} G_{sl}(\theta,\phi)sin\theta d\theta d\phi$.

Once the brightness temperature distribution is sufficiently well known, we can use Equation (2.10) to estimate and remove the fractional sidelobe contributions. Due to the broad gain pattern, Saturn is always sitting in the sidelobes. We use the modeled microwave brightness for Saturn, which varies with emission angle, derived in Janssen et al. (2013) when calculating their sidelobe contributions, and 2.7 K for the cold sky. However, the brightness distribution in Saturn's rings, which also contributes to the sidelobes, is measured as part of the scan as well. Therefore, a two-dimensional reference model of the brightness temperature of Saturn's rings, assumed to be a

function of azimuthal angle (the spacecraft projection on the ring plane lies at zero azimuthal angle) and radius (distance from Saturn center), is required for sidelobe removal. In order to obtain this model, which is essentially our desired measurement, we make an initial guess, then iterate the solution and update the reference model until it converges to a minimum RMS residual error between the modeled and observed antenna temperatures for a given set of observations. This iteration step is the primary modification between the processing procedure proposed herein and the processing algorithms described in Janssen et al. (2009), and Janssen et al. (2013).

Our initial guess for the reference model is a uniformly bright ring system at 7 K with *a priori* knowledge of the innermost (74510 km) and outermost (136780 km) radii of the C and A rings. Considering that the D ring (interior to the C ring) has very low optical depth and is barely observable in microwave regions, its sidelobe contributions can be neglected. The sidelobe contributions from the F ring (exterior to the A ring) are also generally ignored for the same reasons in addition to being quite narrow. We obtain modeled antenna temperatures by convolving the beam pattern with the brightness temperature reference model for each observation point. We then subtract the antenna temperature model from the calibrated and baseline-adjusted observed antenna temperatures to produce a residual map. These residuals are then added back into the model and used as a new reference model in the next iteration. We continue this process until reaching convergence, such that further updating of the input ring model does not result in further reduction of the residuals.

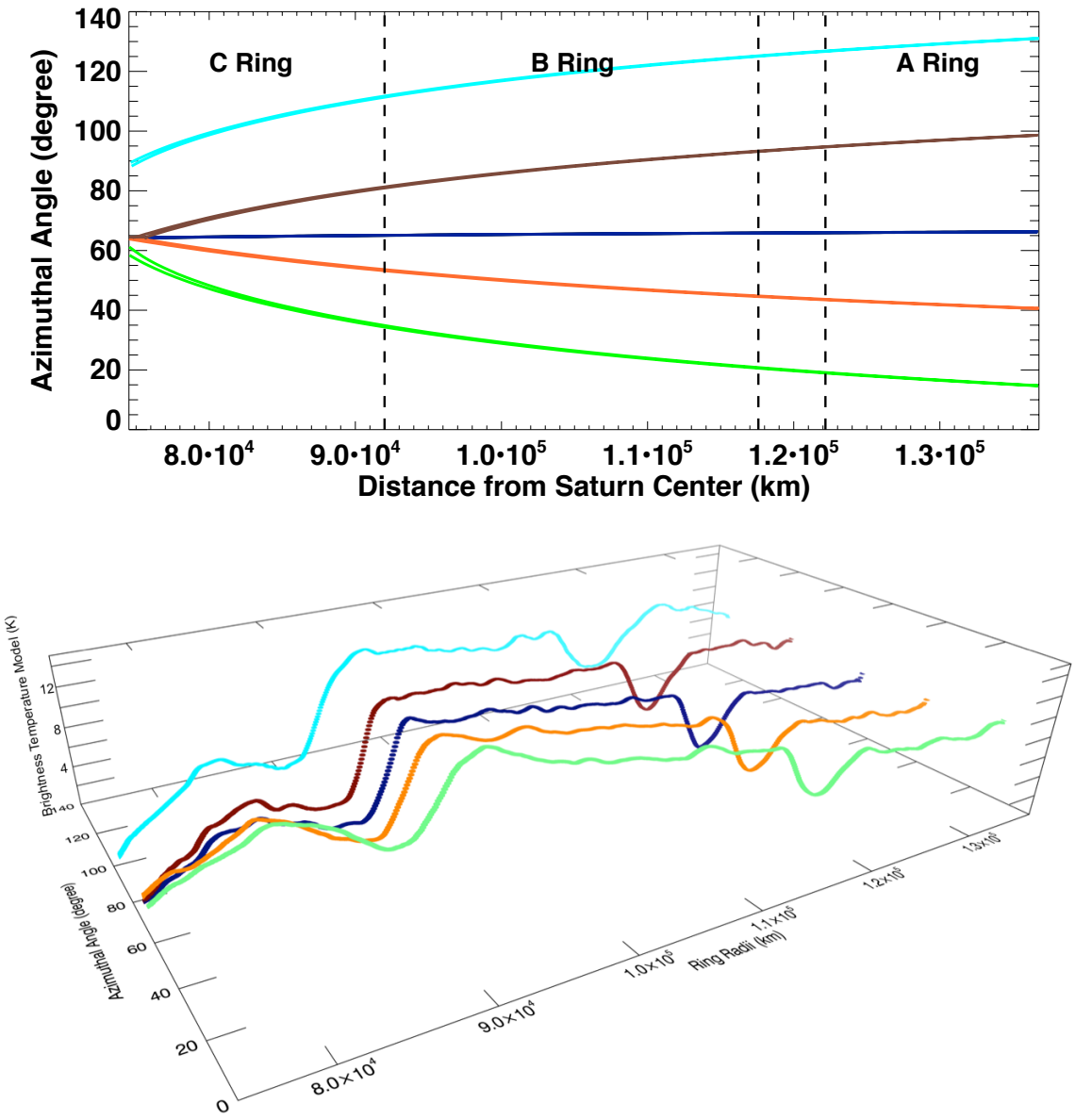

Figure 2.2: High-resolution spoke scans for Rev028_HIGH (Polarization 2); Upper panel: the C ring, B ring, Cassini Division (lying between the B and A rings) and A ring azimuthal angles vs ring radii covered. Data are collected at five distinct azimuthal angles. Lower panel: 1D brightness temperature model (brightness vs ring radius) for each spoke scan at one iteration. The colors correspond to the ones in the upper panel. We then interpolated between them to generate the 2D reference model.

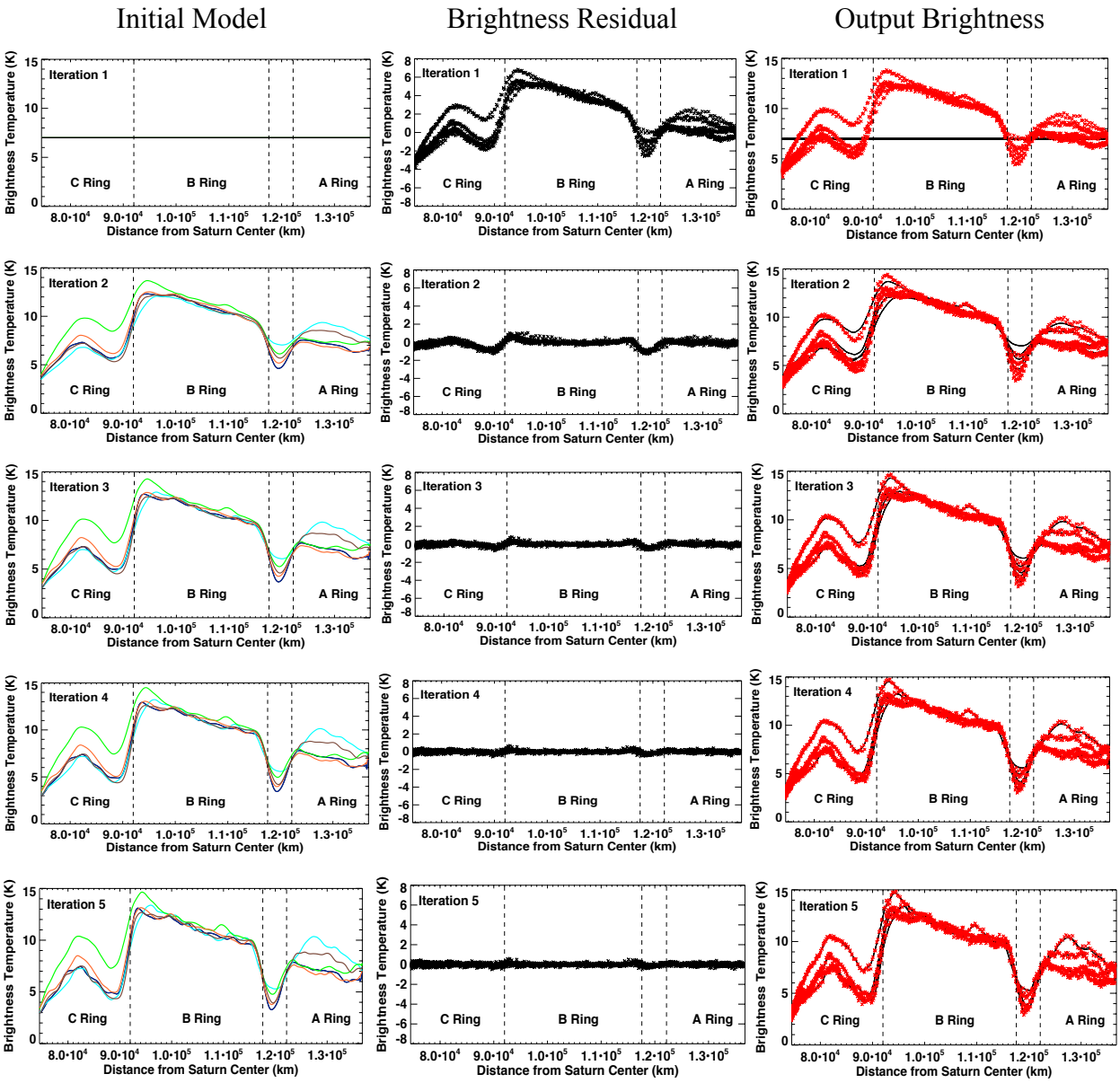

Figure 2.3: Iterative process when applying deconvolution to a set of high-resolution observations (Rev028_HIGH Polarization 2). Each row represents a single iteration. The left column shows the ring's brightness temperature reference model that we use to calculate sidelobe contributions in each iteration. We plot the brightness temperature vs. ring radius of the model at five representative azimuthal angles with different colors. Curves of different colors don't coincide with each other except in the B ring, which suggests a non-isotropic scattering profile in the C ring and asymmetric structure in the A ring. We will discuss this observed azimuthal variance further on in this section. The middle column shows the residual after subtracting modeled antenna temperature from observed antenna temperature, which represents the difference between scans of the reference ring

model and the real ring brightness map. A RMS of ~ 0.2 is reached after 5 iterations with no obvious structure being seen in the residual map at iteration 5. The right column shows the output of each iteration - the adjusted brightness temperature at each observation point (red crosses). The addition of the initial reference model (black curve) and the residual (shown in middle column) is used as the new reference model in the next iteration.

We now have enough information to generate a full-scale 2D brightness map model when calibrating data from low-resolution map scans, since they cover all radii and azimuths. However, for the high-resolution Rev028_HIGH, we only have five spoke scans at five distinct azimuthal angles (see **Figure 2.2**, upper panel), which does not provide enough information to generate a full map. To address this, we generated a 1D brightness temperature model (brightness vs ring radius) for each spoke scan (see Fig. 2.2, lower panel) and interpolated between them to get a full 2D map. This iterative calibration process is not very sensitive to initial model conditions. Even when starting with a totally uniform ring model, we obtain a minimum RMS residual of ~0.2 K after typically ~5 iterations, which is about 2% of the observed brightness temperature (see **Figure 2.3**). Different initial models converge to the same output ring brightness map after a similar number of iterations which gives us confidence in our approach. We note that during our calibration process, there was an issue caused by a beam offset, especially for the low-resolution scans when the observer-target distance is large. We readily resolved this issue by applying an appropriate antenna pointing correction (see Sec.2.3).

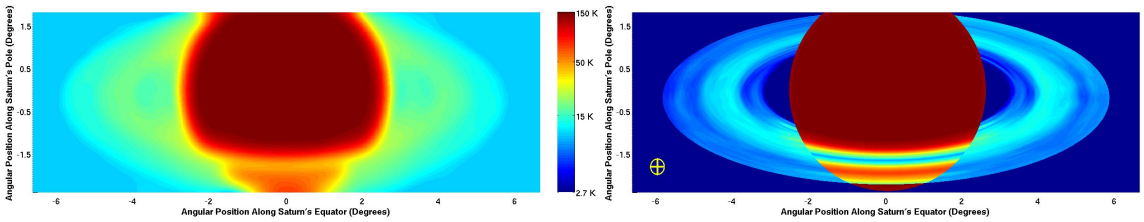

Figure 2.4: Calibration of low-resolution Cassini Radar map scans obtained during Rev038_2_LOW (polarization 2) as projected onto the sky in degrees. Left panel: The collected antenna temperature map covers Saturn and its ring system using a combination of a large number of observations. Due to the wide antenna pattern and extensive sidelobe contribution from Saturn, the antenna temperature shows very little clear structure of the main rings. Right panel: The output brightness temperature map obtained through our calibration. Structures in the main rings are clearly visible with a RMS residual of ~2%. The yellow circle in the lower left corner shows the main beam size, which is also the data resolution we can achieve after the calibration.

Figure 2.4 shows the output of our calibration and processing applied to a low-resolution map scan of Saturn's rings obtained during Rev038_2_LOW. Within low-resolution map scans, observations with the main beam where the rings occult Saturn's disk are referred to as "occultation" data. These data are similar to stellar occultations observed by Voyager and Visual and Infrared Mapping Spectrometer (VIMS), except that the source of radiation is the planet itself. **Figure 2.5** (upper panel) shows the radial brightness temperature profile of the deconvolved occultation data in Rev038_2_LOW. The brightness temperatures at any given ring radius are scattered because we have combined observations at various azimuthal angles. Figure 2.5 (lower panel) shows the coverage of ring radius and azimuthal angles of the occultation observations shown in the upper panel. They are part of the Rev038_2_LOW scan path (see Fig. 2.1 upper panel for an example of low-resolution map scan paths), where the main beam falls on C ring regions that are occulting Saturn. We note that there are fine structures of about ~1/10 of our beam

resolution, which are actually not resolved radial structure but are correlated with the azimuthal angles these data were collected at. These small bumps (as can be seen in the red box, upper panel) in the brightness temperature profile were collected at azimuthal angles approaching zero (red box, lower panel). Their increased brightness is because the C ring particle scattering phase function increases with decreasing scattering angle near zero azimuth (see Sec. 3.6).

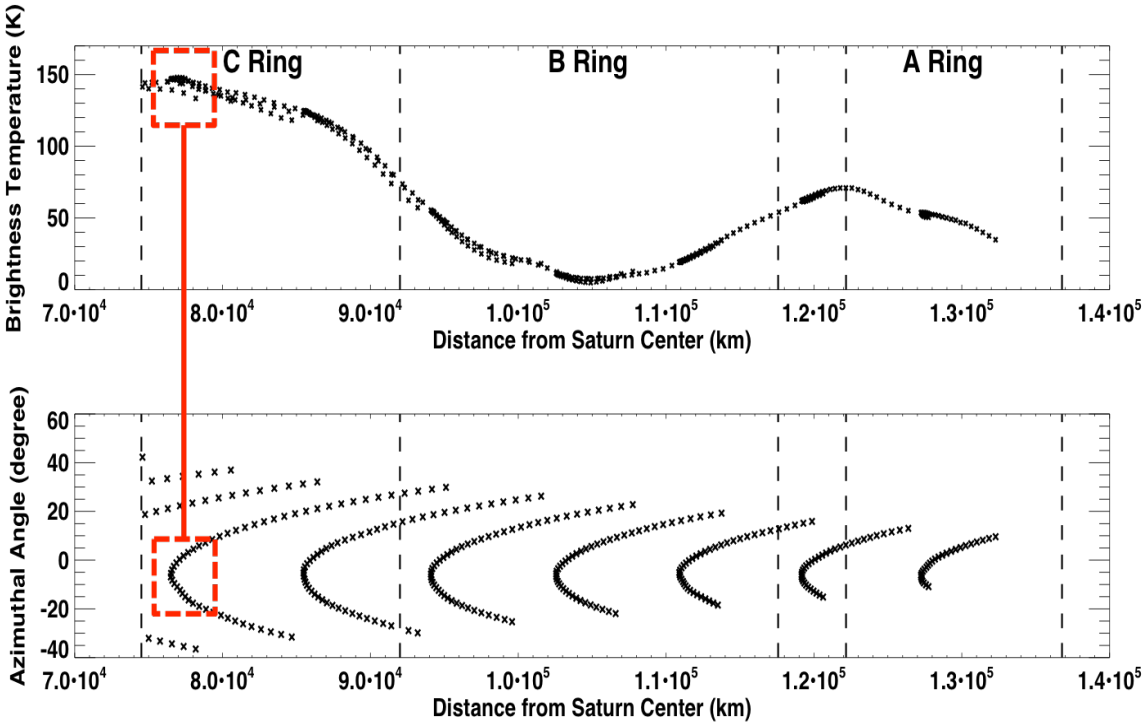

Figure 2.5: Occultation observations in Rev038_2_LOW (Polarization 2); Upper panel: the radial brightness temperature profile of these occultation data (brightness temperature vs ring radius). We have combined observations at various azimuthal angles (as shown in the lower panel). Lower panel: the coverage of ring radius and azimuthal angles of the occultation observations shown in the upper panel. The small bumps in the red box in the upper panel correspond to the azimuth range in the red box in the lower panel, and appear to be ~ 1/10 our radial resolution (our radial resolution is ~8,000 km). However these small bumps, which were collected at azimuthal angles approaching zero, are not radially resolved structure, but are actually caused by the phase function

increase with decreasing scatter angle near zero azimuth.

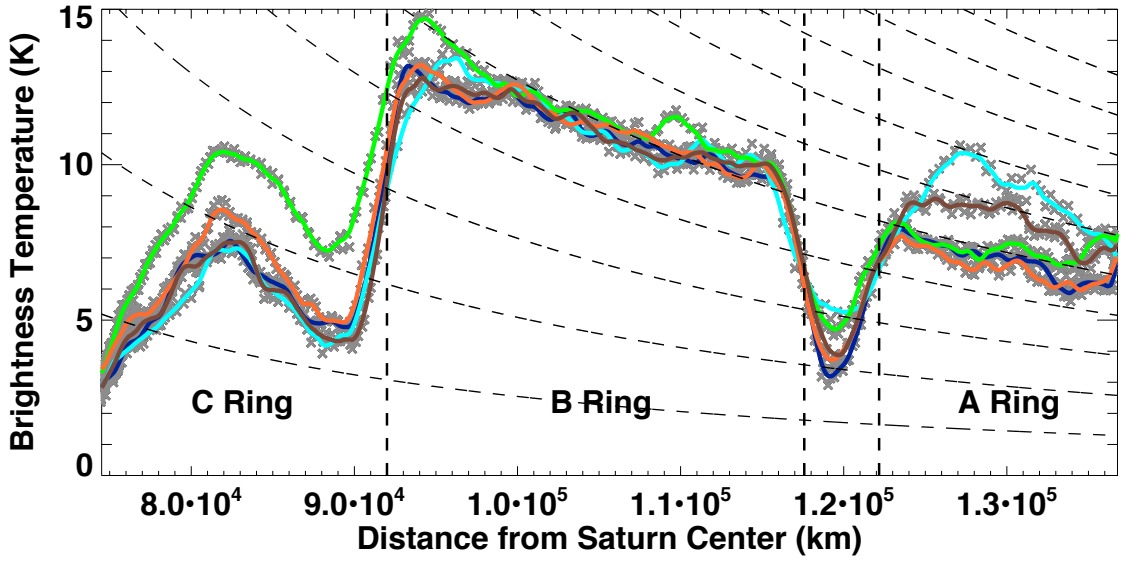

Figure 2.6: Brightness temperature T_b versus ring radius (from Rev028_HIGH polarization 2). For Rev028_HIGH, each polarization has spoke scans at five distinct azimuthal angles (see upper panel in Fig. 2.2). We plot the best reference rings brightness models (solid lines) and output brightness temperatures (grey crosses) for the last iteration of our calibration process. Solid lines of different color indicate spoke scans at different azimuthal angles (the colors correspond to the azimuthal angles in the upper panel in Fig. 2.2). The black dashed lines show the trend of incident Saturn radiation, which decreases as one moves further away from Saturn's center. The bold vertical dashed lines indicate the borders between the different ring regions.

Figure 2.6 shows the brightness temperature T_b profile vs. distance from Saturn center after processing the Rev028_HIGH high-resolution spoke-scans. All of these observations are collected when the rings are not occulting Saturn, at azimuthal angles larger than 20 degrees. Going from the C ring to B ring and then to A ring, the distance from Saturn increases, and hence the planet's angular size decreases as seen from Cassini's vantage point. The dashed curves in Fig. 2.6 illustrate the decreasing trend of incoming radiation from Saturn as the observation point moves further

away from Saturn center. While T_b follows the trend of incoming Saturn radiation in most parts of the rings, the distinct bump (with a peak at ~83,000 km) in the C ring's brightness is too large to be attributed simply to optical depth variation (see Sec. 4.1), which suggests some unusual properties. We will show that this effect may result from a radially variable increase in non-icy material fraction that produces an extra amount of intrinsic thermal emission.

In Fig. 2.6, we also see significant variations between spoke scans at different azimuthal angles in the C and A rings, as opposed to the consistent agreement seen in the B ring. In the C ring, the one especially high scan (green curve) was collected at the smallest azimuthal angle (~40°, see the green curve in Fig. 2.2, upper panel). Because the particle size distribution in the C ring is characterized by a steep power law (q=3.15, see Sec. 3.2) with a minimum size ($a_{\min}$=0.4 cm) an order of magnitude smaller than our wavelength, their scattering behavior can be approximated by Mie scattering, which is forward directed. Therefore, a larger amount of light will be scattered into smaller azimuthal angles. However, in the A and B rings, non-sphericity and close-packing effects become important, and therefore ring particles scatter light more isotropically (see Sec. 3.6). This is why in the B ring, the brightness of spoke scans at different azimuthal angles are quite similar. On the other hand, the difference between different spoke scans in the A ring is caused by the self-gravity wake structures (Nicholson and Hedman, 2010). For this set of high-resolution spoke scans, the spacecraft only scans the west side of the ansae. The spoke scan with the highest brightness in the A ring (light blue curve) was collected at the largest azimuthal angle (~130°), which is consistent with previous VLA observations (Dunn et al., 2004) (see light blue curve in Fig. 2.2, upper panel).

We also investigated the polarization effects (Grossman et al. 1989, van der Tak et al. 1999) in the

data. In the C ring, the observed light is most polarized at ~80° azimuth, where the degree of linear polarization reaches its maximum value of ~-20% (negative for linear polarization perpendicular to the scattering plane). The brightness in the B and A rings is less polarized, with the value of the degree of linear polarization less than 8%. Due to the complicated and widespread directions of the incident Saturn radiation, it is very difficult to simulate the polarization effect. Although our model (see Chapter 3) cannot deal with polarization, fortunately the non-icy material fraction and the amount of thermal emission in the C ring, which are the main focus of this work, don't depend on the direction of the polarization. Therefore, we combine the data from all three polarizations and treat them as unpolarized. However this polarization variation in observed brightness will have the effect of increasing the uncertainty of our final non-icy material fraction profile.

2.3 Correction for Radar Beam 3 Boresight Direction

After investigating the brightness temperature profiles (brightness temperature vs. ring radius) of the occulting rings in our four low-resolution map scans, we uncovered a radial misalignment between profiles from different observations. The misalignment between Rev038_1_LOW and Rev038_2_LOW is the most significant, being as large as 3,000 km (See **Figure 2.7**, panel 1). As an example, in Fig. 2.7, panel 1, we plot the brightness temperature profile of Rev038_1_LOW and Rev038_2_LOW both at polarization 2, which suggests that this misalignment is not due to particle scattering effects. The brightness temperature profiles of occulting rings from the other two occasions lie in between Rev038_1_LOW and Rev038_2_LOW (see Fig. 2.7, panel 2), which implies that it is not a breakdown on any one particular occasion, but a radial misalignment that exists in all the observations. A possible reason for this misalignment may be a shift of the

boresight direction of Radar beam 3 (see below).

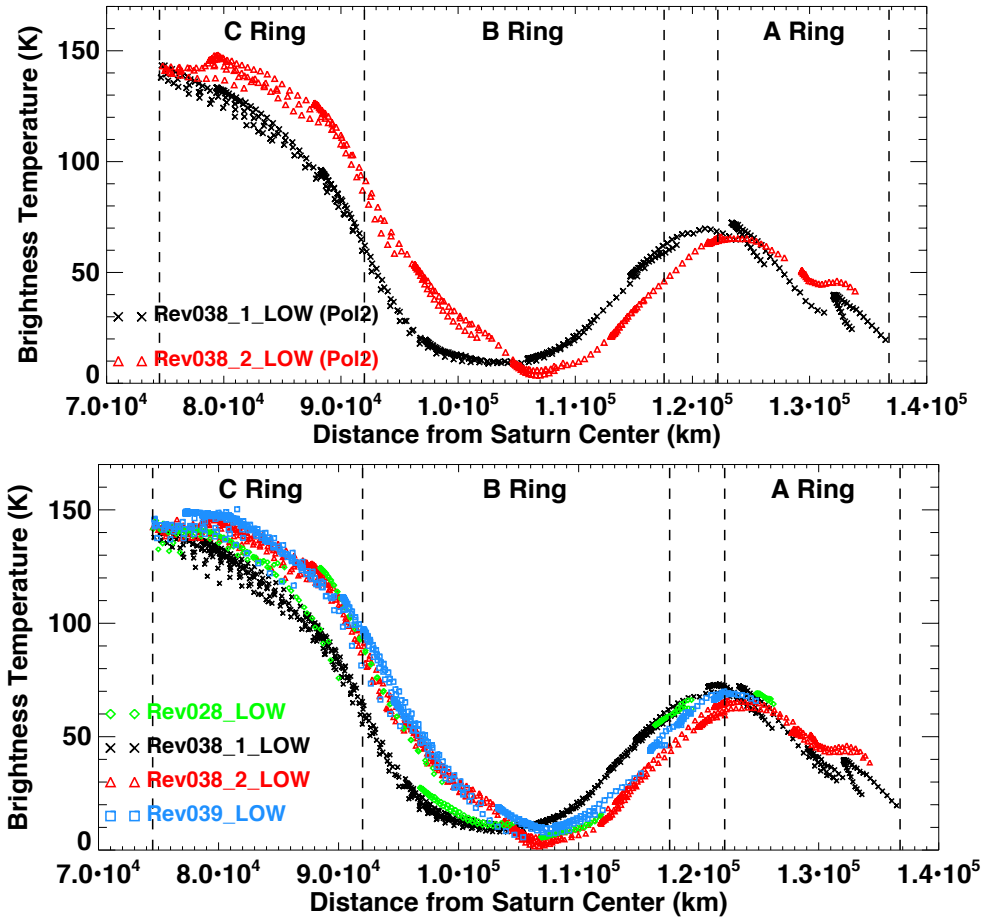

Figure 2.7: Brightness temperature profiles (brightness temperature vs. ring radius) of occulting data in low-resolution map scans. Upper panel: The radial misalignment of the brightness temperature profiles between Rev038_1_LOW and Rev038_2_LOW at polarization 2. Lower panel: the brightness temperature profiles of occultation data from all four low-resolution map-scan occasions. All available polarizations are combined together for each occasion in the lower panel.

The Radar beam 3 boresight axis was designed to lie along the spacecraft –Z axis and no adjustment to its pointing in the spacecraft coordinates has been reported. However, RSS and RADAR observations share the same physical antenna. The X band and Ka band boresights have

been shifted from the spacecraft –Z axis [0, 0, -1] to [0.0004900, 0.0004500, -0.9999998] as recorded in the Cassini spacecraft frame definitions kernel. These boresight directions were corrected as a result of RSS radio occultation observations. It is very likely that Radar beam 3, which shares the same receiving feed with X- and Ka-band, requires the same boresight directional shift. Thus, we applied the above updated boresight direction to our calibration and found that it aligned all four brightness temperature profiles (see Fig. 2.8).

In **Figure 2.8**, the observed brightness points are not as perfectly aligned as is any single observation. There are two main reasons for this ~10 K spread. First, the slight differences between different occasions may be caused by the change in the Cassini-Saturn distance and in the ring opening angle during different occasions. For example, the smallest Cassini-Saturn distance was 19 Saturn radii for Rev028_LOW while the largest distance was 24 Saturn radii for Rev038_1_LOW. The resolution for Rev028_LOW is thus 20% higher than that for Rev038_1_LOW. Furthermore, the ring opening angle for Rev038_1_LOW of ~-18 to -20 degrees increases to ~-22 to -25 degrees for Rev039_LOW. A larger ring-opening angle will not only lead to a slight increase in the resolution (the radial projection of the beam on the ring layer becomes smaller), but also diminish the transmittance. In the C ring, for example, in regions with optical depth of 0.2, the directly transmitted light increases by 15 K as the ring opening angle increase from 18 to 25 degrees. All these differences in geometry may cause small differences in the brightness profiles. Second, in some circumstances, the spread of brightness temperature at a particular ring radius may be due to comparing observations at different azimuthal angles. In the C ring, for example, half of the brightness is contributed by scattered Saturn radiation and the scattering phase function varies quickly at small scattering angles.

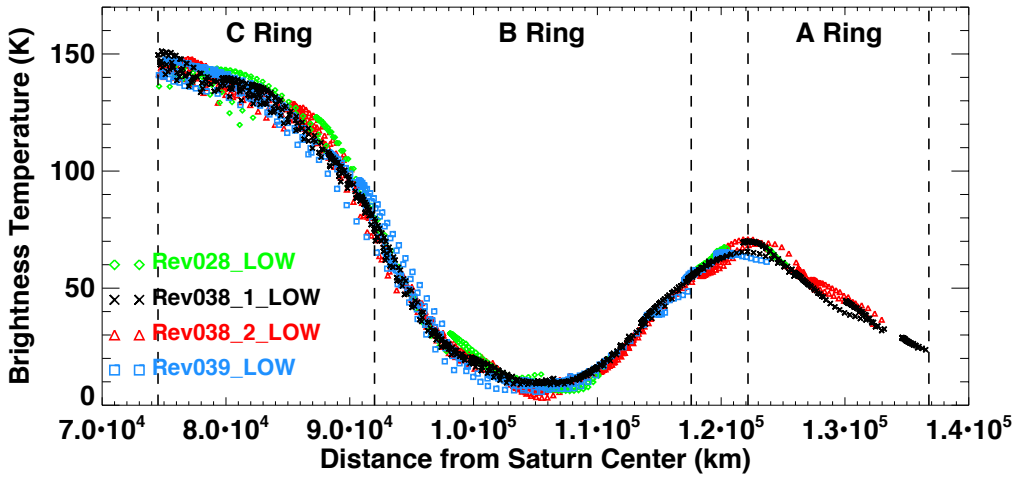

Figure 2.8: Brightness temperature profile of occultation data for all four low-resolution scans after applying the boresight correction. These data now coincide with each other quite well.

3 Brightness Temperature Model

The observed brightness temperature T_b is composed of four components: (1) directly transmitted Saturn radiation (which exists in occultation data only); (2) scattered Saturn radiation; (3) intrinsic thermal emission; and (4) cosmic microwave background (CMB) contributions. To simulate the observed brightness we use the Monte-Carlo-based photon counting code *SimRings* (Dunn et al., 2002). *SimRings* is able to deal with multiple scattering within the ring layer (where the light source is from extended Saturn emission) and derive the amount of directly transmitted Saturn radiation, scattered Saturn radiation and the intrinsic thermal emission that arrives at the observer. *SimRings* requires knowledge of the ring particles' composition and size distribution, which determines the scattering phase function and absorption rate, and the local optical depth. The amount of directly transmitted Saturn radiation merely depends on the ring's optical depth, the viewing angle and whether the ring is occulting Saturn's disk at the observation point, while the rings' intrinsic thermal emission mainly depends on the non-icy material fraction since the emissivity of water ice

at 2.2 cm is negligible. Considering that the imaginary part of the dielectric constant of water ice is 3 orders of magnitude smaller than that of the non-icy material (see Sec.3.2), the absorptivity of water ice is thus 3 orders of magnitude smaller than the non-icy material. According to Kirchhoff's law, emissivity equals absorptivity, therefore the rings' intrinsic thermal emission, which is proportional to the effective emissivity of the ring particles, is dominated by the non-icy material contribution.

3.1 Radiation Sources: Saturn Emission and Cosmic Microwave Background

As seen from a point in Saturn's rings, CMB radiation would come in isotropically from all directions at a temperature of 2.7 K, if Saturn were not there. The incident CMB radiation can be transmitted, scattered or absorbed by the rings, but due to the low emissivity of the rings' icy particles, the fraction of the CMB radiation absorbed by the C ring can be ignored. As we find as a result of this work, even in the middle C ring, where the intrinsic thermal emission is highest, the absorption rate is only about 6%, which will result in an absorption of ~0.16 K from the CMB brightness. Furthermore, according to Dunn et al. (2002), for their VLA observations the case that deviates the most from perfect scattering (the optically thick B ring at a low inclination of -4.91°) has only 9% of the photons absorbed, yielding a CMB contribution just 0.25 K lower. Thus in all cases the deviation due to absorption is small compared to the observational uncertainties, and it has been neglected in our model. Considering the isotropic nature of the incident CMB, no matter in which direction one observes the rings from, one will always receive a CMB contribution of about 2.7 K. However, Saturn blocks out ~ 4% - 10% of the sky as seen from the rings and, with it, also the CMB radiation from those directions. For objects as opaque and absorbing as Saturn, no CMB radiation can be transmitted through or reflected back, and in those directions where the

sky is blocked by Saturn, the rings will receive Saturn radiation instead. In order to calculate the CMB contribution to the observed ring brightness, we will need to simulate how it is scattered by the rings, integrating the incident CMB radiation over 4π steradians but omitting the portion blocked by Saturn. To limit computational complexity, we approximate the CMB contribution by removing 2.7 K from the Saturn thermal radiation and then combining the reduced Saturn radiation with fully isotropic CMB radiation. This leaves us with isotropic radiation of 2.7 K coming in from all directions, which will result in a ~2.7 K contribution to the observed brightness temperature. We therefore use an effective Saturn thermal radiation which is 2.7 K less than the true Saturn thermal radiation to calculate the directly transmitted and scattered component in our Monte-Carlo code. In the end, the total simulated brightness temperature is the sum of directly transmitted effective Saturn radiation, scattered effective Saturn radiation, intrinsic thermal emission from the rings, and the 2.7 K CMB contribution.

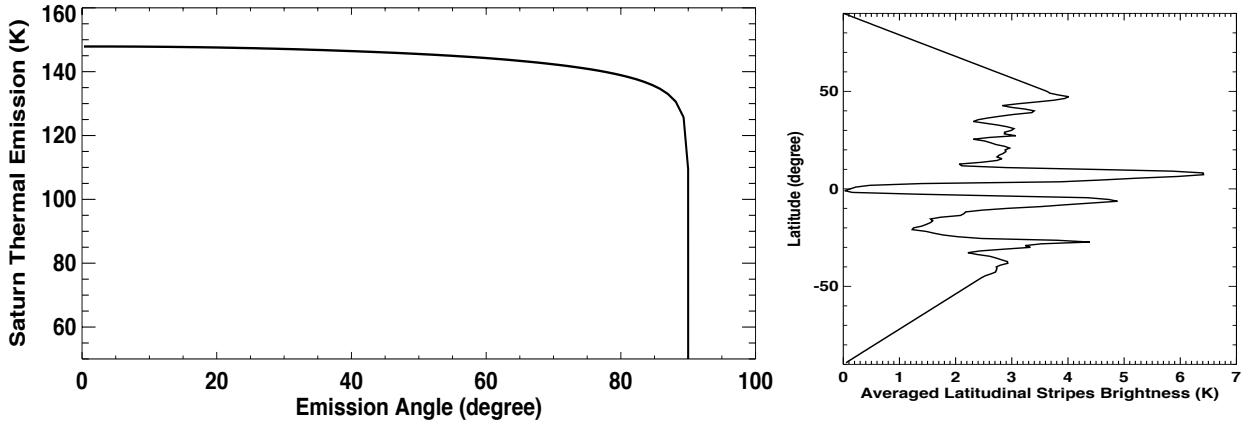

Figure 3.1: Saturn radiation model from results of previous RADAR observations (Janssen et al. 2013). Left panel: Limb darkened Saturn disk with brightness values as a function of emission angle. Right panel: latitude-dependent stripes, brightness temperature variations versus latitude on top of the limb darkened disk.

Finally, due to Saturn's large solid angle as seen from the rings, a resolved Saturn thermal emission model is required. In this work, we use the Saturn radiation model derived from previous RADAR observations by Janssen et al. (2013). The model is presented as a limb-darkened disk with brightness temperature as a function of emission angle (see **Figure 3.1**, panel 1), and with latitude-dependent stripes (see Fig. 3.1 panel 2) on top of the limb darkened disk. Since these stripes have been longitudinally averaged, any longitudinal brightness variations are not captured by our model. In Janssen et al. (2013), the latitudinal stripes are derived independently from five observations. These variations are mainly concentrated at the equatorial region, and can be up to ~10 K, which can cause noticeable uncertainties in the direct transmitted and forward scattered light when the observed rings are occulting Saturn. Fig. 3.1 panel 2 shows the averaged stripes among those five observations, which is what we applied in this work.

3.2 Ring Particle Composition and Size Distribution

The ring particle composition is used to determine the material's effective dielectric constant based on the Maxwell-Garnett mixing rule of Effective Medium Theory (EMT; see, Bohren and Huffman, 1983). We assume the ring particles are made of porous water ice with non-icy material embedded in the form of small inclusions. Assuming the inclusions are spherical, the complex effective dielectric constant of a porous mixture of water ice and intermixed non-icy material can be expressed as

$$\varepsilon_{\text{eff}} = \varepsilon_{\text{ice}}\left[1 + \frac{3(f_v(1-f_p)\frac{\varepsilon_{\text{non-ice}}-\varepsilon_{\text{ice}}}{\varepsilon_{\text{non-ice}}+2\varepsilon_{\text{ice}}}+f_p\frac{1-\varepsilon_{\text{ice}}}{1+2\varepsilon_{\text{ice}}})}{1-(f_v(1-f_p)\frac{\varepsilon_{\text{non-ice}}-\varepsilon_{\text{ice}}}{\varepsilon_{\text{non-ice}}+2\varepsilon_{\text{ice}}}+f_p\frac{1-\varepsilon_{\text{ice}}}{1+2\varepsilon_{\text{ice}}})}\right], \quad (3.1)$$

where $\varepsilon_{\text{non-ice}}$ and ε_{ice} are the complex dielectric constants of the non-icy mixture and pure ice,

respectively, f_p is the particle porosity and f_v is the volume fraction of non-icy material mixed within the ice. In the limit that $f_v \to 0$, Eq. (3.1) simply describes the dielectric constant of a porous ice particle, whereas in the limit $f_p \to 0$, Eq. (3.1) reduces to the more general formula for a single component embedded in an ice medium (e.g., Bohren and Huffman, 1983; Cuzzi et al., 2014). We primarily use silicates as the candidate for the intermixed non-icy material (see Sec. 5.2.4) which has dielectric constant $\varepsilon_{\text{silicate}} = 5.38\text{-i} \cdot 0.134$ (Cuzzi et al., 1980).

As for the dielectric constant of water ice, we follow the relations used by Grossman (1990) and Dunn et al. (2002). The complex index of refraction is $n=n_r\text{-}in_i$. The real part of the refractive index, n_r, is 1.78, while the imaginary part of the refractive index is $n_i = \alpha_\lambda \lambda / 4\pi$, where α_λ is the absorption coefficient. Mishima et al. (1983) provided the laboratory results for absorption coefficient

$$\alpha_{H_2O_{ice}} = \frac{A_0}{T} \frac{e^{hc\upsilon_0/kT}}{\left(e^{hc\upsilon_0/kT}-1\right)^2} \left(\frac{\upsilon}{\upsilon_0}\right)^2 + B_0 \upsilon^4 \tag{3.2}$$

where ν is wavenumber in cm^{-1}, $\nu_0 = 233\ cm^{-1}$, $A_0 = (1.188 \pm 0.01)\times 10^5\ cm^{-1}K$, and $B_0 = (1.11 \pm 0.03)\times 10^{-6}\ cm^3$. We can calculate the dielectric constant using the relation between refractive index and dielectric constant $\varepsilon = n^2$. The dielectric constant of water ice varies with the rings physical temperature (Mishima et al., 1983) and observed wavelength. At a wavelength of $\lambda = 2.2$ cm, the values for water ice at characteristic ring temperatures are summarized in **Table 3.1**. All our data are collected at the unlit side of the ring plane, which shows less temperature variations with the phase angle (Sun-particle-observer angle) especially in the B and A rings. The low-resolution occultation data are collected at either low phase 50° ~ 58° or high phase 154° ~ 162°, while the high-resolution ansa data are collected at 94° ~ 103° phase

angle. The solar elevation angle is always about -13.5° ~ -16.0°. We took into account all these factors and obtained the rings physical temperature based on Hanel et al., 1981;1982, Spilker et al. 2006 and Flandes et al. 2010. Due to the limited measurements that have been reported, we still have some uncertainties in the rings physical temperature. The uncertainties in the rings physical temperature don't affect the real part of the water ice dielectric constant. Also considering that the imaginary component of the water ice dielectric constant is orders of magnitude smaller than that of the silicates, the uncertainties in the rings physical temperature don't affect the calculation of the ring particles effective dielectric constant much. As a comparison, the water ice dielectric constant used in Cuzzi et al. (1980) for C ring particles at $T_{ring} = 100\ K$ and $\lambda = 2.2\ cm$ is $\varepsilon_{ice} = 3.17 - i \cdot 1.2\times10^{-4}$, while the calculated value at corresponding T_{ring} and λ with the relations we use is $\varepsilon_{ice} = 3.17 - i \cdot 1.1\times10^{-4}$.

Table 3.1: Physical temperature and water ice dielectric constant in the main rings at 2.2 cm.

	Physical Temperature	ε_{ice}		
C Ring	85 K ~ 95 K	$(3.17 - i \cdot 6.68\times10^{-5})$	~	$(3.17 - i \cdot 9.24\times10^{-5})$
B Ring	60 K ~ 65 K	$(3.17 - i \cdot 1.77\times10^{-5})$	~	$(3.17 - i \cdot 2.53\times10^{-5})$
Cassini Division	80 K ~ 85 K	$(3.17 - i \cdot 5.50\times10^{-5})$	~	$(3.17 - i \cdot 6.68\times10^{-5})$
A Ring	70 K ~ 75 K	$(3.17 - i \cdot 3.41\times10^{-5})$	~	$(3.17 - i \cdot 4.41\times10^{-5})$

The ring particles are assumed to have a power law size distribution as described in Sec. 3.2, $n(a) = n_0 a^{-q}$, with minimum size a_{min}, maximum size a_{max}, power law index q and a constant n_0 which depends on the particle areal number density in the rings. An important result derived from density wave measurements that relate the particle sizes and their mean densities is the opacity:

$$\kappa = \frac{\tau_{geometry}}{\sigma} = \frac{\int_{a_{\min}}^{a_{\max}} \pi a^2 \cdot n_0 a^{-q} \cdot da}{\int_{a_{\min}}^{a_{\max}} \frac{4\pi}{3} a^3 \overline{\rho} \cdot n_0 a^{-q} \cdot da} \sim \frac{3(4-q)}{4(3-q)\overline{\rho}} \cdot \frac{a_{\max}^{3-q} - a_{\min}^{3-q}}{a_{\max}^{4-q} - a_{\min}^{4-q}} . \quad (3.3)$$

where σ is the surface mass density, and $\tau_{geometry}$ is the geometric optical depth. Furthermore, the mean particle density can be approximated as $\overline{\rho} \sim (1 - f_p)\rho_{water\_ice}$ for particles containing less than 10% silicates (the derived non-icy material fractions in the C ring, B ring, A ring and Cassini Division are all less than 10%, see Sec. 4). Thus we can approximate the opacity as:

$$\kappa \sim \frac{3(4-q)}{4(3-q)} \cdot \frac{a_{max}^{3-q} - a_{min}^{3-q}}{a_{max}^{4-q} - a_{min}^{4-q}} \cdot \frac{1}{(1-f_p)\rho_{water\_ice}} \quad (3.4)$$

For the C ring particles, the particle size distribution parameters determined from the Voyager radio occultation observations give a power law index q = 3.11, and a maximum particle size $a_{\max}$ = 4.5 m for the inner and middle C ring region (74,430 - 84,460 km), and q = 3.05, and a maximum particle size $a_{\max}$ = 2.4 - 5.3 m for the C ring ramp (90,640 - 91,970 km), assuming a thin-layered ring model (Zebker et al., 1985). Furthermore, the C ring shows a minimum particle size of 0.4 cm from the stellar occultation observations (Harbison et al., 2013). The differential optical depth values from the Cassini RSS occultation also supports the 0.4 cm minimum size, but with a steeper size distribution slope of q = 3.2 or slightly larger (Cuzzi et al., 2009; Marouf et al., 2008). In this work, we choose as our nominal values $a_{\min}$ = 0.4 cm, $a_{\max}$ = 450 cm, and q = 3.15 for the C and D ring particles.

For the B ring particles, the particle size distribution parameters determined from the Earth-based 28 Sgr stellar occultation (French and Nicholson, 2000) give a single uniform values across the B

ring[1] of a power law index of $q = 2.75$, a minimum particle size $a_{min} = 30$ cm and a maximum size $a_{max} = 20$ m. This maximum size is a factor of two larger than the Voyager RSS result, in which it was determined that $a_{max} = 5$ - 11 m (Zebker et al., 1985). However, recent measurements from density waves suggest that the B ring has opacity ~ 0.03 - 0.05 $cm^2\ g^{-1}$ (Hedman and Nicholson, 2016). If $a_{max} = 11$ m or 20 m, then the particle porosity would need to be as high as 95% in order to match the wave measurements, while a maximum size of 5m would require a significant particle porosity of 85%-90%. Therefore if the B ring particles are well characterized by a power law distribution, the maximum size is more likely to be close to ~5 m. It turns out, however, that our simulations do not vary much with the maximum particle size, since smaller particles play a more important role in the scattering process. On the other end, the minimum size $a_{min} = 30$ cm derived from the 28 Sgr occultation is consistent with models of the Cassini RSS data in the middle and outer B ring, but note those same models imply a smaller a_{min} in the mm-cm range in the inner B ring "flat" region (see Marouf et al., 2008; Cuzzi et al., 2009). However, for this work we adopt the values $a_{min} = 30$ cm, $a_{max} = 630$ cm, and $q = 2.75$ as our nominal set of parameters for the particle size distribution across the B ring. Particle porosity is also important in determining the scattering phase function and effective dielectric constant of the ring particles. Thus, we simulate several cases with porosity values of 55%, 75%, 80%, 85% and 90%.

For the Cassini Division, the Voyager radio occultation observations suggested a minimum size $a_{min} = 0.1\ cm$, maximum size $a_{max} = 7.5\ m$ and power law index $q = 2.79$ (Zebker et al. 1985) which we use as our nominal set for the ring particles there. As we do for the B ring, we simulate cases where the Cassini Division particles have the range of porosity defined above. On

[1] With the exception of the region that includes the B ring core which was noise limited.

the other hand, according to wave measurements, the opacity in the Cassini Division is ~0.064 - 0.111 $cm^2\ g^{-1}$ (Colwell et al. 2009). With the particle size distribution parameters measured by the Voyager radio occultation, Eq. (3.4) for κ basically demonstrates that the more porous the particles are (*i.e.,* the lower their mean densities), the higher the opacity would be. However, even for particles with porosities of 90%, the calculated opacity of ~0.052 $cm^2\ g^{-1}$ is still not as high as the observed value. This may be due to the possibility that the maximum particle size is actually smaller than 7.5 m, or that the power law index is steeper than the assumed value of 2.79, which will both increase the derived opacity. Yet it may also be the case that the Cassini Division particles might have porosities as high, or greater than 90%.

Finally for the A ring particles, the minimum particle size and power law index again are determined from the 28 Sgr stellar occultation (French and Nicholson, 2000). These values are given by $a_{min} = 30\ cm, q = 2.75$ in the inner A ring (*i.e.*, interior to the Encke gap), and $a_{min} = 1\ cm, q = 2.9$ at the outer edge of the A ring (exterior to the Encke gap). Furthermore, the maximum particle size varies with ring radius (see **Table 3.2**), as determined from the Voyager radio occultation observation (Zebker et al. 1985). However, the X-S and Ka-X differential optical depth comparison from the RSS observation suggests a smaller minimum particle size of ~5 mm and a steeper power distribution with q ~ 3.2 in the outer A ring exterior to the Encke gap (Marouf et al., 2008; Cuzzi et al., 2009). Moreover, Cassini VIMS solar occultation observations also indicate that the minimum particle size in the A ring might be even smaller than 1mm contradicting the results of earlier analyses in the visible and IR (Dones et al., 1993; French and Nicholson, 2000), though relatively little optical depth is provided by these small particles (Harbison et al.,

2013). Due to these variations in the A ring parameters, we explore three cases with different particle size distributions for outside the Encke gap region for a range of porosities. We have separated the A ring into regions A0, A1, A2, and A3 with the radial ranges denoted in Table 3.2.

Table 3.2: Particle size distribution parameters in the main rings.

Ring Radius (km)	$a_{\min}$ **(cm)**	$a_{\max}$ **(m)**	q
C Ring: 74,510 – 92,000	0.4	4.5	3.15
B Ring: 92,000 - 117,580	30.0	6.3	2.75
Cassini Division: 117,580-122,170	0.1	7.5	2.79
A Ring			
A0: 122,170 - 127,900	30.0	5.4	2.75
A1: 127,900 - 130,860	30.0	6.3	2.75
A2: 130,860 - 133,423	30.0	11.2	2.75
A3: 133,423 - 136780			
A3-Case 1:	0.5	8.9	3.2
A3-Case 2:	1.0	8.9	2.9
A3-Case 3:	30.0	6.3	2.75

3.3 Optical Depth

An important parameter in our model is the optical depth τ, which is a measure of the particle column density, and therefore determines how much incident light is directly transmitted through the rings without interacting with any particles, how many times the incident light gets scattered by the ring particles before getting out of the ring layer, and also how much intrinsic thermal emission is generated within ring particles. We employ the normal optical depth profile measured by the Cassini Radio Science Subsystem (RSS) at λ_0 = 3.557 cm (PDS Rings Node, Cuzzi et al., 2009). This profile was observed during the Rev 7 ingress ring occultation in 2005, at ring opening angle B = -23.6^o. We then convert τ to the value at our wavelength, λ =2.2 cm. The ratio of the

optical depth at these two wavelengths is obtained by integrating the ring particles' extinction cross-section calculated through Mie scattering theory.

At wavelength λ_0 and λ, the optical depths of the ring slab are:

$$\tau_0(\lambda_0) = \int_{a_{min}}^{a_{max}} Q_{ext}(a,\lambda_0)\cdot\pi a^2\cdot n(a)da = n_0\int_{a_{min}}^{a_{max}} Q_{ext}(a,\lambda_0)\cdot\pi a^{2-q}\cdot da = n_0\cdot C_0\ ,\lambda_0 = 3.557cm.$$

$$\tau(\lambda) = \int_{\square_{min}}^{a_{max}} Q_{ext}(a,\lambda)\cdot\pi a^2\cdot n(a)da = n_0\int_{a_{min}}^{a_{max}} Q_{ext}(a,\lambda)\cdot\pi a^{2-q}\cdot da = n_0\cdot C\ , \qquad \lambda = 2.2cm.$$

$$\tau(\lambda) = (\frac{C}{C_0})\cdot\tau_0(\lambda_0)\ . \tag{3.5}$$

where $Q_{ext}(a, \lambda)$ is the extinction coefficient for particles of size a at wavelength λ calculated from Mie scattering theory, and $n(a)$ is the areal number density of particles with size a. The ring particles are assumed to have a power law size distribution $n(a)= n_0a^{-q}$, where n_0 is a constant. We calculate the parameter C_0 at λ_0 = 3.557 cm, and C at λ = 2.2 cm in order to convert optical depth $\tau_0(\lambda_0)$ at λ_0 = 3.557 cm to $\tau(\lambda)$ at λ = 2.2 cm. For particle size parameters, we use the nominal values of a_{min}, a_{max}, and q for the C, B, A ring and Cassini Division particles as described in Sec. 3.2.

However, in the middle B ring, the slant path optical depth becomes so large that the measured signal-to-noise ratio (SNR) drops below unity and the RSS data become saturated (see the black curve in **Figure 3.2**). The RSS coherent occultation of a narrowband radio source can separate the directly-transmitted and diffracted signals, and thus measures the total extinction cross-section of the ring particles. On the other hand, stellar occultations, which use a broadband source, cannot separate the direct and diffracted flux. That is to say, the effective extinction efficiency Q_{RSS} for the RSS occultation is about twice the effective extinction efficiency Q_{UVIS} for the UVIS stellar

occultation. We can avoid this problem using optical depths measured during stellar occultations by the Cassini UVIS experiment (Colwell et al., 2010). For the UVIS and RSS optical depths, we then have

$$\tau^{RSS}(\lambda_{radio}) = \overline{Q_{RSS}} \cdot \int_{a_{\min}}^{a_{\max}} \pi a^2 \cdot n(a)\, da$$
$$\tau^{UVIS}(\lambda_{uv}) = \overline{Q_{UVIS}} \cdot \int_{a_{\min}}^{a_{\max}} \pi a^2 \cdot n(a)\, da \quad . \tag{3.6}$$

As long as the particle size distribution doesn't change throughout the B ring, the effective extinction efficiency remains the same, and the ratio between the RSS and UVIS optical depth should remain constant within the B ring. This enables us to remove the optical depth saturation problem in the middle B ring. We obtain the RSS/UVIS optical depth ratio at a flat, comparatively optically thin region in the inner B ring between 94,500 km and 95,200 km (see the blue box in the upper panel in Fig. 3.2), where the RSS optical depth measurements still have enough SNR. We then derive the optical depth in the middle B ring by multiplying the UVIS optical depth with the RSS/UVIS optical depth ratio. As a result, the middle B ring optical depth reaches ~7 (see red curve, Fig. 3.2).

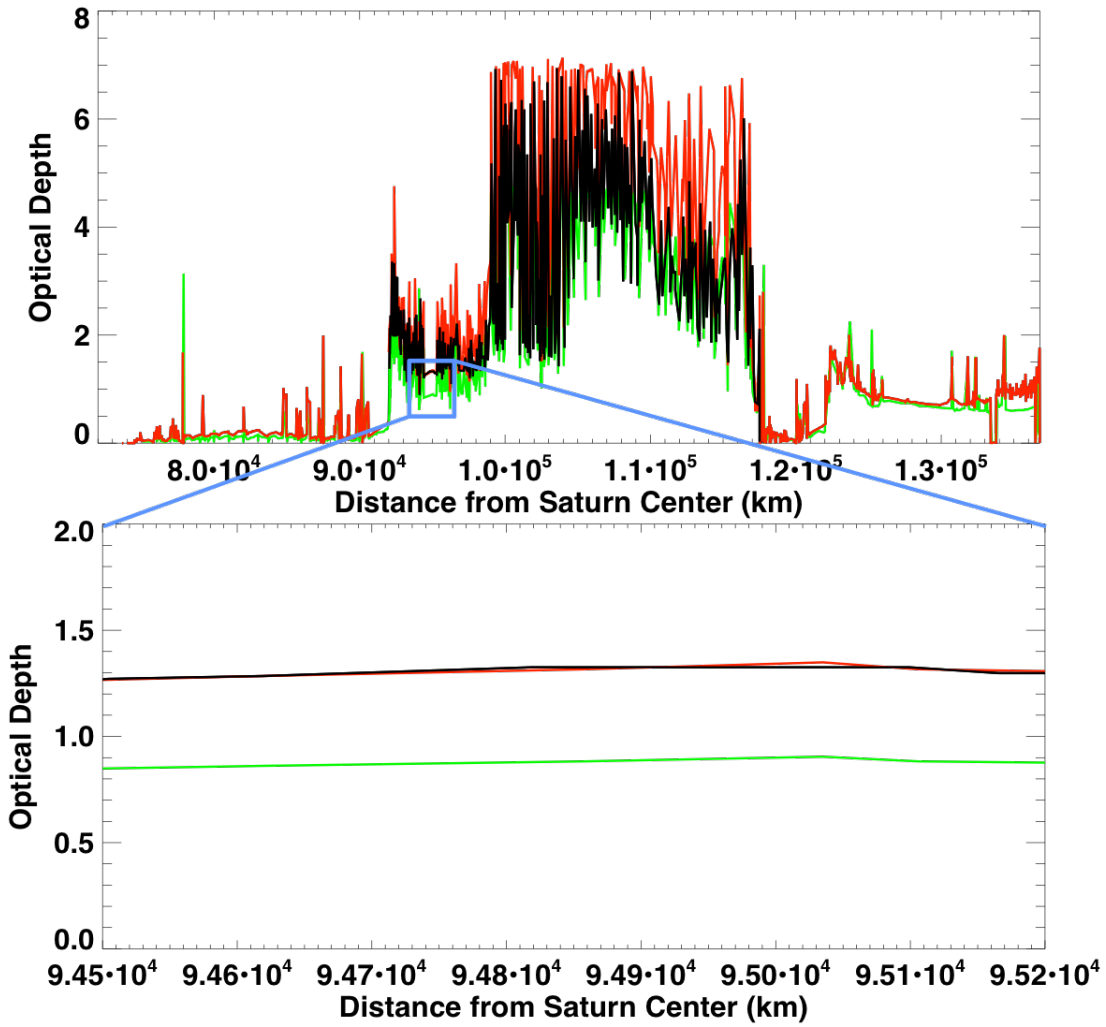

Figure 3.2: Black curve**:** the optical depth measured by the RSS occultation. Green curve**:** the optical depth measured by the UVIS occultation. Red curve**:** the optical depth used in this work, which is the same as the RSS optical depth in the A rings. The B ring optical depth is obtained by multiplying the UVIS optical depth with the RSS/UVIS optical depth ratio. The boxes show details of the flat region for clarity.

It is important to point out that, because of unresolved gaps caused by the wake structures in the B and A rings, the inferred apparent normal optical depth depends on the viewing angle of the original scan, with lower original viewing angle leading to a smaller normal optical depth value

(Colwell et al., 2007; Colwell et al., 2010). The viewing angle is defined as the absolute value of the angle between the line-of-sight and the ring plane. The RSS optical depth profile we used here was collected at a viewing angle 23.6^o, which is close to the viewing angle ~ 20^o of our radiometry data, and this represents the largest value of viewing angle scan we have from the RSS occultation. This normal optical depth variation with viewing angle is negligible in the C Ring.

3.4 Averaged Simulated Brightness Temperature in the Main Beam

Constrained by the resolution of Cassini Radar, what we obtain after the de-convolution process is a main-beam averaged brightness temperature. In general, to derive the ring particle properties, we simulate the brightness temperature with the local optical depth within the main beam and compare it with the calibrated observed brightness. Considering that the main beam can cover a length-scale of 2,000 km by 6,000 km on the ring plane in high-resolution spoke scans, the optical depth within the main beam can vary significantly. When light with intensity I is incident upon a ring plane with normal optical depth τ at incidence angle β, the light that is transmitted is proportional to $e^{-\tau/cos\beta}$, and thus the light scattered by the ring particles is proportional to (1-$e^{-\tau/cos\beta}$). Therefore, for the high-resolution observations, we calculate the effective optical depth within the main beam by averaging the optical depth with the main beam gain pattern as:

$$\left(1-e^{-\tau_{eff}/\mu_{eff}}\right)=\frac{\iint_{mainbeam}\left(1-e^{-\tau(\theta,\phi)/\mu(\theta,\phi)}\right)G(\theta,\phi)\sin\theta\,d\theta\,d\phi}{\iint_{mainbeam}G(\theta,\phi)\sin\theta\,d\theta\,d\phi}. \tag{3.7}$$

where (θ,ϕ) is the angular distance from the main-beam axis, G is the antenna gain pattern, discussed in Sec. 2.3 and $\mu_{\rm eff}$ is the cosine of the incidence angle. At each angular direction (θ,ϕ), we determine the corresponding local optical depth $\tau(\theta,\phi)$ using the radially dependent optical

depth profile as described in Eqn.3.5.

Additionally, for the wake parameters in the A ring, we take the added step of simply smoothing those radially varied parameters (*i.e.,* wake optical depth, gap optical depth, wake height over wake wavelength ratio, wake width over height ratio, wake orientation direction, etc) discussed in section 3.5 to get the value at the observed ring radius (see Figs. 3.8, 3.9 and 3.10). Finally, in those special cases in which one is observing on the boundary between two different ring regions (*i.e*., B/C ring boundary, B ring/Cassini Division boundary, Cassini Division/A ring boundary), the main beam can be separated into two pieces. At the inner edge of the C ring, the main beam may lie partially in the D ring. Since the D ring has very low optical depth and contributes little to the brightness, we assume that D ring particles are similar to C ring particles and combine them together denoted as C&D.

We calculate the effective optical depth (or wake parameters) and simulate their brightness temperature for each piece individually. We then combine the simulated brightness in the two pieces according to their fractional contribution to the main beam in order to get the averaged simulated brightness for the whole main beam. The fractional contribution for each piece is given by:

$$f_i = \frac{\iint\limits_{mainbeam\_on\_i} G(\theta,\phi)\sin\theta\, d\theta\, d\phi}{\iint\limits_{full\_mainbeam} G(\theta,\phi)\sin\theta\, d\theta\, d\phi}. \tag{3.8}$$

In **Figures 3.3** (C ring), **Figures 3.4** (B ring), **3.5** (Cassini Division) and **3.6** (A ring), we investigate the radially varied effective normal optical depth (see Eqn. 11) in the main beam or in a fraction of the main beam when observing on a given boundary. We also plot the fractional

contribution f_i (see Eqn. 3.8) to the averaged brightness in the main beam, for the high-resolution ansa observations of the C ring (or C&D ring regions), B ring, Cassini Division and A ring. Note that this high-resolution dataset Rev028_HIGH is a combination of five spoke scans. At each ring radius, data are collected at five distinct azimuthal angles and the area covered by the beam can be different at different azimuthal angles.

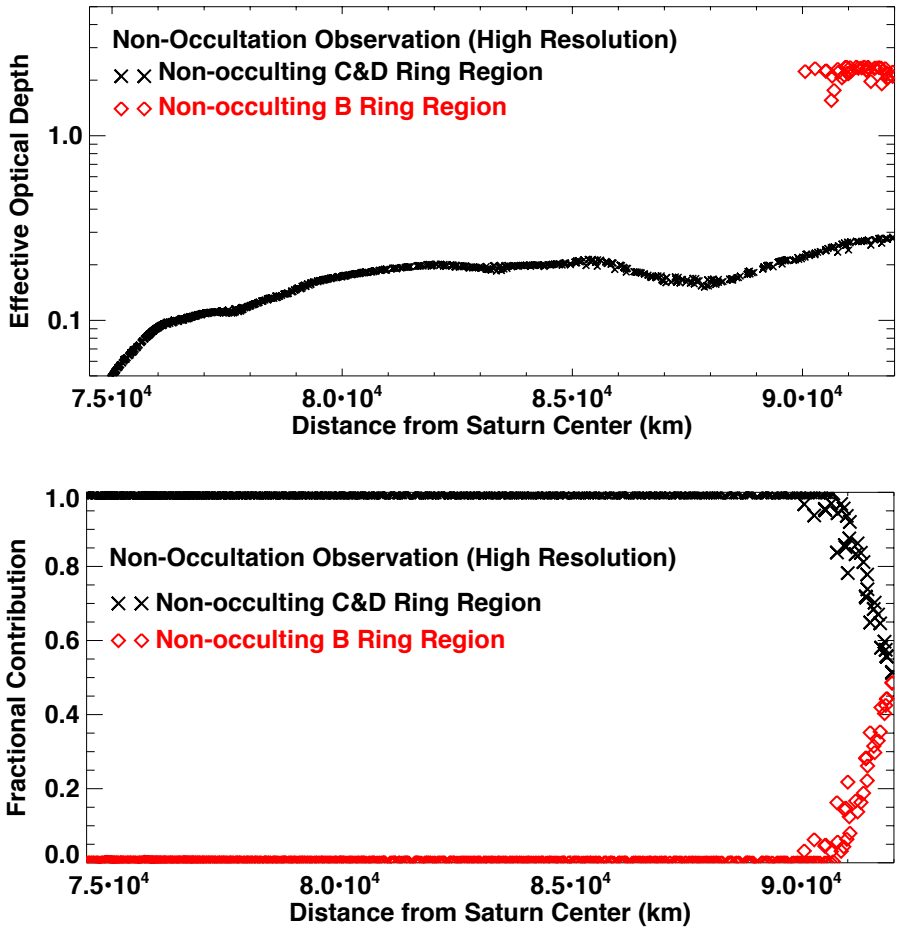

Figure 3.3: Non-occultation observation in Rev028_HIGH on the C Ring: Radially varied effective optical depth τ_{eff}^{i}, i=(C&D, B) (upper panel) and corresponding fractional contribution to the main beam brightness f_i, i=(C&D, B) (lower panel) from C&D rings (black crosses) and B ring (red diamonds).

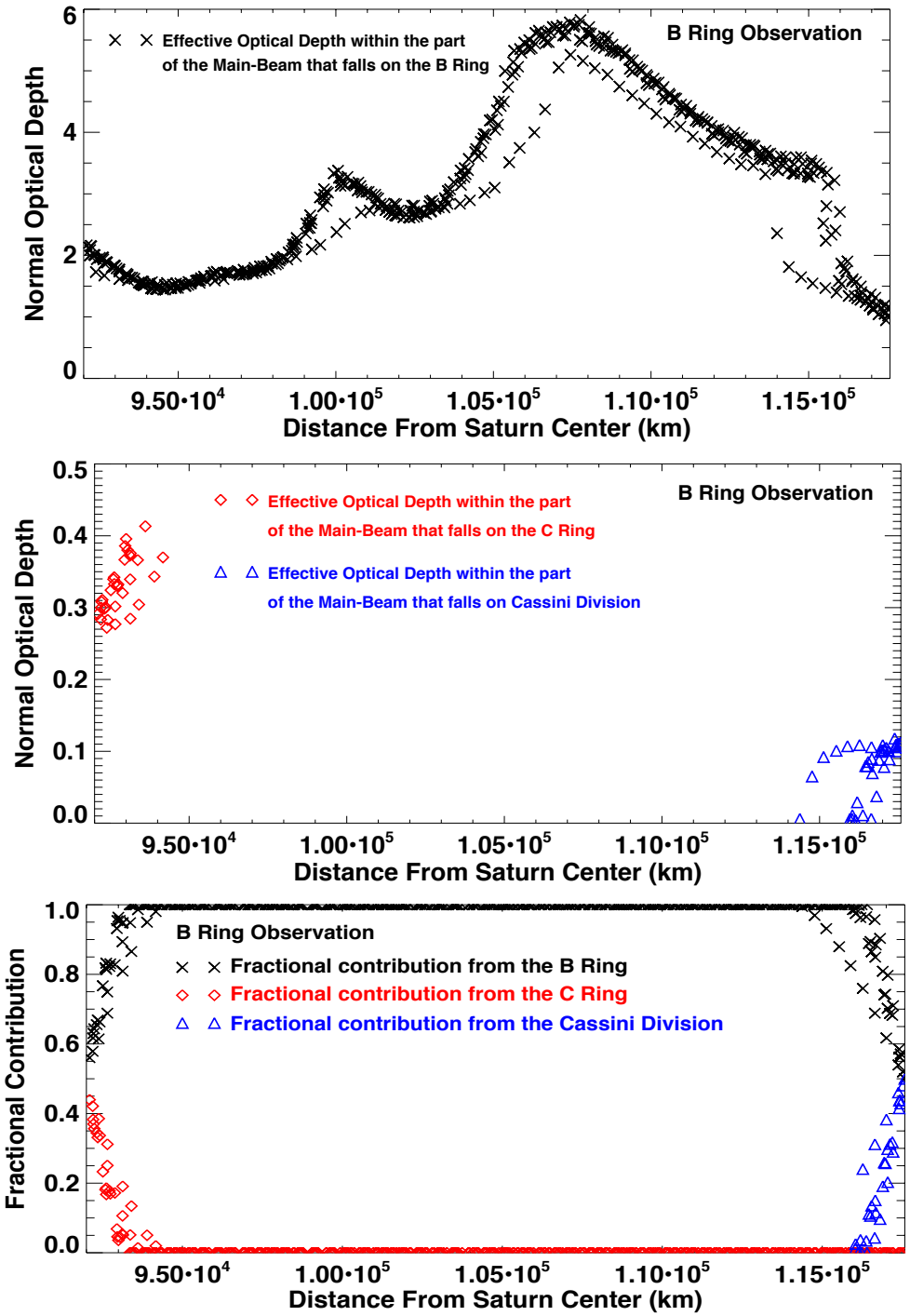

Figure 3.4: High resolution spoke scans on the B ring: the effective optical depth in the part of the main beam falls on the B ring (upper panel), C ring and Cassini Division (middle panel). Lower panel: Fractional contribution to the brightness temperature in the main beam from the B ring, C ring and Cassini Division.

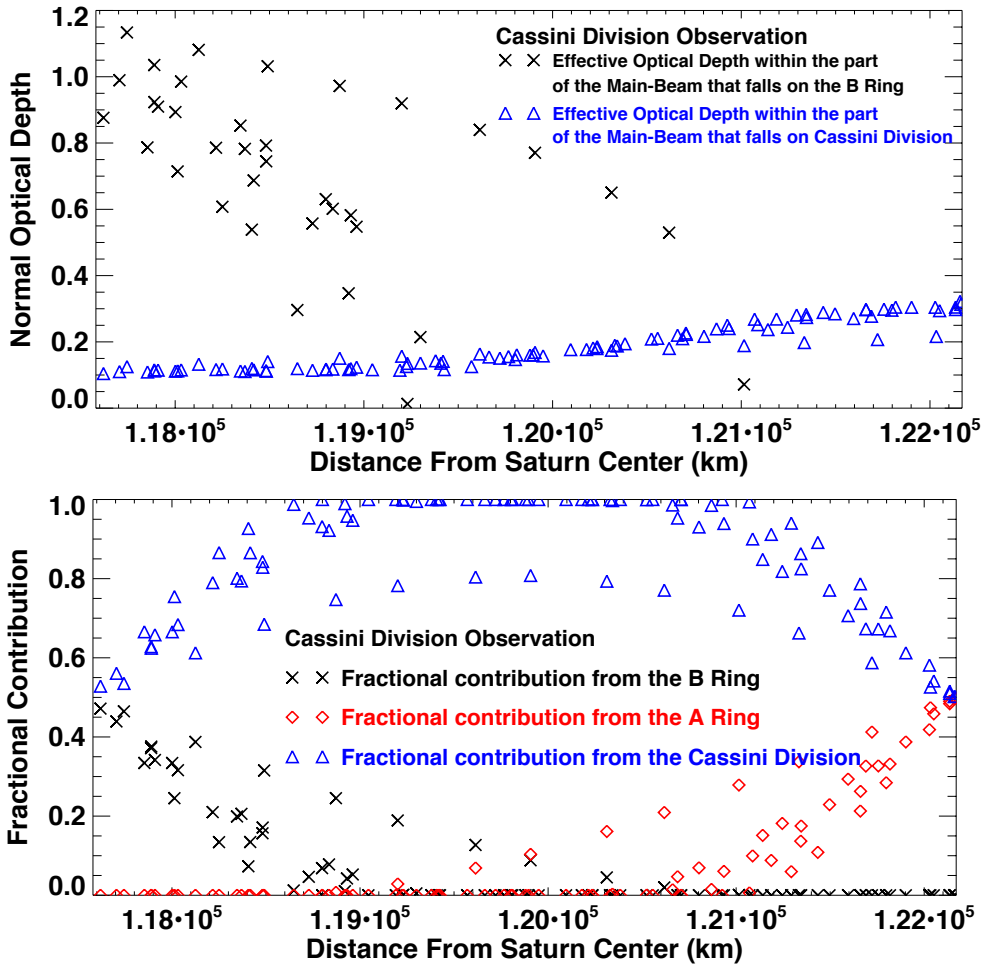

Figure 3.5: High resolution spoke scans on the Cassini Division: the effective optical depth within the part of the main beam that falls on the B ring and Cassini Division (upper panel). Lower panel: Fractional contribution to the brightness temperature in the main beam from the B ring, A ring and Cassini Division.

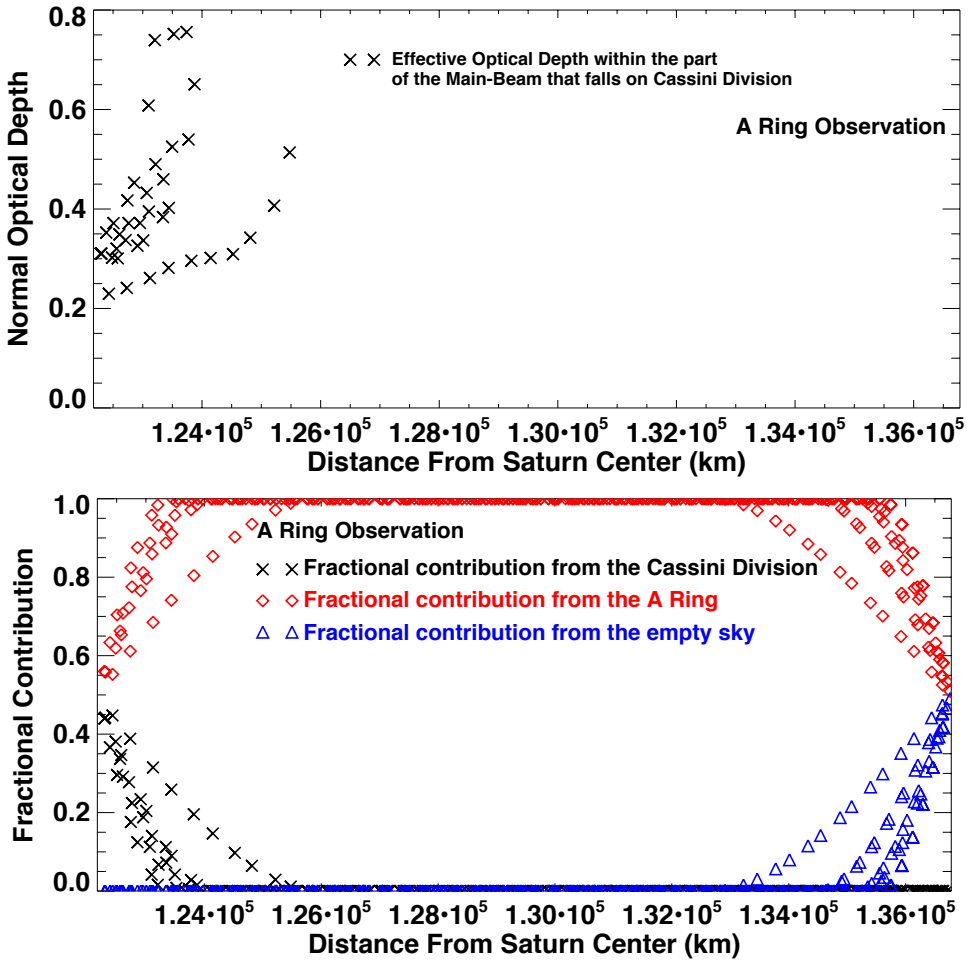

Figure 3.6: High resolution spoke scans on the A ring: the effective optical depth in the part of the main beam that falls on the Cassini Division (upper panel). Lower panel: Fractional contribution to the brightness temperature in the main beam from the A ring, Cassini Division and the empty sky.

Taking into account the CMB radiation issue we discussed in Sec. 3.1, we simulated the averaged brightness in the main beam with the effective optical depth and an effective Saturn thermal emission that is 2.7 K lower than the true radiation value. In the end, the simulated brightness temperature of each high-resolution observation point is:

$$T_{simulate} = T_{scatter} + T_{thermal} + 2.7K. \tag{3.9a}$$

and for observations on the boundary:

$$T_{simulate} = (T_{scatter\_i1} + T_{thermal\_i1}) \cdot f_{i1} + (T_{scatter\_i2} + T_{thermal\_i2}) \cdot f_{i2} + 2.7K. \quad (3.9b)$$

where $T_{scatter}$ is the scattered effective Saturn thermal emission; and $T_{thermal}$ is the intrinsic thermal emission from the rings particles all simulated by *SimRings*. For observations on the boundary, *i1* and *i2* represents the two pieces that compose the main beam.

Because the main beam coverage on the ring plane is even wider in low-resolution map scans (with resolutions of ~8,000 km by 24,000 km), the particle properties (*i.e.*, particle sizes, particle composition) and overall ring properties (*i.e.*, occulting Saturn or not, optical depth) within the main beam can vary even more dramatically. Part of the main beam may also fall on different objects (*i.e.,* cold sky or Saturn's disk). In order to simulate the observed brightness in these cases, which is the convolution of brightness within the main beam gain pattern, we divided the main rings into 349 thin ring annuli each of width 200 km. We simulated the azimuthal distribution of the brightness temperature within each ring annulus (with angular resolution of $1°$) to generate a full brightness map model. We then convolved the map model with the main beam pattern in order to get the simulated observed brightness.

3.5 Wake Structure Parameters in the A Ring

We model the self-gravity wakes as regularly spaced, aligned infinitely long slabs in the rings with normal optical depth τ_{wake}, and width *W* separated by relatively clear gaps of normal optical depth τ_{gap} and width *S*. Both the self-gravity wakes and the gaps are assumed to have a height *H*, and an alignment relative to the local radial direction of ϕ_{wake} (see **Figure 3.7**). The wavelength of the

wake structure is $L = S+W$ (Dunn et al., 2004; Colwell et al., 2006). The gap optical depth τ_{gap}, the orientation of the wakes and the ratio of the dimensions H/W and S/H have been calculated using UVIS occultation observations of Colwell et al. (2006; 2007). We apply the results of these works in our model to simulate the observed brightness. The values of S/H remain nearly constant across the A ring with $\langle S/H \rangle = 6.8$ in the inner and middle A ring, and $\langle S/H \rangle = 7.7$ beyond the Encke gap. **Figure 3.8** shows the values of H/W, H/L, W/L, τ_{gap} and ϕ_{wake} we utilized across the A ring. The H/W value in Colwell et al. (2007) is significantly scattered so we have chosen to employ the median value. However, the value of τ_{gap} we applied is ~2 times the value derived from the UVIS occultation (Colwell et al., 2006; 2007). Considering that the UVIS wavelength is much smaller than the typical ring particle size, the diffraction lobes of large particles can be very small and thus can likely be captured by the UVIS detector. Therefore the UVIS τ_{gap} is close to the geometric optical depth.

The stellar occultation analysis of Colwell et al. (2006) can not determine the wake optical depth, since once the wake optical depth becomes large enough, nearly no light can transmit through it and the occultation observation is no longer sensitive to the wake optical depth. However, in our case the light detected by Cassini contains scattered Saturn radiation and intrinsic thermal emission, both of which depend on the value of the wake optical depth. Here we derive the wake optical depth using the surface mass density measured from density wave measurements (see **Figure 6**; e.g., Spilker et al., 2004; Tiscareno et al., 2007; Colwell et al., 2009).

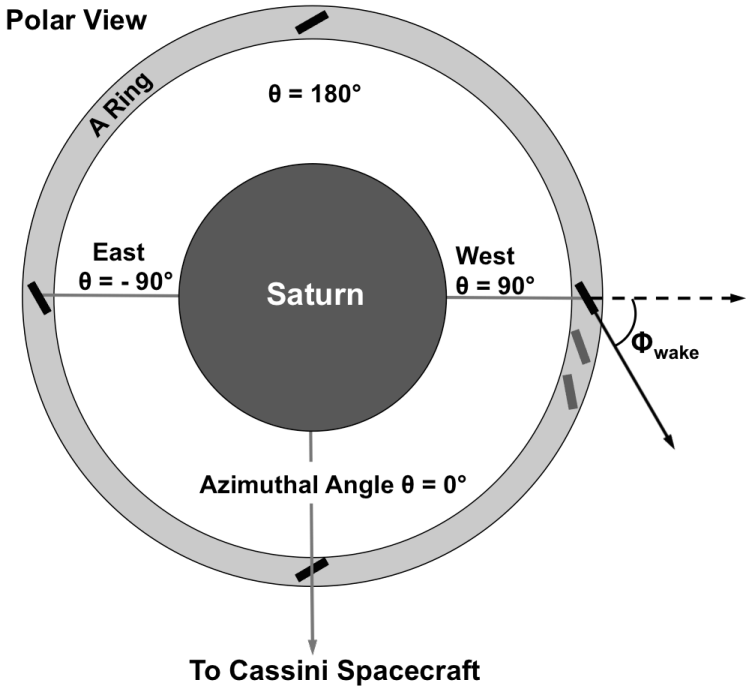

Figure 3.7: Geometric structure of wakes in the A ring as seen from the Saturn north pole in our simplified wake model. The small dark bars schematically indicate the alignments of the wakes. The grey regions in between adjacent wakes are the gap regions.

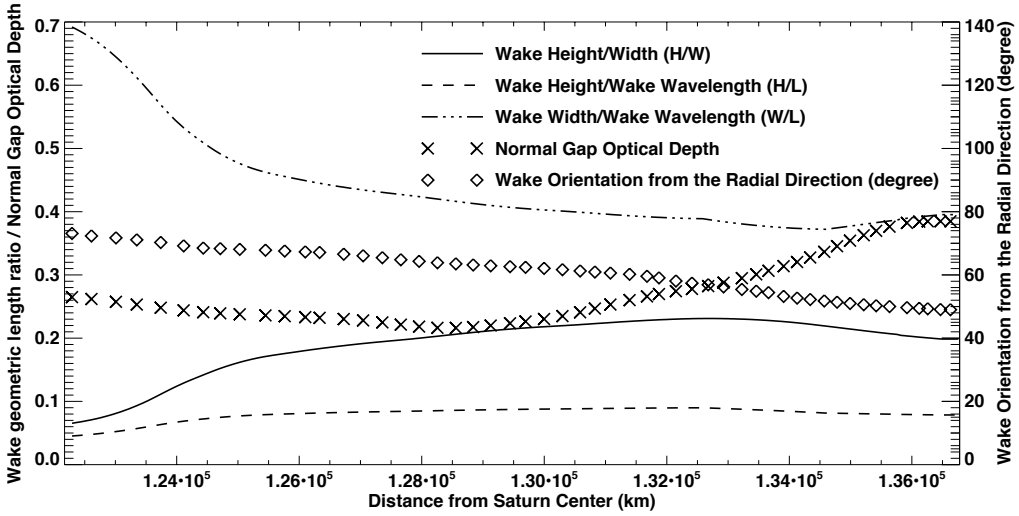

Figure 3.8: The radial profile of H/W, H/L, W/L, τ_{gap} and ϕ_{wake} we utilized across the A ring. Wake parameter values are adopted from Colwell et al. (2007) where we have chosen to employ the median value in that work.

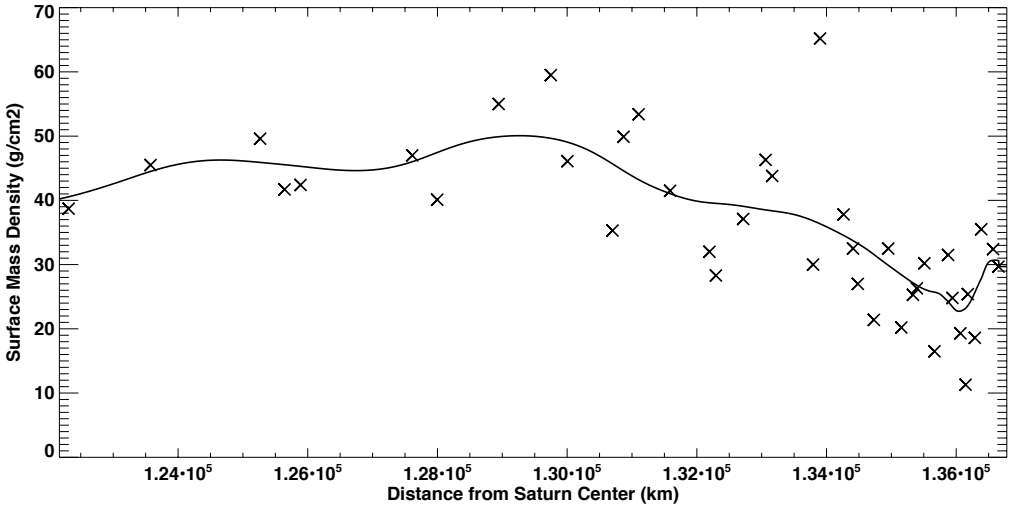

Figure 3.9: Surface mass density measured from density wave measurements (crosses) (Spilker et al., 2004). The black solid line shows the smoothed value we employed in this work.

By assuming that the ring particles in the gap and wake have the exact same size distribution as well as composition, we obtain the same opacity in both gap and wake (see Eqn. 3.3):

$$\sigma_{gap} = \frac{\tau_{gap}^{geometry}}{\kappa} = \frac{\tau_{gap} / \bar{Q}_{ext}}{\kappa} \tag{3.10}$$

$$\sigma_{wake} = \frac{\tau_{wake}^{geometry}}{\kappa} = \frac{\tau_{wake} / \bar{Q}_{ext}}{\kappa}, \tag{3.11}$$

where $\bar{\rho}$ is the mean particle density, and $\bar{Q}_{ext}$ is the average extinction coefficient for A ring particles at a wavelength of 2.2 cm which approaches a value of 2 when the particle size is much larger than the wavelength. The measured surface mass density is then given by

$$\sigma = \frac{W}{L}\sigma_{wake} + \frac{S}{L}\sigma_{gap}. \tag{3.12}$$

After combining Eqns. 3.3, (3.10-3.12), we can calculate the wake optical depth:

$$\tau_{wake} = \left(\frac{3(4-q)}{4\bar{\rho}(3-q)} \frac{a_{max}^{3-q} - a_{min}^{3-q}}{a_{max}^{4-q} - a_{min}^{4-q}} \cdot \bar{Q}_{ext} \cdot \sigma - \frac{S}{L} \cdot \tau_{gap}\right) \Big/ \left(\frac{W}{L}\right). \quad (3.13)$$

Finally, the last parameter we need to determine for the wake optical depth calculation is the mean particle density. Consider that if the non-icy material mixed within the A ring particles is very small (less than 1%), the mean particle density will mainly depend on the ring particle porosity. For the particle size distributions in regions A0, A1, A2, and each of the three particle size distribution cases in region A3, we simulated five different porosities: 55%, 75%, 80%, 85% and 90%. **Figure 3.10**, panel 1 shows the derived wake optical depth for five different porosities in regions A0, A1 and A2. In Fig. 3.10, panel 2 shows the wake optical depth using five different porosities for all three particle size distribution cases we adopt in region A3. As compared to that in regions A0, A1 and A2 (see Table 2), the derived wake optical depth in region A3 is exceptionally high in the A3-Case2, and even higher in the A3-Case1. As the minimum particle size becomes smaller for the A3-Case1 and A3-Case2, the introduction of more particles in the smaller size range increases the ring opacity, which in turn increases the wake optical depth. The larger power law index in the A3-Case1 indicates an even larger number of smaller particles than the A3-Case2 and therefore an even higher wake optical depth. When applying the particle size distribution in A3-Case1 and A3-Case2, due to the significant difference in the adopted particle size distribution inside and outside the Encke gap, the wake optical depth exhibit a large discontinuity at the Encke gap (see panel 1&2). In the event that this discontinuity may cause a problem, and also as a comparison, we used a nominal case with $a_{min} = 30\ cm, a_{max} = 6.3\ m, q = 2.75$ in the A3 (A3-Case3) region.

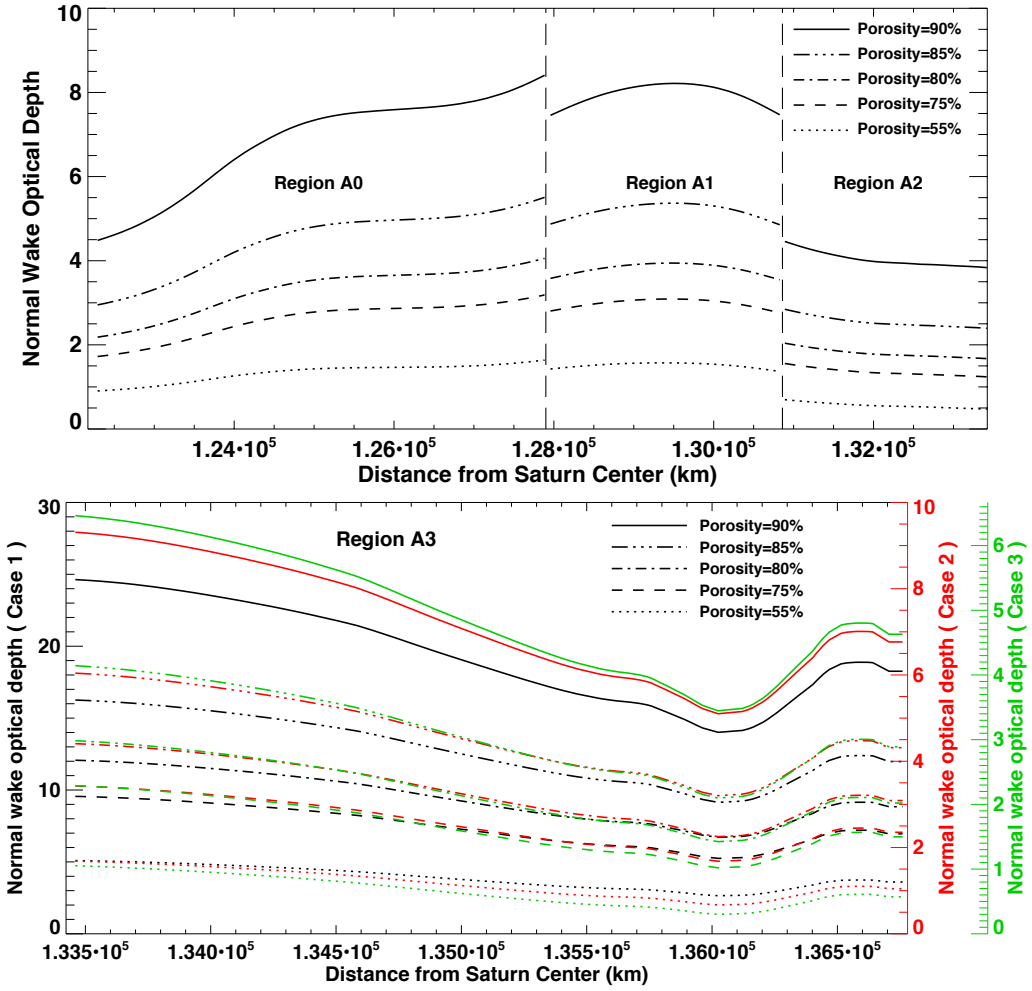

Figure 3.10: Derived normal optical depth in the wake. A0, A1 and A2 regions (Panel 1): porosity values of 55% (dotted), 75% (dashed), 80% (dash-dot), 85% (long dash-dot) and 90% (solid). The derived wake optical depth becomes higher when the particles have higher porosity. Panel 2: The A3 region which includes A3-Case 1 (black), A3-Case 2 (red) and the A3-Case3 (green). Different cases are referred to different y-axis. The different porosities are indicated by the different line types: 55% (dotted), 75% (dashed), 80% (dashed-dot) and 90% (solid).

3.6 Scattering Phase Function

For the scattering and extinction cross-sections of individual ring particles, which vary with particle size and dielectric constant, we use Mie theory. When the ring particle size parameter x,

which is the ratio of particle circumference to wavelength, is less than an upper bound of x ~10 (Cuzzi and Pollack, 1978), a Mie phase function, which is derived from spherical particles, is adequate to describe each single scattering, even for non-spherical particles. In Saturn's C ring and Cassini Division, millimeter - centimeter scale particles are dominant in the scattering process and the size parameters of most small particles are less than the upper bound at a wavelength of 2.2 cm. Therefore a Mie phase function is a good approximation in most regions in the C ring and Cassini Division.

However, in Saturn's B and A rings, particles are mostly larger than 30cm and thus the size parameter for these particles are larger than 85 at a wavelength of 2.2 cm. As a result, the phase function deviates from being simply Mie scattering. In addition, due to the larger number density found in the middle B ring and A ring wakes, close packing of ring particles can also cause the phase function to be more isotropic (see Sec. 3.7.2 for more discussion). To that end, where Mie scattering alone is inadequate, we introduce a phase function that is a linear combination of Mie and isotropic scattering phase functions (Dunn et al., 2002):

$$P(\theta) = (1\text{-}f_{iso}) \cdot P_{mie}(\theta) + f_{iso} \cdot \frac{1}{4\pi} \quad . \qquad (3.14)$$

Here f_{iso} is the fraction of isotropic scattering, and we consider f_{iso} for the B and A rings particles as a variable to be determined in our analysis. According to previous VLA observations at a wavelength of 2.0 cm, the combination of Mie and isotropic phase functions works well for the B ring, while a pure Mie phase function works best for the C ring (Dunn et al., 2002).

3.7 Discussion of the more isotropic phase function in the B and A rings

We introduce the hybrid phase function in the A and B rings to account for the fact the large particles in the A and B rings scatter more isotropically than predicted by Mie scattering. We will show later in Chapter 4 that while a Mie phase function predicts the distribution of scattered light well in the C ring and Cassini Division owing to the smaller particles there, a hybrid phase function, which is a mixture of Mie and isotropic phase functions, is required to match the observations in the A and B rings. There are three reasons why the A and B ring particles scatter more isotropically:

1) The A and B ring particles are much larger than our wavelength. Nonsphericity effects become important and make the scattering phase function more isotropic.
2) The A and B rings are physically thin but opaque, and are thus characterized by a high ring particle number density and particles are closely packed. Therefore, the near-field effect is important there which also results in a more isotropic scattering phase function.
3) In the optically thick A and B rings, incident light encounters an increasing amount of multiple scattering and is more likely to "forget" the initial incident direction. That is to say, the incident light is more likely to contribute equally to all scattering angles.

The third reason has already been taken into account in our Monte Carlo simulation. In this section, we investigate the nonsphericity and near-field effect in more detail. In section 3.7.1, we study how the nonsphericity of large particles affects the scattering phase function by using a hypothetical ring model in which the ring is optically thin, the ring particles have similar size distribution as the B ring and inner A ring (inside Encke gap), and all scatterings within the ring

are independent. Using this model, we show that the scattering phase function is similar to a 70% Mie/30% isotropic hybrid phase function when the effect of nonsphericity is included. In section 3.7.2, we propose an approximation model for calculating the near-field effect by investigating the near-field Mie phase function. We then apply this approximation model to the semi-empirical phase function for nonspherical particles as described in section 3.7.1. We demonstrate that, in addition to the effect of nonsphericity, the near-field effect makes the scattering phase function in the B and A rings even more isotropic, and in fact close to that predicted by a 30% Mie/70% isotropic hybrid phase function.

3.7.1 Nonsphericity

When the particle size parameter x (Sec. 3.2) is less than some upper bound x_0, the nonsphericity for randomly oriented particles is not significant and Mie scattering for spheres is a good approximation for the scattering process (Pollack and Cuzzi, 1980). This is especially true for the C ring (see Sec. 4.1) and the Cassini Division (see Sec. 4.4), where the bulk of the ring particles are comparable or even smaller than our wavelength of 2.2 cm. However, large ($x > x_0$) nonspherical particles are known to scatter light more isotropically, and thus a Mie phase function is no longer adequate to predict the distribution of scattered light (Pollack and Cuzzi, 1980; Dunn et al., 2002). The upper bound size parameter x_0 is related to the roughness of nonspherical particles with x_0 decreasing as the level of roughness of a particle increases. For convex-concave particles, we have $x_0 \sim 10$ (Pollack and Cuzzi, 1980). Therefore, for the B ring particles, and for the A ring particles interior to the Encke gap where the minimum size is ~30 cm, the size parameter (x~86) is much larger than x_0 and the effect of nonsphericity becomes important.

To explore the nonsphericity effect we investigate the semi-empirical theory of Pollack and Cuzzi (1980) for particles with $x > x_0$ where the interaction between particle and incident light is divided into three components: diffraction, external reflection and transmission. The diffraction component is obtained from physical optics theory, the external reflection is determined from geometrical optics and the transmission has a simple parameterization (Pollack and Cuzzi, 1980). The composite phase function is then obtained by summing these three components, with each one being weighted by its contribution to the total scattering, as measured by the ratio of its cross section to the total scattering cross section. We then compare the far-field behavior (the near-field is explored in Sec. 3.7.2) of this composite phase function with the simple hybrid phase function (see Sec. 3.6, Eq. [3.14]) that we applied in the B and A ring model to simulate the observed brightness temperature.

The diffracted component is assumed to be that of an opaque circular disk having an area equal to the nonspherical particle's projected area which is equal to one-fourth its total surface area for a convex particle in random orientation (Vouk, 1948). Since a nonspherical particle tends to have a larger surface area than that of an equal volume sphere with physical radius a, the approximate disk should have a radius larger than a. However in this work, we adopt the nominal particle size a as the radius of the disk to obtain the diffraction component since these ring particle sizes are measured from their diffracted and scattered light observed in stellar and radio occultations (Zebker et al., 1985, French and Nicholson, 2000). The diffracted component I_D for this opaque circular disk in terms of the size parameter x and the scattering angle θ is (Hodkinson and Greenleaves, 1963):

$$I_D(\theta,x)=\frac{C_D x^2}{8\pi\left(1+\cos^2\theta\right)}\left[\frac{2J_1\left(x\sin\theta\right)}{x\sin\theta}\right]^2 . \tag{3.15}$$

where C_D is the normalization factor determined from the condition

$$\int I_D\left(\theta,x\right)\frac{d\Omega}{4\pi}=1 . \tag{3.16}$$

Note that Eq. (3.15) is symmetric with respect to the scattering angle at 90 degrees. However, the diffraction pattern at angles larger than 90 degrees is not physical and so we assume their values to be zero for the normalization in Eq. (3.16). According to Babinet's principle, the amount of incident light that is diffracted is equal to that which falls on the particle's physical cross section, and thus the diffraction contribution to the extinction efficiency is unity, that is $Q_D = 1$. Q_D is the scattering efficiency for the diffraction component which is the ratio of the diffraction interaction cross section of a particle to its geometrical cross section πa^2.

The phase function I_R for the external reflection component is independent of particle size for $x > x_0$ and is given by (Hodkinson and Greenleaves, 1963):

$$I_R\left(\theta\right)=\tfrac{1}{2}C_R\left\{\frac{\sin\left(\theta/2\right)-\left[\left|\tilde{m}\right|^2-1+\sin^2\left(\theta/2\right)\right]^{1/2}}{\sin\left(\theta/2\right)+\left[\left|\tilde{m}\right|^2-1+\sin^2\left(\theta/2\right)\right]^{1/2}}\right\}^2+\tfrac{1}{2}C_R\left\{\frac{\left|\tilde{m}\right|^2\sin\left(\theta/2\right)-\left[\left|\tilde{m}\right|^2-1+\sin^2\left(\theta/2\right)\right]^{1/2}}{\left|\tilde{m}\right|^2\sin\left(\theta/2\right)+\left[\left|\tilde{m}\right|^2-1+\sin^2\left(\theta/2\right)\right]^{1/2}}\right\}^2 \tag{3.17}$$

where $\tilde{m}$ is the complex refractive index. The efficiency factor for external reflection $Q_R = 1/C_R$, where C_R is the normalization factor determined from the integration of I_R over all solid angles (e.g., Eq. [3.16]).

The internally transmitted component is the main deviation between the scattering behavior of

non-spherical and spherical particles. Due to the occurrence of total internal reflection in nonspherical particles, more light gets redistributed from the forward hemisphere to the backward hemisphere. We apply the parameterization suggested by Pollack and Cuzzi (1980) in which the logarithm of the transmitted component's phase function I_T varies linearly with scattering angle:

$$I_T(\theta) = C_T \exp(1 + b\theta) \quad , \tag{3.18}$$

where C_T is again the normalization factor derived from the result that the integral of $I_T/4\pi$ over all solid angles is unity. The slope of $\log I_T$ given by the parameter b is related to an empirical constant M given by:

$$M = \int_0^{\pi/2} I_T \, d\theta \Big/ \int_{\pi/2}^{\pi} I_T \, d\theta$$

$$b = -\frac{2}{\pi} \ln M \quad . \tag{3.19}$$

The constant factor M depends on the particle's shape and is determined through a comparison between the semi-empirical phase function I_T and laboratory measurements. In this work, we adopt the value M = 1.5 (Pollack and Cuzzi, 1980) which yields b = -0.26. The scattering efficiency for the transmitted component Q_T can be calculated via

$$Q_T = Q_s - Q_D - Q_R \, , \tag{3.20}$$

where $Q_s \sim 2$ for particles which are much larger than a wavelength and have low absorptivity (such as the A and B ring particles, which contain mostly water ice and have low absorption). The total phase function I is then given by

$$I = I_D \frac{Q_D}{Q_s} + I_R \frac{Q_R}{Q_s} + I_T \frac{Q_T}{Q_s} \, . \tag{3.21}$$

This semi-empirical phase function has been shown to be in very good agreement with laboratory measurements (see Pollack and Cuzzi, 1980, and references therein).

We would like to investigate using Eq. (3.21) how isotropic the phase function becomes (in deviating from a pure Mie phase function) for large nonspherical particles. To do so we apply our hybrid (Eq. [3.14]) $p(\theta) = (1\text{-}f_{iso}) \cdot p_{mie}(\theta) + f_{iso} \cdot \frac{1}{4\pi}$ and semi-empirical phase functions to our Monte Carlo simulation in order to determine the best-fit parameter f_{iso} that predicts a scattering profile that is closest to that predicted by the semi-empirical phase function. However, a complication is that due to the small physical thickness of the rings, even in the inner and outer B ring where $\tau \sim 1$, the near-field effect is not negligible. Thus, in order to study the nonsphericity effect alone and avoid the near-field effect for closely packed particles (see Sec. 3.7.2), we consider a hypothetical ring which is optically thin but is composed of particles with the same size distribution ($a_{min} = 30\ cm, a_{max} = 6.3\ m,\ q = 2.75$), porosity (55%) and composition as the B ring. **Figure 3.11** plots, for a ring annulus at the location of middle B ring (~104,790 km), the scattering profiles (scattered light only, with respect to azimuthal angle) when applying our hybrid and semi-empirical phase functions. For these simulations, we have assumed $\tau = 0.2$ which ensures the independence of each single scattering.

It can be seen that, because the scattering profiles for the hybrid phase functions with different f_{iso} vary most at small azimuthal angles where the ring annulus occults Saturn, we have the chance to estimate the best-fit f_{iso} to the semi-empirical phase function. Matching the scattering profile near zero azimuth is important since in our observations the occultation data is also most sensitive to the phase function. We note that the scattering profile of the 70% Mie/30% isotropic

phase function is closest to that of the semi-empirical phase function with the exception that it predicts a higher fraction of scattered light at azimuthal angles of ~20—40 degrees. Furthermore, the scattering profiles of the semi-empirical phase function at azimuthal angles larger than 40 degrees is very close to that of the hybrid phase function with $f_{iso} = 0.3$ and $f_{iso} = 0.5$.

As we have mentioned in Sec. 3.2, there is some ongoing disagreement between the 28 Sgr and Cassini RSS derived particle size distributions in the B and A rings. Specifically, a smaller minimum particle size is indicated in the inner B ring "flat" region (Marouf et al., 2008), whereas the notable X-S band differential increase over the middle to outer portion of the A ring suggests a smaller $a_{\min}$ and a larger q (Cuzzi et al., 2009). It may be that a semi-empirical phase function including some small particle component might match the hybrid phase function even better, but for now we simply acknowledge the ongoing debate. Thus, we conclude that the semi-empirical phase function for large nonspherical particles can be best approximated by the 70% Mie/30% isotropic phase function, and that nonsphericity is one reason why A and B ring particles scatter more isotropically than a pure Mie phase function. In the next section, we further show that when we consider optically thicker rings more representative of the A/B rings, the scattering profile will be even more isotropic, which can be attributed to the near-field effect.

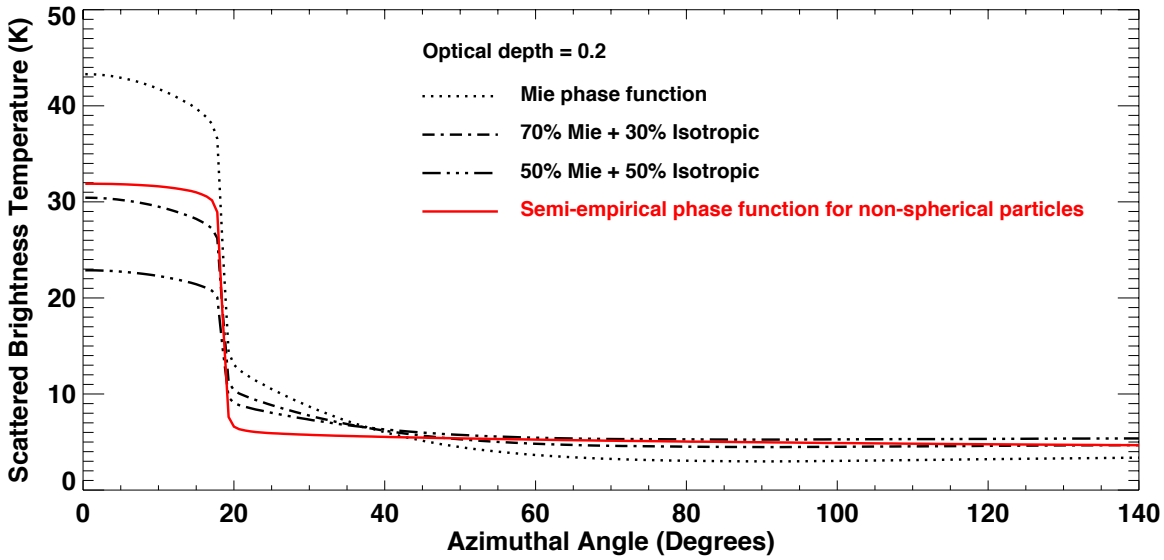

Figure 3.11: The simulated scattered light with respect to azimuthal angle for a ring annulus with optical depth 0.2, when using four different scattering phase functions: Mie, 70% Mie + 30% isotropic, half-Mie-half-isotropic and the semi-empirical phase function for nonspherical large particles. We have assumed that the ring particles have the same particle size distribution as the B ring and are 55% porous. In the Cassini high-resolution observation geometry (at the ring inclination angle ~ 20° and distance ~6 R_S from Saturn center), the portion of a ring annulus located at the radius of the middle B ring, where azimuthal angles larger than 140° are blocked by Saturn and cannot be observed.

3.7.2 Close-packing Effect

Another factor that makes ring particles in the B ring and A ring wakes scatter even more isotropically is due to the near-field effect. In these physically thin but opaque ring regions, ring particles are closely packed and the ring layer has a high particle number density. When light is scattered within such a ring layer, each scatter by a ring particle is no longer independent. For example, if light is scattered by a first particle, and subsequently encounters a second particle that lies within the near-field zone of the diffraction in the forward-scattering direction, the scattered wave contributions from different parts of the first particle have not yet fully interacted and there

would be a decrease in the intensity forming a shadow zone. Since the far-field zone hasn't been reached, the semi-empirical phase function for nonspherical large particles described above cannot be used to predict the scattered light distribution. Therefore, we need to take into account the near-field effect in these regions.

The near-field can be specified by the Fresnel number, $F = a^2 / L \cdot \lambda$, where a is the radius of the scatterer and L is the distance from the scatterer. When $F >> 1$ the diffraction wave is considered to be in the near field and when $F << 1$ the diffraction in the far field is given by the Fraunhofer diffraction pattern. The extension of the near-field (shadow zone) L_s is in the forward scattering direction where $L \ll a^2/\lambda$ and can be estimated as $L_s = C_{Fresnel} \cdot \left(a^2 / \lambda \right)$ (Brillouin, 1949; Cuzzi et al., 1980). In our model, the constant $C_{Fresnel}$ characterizes the distance at which one would be in the far field. For our approximation model, we assume $C_{Fresnel} = 1$. We note that $C_{Fresnel} = 2\pi$ is generally applied in the literature when calculating the extension of the Fresnel zone (Brillouin 1949, Cuzzi et al., 1980). However, we explain in more detail below as we investigate the near-field Mie phase function (see Fig. 3.13) why we find $C_{Fresnel} = 1$ a better choice for our model.

The shadow region in **Figure 3.12** illustrates the spread of this near-field zone within which the scattered light is redistributed. The half-angular range $\Theta(L) = a\sin(s/L)$ of this near-field zone decreases with increasing distance L as

$$s = \frac{a}{L_s}\left(\sqrt{L_s^2 - a^2} - \sqrt{L^2 - a^2} \right). \tag{3.22}$$

In Saturn's rings, the near-field effect is very important in regions with larger particles where

particles have more extensive shadow zones, as well as regions with higher particle number density where particles are close to each other such as the middle B ring and A ring wakes. Under these circumstances, the extension of the shadow zone L_s is greater than the line-of-sight distance to the next particle and the near-field effect becomes important (Cuzzi et al. 1980).

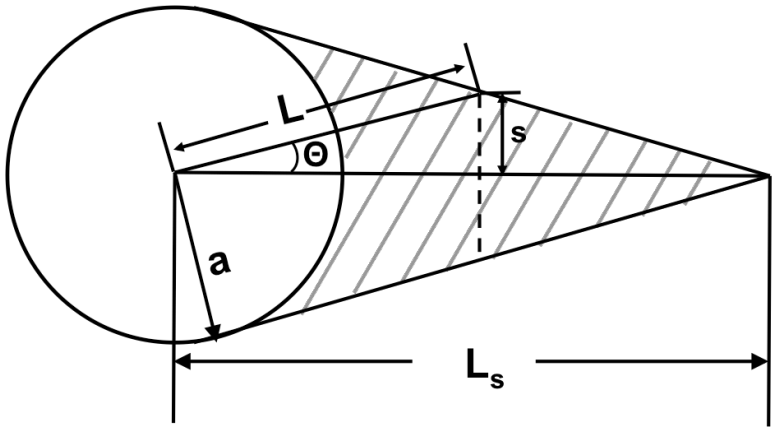

Figure 3.12: Shadow zone (grey-lined area) of a particle with radius *a*. $\Theta(L)$ is the half angular width of the shadow zone at distance L. L_s is the extension of this shadow zone (see text). The ratio of the lengths of L_S and *a* in the figure is meant to be demonstrative and is not to scale.

No theory has thus far ever been reported on how the near-field effect would reshape the scattering phase function for nonspherical particles within the shadow zone (see Sec. 3.7.1). We acknowledge that an accurate simulation of the near-field effect requires a Discrete Dipole Approximation (DDA) calculation which is computationally very expensive, thus a more detailed effort will be the subject of future work. However, we are able to investigate how the near-field effect reshapes the Mie phase function within the shadow zone by employing the computational code developed by Barber and Hill (1990) which numerically calculates the near-field Mie phase function. Using this code, we can look for a general tendency by which the near-field effect reshapes the Mie phase function within the shadow zone and apply it to the semi-empirical phase

function in order to generate an approximation of the near-field semi-empirical phase function for nonspherical particles.

First, using the Barber and Hill (1990) code, we calculate the near-field Mie phase function (hereafter, denoted as BH90 near-field Mie phase function) at distances $L<L_s$ for a particle with size parameter $x = 1000$ as is shown in **Figure 3.13**. For this calculation, we selected four scattering angles θ (0, 0.36, 0.67 and 2.04 degrees away from the incidence direction) with the last three scattering angles corresponding to the half-angular range $\Theta(L)$ of the near-field zone at distances of $L = 0.5L_s$, $0.35L_s$ and $0.15L_s$, assuming $L_s = a^2/\lambda$. These L correspond to the distances that define the far-field zone for the corresponding θ, respectively. In the case $\theta = 0$, the far-field and near-field boundary lies at $L = L_s$. For each scattering angle, we plot how their phase functions vary with distance L from the scattering center. The vertical dashed lines in Fig. 3.13 show the distance boundaries between the respective near-field and far-field zones for each scattering angle θ. The rectangles at L/L_s=1 show the BH90 near-field Mie phase function calculated at that distance for each scattering angle, and the rectangles located furthest to the right (on the rightmost axis) of the figure indicate the far-field Mie phase function values at these scattering angles. We also notice that at any given scattering angle, the phase function inside the near-field zone increases with distance to a local maximum at its near-field-far-field boundary (the vertical dash lines) and starts to drop off exterior to this boundary. At this point, the phase function no longer has the same values as the phase function inside the shadow zone. We note that in actuality the near-field-far-field boundaries would not be this definite; that is $L_s = C_{Fresnel} \cdot \left(a^2/\lambda\right)$, where $C_{Fresnel}$ may not be equal to unity. The fact that the calculated phase function at $L=L_s=a^2/\lambda$ using the near-field Mie

code doesn't coincide with the far-field Mie phase function in Fig. 3.13 indicates that the far-field Mie phase function cannot completely describe the phase functions at distances $L \gtrsim L_s$. That is to say, the far field has not been fully reached. As we mentioned previously, the value of $C_{Fresnel} = 2\pi$ is usually adopted, but for this choice the near-field-far-field boundary (the vertical dashed lines) would not agree with the local maximum point very well. Therefore, we find that $C_{Fresnel} = 1$ is a better choice for our approximated near-field phase function model, which will be described later. Furthermore, considering that the variation of the phase function at $L > L_s = a^2/\lambda$ is not very dramatic, $L_s = a^2/\lambda$ can approximately serve as the criterion for us to determine whether we should use the near-field or the far-field phase function.

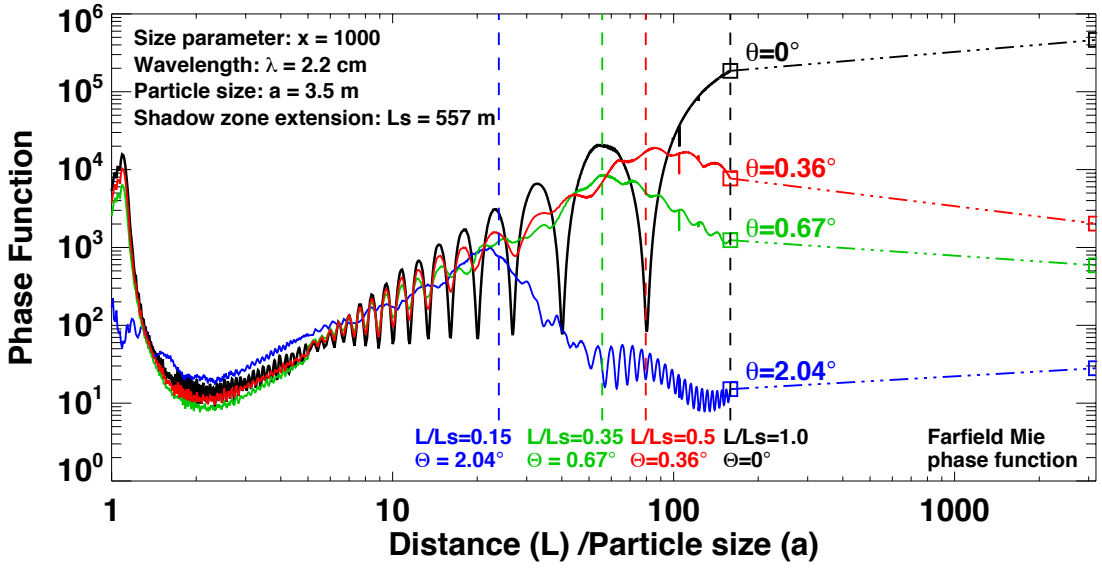

Figure 3.13: The variation of the near-field Mie phase function with distance-over-particle size (L/a) from the scattering center at five scattering angles θ (0, 0.36, 0.67 and 2.04 degrees away from the incidence direction) for a size parameter of x=1000. The vertical dashed lines show the boundary of the shadow zone at each scattering angle θ. The rectangles at L/L_s=1 shows the BH90 near-field Mie phase function calculated at that distance for each scattering angle, and the rectangles on the rightmost axis of the figure indicates the far-field Mie phase function values at these scattering angles.

For a given value of the distance-over-particle size (L/a), the phase function at different scattering angles inside the near-field zone have roughly the same value despite some small-scale fluctuations in the magnitude of the phase function there. This suggests that we may propose an approximation method to deal with the near-field effect, which can later be applied to the semi-empirical phase function for nonspherical particles. At each distance from the scattering center, if the scattering angle is outside the near-field (shadow) zone, we use the value of the far-field phase function (e.g., the values in the rectangles on the rightmost axis of Fig. 3.13). On the other hand, for all scattering angles inside the near-field zone, we assume that their phase function values are constant and can be determined by the normalization of the new phase function. Furthermore, at any given distance $L < L_s$, we also notice a transition region outside the shadow zone (more on this below), where the phase function gradually changes from near-field values to far-field values (see Fig. 3.15). We investigate the characteristics of this transition region and initially propose one method (Method 1, described below) to approximate this trend. Though this additional step to take into account the transition region can make our approximated phase function much closer to the real near-field Mie phase function, the computational time is much longer especially for Monte Carlo codes such as *Simrings*. To that end, we also provide a fast normalization method (Method 2) that ignores the transition region that significantly increases the calculation speed at the expense, however, of having an abrupt change in the value of the phase function at the boundary of the shadow region.

Method 1: At each distance from the scattering center, we define a transition region between the shadow zone and the far-field, which has a half angular range (the angle between the outer boundary of the transition region and the incident direction) $f_{transition}$ times the half angular range

of the shadow zone $\Theta_{transition} = f_{transition} \cdot \Theta_{shadow}$. The factor $f_{transition}$ is a number larger than 1 and varies with distance. In the shadow region, the phase function is taken to be constant. In the transition region we decrease the phase function linearly from the shadow region value to the far field value. For example, at a distance $L < L_s$, the approximated near field phase function can be written as:

$$\begin{cases} \theta \le \Theta_{shadow}, & P(\theta) = P_0 \\ \Theta_{shadow} < \theta \le \Theta_{transition}, & P(\theta) = P_0 - \left(P_0 - P_{FarField}(\Theta_{transition})\right) \times \dfrac{\theta - \Theta_{shadow}}{\Theta_{transition} - \Theta_{shadow}} \\ \Theta_{transition} < \theta, & P(\theta) = P_{FarField}(\theta) \end{cases} . \quad (3.23)$$

where P_0 is the normalization factor which is determined by the condition $\int_0^\pi P(\theta) sin\theta d\theta =$ We determine the radially varying factor $f_{transition}$ by comparing our approximated near-field Mie phase function with the BH90 near-field Mie phase function, searching for the best-fit $f_{transition}$ value at various near-field distances for several typical particle sizes defined by x = 100, 200, 500, 1000, and 1800. We varied $f_{transition}$ from values of 1 to 4 in steps of 0.1 to find the $f_{transition}$ value at each distance and for each particle size that has the least square deviation between our approximated near-field phase function and the BH90 near-field Mie phase function. We set the maximum possible $f_{transition}$ value as 4, because $f_{transition}$ only approaches this value at distances near L_s, where the angular range of the shadow zone is approaching zero and the value of $f_{transition}$ doesn't much affect the approximated phase function. This is demonstrated in **Figure 3.14**, where we show the best-fit $f_{transition} = \Theta_{transition} / \Theta_{shadow}$ values with respect to the relative distance L / L_s. The results for different particle sizes coincide fairly well with each other with the red curve representing the averaged trend that we will apply in our calculation.

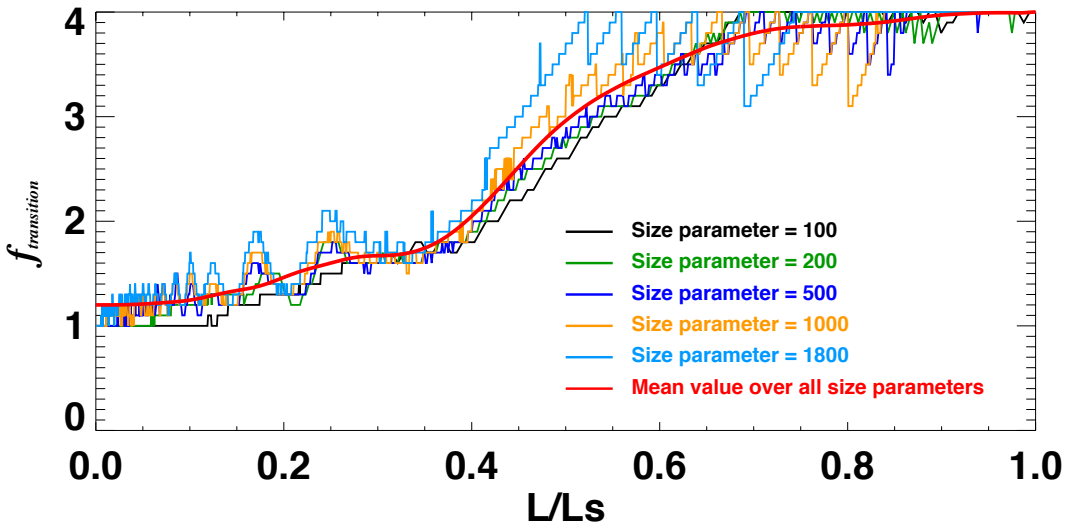

Figure 3.14: Best-fit $f_{transition} = \Theta_{transition}/\Theta_{shadow}$ values with respect to the relative distance L / L_s for several typical particle sizes x = 100, 200, 500, 1000, and 1800. The red curve represents the mean value over all size parameters.

In the top panel of **Figure 3.15**, the phase function is calculated at a distance 70% L_S for a particle with size parameter x = 100 (a = 35 cm at λ = 2.2 cm), corresponding to roughly the smallest particle size ($a_{min} = 30\ cm$) in the A and B rings. The half angular size of the shadow region at this distance is 1.65°. The best-fit $f_{transition} = 3.7$ (see Fig. 3.14) and the half angular size of the transition region is 6.1° (demarcated by the black dotted lines on the right in Fig. 3.15). To better show the shadow region, we have plotted the scattering angle (x-axis) on a logarithmic scale. Our approximated near-field phase function for Method 1 (red dashed curve) is calculated using Eq. (3.23) and coincides with the calculated BH90 near-field Mie phase function (black curve). It can be seen that the near-field phase function inside the shadow region is essentially flat as we mentioned before and has a value much lower than the far-field Mie phase function (green dot-dashed curve) which results in more light being scattered into larger scattering angles. That is to say, the light is scattered more isotropically. In the lower panel, a similar calculation is shown at a

distance 1.2% L_S for a much larger particle with size parameter x = 1000 (a = 3.5 m at λ = 2.2 cm). The half angular size is considerably larger at 26.3° for the shadow region, while the transition region extends out to 31.56°. In this case, we find the best fit $f_{transition} = 1.2$. Here we plot the scattering angle (x-axis) on a linear scale to show possible deviation from the BH90 near-field phase function outside the shadow zone by using the far-field phase function as an approximation. In spite of some fluctuation of the near-field Mie phase function within the shadow zone, our approximated phase function matches the true near-field Mie phase function pretty well.

Method 2: Although Method1 nicely takes into account the transition region, the required calculation time is expensive, especially for our Monte Carlo simulations. Thus, we propose a fast calculation method in which we ignore the transition region altogether. For this method, at a distance $L < L_S$, the near field phase function for a given size particle can be written as:

$$\begin{cases} \theta < \Theta_{shadow}, & P(\theta) = P_0 \\ \theta \geq \Theta_{shadow}, & P(\theta) = P_{FarField}(\theta) \end{cases}, \tag{3.24}$$

where P_0 is the normalization determined from $P(\theta)$. The approximated near-field Mie phase function calculated by Method 2 is still able to match the averaged flat phase function value inside the shadow zone; however, as we mentioned before, without consideration of the transition region, the phase function abruptly drops to the far-field Mie phase function value outside the shadow zone boundary.

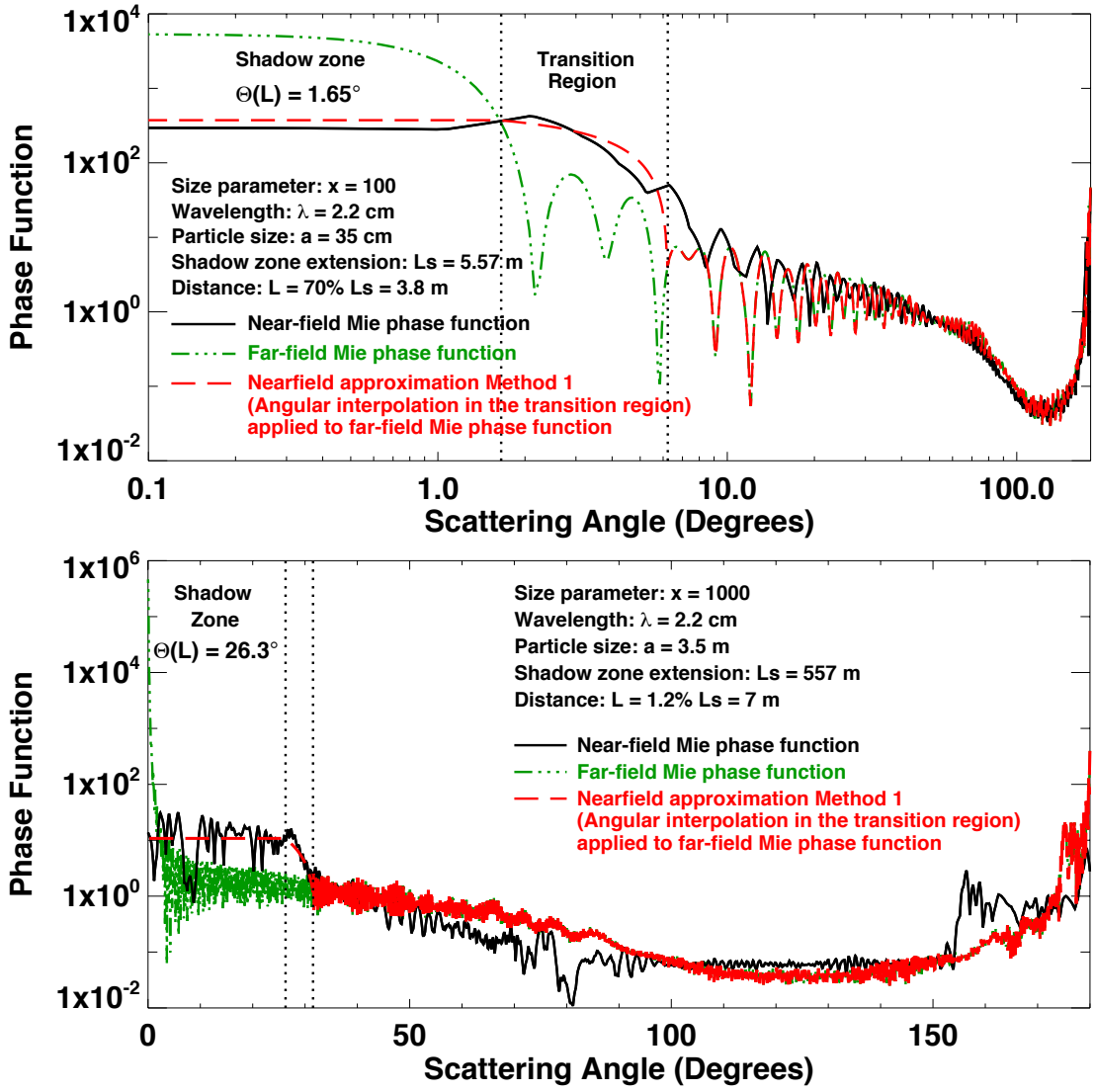

Figure 3.15: Comparison between the far-field Mie phase function (green dash-dotted line), near-field Mie phase function calculated at a distance of 70% L_S (top panel) and 1.2% L_s (lower panel) using the code of Barber and Hill (black solid lines) and our approximated near-field Mie phase function using Method 1 (red dashed line) for a particle with size parameter x = 100 (top panel) and x = 1000 (lower panel). Our approximated near-field phase function is calculated using Eq. (A-10), and the best-fit $f_{transition} = 3.7$ for x =100 and $f_{transition} = 1.2$ for x =1000 (see Fig. 3.14). The vertical black dotted lines bracket the half angular size of the transition region. That is, the left vertical line marks the boundary of the shadow region, while the right vertical black dotted line marks the outer boundary of the transition region.

We employ Methods 1 and 2 for the near-field effect to the semi-empirical phase function described in Sec. 3.7.1, and apply these approximated near-field semi-empirical phase functions for nonspherical particles in our Monte Carlo simulation for optically thick layers with large particles. The difference in constructing a near-field semi-empirical phase function from a near-field Mie phase function is that now the far-field phase function is assumed to be the semi-empirical phase function (see Sec. 3.7.1) instead of the far-field Mie phase function. In our Monte Carlo code, we track the path of each virtual photon as it enters the ring layer. Each time a photon is scattered by a ring particle (Particle1, if any), we randomly determine four events which affect the fate of the photon: (1) the distance L it travels before it encounters the next ring particle or leaves the ring layer; (2) the size of the next ring particle (Particle2) the photon encounters (if any); (3) whether the photon is absorbed; and (4) the scattering phase angle (if scattered). The determination of the scattering phase angle depends on the scattering phase function of Particle1. If we ignore the near-field effect and assume all scatterings are independent, the scattering phase function doesn't depend on the distance L between Particle1 and Particle2, which would only be valid in the case where particles are small or not closely packed (e.g., the C ring, Cassini Division). We modified our code to apply this new phase function for large nonspherical particles that are closely packed (*i.e.*, in the optically thick B ring regions and A ring wakes). After each time a photon is scattered by a ring particle (Particle1), we determine the distance L it travels before it encounters the next particle (Particle2). If $L \geq L_s$ (L_s is the extent of the near-field zone of Particle1), we use the far-field semi-empirical phase function we discussed in Sec. 3.7.1 if the particle size parameter x is larger than x_0, otherwise we use the Mie phase function. If $L < L_s$, we calculate the near-field semi-empirical phase function as described above using Method 1

(angular interpolation in the transition region) and Method 2 (fast calculation) if the particle size parameter x is larger than x_0. If the particle size parameter x is smaller than x_0, the near-field Mie phase function is applied.

To demonstrate our approximation model, in **Figure 3.16** we show a simulation of the brightness temperature for a ring annulus with high optical depth $\tau = 7$, particle porosity of 55% and particle size distribution $a_{\min} = 30cm, a_{\max} = 6.3m, q = 2.75$ (identical to the B ring and inner A ring, see Table 3.2), and compare how the scattered light varies with azimuthal angle using these new phase functions (both method 1 and method 2), as well as using the hybrid phase function that is a mixture of Mie and isotropic phase functions. We find that for this optically thick ring annulus, the new phase functions result in a similar azimuthal brightness distribution as that of a hybrid phase function that is 30% Mie/70% isotropic. Given that the results are quite similar for Methods 1 and 2, it is clear that there is a distinct advantage to using Method 2 in terms of calculation costs. These results explain the observation in the B ring that the particles scatter more isotropically in optically thicker regions (middle B ring), which is due to both particle nonsphericity and the near-field effect. Furthermore, though the averaged optical depth in the A ring is smaller than that in the middle B ring, due to the wake structures the optical depth inside the wakes can be much higher and therefore particles in the A ring also tend to scatter light more isotropically.

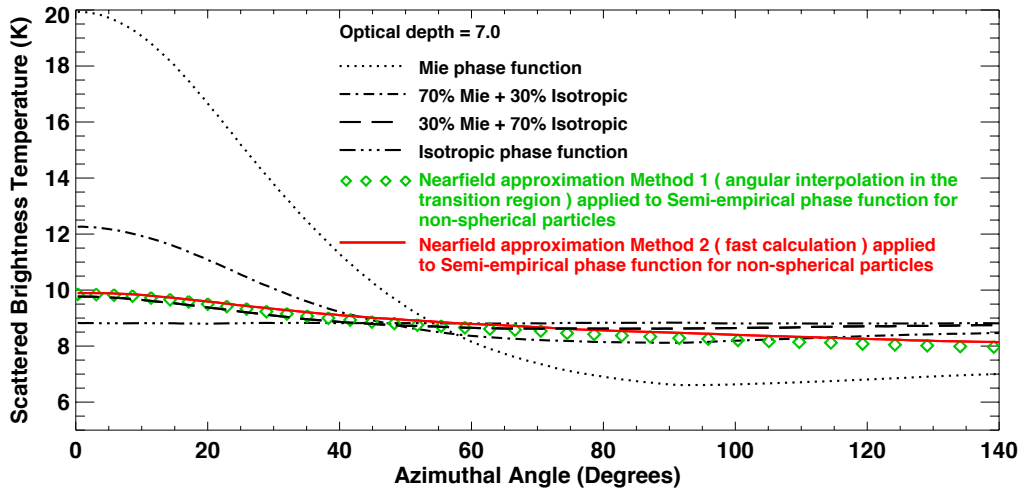

Figure 3.16: The simulated brightness temperature with respect to azimuthal angle for a ring annulus with $\tau = 7$, when using five different scattering phase functions: 1) the new phase function as we described in this appendix using Method 1 (green diamonds) which employs an angular interpolation within the transition region, and Method 2 (red solid curve) which is a fast calculation that ignores the transition region; 2) Mie; 3) 70% Mie/30% isotropic (which predicts similar scattering profile as the far-field semi-empirical phase function when only nonsphericity effect exists, see Fig. 3.11); 4) 30% Mie/70% isotropic; and 5) a purely isotropic phase function. In the Cassini high-resolution observation geometry (at the ring inclination angle ~ 20° and distance ~6 R_S from Saturn center), the portion of a ring annulus located at the radius of the middle B ring, where azimuthal angles larger than 140° are blocked by Saturn and cannot be observed.

4 Non-icy Material Fraction Determined by Cassini Observations

4.1 C Ring

For a particle size distribution with our nominal choice of power law index q=3.15, small particles dominate the scattering process in the C ring. Most of these small particles have a size parameter smaller than the bound beyond which non-sphericity becomes important. Furthermore, considering that the C ring particles are relatively widely separated due to the low optical depth there, they can

be treated as independent spheres. Therefore, Mie scattering theory is expected to be a good approximation for the scattering process in the C ring. In this section, we compare the simulated brightness temperature with the observations in order to determine the C ring particle composition in terms of porosity and non-icy material fraction.

4.1.1 Occultation Region at Small Azimuths: Ring Particle Porosity

We first analyzed the occulted region of Saturn on the C ring in low-resolution map scans. These brightness data are composed of directly transmitted radiation, scattered Saturn radiation, and intrinsic thermal emission. However, the directly transmitted and forward-scattered sources of Saturn radiation are an order of magnitude larger than the intrinsic thermal emission. Therefore, in these occultation observations the brightness temperature is not very sensitive to the non-icy material fraction, providing us with an opportunity to investigate ring particle porosity alone. As shown in the output brightness temperature profile of Rev028_HIGH (Fig. 2.8), most parts of the C ring are no brighter than 10 K at larger azimuthal angles. The non-occultation brightnesses are composed of scattered Saturn radiation and intrinsic thermal emission. In these cases, even if the intrinsic thermal emission contributes half of the brightness, it is still no larger than 5 K. Moreover, the intrinsic thermal emission is originally emitted by the ring particles isotropically and thus its value shouldn't depend in a significant way on the azimuthal angle of the observing point. That is to say, the intrinsic thermal emission at smaller azimuthal angles should also be no larger than 5 K, which is an order of magnitude smaller than the directly transmitted and forward-scattered Saturn radiation in the occultation data.

The data were collected during Rev028_LOW, Rev038_1_LOW, Rev038_2_LOW and Rev039_LOW, when the rings had opening angle $B = \sim 20^{\circ}$. Considering that our main beam can cover a ~8,000 km to 24,000 km region, when observing radial locations outside 82,000 km the averaged brightness in the main beam contains contributions from the inner B ring (see Fig. 3.3). Therefore, in order to simulate the brightness temperature in these observations, the scattering properties of the inner B ring particles are also required. As opposed to the C ring particles, non-sphericity and close packing effects become important for the B ring particles and a modified phase function such as the one given in Eq. (3.14) is required. See detailed discussion on the B ring particles scattering properties (i.e. scattering phase function) in Sec.4.2. Initially, we assumed non-porous ring particles with our nominal size distributions throughout the whole of the C and B rings, respectively (see Sec. 3.2). However, we found that the modeled brightness temperature is much smaller than observed (see **Figure 4.1** with, e.g., data from Rev038_1_LOW). Notice that the observations show significant scatter, because at each ring radius data are collected at various azimuthal angles (see Fig. 2.7, lower panel). In the C ring, half of the brightness in "occultation" geometries is contributed by scattered Saturn radiation and the scattering phase function varies quickly at these small azimuthal angles.

The directly-transmitted Saturn radiation is fixed since the optical depth is fixed. Therefore, this mismatch indicates that we need a more forward-directed scattering phase function for the C ring particles. We can improve the fit of the phase function either by increasing the average C ring particle size, as large particles are strong forward-scatterers, or decreasing the real component of the dielectric constant, for example, by making the whole particle uniformly more porous, or assuming a core-mantle ring particle structure with a solid core and porous mantle. Due to the complication of the core-mantle ring particle structure in our simulation, we defer treatment of the

core-mantle particles to Section 5.2.2. We will show there that by selecting appropriate parameters for the core-mantle model, its phase function can be made to closely match that of the intramixed model, and thus will not change the simulated scatter component for the occultation and non-occultation data.

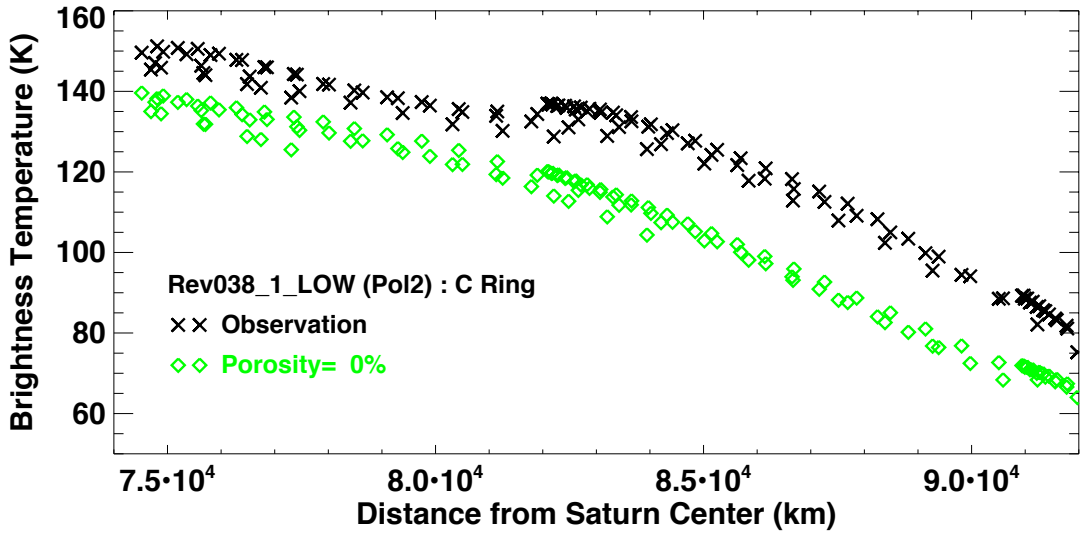

Figure 4.1: Brightness temperature vs. ring radius plot of occultation observations in the C ring during Rev038_1_LOW (polarization 2). Black crosses: observed brightness temperature. Green diamonds: simulated brightness temperature assuming zero porosity.

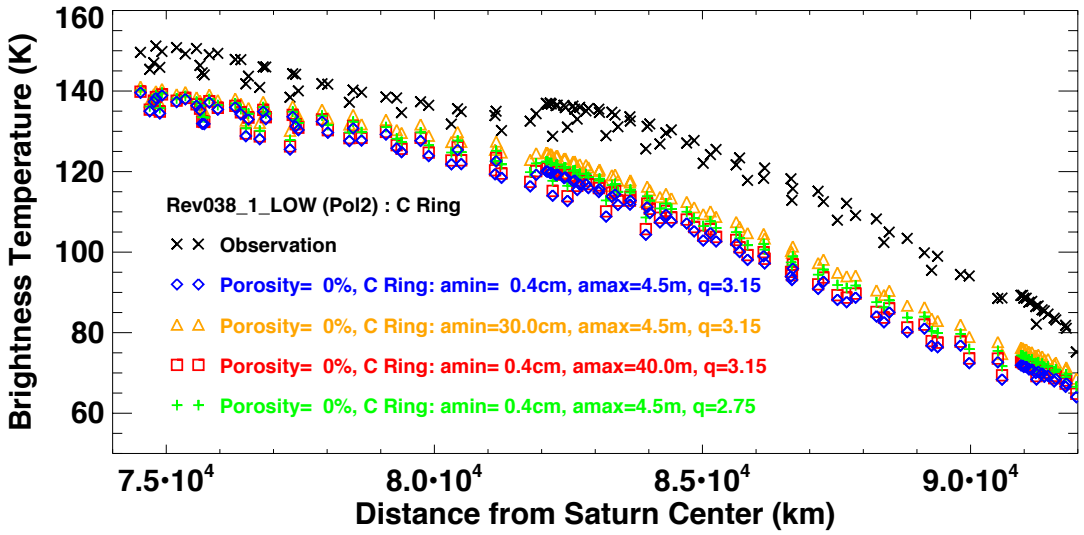

Figure 4.2: Brightness temperature vs. ring radius for occultation observations of the C ring during

Rev038_1_LOW (polarization 2). The black crosses are the observed brightness temperature, while the blue diamonds are the simulated brightness temperature assuming zero porosity and the nominal C ring particle size distribution $\mathrm{a_{min}} = 0.4\ \mathrm{cm}, \mathrm{a_{max}} = 450\ \mathrm{cm}, \mathrm{q} = 3.15$. Orange triangles: An increase of a_{min} from 0.4 cm to 30 cm. Red squares: An increase of a_{max} from 4.5 m to 40 m. Green plus signs: A decrease of q from 3.15 to 2.75.

We first attempted to increase the number of larger particles in the C ring by altering the parameters in the particle size distribution by either increasing the minimum size a_{min}, maximum size a_{max} or decreasing the power law index q. We note that the parameters in the power law size distribution have been fairly well constrained by previous work, with a much smaller range than what we test here (Marouf et al., 2008). However, we found that even for choices of the parameters at the extremes of what we consider a reasonable range, the simulated brightness temperature is still much lower than observed (see **Figure 4.2**, specifically Rev038_1_LOW, polarization2 as an example). We also included an additional thermal emission contribution due to non-icy material, which can at most be about 5 K, but again found that the total simulated brightness is still not high enough to match the observations.

Second, we chose to model the ring particles as porous. Because the outer C ring brightness temperature has a large contribution from the inner B ring, the porosity of the C ring and B ring particles, $f_{\mathrm{p\_CRing}}$ and $f_{\mathrm{p\_BRing}}$ need to be determined at the same time. For the C ring porosity, we vary f_{p_CRing} from 0% to 90%, in steps of 5%. At this stage, we are not able to determine the B ring particle porosity independently from the C ring observations. In fact, as the scattering phase function for the B ring particles is a combination of Mie and isotropic functions, and porosity only affects the Mie phase function piece, the B ring particle scattering phase function is much less

sensitive to porosity than compared to the C ring. Moreover, previous work has suggested that A ring particles could be as much as 55% porous (Porco et al., 2008; see, also Morishima et al., 2016), thus it is reasonable to assume that the B ring particle porosity may lie somewhere in between the A ring and C ring values. Recent work also suggests high porosity of the B ring particles based on its seasonal temperature variation (Reffet et al. 2015). We considered two cases: (1) $f_{\mathrm{p\_BRing}} = f_{\mathrm{p\_CRing}}$; and (2) $f_{\mathrm{p\_BRing}} = f_{\mathrm{p\_ARing}} = 55\%$. We combine the occultation data in all four low-resolution map scan occasions and find that our best fit model is obtained when C ring particles are 75% porous in both cases, with a RMS ~3.8 K, about 2-5% of the observed brightness. By adding 75% porosity to the ring particles, the real part of the effective dielectric constant becomes ~1.45. Figure 4.3 shows how our best-fit parameters match the observations. The simulation results don't change much no matter what value for the B ring porosity is assumed and in Fig.4.3 we only show the case when assuming $f_{\mathrm{p\_BRing}} = 55\%$. The result confirms our earlier assumption that the brightness contribution from B ring particles is not very sensitive to their porosity, since the best-fit C ring porosity value remains the same as the B ring particles porosity varies between 55% and 75%.

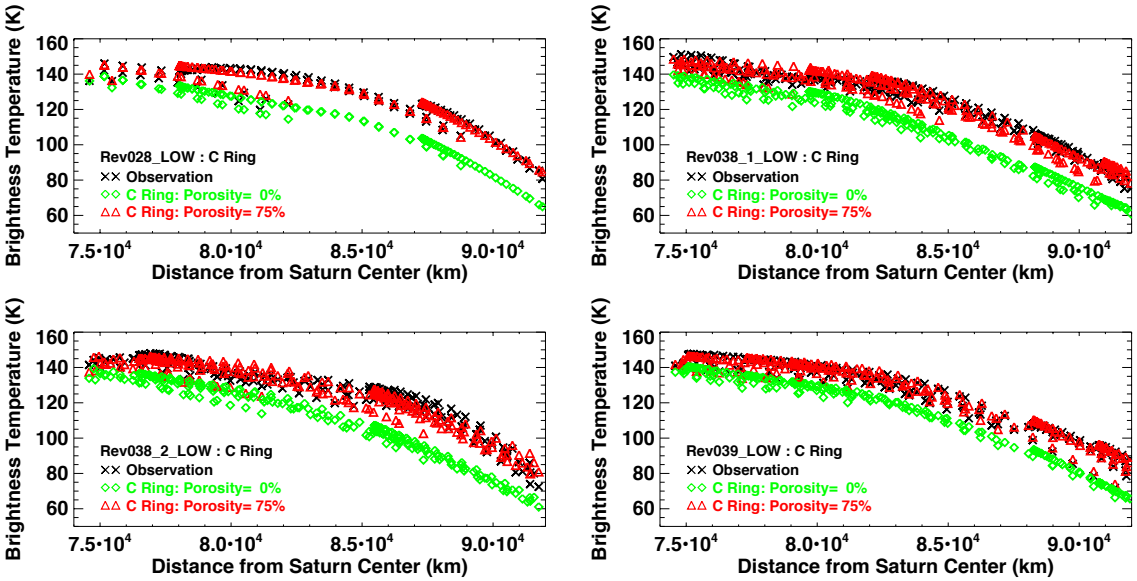

Figure 4.3: Brightness temperature model as compared to actual observations for C ring particles with 75% porosity. Plotted is the brightness temperature vs. ring radius for occultation observations of the C ring during Rev028_LOW (upper left), Rev038_1_LOW (upper right), Rev038_2_LOW (lower left) and Rev039_LOW (lower right). For each occasion, we have combined data from all available polarizations. Black crosses: observed brightness temperature. Green diamonds: simulated brightness temperature assuming zero porosity. Red triangles: simulated brightness when assuming C ring particles are 75% porous.

In **Figure 4.4**, we plot the single scattering phase function integrated over the C ring particle size distribution for all our attempts to match the high brightness in the occultation data (*i.e.*, increasing the minimum particle size, maximum size, decreasing the power law index, and adding porosity), which shows how adding 75% porosity is able to increase the simulated brightness enough to match the observation while merely changing the particle size distribution parameters cannot. By adding 75% porosity, the bending angle of intrinsic refraction tends to be smaller and more light gets scattered into the forward direction. The light scattered into large scattering angles is suppressed, while the light scattered into angles smaller than ~30^{o} increases greatly. Since Saturn has a ~40 - 55^{0} angular radius as seen from the C ring, most incident Saturn radiation is scattered

less than 30^0 before reaching the observer, and therefore the simulated occultation observations increase considerably by adding 75% porosity.

The average brightness temperature of these observations is in between ~80-150 K. We find that the best fit RMS is about 2 - 5% of the average observed brightness temperature, which is comparable to our calibration error (~2%). On the other hand, the portion of the Saturn disk blocked by the C ring lies between the latitudes of 5 to 25 degrees south, where a longitudinally-variable bright Saturn radiation band has been discovered (Janssen et al., 2013). The variation in longitude can be as large as ~10 K, which can cause an increase in the C ring brightness temperature of ~6 K even for the comparatively optically thick middle C ring with $\tau \sim 0.2$. This may be another factor that can cause errors in the fitting process.

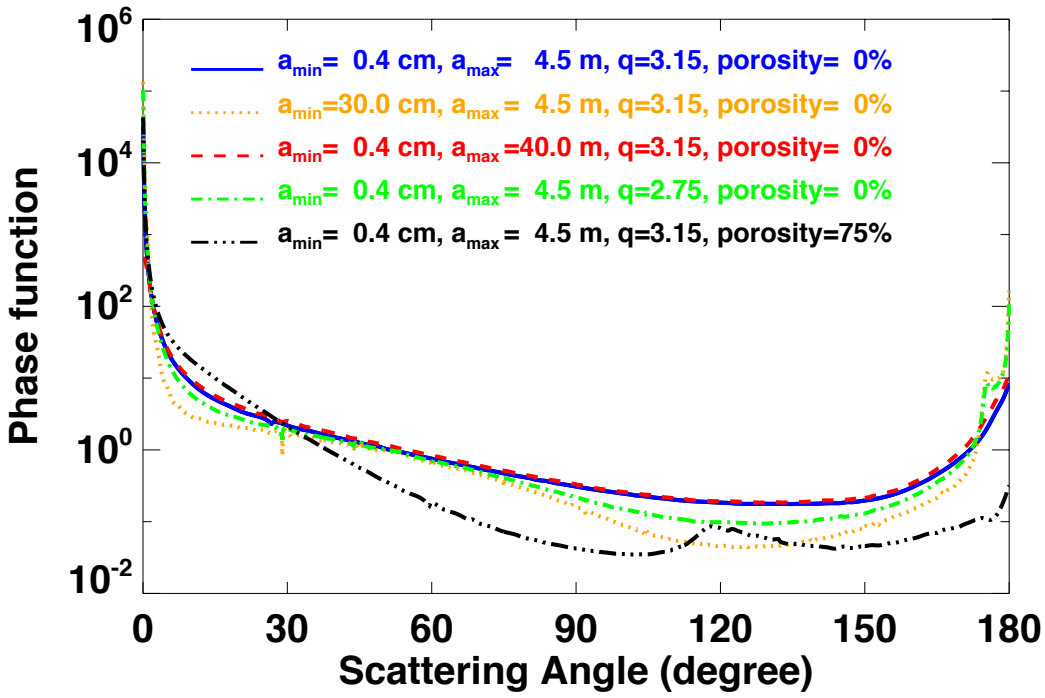

Figure 4.4: Single scattering phase function integrated over the C ring particle size distribution for all our trial cases. Case 1 (blue): nominal particle size distribution; zero porosity. Case 2 (yellow): increase of the minimum size from 0.4 cm to 30 cm; zero porosity. Case 3 (red): increase

of the maximum particle size from 4.5 m to 40 m; zero porosity. Case 4 (green): decrease of the distribution power law index from 3.15 to 2.75; zero porosity. Case 5 (black): nominal particle size distribution; 75% porosity.

Arecibo observations (Nicholson et al., 2005) have yielded a stringent upper limit of 3% on the back scattering cross-section of the C ring. With these highly porous ring particles, we simulated the back scattering from the C ring and obtained a very low, normalized backscatter cross-section of about 3%, consistent with the observations. Given that some of the smaller satellites in the Saturn system have bulk porosities in excess of 60% (Thomas et al., 2007; Johnson et al., 2005), and the recent works by the Rosetta team that reported a bulk porosity of 70 - 80% for comet 67P/Churyumov-Gerasimenko (Sierks et al., 2015; Kofman et al., 2015), it may not be surprising that individual ring particles can be so porous. Porco et al. (2008) also suggested that the A ring particles are very porous due to the low internal mass density. Recently, Morishima et al. (2016) have matched CIRS data within the A ring by assuming that A ring particles have cores with porous icy mantles with values for the porosity similar to what we find here (see also, Sec. 5.2.1). The finding is interesting because although particle mean densities in the A ring are not expected to be so low due to the presence of self gravity wakes (e.g., see French et al., 2007), particles that have dense cores but, with fairly porous surface layers were found to best fit the data. This suggests that particles can be porous even under relatively vigorous collisional conditions. Given that there are no observed self gravity wakes in the C ring, it may not be unreasonable then to consider that particles may also be porous in the C ring.

One possible explanation might be that impact gardening due to micrometeoroid bombardment, which creates a regolith of increasing depth over time (e.g., Elliott and Esposito, 2011), may play

a role in increasing particle porosity. Collisions among ring particles occur frequently within the C ring, but at relatively low (mm/s) velocities, when compared to impacts by extrinsic micron-sized meteoroids (~10 times more frequent for the nominal choice of flux, Sec. 5.2.1). However, secondary impacts that arise as a result of the ejected material from the primary micrometeoroid impact should occur much more frequently than inter-particle collisions and at velocities of up to tens of meters per second (see ballistic transport process as discussed in Cuzzi and Estrada, 1998). These secondary impacts might kick up loosely bound regolith particles such that a considerable "exchange" of material may happen *locally* between neighboring ring particles keeping their regoliths fluffy. Thus, even though inter-particle collisions may have a tendency to compact a ring particle surface, it might be possible that the ring particles can achieve a quasi-equilibrium porous regolith that results from a balance of these combined impact and collisional processes.

4.1.2 High Resolution Scans at Ring Ansa: Ring Particle Non-icy Material Fraction

While occultation observations mainly reveal the strength of the forward directed part of the scattering phase function, non-occultation observations in high-resolution spoke scans depend more on the scattering phase function at larger scattering angles. By adding 75% porosity we have made the phase function more forward-directed to match the small angle scattering in the occultation observations. We further investigated the scattering profile in high-resolution spoke-scan non-occultation observations to check how this phase function behaves at large scattering angle. **Figure 4.5** shows observations from three ring annuli in the inner, middle and outer C ring. The simulated scattering profile (brightness temperature vs azimuthal angle) matches the data fairly well. At the middle C ring, intrinsic thermal emission contributes almost half of the

brightness, which indicates that there must be some non-icy material included in the ring particles.

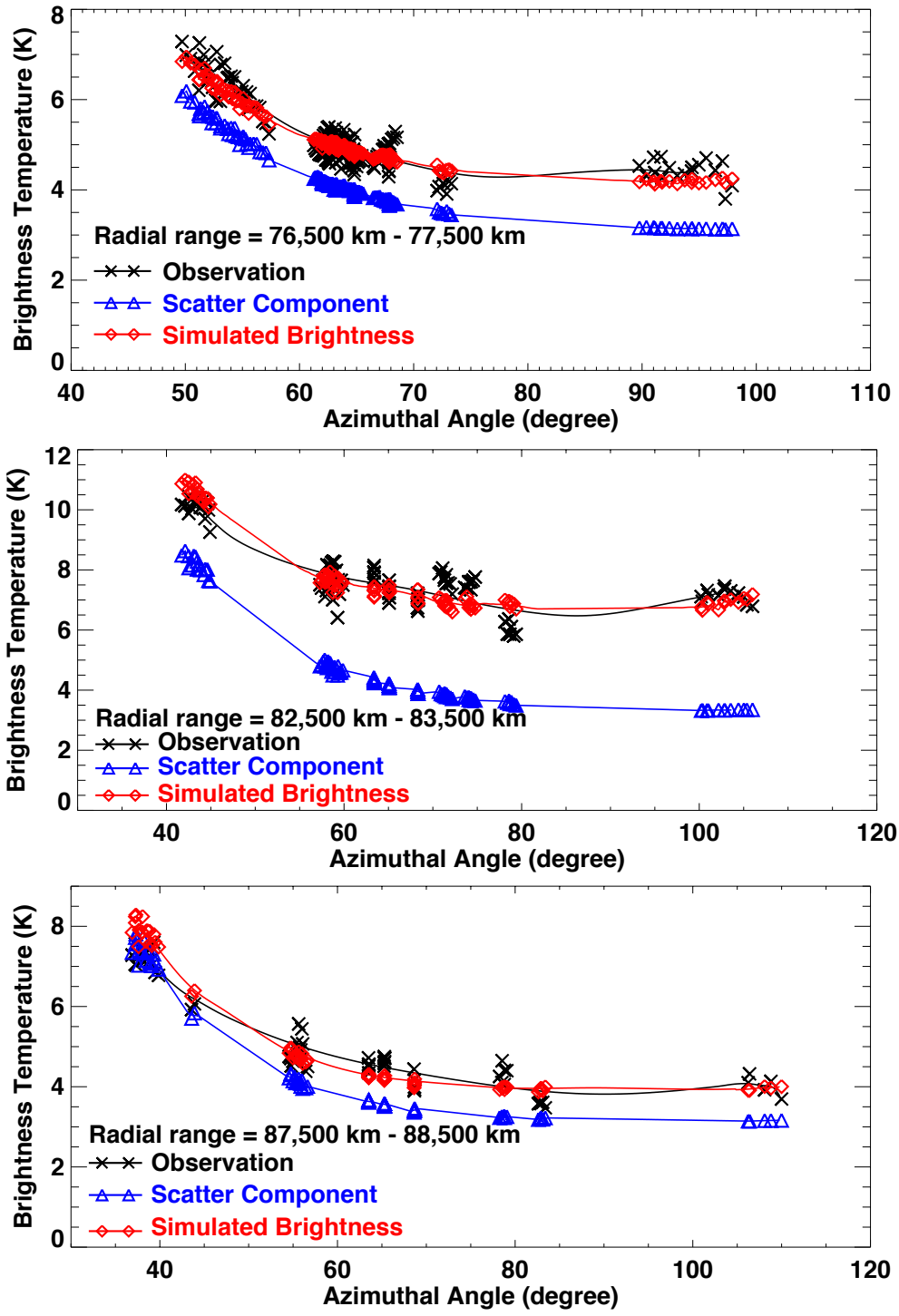

Figure 4.5: Scattering profile: brightness temperature versus azimuthal angle curves at three different ring radii for the inner (76,500 km-77,500 km), middle (82,500 km-83,500 km) and outer C ring (87,500 km-88,500 km). The azimuthal angle is the angle between the projection of Cassini

onto the ring plane and the observation point in Saturn-centered coordinates. All observation data come from Rev028_HIGH. We plot the observed brightness temperature (black crosses), scattering component with CMB contribution (blue triangles) and simulated brightness temperature (red diamonds; addition of scatter component, CMB contribution and intrinsic thermal emission). We have added ~2%, ~6% and ~1.5% non-icy material in the ring annulus for panels 1, 2 and 3, respectively. The simulated brightness temperature matches the observations well. The observed brightness at some azimuthal angles are scattered due to the relatively large radial width of the ring annulus. In the middle C ring (panel 2), the polarization effect is most obvious between 60 to 80 degrees azimuth. All the observations (black crosses) above the simulated brightness (red diamonds) are collected at polarization 2 and 3, while the ones below the simulated brightness are at polarization 1 (horizontal to the ring plane, see Chapter 2 for more details). This polarization variation in observed brightness will have the effect of increasing the uncertainty of our final non-icy material fraction profile.

We simulated the Saturn radiation scattered by porous ring particles with f_p = 75% for non-occultation observations during Rev028_HIGH. Given the non-icy fraction of each ring particle's composition, our Monte-Carlo code is able to simulate the magnitude of the thermal emission. The scattered component doesn't significantly change as we add non-icy material (i.e. silicate) to the ring particles. We therefore are able to determine the non-icy material fraction by adding non-icy material to the C ring particles untill the simulated brightness, which is a combination of scattering component, thermal emission and CMB contribution, matches the observation. The results of this analysis justify the necessity for including intrinsic thermal emission in order to match the observed brightness temperature, especially around ~83,000 km in the middle C ring, where the brightness is observed to increase significantly beyond what can be attributed to scattered radiation from Saturn. We find that more than half of the brightness temperature comes from intrinsic thermal emission, while the shape of the profile is well-matched by scattered radiation (see Fig.

4.5, middle panel).

Microwave thermal emission is directly related to the abundance of non-icy material. For reasons that will become clear below (see Chapter 5, and specifically Sec. 5.2.4 for a brief discussion of other candidate materials), we find that the best candidate material for the non-icy component is silicate. On this assumption, we are able to derive the volume fraction of non-icy material mixed with water ice throughout the C ring. We divided the C ring into eighteen 1,000km-wide radial bins. For each radius bin, we derived the best-fit silicate fraction for each observation point within that radius range and take their average as the non-icy material fraction for that radius bin. The derived radial variation of non-icy fraction of each radius bin is shown in **Figure 4.6**. We find that the silicate fraction reaches its maximum of ~ 6.3% by volume in the middle C ring. Away from its peak value, the material fraction decreases gradually inward, but much more strongly outward of ~ 83,000 km. The grey lines show the range of one standard deviation, for each radial bin.

We find fairly large uncertainties. There are a couple of reasons for this: (1) because we are limited by the radial resolution of our observation (~2,000 km), we aren't able to resolve the radial variation of the non-icy material fraction on smaller radial scales; (2) the Mie scatter phase function is an approximation that fits the overall observation profile shape well, but when it comes to each observation point, data at certain azimuthal angles may deviate from the Mie scatter profile by some small amount; (3) Observational uncertainties might also cause these deviations which will then cause uncertainties in the amount of the intrinsic thermal emission, and therefore the non-icy material fraction; and, (4) considering that the non-icy material fraction shouldn't be polarization-dependent, we have combined all data from the three different polarizations. Yet, we see that there is a slight difference in the observations at different polarizations (see Chapter 2). However, our

Monte Carlo code is not able to deal with polarized light. The difference between different polarizations also increases the deviation. Despite these uncertainties, the increased non-icy material fraction in the middle C ring remains a statistically robust result.

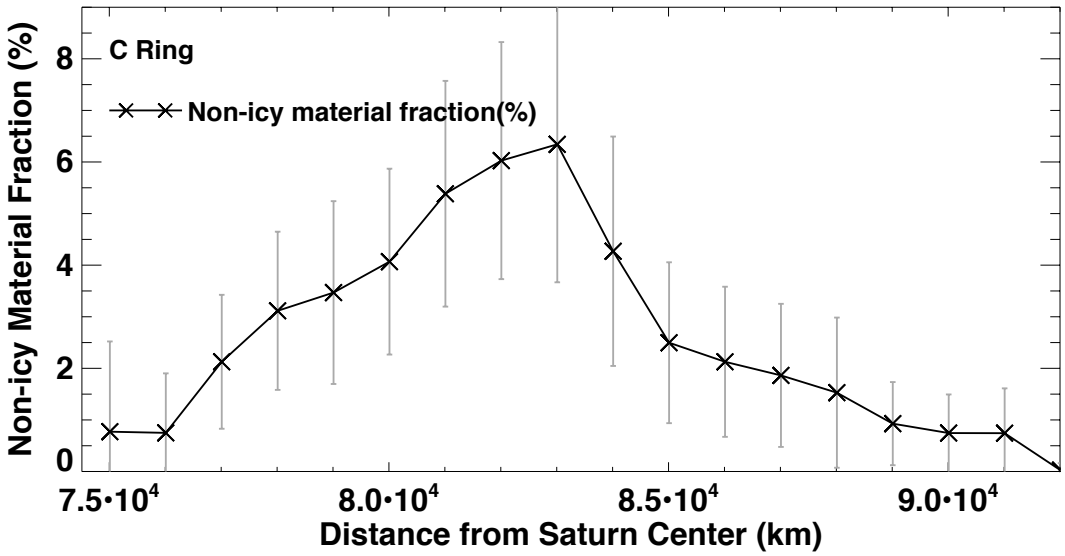

Figure 4.6: The derived radial variation of non-icy fraction reaches its maximum of ~6.3% silicate by volume in the middle of the C ring and gradually decreases inward, and more sharply outward. The grey vertical lines show the range of one standard deviation.

4.2 B Ring

4.2.1 Observations on the Ansa in High-resolution Spoke Scans -- Determining the non-icy material fraction

We divided the B ring into annuli and compared the scattering profiles in each ring annulus (brightness temperature vs azimuthal angle) from our simulation results with the observation data, in order to find the best-fit scattering phase function (*i.e.*, the fraction of isotropic phase function mixed with Mie phase function) at each ring annulus.

In the inner and outer B ring, a Mie phase function unsurprisingly (see Sec. 3.6) predicts too much brightness at small azimuthal angles, while an isotropic phase function is too flat as compared to the observations (see **Figure 4.7** upper panel). We find that a hybrid phase function that is 55% Mie/45% isotropic fits the observations best in the inner B ring, while a half-Mie-half-isotropic phase function provides the best fit in the outer B ring. On the other hand, although we match the observations best when assuming a purely isotropic phase function in the middle B ring, the difference between the half-Mie-half-isotropic and the purely isotropic phase function is very small (see Fig. 4.7 middle panel). Therefore we derived the required non-icy material fraction for both cases and used them as a range for the non-icy material fraction mixed within the ring particles. Across the B ring, the best-fit phase function gradually becomes more isotropic as one moves from the inner B ring to the middle B ring, but then becomes less isotropic going from the middle B ring to the outer B ring (see Fig. 4.7). Previous analysis of VLA observations on the rings (Dunn et al. 2002) has suggested a half-Mie-half-isotropic scattering phase function for the B ring particles, but with lower resolution.

Due to the small differences between these phase functions at any given ring radius, we calculated the required non-icy material fraction for a range of phase functions from half-Mie-half-isotropic to isotropic (except for the inner B ring edge where the range used is from 55% Mie/45% isotropic hybrid phase function to pure isotropic) and plotted the range of the required non-icy material fraction versus ring radius in **Figure 4.8**. The derived non-icy material fraction profile varies with different ring particle porosity. The required non-icy material fraction is highest when assuming particles with 90% porosity, but in all cases the fraction of non-icy material is < 1%, which is consistent with previous results (Grossman et al., 1990; Epstein et al., 1980, 1984). For each assumed value of the porosity, the non-icy material fraction is lowest in the middle B ring.

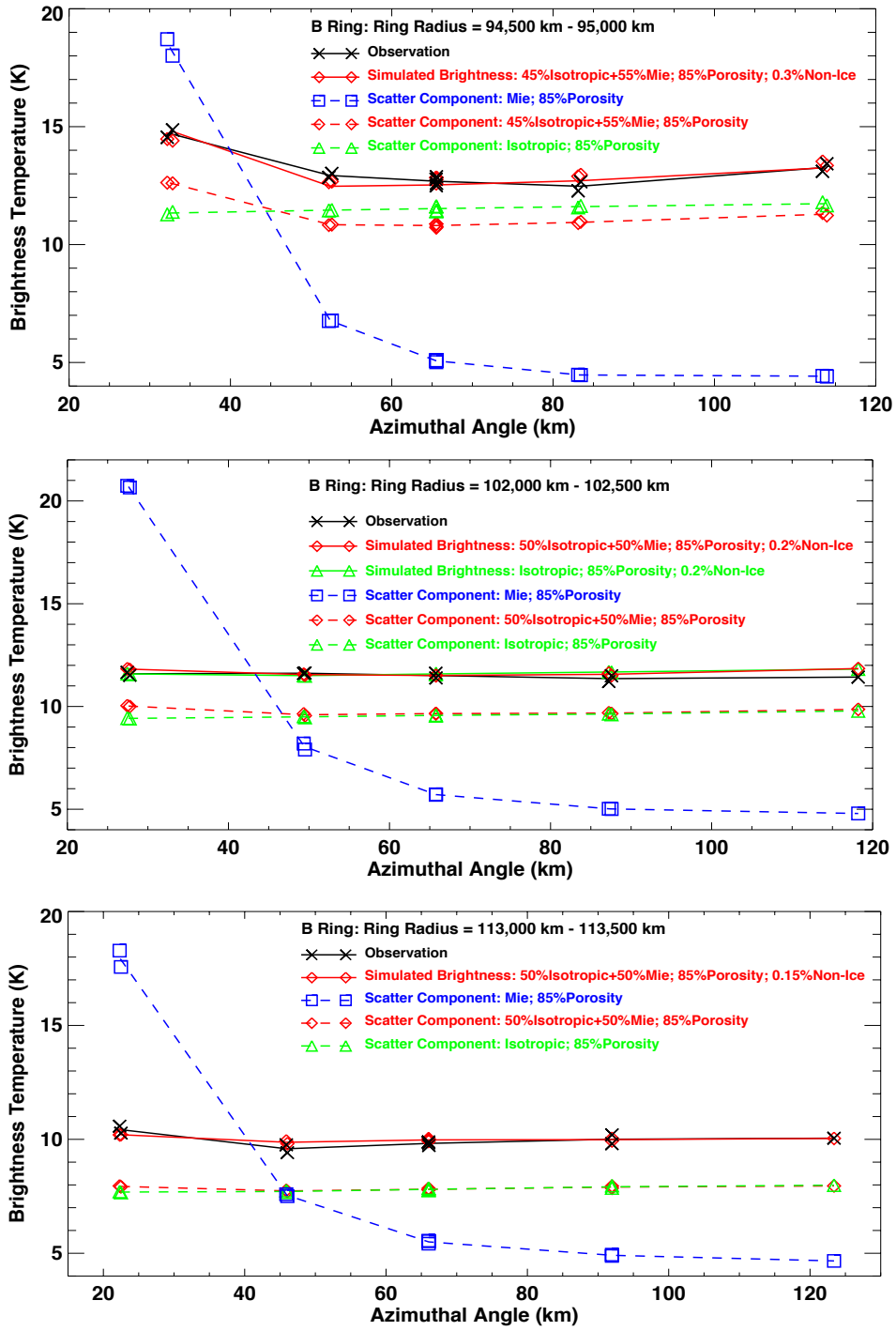

Figure 4.7: Scattering profile (brightness temperature vs. azimuthal angle) within annuli in the inner (upper panel), middle (middle panel) and outer (lower panel) B ring. All observation data come from high resolution spoke scans on the rings ansa. We plot the observed brightness temperature, scattering component (containing the CMB contribution) and simulated brightness

temperature (addition of scatter component, CMB contribution and intrinsic thermal emission).

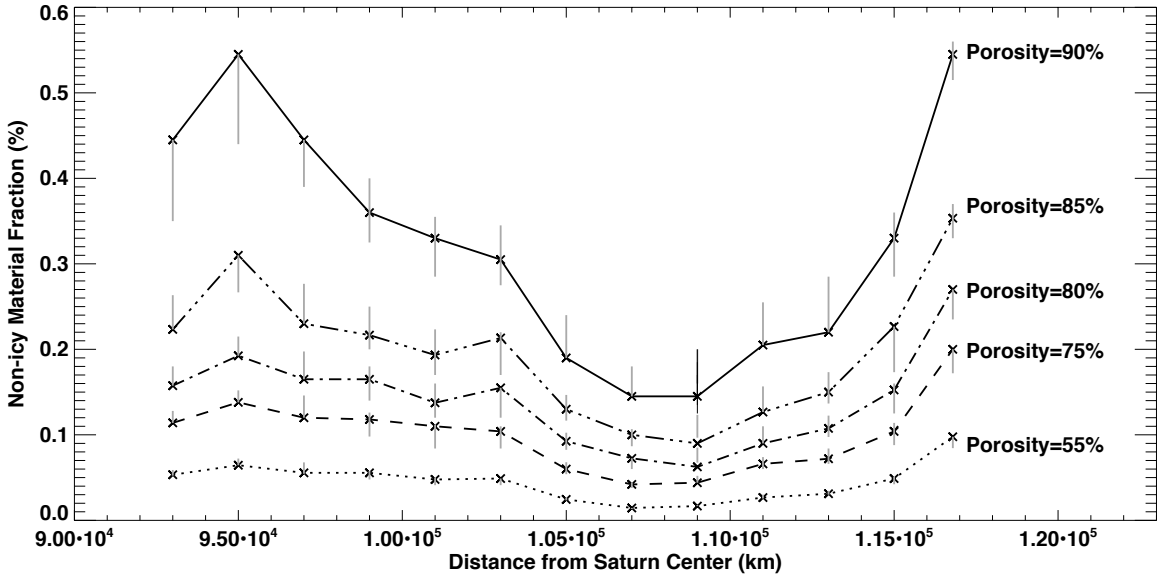

Figure 4.8: Derived non-icy material fraction in the B ring particles when assuming various porosity values: 55%, 75%, 80%, 85% and 90% (represented with different line types). The higher the porosity, the more non-icy material fraction is required to match the observation. The grey error bars indicate the range of the derived non-icy material fraction when using different particle scattering phase function (ranging from half-Mie-half-isotropic to purely isotropic, except for the inner B ring edge where the range used is from 55% Mie /45% Isotropic hybrid phase function to pure isotropic).

4.2.2 Low Resolution Map Data Ring Observations that occult Saturn – verifying the phase function

We tested the validity for using a combination of a half-Mie-half-isotropic and a pure isotropic phase function by matching the occultation data in the low-resolution mapping. Considering that the high-resolution data are all collected on the ring ansae at azimuthal angles between 20 and 120

degrees, these occultation data help test whether the phase function we used also works in the forward direction. In **Figure 4.9**, upper panel, the observed brightness (black crosses) lies in between the prediction of a half-Mie-half-isotropic (green rectangles) and a purely isotropic (purple triangles) phase function. Therefore, it is reasonable to assume that the scattering phase function for B ring particles should lie in between these two types of phase functions. We note that the simulated brightness determined using the best-fit phase function we derived from the high-resolution data (see Sec. 4.2.1), which begins in the inner B ring as an approximately half-Mie-half-isotropic phase function, but gradually evolves to become purely isotropic in the middle B ring before returning to a half-Mie-half-isotropic behavior in the outer B ring, matches our observation very well (see lower panel in Fig. 4.9). Furthermore, the value of the porosity does not much affect the brightness temperature at near-zero azimuth. We note that as shown in Fig. 4.9 the observed brightness temperature is higher at the inner and outer edge and lowest in the middle region. This is due to two main reasons: 1) the directly transmitted light is higher in the optically thinner inner and outer B ring, while it is lowest in the middle region where it is most optically thick; and 2) due to the large main beam size, the averaged main beam brightness temperature is higher in the inner (outer) B ring when the main beam partially falls on the C ring (Cassini Division).

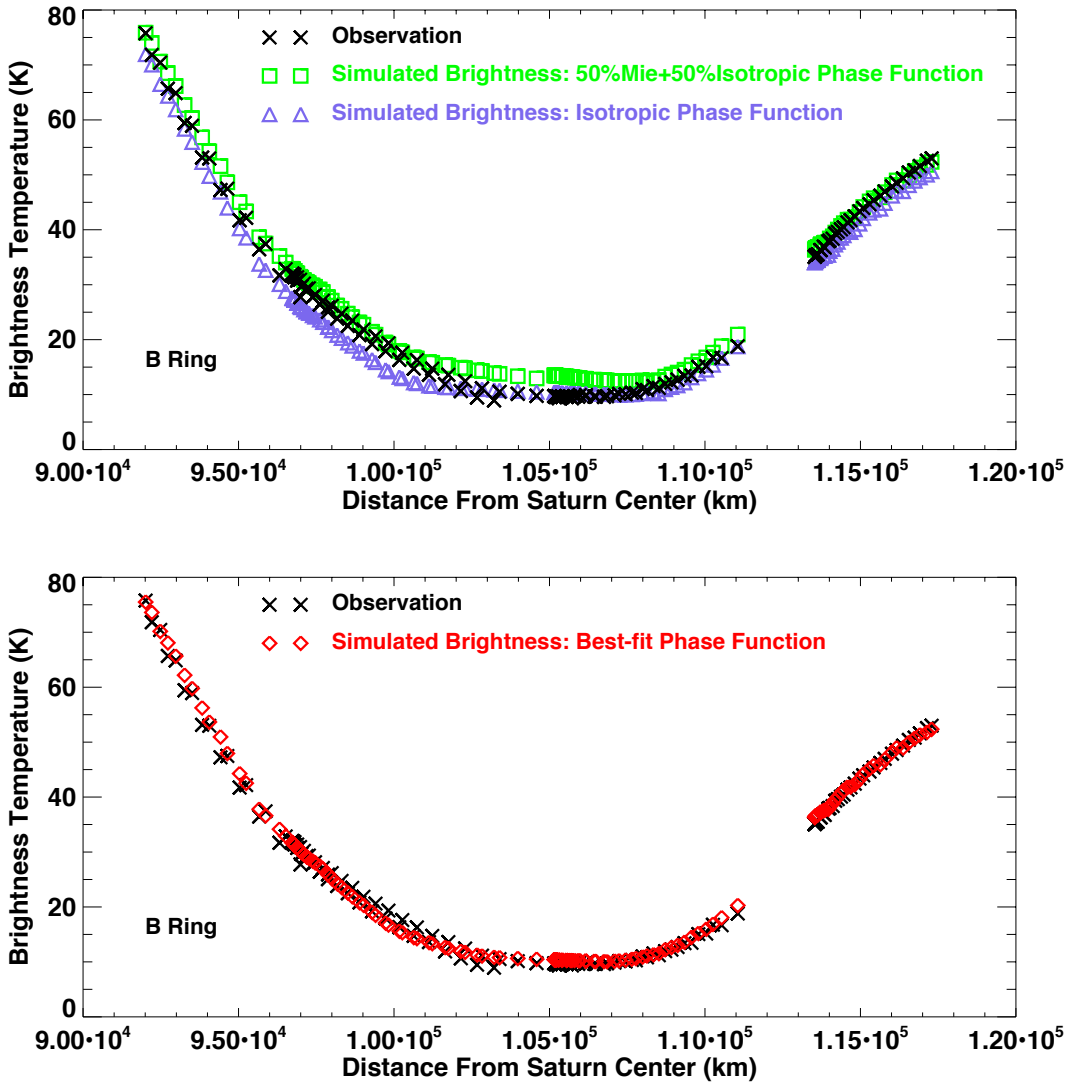

Figure 4.9: Occultation observations of the B ring in the low-resolution map scan. (Upper panel) black crosses: observed brightness temperature; green rectangles: simulated brightness temperature assuming a half-Mie-half-isotropic phase function; purple triangles: simulated brightness assuming an isotropic phase function. (Lower panel) black crosses: observed brightness temperature; red diamonds: simulated brightness with the best-fit scattering phase function, which is half-Mie-half-isotropic in the inner and outer B ring, and purely isotropic in the middle B ring.

4.3 A Ring

4.3.1 Observations that occult Saturn in Low Resolution Map Data – Determining the phase function

We now analyze observations of the A ring when it is occulting Saturn, at near-zero azimuthal angles, to further investigate the phase function we apply in our simulations. These data differ from the data collected on the ansae in that they show different aspects of the scattering phase function in the forward direction, where the phase function varies more dramatically.

To simplify the problem, we assume that all particles in the A ring have the same porosity with values of either 55% or 90%. **Figure 4.10**, upper panel shows for a porosity of 55% that the simulated brightness, when assuming an isotropic phase function (green triangles), matches the observations well inside a ring radius of ~128,000km (region A0), while the simulated brightness when using a half-Mie-half-isotropic phase function (orange rectangles) is much higher than observed. As shown in Fig. 4.10, lower panel, in region A3 different symbols represent the different particle size distribution cases. We examine all three different cases for region A3 (A3-Case1: red triangle, A3-Case2: orange circle, A3-Case3: green squares), using both half-Mie-half-isotropic phase function (filled symbols) and isotropic phase function (open symbols). We find that all of them predict a brightness that is higher than observed. The simulated brightness is lowest in the A3-Case 1 where the particles tend to be smaller than the other two cases. We did not utilize the observations in regions A1 and A2, because for those observations the main-beam partially falls on region A3. That is to say, the simulated beam-averaged brightness temperature in the A1 and A2 regions are affected by the simulated brightness in the A3 region which is too high compared to the observations. Because of this, it is difficult to draw any conclusions about regions

A1 and A2.

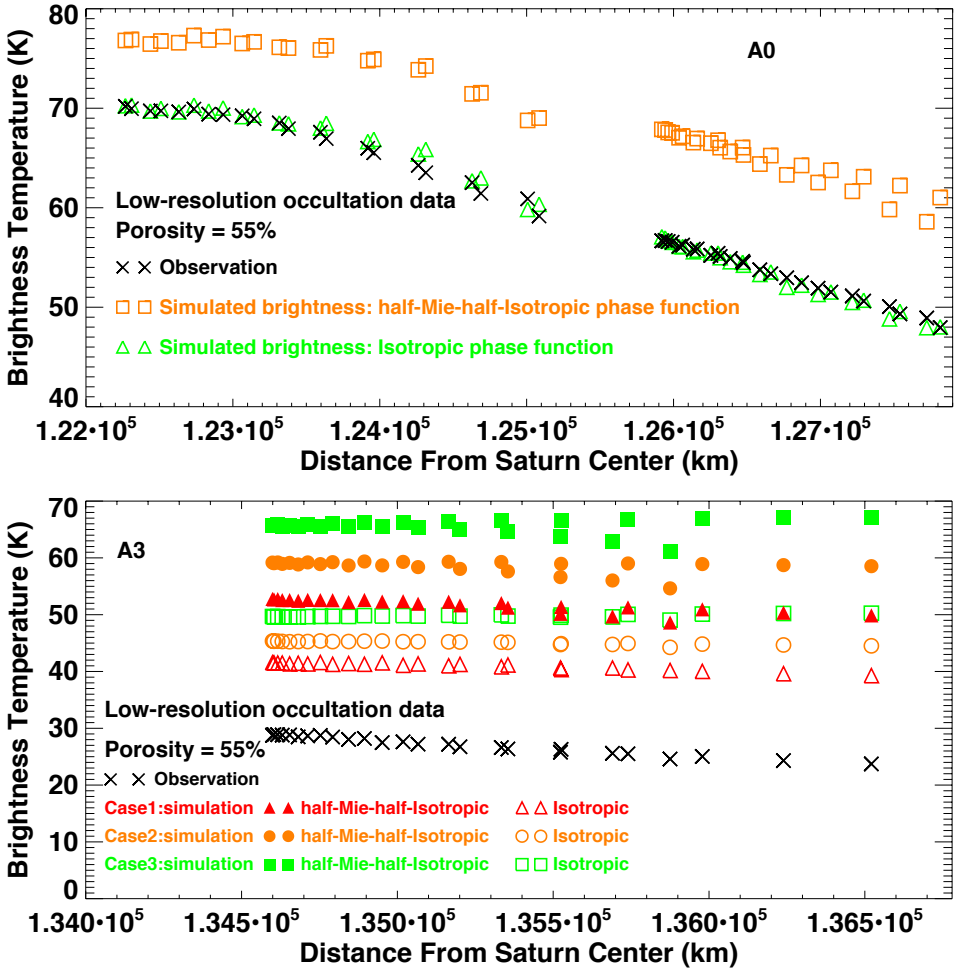

Figure 4.10: Occultation observations in the A ring in the low-resolution map scan. The A ring particles are assumed to have 55% porosity. Upper panel (region A0): The observed brightness temperature is shown with black crosses. The simulated brightness when assuming a purely isotropic phase function (green triangles) fits the observation well. However, when assuming a half-Mie-half-Isotropic phase function, the simulated brightness (orange rectangles) is much higher than observed. Lower panel (region A3): Black crosses: observations; Filled symbols: simulated brightness assuming a half-Mie-half-isotropic phase function. Open symbols: simulated brightness assuming a purely isotropic phase function. All three different particle size distributions as listed in Table 2 are simulated in region A3: case 1 (red triangle), case 2 (orange circles) and case 3 (green rectangles).

Second, we assume that the A ring particles have a porosity of 90%. In **Figure 4.11** lower panel, we show the simulated brightness in region A3 using our three different particle size distribution cases, using either an isotropic (open symbols) or half-Mie-half-isotropic (filled symbols) phase function. We can see that only when the minimum particles size is the smallest (A3-Case1) and when the particles scatter light isotropically, that the simulation result is close to the observations. However, for all these cases, the simulated brightness is still higher than observed. On the other hand, in Fig. 4.11 upper panel, we compare the observed brightness in regions A0/A1/A2 with simulated results by using an isotropic (green triangles), a half-Mie-half-isotropic (orange squares) and our best–fit 30% Mie/70% isotropic phase function (red circles). Due to the large main beam size, the averaged main beam brightness in the A1 and A2 regions contains contributions from the brightness of the A3 region. Here we have applied the best-fit for region A3 (see Fig. 4.11 lower panel) in which the particles in region A3 follow the particle size distribution of A3-Case1 and scatter light isotropically.

Noting that for all the variations of our hybrid phase function that we have utilized, a 100% (or purely) isotropic phase function already predicts the lowest brightness in the forward direction. However, we still predict a brightness temperature higher than observed in region A3. This might be due to insufficient knowledge of the wake parameters in region A3 or the over-simplified wake model in our Monte Carlo code. In this work, we opt to use an isotropic phase function in all the defined A ring regions (Table 3.2) for particles with 55% porosity. In contrast, if the particles are 90% porous, the occultation data show that a hybrid phase function of about 30% Mie/70% isotropic works best in regions A0 - A2, while an isotropic phase function works best in region A3. Thus we choose to allow the phase function to vary in between a half-Mie-half-isotropic and a purely isotropic phase function interior to the Encke gap in order to determine the range of the

required non-icy material fraction, while we choose a purely isotropic phase function exterior to the Encke gap.

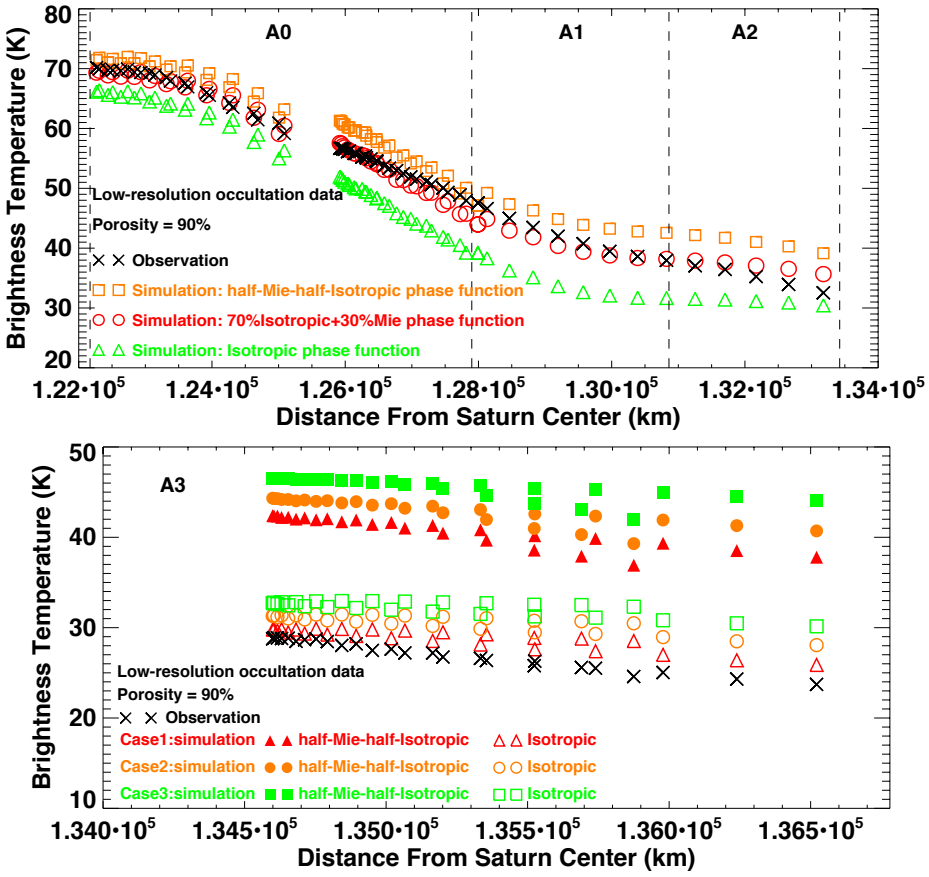

Figure 4.11: Occultation observations in the A ring in the low-resolution map scan. The A ring particles are assumed to contain 90% porosity. Upper panel (A0/A1/A2 regions, interior to the Encke gap): Plotted are the observed brightness temperature (black crosses), and the simulated brightness temperature assuming a half-Mie-half-isotropic phase function (orange rectangles); pure isotropic phase function (green triangles); and our best-fit hybrid phase function with 70% isotropic/30% Mie (red circles). Lower panel (A3 region, exterior to the Encke gap): Plotted is the observed brightness (black crosses), and simulated brightness assuming a half-Mie-half-isotropic phase function (filled symbols); and assuming a purely isotropic phase function (open symbols). All three different particle size distributions in region A3 as listed in Table 2 are simulated: case 1 (red triangles), case 2 (orange circles) and case 3 (green rectangles).

Despite the fact that in the A3 region our best-fit of a purely isotropic phase function assuming a porosity of 55% produces a simulated brightness produced much higher than observed no matter which particle size distribution case is applied, we cannot yet rule out the possibility of ring particles containing 55% porosity and scattering light isotropically in the A1/A2 regions based on the low-resolution occultation data only. Although the simulated brightness matches the occultation observation better when assuming 90% porosity, we apply the porosities ranging from 55% to 90% in simulating the ansa data in Sec. 4.3.2 in order to get a range for the possible non-icy material fraction.

4.3.2 Observations of the Ansa in High-resolution Spoke Scans -- determining the non-icy material fraction

Here we examine the scattering profiles of the high-resolution ansa data, compare them with our simulation results for a range of particle porosities from 55% to 90% applying the best-fit phase function we obtained in Sec. 4.3.1, and derive the required non-icy material fraction.

Inner A0 Region

Our best-fit simulated brightness matches the observations well inside a radius of 125,200km (the A0 region). In **Figure 4.12**, we plot the brightness vs azimuthal angle at a typical ring annulus inside 125,200km and compare it with our simulation results. We show the simulated brightness using 55% (upper panel) and 90% porous particles (lower panel) as examples. We also examined three intermediate porosities (75%, 80% and 85%) for which the results lie in between. In the upper panel, if particles are 55% porous, the simulation matches the observation best when using an isotropic phase function, consistent with the results we get from the occultation data in Sec. 4.3.1.

To match the observation, a fraction 0.21% of non-icy material is required. For the 90% porosity case, the difference in the scattering profiles and the required non-icy material fractions when using a half-Mie-half-isotropic and purely isotropic phase functions is very small (see Fig. 4.12 lower panel). Thus if we assume a 30% Mie/70% isotropic hybrid phase function, which is our best-fit phase function based on the occultation data (see Fig. 4.11), our simulation results lie in between, with the non-icy material fraction falling within the range of 0.21% to 0.23%. Overall, we note that the scattering profile when using 90% porous particles actually matches the observations better.

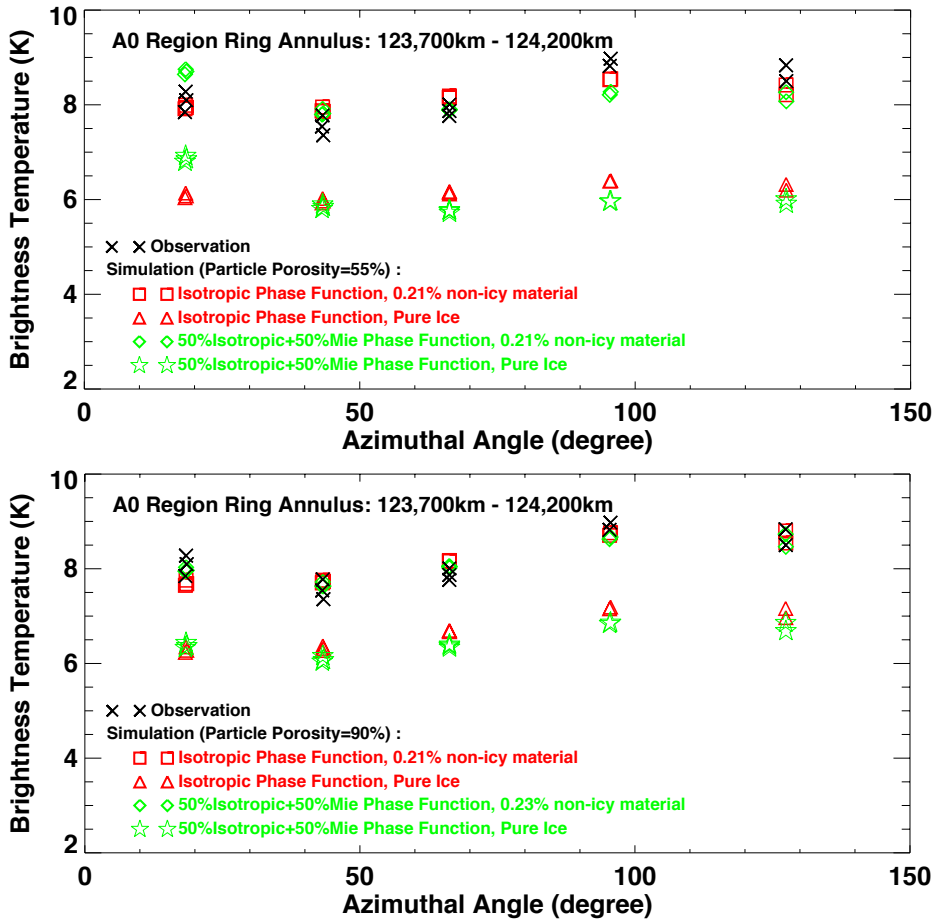

Figure 4.12: Scattering profile in the inner A0 region. Upper panel: 55% porosity. Lower panel: 90% porosity. Black crosses represent the observed brightness temperature. For the case in which ring particles scatter Saturn emission with a purely isotropic phase function, we show the simulated

brightness assuming pure water ice (red triangles) and ring particles with 0.21% non-icy material (red rectangles). For the case that the ring particles scatter Saturn emission with a half-Mie-half-Isotropic phase function, the simulated brightness is shown for pure water ice (green stars) and ring particles with 0.21% non-icy material (green diamonds).

Outer A0, A1 and A2 Region

In the A0 region exterior to a ring radius of 125,200 km, as well as the A1 and A2 regions, the scattering profiles are similar. As shown in **Figure 4.13**, when assuming 55% porosity the simulation matches the observation best when using an isotropic phase function and requires 0.2% non-icy material (upper panel), while for 90% porosity the difference in the scattering profiles and the required non-icy material fractions when using a half-Mie-half-isotropic and isotropic phase functions is also very small (lower panel). As was the case for the inner A0 region, the results using our best-fit 30% Mie/70% isotropic hybrid phase function also lie in between these two cases yielding a range of non-icy material fraction from 0.18% to 0.21%. Again, the scattering profile in the 90% porosity case matches the observations better than the 55% porosity case. However, we note that we are unable to match the high back-scattered reflectivity (brightness at large azimuthal angles $\gtrsim$ 140 degrees, see Fig. 4.13). This high level of backscattering is due to self-gravity wakes. The best-fit simulated brightness matches the observations better when using 90% rather than using 55% porous particles because for more porous particles, the derived normal wake optical depth is higher (see Fig. 3.10) and the self-gravity wake effect becomes stronger. However, as the wake optical depth becomes high enough, a further increase will not increase the back-scattered brightness for them. As a check, we have modeled an even higher porosity of ~ 95%, but we do not find any obvious difference from that result and those for 90% porous particles.

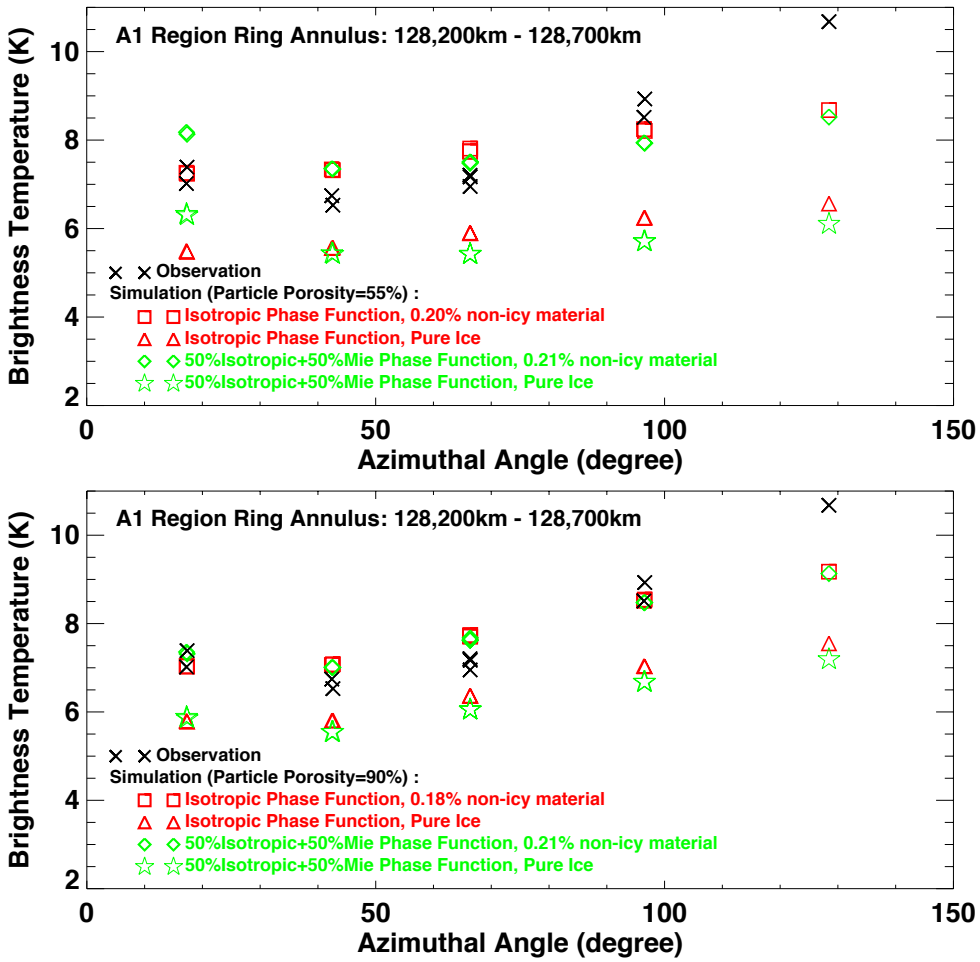

Figure 4.13: Scattering profile (brightness temperature vs. azimuthal angle) for the A1 region. Upper panel: 55% porosity. Lower panel: 90% porosity. Black crosses represent the observed brightness temperature. For the case in which ring particles scatter Saturn emission with a purely isotropic phase function, we show the simulated brightness assuming pure water ice (red triangles) and ring particles with 0.20% (0.18%) non-icy material (red rectangles) for porosity of 55% (90%). For the case that the ring particles scatter Saturn emission with a half-Mie-half-Isotropic phase function, the simulated brightness is shown for pure water ice (green stars) and ring particles with 0.21% non-icy material (green diamonds) for porosity values of 55% and 90%.

Besides increasing the ring particle porosity, in order to increase the level of back scattering, we have also attempted to alter the ring particle properties (e.g., particle size distribution power law

parameters), wake geometric structure (*i.e.*, wake height, width and wavelength ratio) and the normal optical depth in both the gap and wake by varying each parameter individually while keeping all other parameters constant. We find that by increasing the height to wavelength ratio or decreasing the wake width to wavelength ratio, we can also lead to a significant increase in back scattering. As an example, we consider a ring annulus in the middle A ring within a radial range of 128,200 km – 128,700 km. With the geometric structure derived from stellar occultations (see Figs. 5-7, Colwell et al., 2006), the wake height to wavelength ratio H/L is about ~ 0.084 and the width to wavelength ratio is about ~ 0.43. However, none of the simulated results with nominal wake structures capture the high brightness at large azimuthal angles (see Fig. 4.13).

To address this, we vary the values of H/L and W/L. The best-fit simulated brightness is shown in **Figure 4.14**. We first kept all model parameters constant while we varied H/L from its nominal value of 0.084 to values of 0.1, 0.15, 0.2 and 0.25. For each value of H/L, we adjust the particle scattering phase function to match the observed scattering profile. Among all the tested H/L values, for ring particles with 90% porosity, the simulated brightness best matches the observations when H/L=0.2 (green triangles, lower panel), and the ring particle scattering is characterized by a hybrid phase function that is 60% Mie/40% isotropic. In such a case, the required non-icy material fraction is still only ~0.2% (0.18%-0.21% when using the nominal value of H/L). For particles that have a porosity of 55%, the simulated brightness best matches the observations when H/L=0.25 (green triangles, upper panel), and a purely isotropic phase function is appropriate. The required non-icy material then drops from 0.2% (when using nominal value of H/L) to 0.16%, though the back scattering is still not as high as observed. Therefore, by increasing the value of H/L, we are able to obtain a larger backward scatter, especially in the case when the porosity is 90%. We also notice that the significant increases to H/L do not lead to significant changes in the required non-icy

material fraction, and apparently only have the effect of altering the shape of the scattering profile.

Second, we varied *W*/*L* using values of 0.43 (nominal), 0.4, 0.3, 0.2 and 0.1. For ring particles with either 55% or 90% porosity, the simulated brightness matches the observations best when *W*/*L* is as small as 0.1 (purple squares, Fig. 4.14). For 90% porous particles, the best-fit phase function we find is an 80% Mie/20% isotropic one, and the required non-icy material fraction is 0.45% (0.18%-0.21% when using nominal value of *W/L*). For 55% porous particles, the best-fit phase function is a 30% Mie/70% isotropic function, and the required non-icy material fraction is 0.26% (0.20%-0.21% when using the nominal value of *W/L*).

In **Figure 4.15**, we explore for all of these cases how well one can match the observations at near-zero azimuth in the outer A0, A1 and A2 regions (for the occultation observations in the low-resolution map). Since the nominal wake structure parameters (Sec. 3.5) work well for the regions inside 125,000 km, we only apply these new best-fit cases to regions outside 125,000 km (outer A0). As shown in Fig. 4.15 (and referring to Fig. 4.14), for ring particles with porosities of either 55% or 90%, the best-fit cases when varying the value of *H*/*L* fit the outer A0, A1 and A2 regions fairly well, especially when the porosity is 90% (H/L=0.2; 60% Mie/40% isotropic hybrid scattering phase function). The best fit cases when varying the value of *W*/*L* predict the brightness to be much higher than what is observed for both porosities. Therefore, it is very unlikely that the wakes can be much narrower than the nominal value suggested by stellar occultation observations (Colwell et al., 2006). Our initial intent for varying the value of *H/L* and *W/L* is to match our simulations with the bright back scattering seen in the observations. However, there is the possibility that this mismatch is due to our simplified wake model.

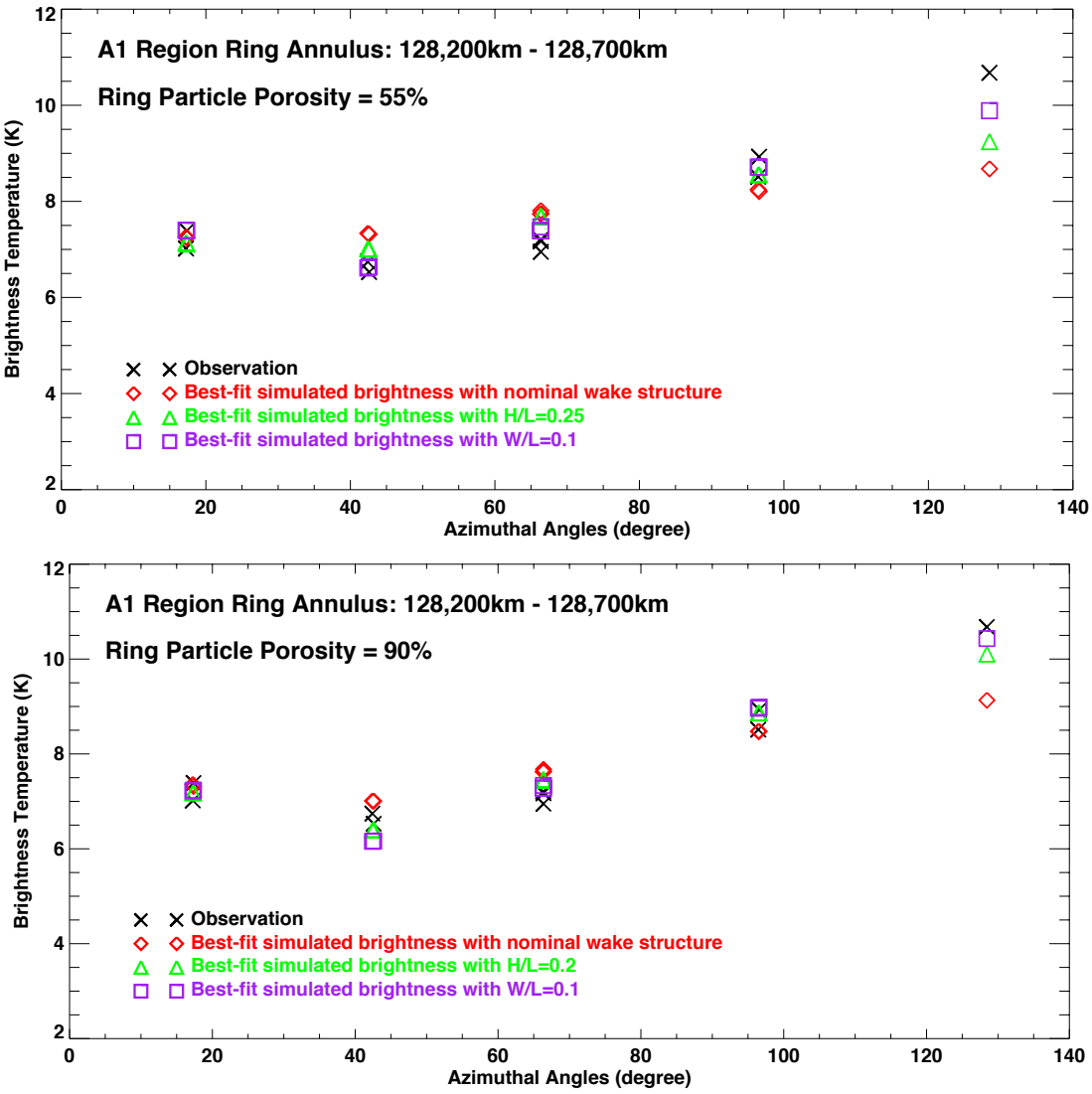

Figure 4.14: Scattering profile within ringlets in the A1 region using modified wake parameters. Upper panel: 55% porosity. The best fit for *H/L* (green triangles) uses a purely isotropic phase function. The best fit for *W/L* (purple squares) uses a 30% Mie/70% isotropic phase function. Lower panel: 90% porosity. The best fit for *H/L* uses a 60% Mie/40% isotropic phase function. The best fit for *W/L* uses an 80% Mie/20% isotropic phase function. For the corresponding derived non-icy material fractions, see text.

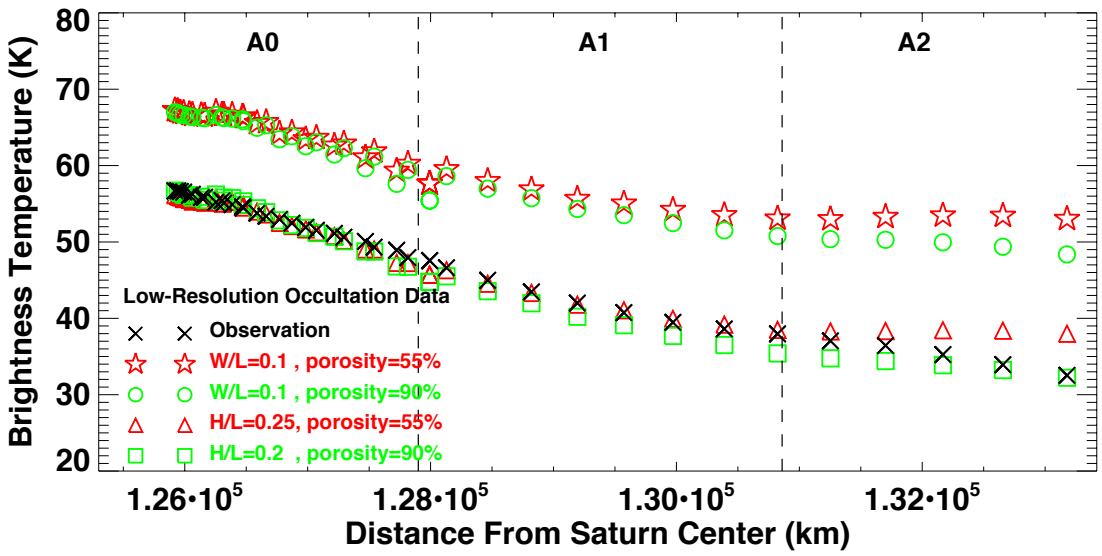

Figure 4.15: Comparison to the occultation observations of the A ring in the low-resolution map using the modified wake parameters from Fig. 4.14 and their associated best-fit phase functions over the regions A0, A1 and A2.

A3 Region

We have also investigated the region A3 outside the Encke gap, for our three different particle size distribution cases. According to the occultation data in Sec. 4.3.1, our simulations are closest to the observations in region A3 when the ring particles have a porosity of 90%, are characterized by the particle size distribution A3-Case 1, and scatter light isotropically. In **Figure 4.16**, we plot the simulated brightness in region A3 region as compared to the observations for ring annuli with radii in the range 134,700-135,200 km. For both panels, we have applied an isotropic phase function. It is clear from these simulations that different particle size distribution cases do not lead to variation in the shape of the scattering profile, but we do find that the non-icy material fraction required in order to match the observations does vary from case to case. We also note that, quite different from the results in the outer A0, A1 and A2 regions, we are able to match the brightness at large azimuthal angles, but our simulated brightness at small azimuthal angles (~10-20 degrees) is

noticeably lower than the observations. And our simulated scattering profiles are much flatter than observed.

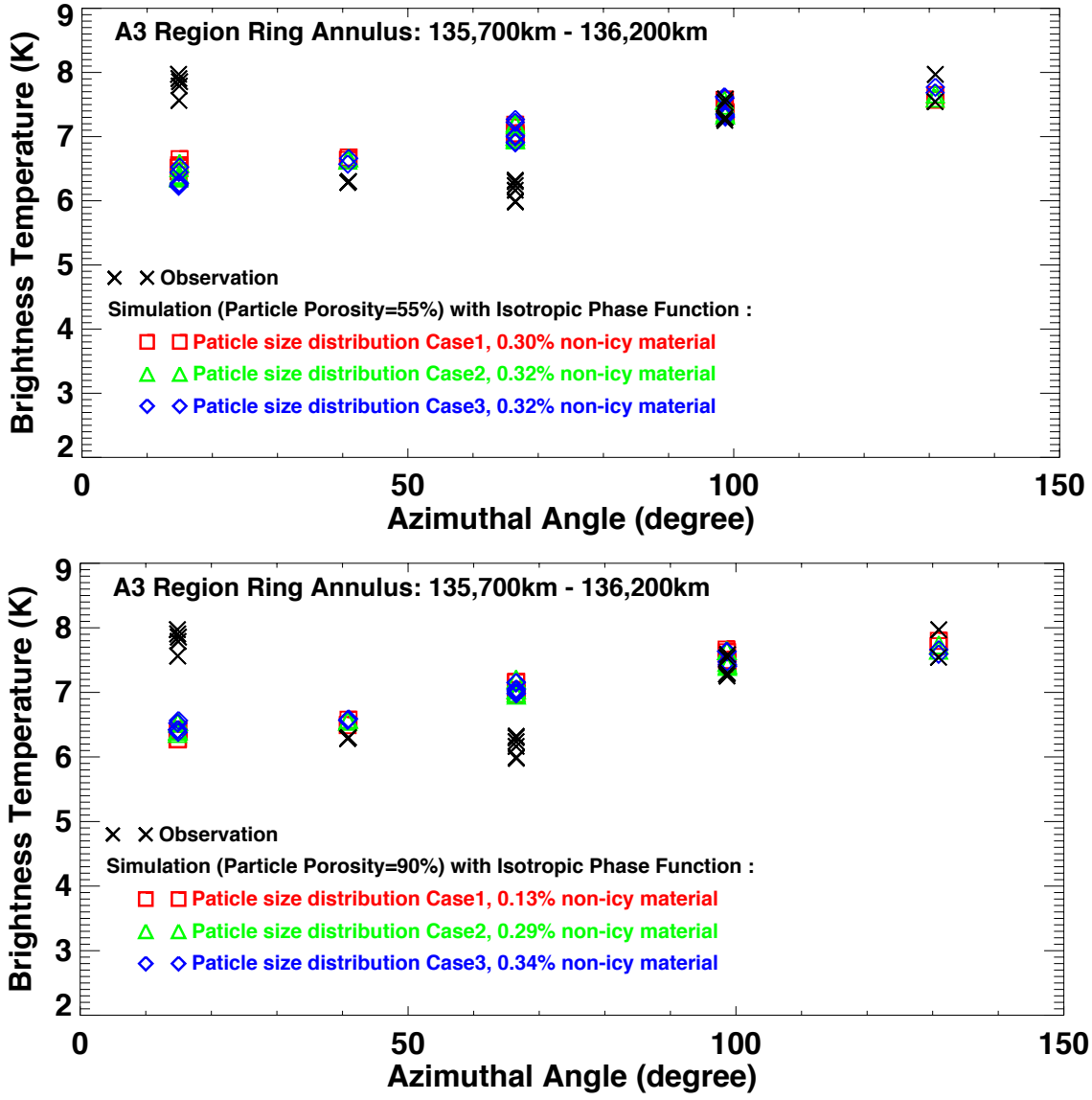

Figure 4.16: Scattering profile in the A3 region using a purely isotropic phase function. Upper panel: 55% porosity. Lower panel: 90% porosity. Simulation results with three different particle size distribution cases are shown in each panel. The brightness is matched well at large azimuthal angles, but is notably much lower than the observations at small angles.

In order to increase the simulated brightness temperature at small azimuthal angles, we vary the

scattering phase function for the A ring particles by using different weightings f_{iso} for the fraction of isotropic and Mie scattering (*i.e.*, our hybrid phase function). **Figure 4.17** shows the simulated brightness temperature (particle size distribution A3-Case2 as an example) when using our hybrid phase function as well as a pure Mie and a purely isotropic function. We find that the simulated brightness matches the observed scattering profile best when using a hybrid phase function that is 60% Mie/40% isotropic for the 55% porosity case and 70% Mie/30% isotropic for a porosity of 90%. The required non-icy material fractions when using purely isotropic and 60% Mie/40% isotropic phase functions do not vary by much. However, by introducing a phase function that is more forward directed than a purely isotropic phase function, the problem then becomes that the simulated brightness temperature at near-zero azimuth (low resolution occultation data) is much higher than observed (see Figs. 4.10 and 4.11). As noted, the fractional difference in the required non-icy material fraction between using the best-fit phase function and using a purely isotropic one is no larger than 20% for ring particles with 90% porosity, and no larger than 3% for particles with 55% porosity. Since we mainly focus on deriving the non-icy material profile in this work, we choose to apply a purely isotropic phase function to the A3 region.

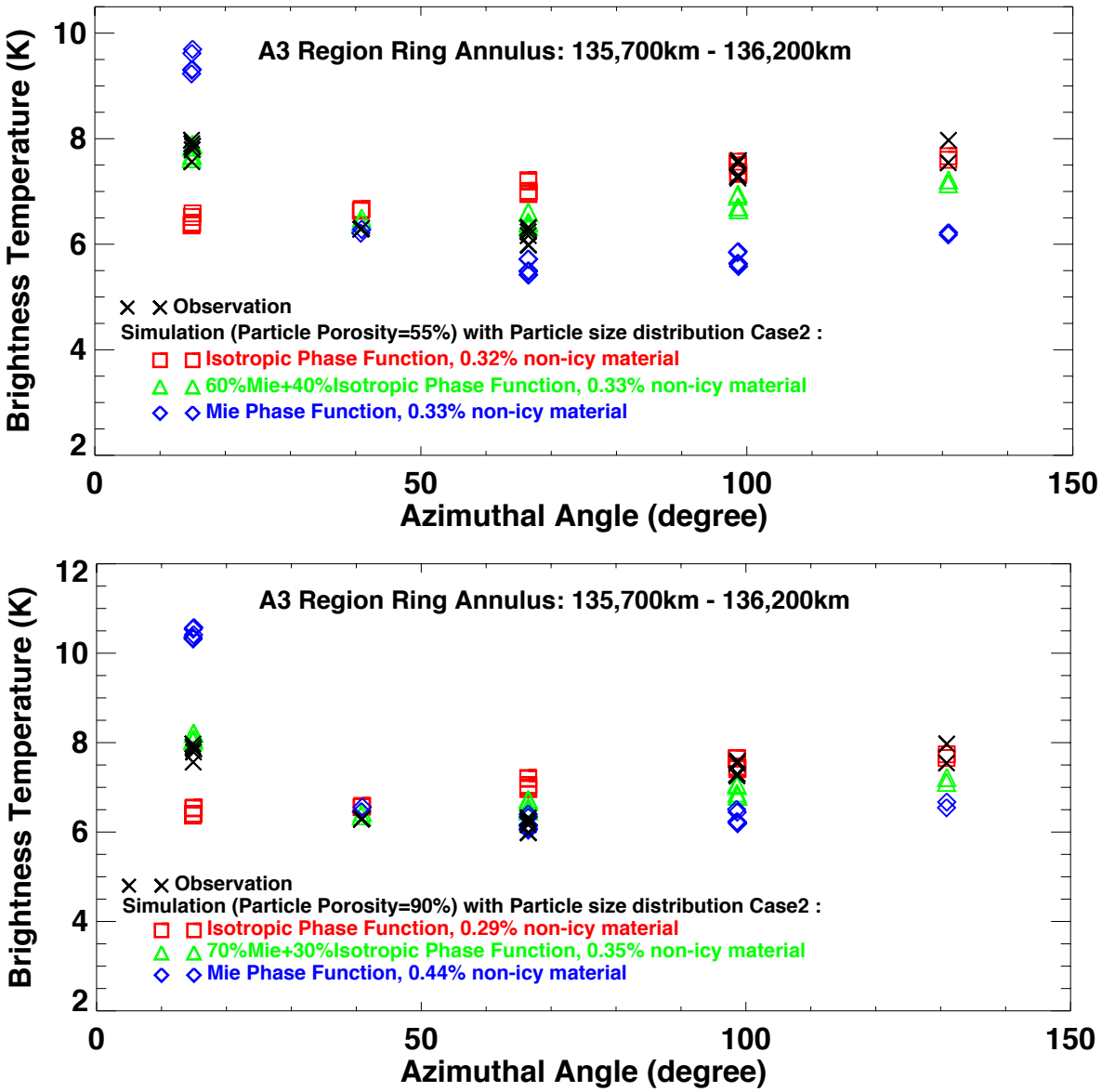

Figure 4.17: Scattering profile in the A3 region assuming the A3-Case 2 particle size distribution. Upper panel: 55% porosity. Lower panel: 90% porosity. Simulation results with different scattering phase functions (Mie, isotropic and our best-fit hybrid phase function) are shown in each panel.

4.3.3 Ring Particle Non-icy Material Fraction in the A Ring

Combining all of our results from the previous section, we use our nominal wake structure parameters to derive the non-icy material fraction. In **Figure 4.18**, upper panel we plot the radially varying non-icy material fraction required in order to match the observations for a porosity value of 55% (red solid line and diamonds) and 90% (black dash-dot line and squares) using the best-fit phase function interior to the Encke gap. The vertical grey lines and red lines show the range resulting from varying the phase function from a half-Mie-half-isotropic to a purely isotropic phase function for porosities of 90% and 55%, respectively. We can see that the shape of the scattering profile does not change much when we vary the phase function, which complicates efforts to determine the best-fit phase function for 90% porosity case. Yet, we have already established that the value should be lie in between a purely isotropic and half-Mie-half-isotropic phase function (Sec. 4.3.2). In contrast, we find that the best-fit phase function is generally purely isotropic for 55% porous particles, as indicated by both the occultation and ansa data.

For the regions exterior to the Encke gap, we show the required non-icy material fraction for our three different particle size distribution cases in the lower panel of Fig. 4.18, where we have applied a purely isotropic phase function. All the cases fit the scattering profile for the ansa observations equally well. However, as shown in section 4.2.1, ring particles with 90% porosity, and with a size distribution given by A3-Case 1 best match the occultation data in the low-resolution map.

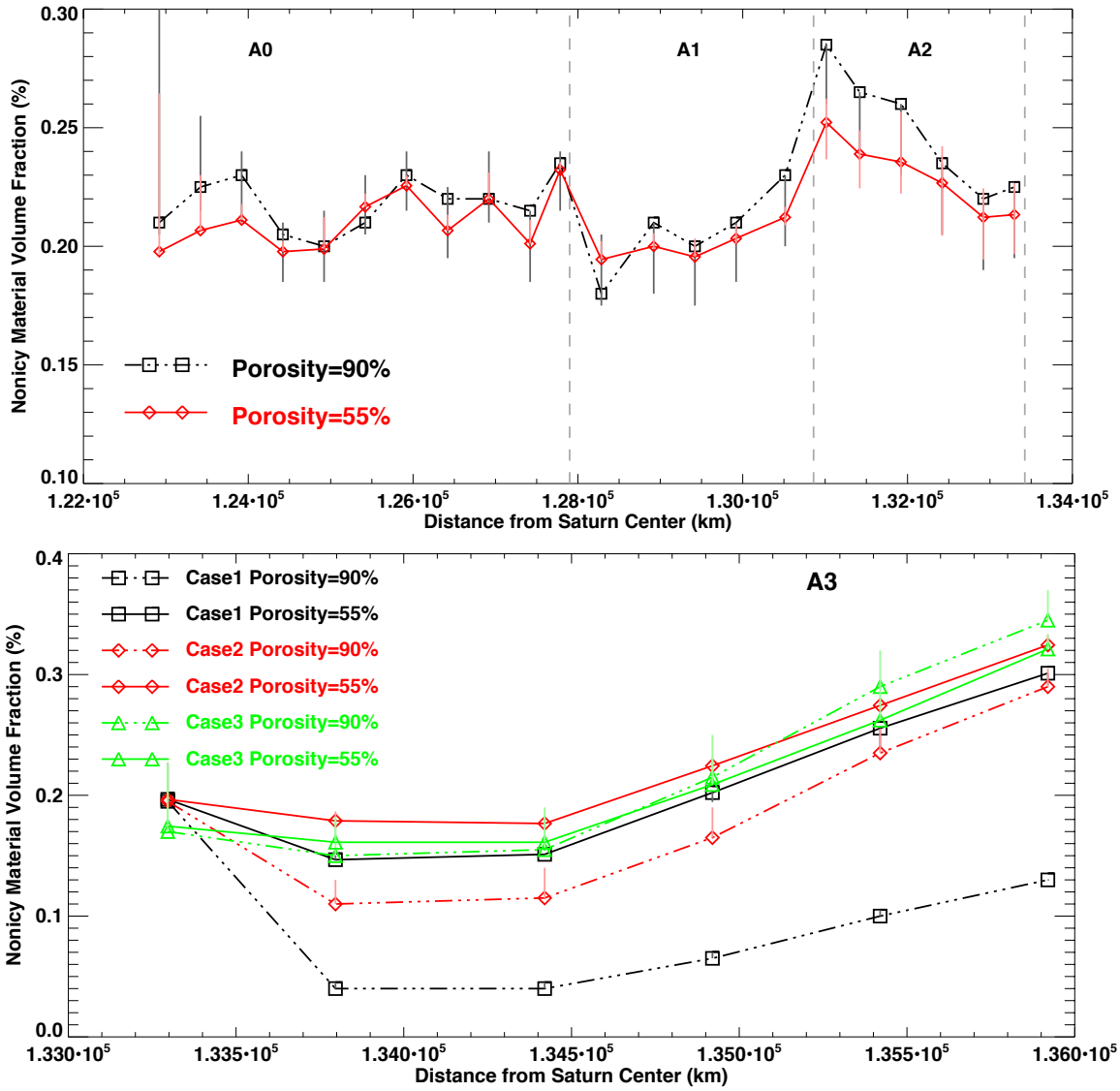

Figure 4.18: Derived non-icy material fraction. Upper panel (inside Encke gap): simulated fractions using the best-fit phase function for a porosity of 55% (red diamonds) and 90% (black squares). Lower panel (outside Encke gap): simulated fractions using a purely isotropic scattering phase for particle size distributions A3-Case 1 (black squares), A3-Case 2 (red diamonds) and A3-Case3 (green triangles). The solid curves correspond to 55% porosity, and the dashed curves to 90% porosity. The error bars indicate the range of the non-icy material fraction using phase functions that cover the range between half-Mie-half-isotropic and pure isotropic phase functions.

4.4 Cassini Division

4.4.1 Ring Particle Non-icy Material Fraction

Considering that most of the ring particles in the Cassini Division are very small compared to our preferred wavelength (similar to C ring particles), we apply a pure Mie phase function and explore simulations for five different porosity values: 55%, 75%, 80%, 85% and 90%. In **Figure 4.19**, we show the scattering profiles (brightness vs. azimuthal angle) for an annulus in the mid Cassini Division from 119,600-120,100 km. The scattering profile when particles have 90% porosity matches the observations best, while the scattering profile for the cases with 55% to 85% porosity is more forward directed than observed. Moreover, the required non-icy material fraction varies significantly for this annulus from 0.12% - 1.55% for different porosity values, being lowest for the 55% porosity case and highest for 90% porosity particles.

In **Figure 4.20**, we plot the derived non-icy material fraction in order to match the observations for all five porosity values. As shown in Sec. 4.1, the C ring acquires ~1-2% non-icy material merely from micrometeoroid bombardment since it first formed. This result is consistent with our results here for the Cassini Division if the ring particles have porosities of 85%~90%. The required non-icy material fraction is highest when assuming 90% porosity, reaching 1.7%. Thus, the higher the particle porosity, the more non-icy material fraction that is required to match the observations. We have found previously for the C ring that increasing the porosity of ring particles that are characterized by a Mie scattering phase function will increase the brightness at near-zero azimuthal angles significantly (see Sec. 4.1.1). However, due to the combination of the wide main-beam coverage in the low-resolution occultation data, and the narrow width of the Cassini Division, we are unable to use those occultation data in the Cassini Division to determine

the particle porosity there. Nonetheless, according to the scattering profile shown in Fig. 4.19, the ring particles there are most likely to have a porosity of ~90%. In addition, according to the high opacity ~0.064 - 0.111 cm^2 g^{-1} derived from density waves (Colwell et al., 2009), if the Cassini Division particles follow the power law size distribution with a minimum size $a_{\min} = 0.1cm$, maximum size $a_{\max} = 7.5m$ and power law index $q = 2.79$ (Zebker et al. 1985), the particles are likely to have very high opacity, and may have porosities even higher than 90%.

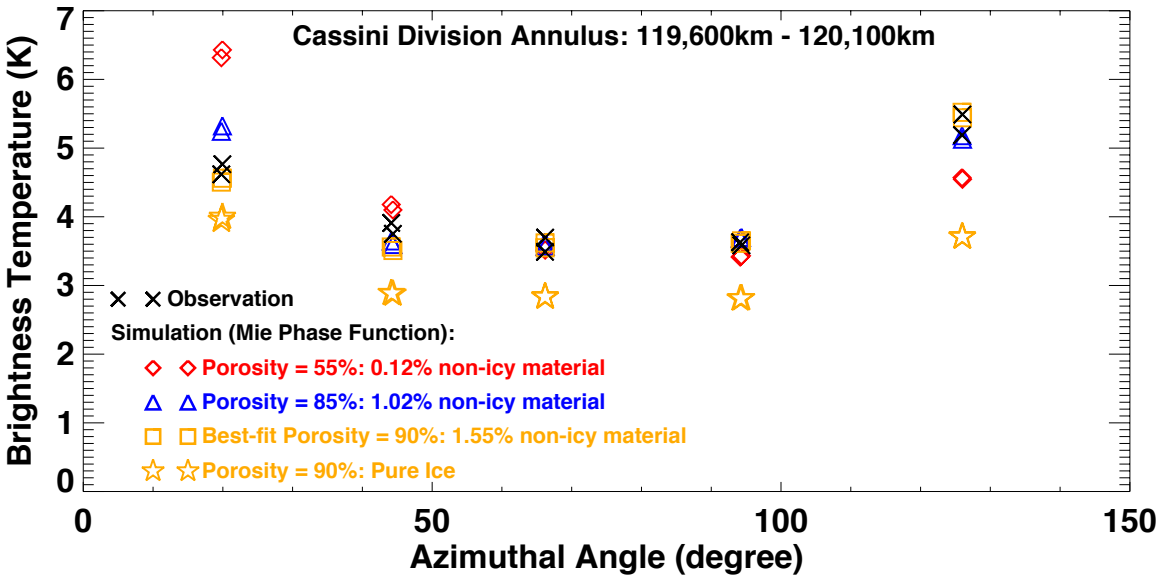

Figure 4.19: Scattering profile (brightness temperature vs. azimuthal angle) for an annulus in the mid Cassini Division on the ansa. The observed brightness temperatures are shown in black crosses. For porosity cases of 55%, 85% and 90%, we plot the best-fit simulated brightness (including the required amount of non-icy material) in red diamonds (55%), blue triangles (85%) and yellow rectangles (90%). We find that the 90% porosity case matches the observed scattering profile best. For the 90% porosity case, we further plot the simulated brightness when assuming ring particles composed of pure water ice (yellow stars).

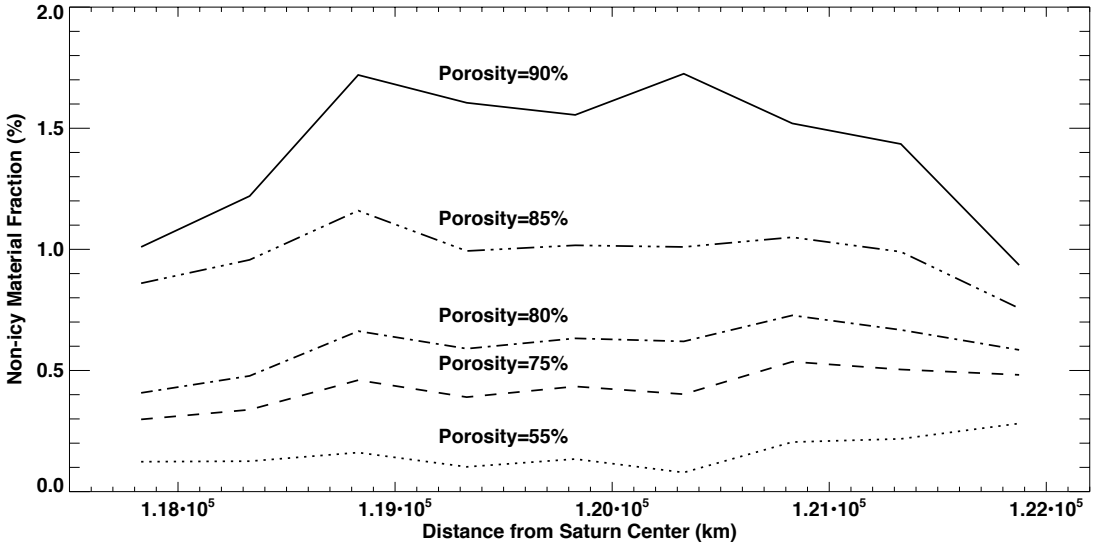

Figure 4.20: Derived non-icy material fractions within the Cassini division for a range of porosities. Depending on the choice of porosity, the variation in the non-icy fraction can be considerable.

5 Interpretation & Discussion On Cassini Observation Results

5.1 Exposure time due to micrometeoroid bombardment

After their formation, the rings have been continuously bombarded by extrinsic meteoroid impacts that have the effect of polluting them with non-icy material over time. The required exposure time to accumulate the observed fraction of non-icy material implies a lower limit on the rings age. Here we discuss in some detail how we determine the exposure times due to micrometeoroid bombardment. The nominal one-sided incident micrometeoroid flux on a flat plate (*i.e.*, flux at "infinity") is given by $\dot{\sigma}_{\infty} = 4.5 \times 10^{-17} gcm^{-2}s^{-1}$ (Grün et al., 1985; Cuzzi and Estrada, 1998; Estrada et al., 2015). But this does not reflect the flux of material that actually passes through or impacts the rings since the flux will be gravitationally focused by the planet. For the gravitational

focusing, we use the expression: $F(r) = F_G(r/1.8\ R_S)^{-0.8}$, where the planet's focusing is numerically averaged into the factor F_G at a reference radius of 1.8 R_S, and the radial dependence is a numerical fit to the calculated focusing of Durisen et al. (1992). In this paper, as was done by Cuzzi and Estrada (1998), we adopt a value of $F_G = 3$, appropriate for cometary projectiles which are assumed to have a 50% fraction of a non-icy, darkening agent (also, see Estrada et al., 2015). The two-sided incident flux of material crossing the ring plane at a ring radius r is then $\dot{\sigma}_e(r) = 2F_G\left(r/1.8R_s\right)^{-0.8}\dot{\sigma}_\infty$. However, some fraction of these incident meteoroids impact the rings as they pass through them with an impact probability ς that depends on the local geometric optical depth $\tau_{geometry}$:

$$\varsigma = (1 - e^{-(\tau_{geometry}/\tau_s)^P})^{1/P}. \tag{5.1}$$

where $\tau_s = 0.515$, and $P = 1.0335$ (Cuzzi and Durisen, 1990). The geometric optical depth is related to the optical depth given in Eq. (3.5): $\tau_{geometry} = \int_{a_{\min}}^{a_{\max}} \pi a^2 \cdot n(a)da$ and $\tau_{geometry} \sim 1/2\,\tau_\iota(\lambda = 2.2cm)$. Together, this gives the local impacting flux: $\dot{\sigma}_{im}(r) = \varsigma\dot{\sigma}_e(r) = 2\dot{\sigma}_\infty\varsigma F(r)$. Thus, the exposure time scale due to micrometeoroid bombardment is inversely proportional to this impact flux.

The absolute time scale derived from the above is complicated by existing uncertainties in the flux and the assumed source of the micrometeoroid population (Estrada et al., 2015). Recently, results of the Cassini Cosmic Dust Analyzer (CDA) have been reported that appear consistent with the current value of the flux at infinity, but also indicate that the micrometeoroid population is not cometary in origin (Kempf et al., 2013; Altobelli et al., 2015). If so the amount of gravitational focusing by Saturn will be different. In such a case, the time scales associated with micrometeoroid

bombardment and ballistic transport can be scaled accordingly with the equation:

$$T_{new} = T_{current} \cdot \frac{3}{F_{G\_new}} \cdot \frac{4.5\times10^{-17} g cm^{-2} s^{-1}}{\dot{\sigma}_{\infty}} \quad (5.2)$$

Furthermore, in our exposure time calculations, we assume that since the rings were formed, the meteoroid flux has remained constant and that the rings optical depth and surface density has not changed significantly.

5.2 C Ring

The radial variability of the derived non-icy material fraction is surprising and warrants discussion. Considering that the gravitational focusing only has a somewhat weak radial dependence within the C ring, the local impacting flux depends approximately linearly on the local geometric optical depth in most regions of the C ring. The final non-icy material fraction is then inversely proportional to the local surface density. This implies that in the optically thin C ring, the non-icy material fraction should be determined by opacity, which equals geometric optical depth divided by surface density ($\kappa = \tau_{geometry}/\sigma$). The larger the opacity, the higher the non-icy material fraction should become. Though a complete opacity radial profile for the C ring is still unknown, the current values at a few radial locations from density wave measurements suggest a higher opacity in the inner (and outer) C ring of ~0.15 $cm^2 g^{-1}$, and a significantly lower opacity in the middle C ring of ~0.022 $cm^2\ g^{-1}$ (Baillie et al., 2011; Hedman and Nicholson, 2013; see the diamonds and circles in **Figure 5.3**), which is the opposite trend to the shape of the non-icy material fraction we have found. Therefore, if the impacting micrometeoroid flux is the only source of pollution, it would generate a non-icy material fraction profile in the C ring opposite to what is observed: a higher fraction

outside the middle C ring bump, and lower at its center assuming the optical depth has also remained constant over this time.

In **Figure 5.1**, we demonstrate how the non-icy material fraction would evolve over 15 Myr and 45 Myr after the C ring first formed assuming that the rings were initially pure water ice, that meteoroid bombardment is the only pollution source and that the C ring optical depth and surface density have not changed significantly during that time. The non-icy material fraction originating from meteoroid bombardment is determined by the local opacity. However, as we have already indicated, we only have opacity measurements in a few radial locations (see the red diamonds, Fig. 5.1). For now, we interpolate the opacity in between these measured values, but acknowledge that future measurements will be required in order to determine the true opacity profile. The opposite trend between the observed (black curve) and simulated (red dashed curve) non-icy material fraction profiles in Fig. 5.1 implies that if the rings started as mainly pure ice ~15-45 Myr ago, there must be some non-icy material source other than the nearly radially constant micrometeoroid flux in order to explain the enhanced non-icy fraction in the middle C ring.

We also show the required exposure time as a function of ring radius for the same models in Fig. 5.1 in order to accumulate the observed non-icy material fraction merely from meteoroid bombardment at all C ring radius (see **Figure 5.2**). This gives an upper bound on the age required to match the peak non-icy material fraction value at the center C ring of ~ 900 Myr, with the assumption that the C ring optical depth and surface density has not changed significantly during that time. However, if this is the case, it would imply that the non-icy material fraction in the inner and outer C ring would be much higher than the observed values and a process that preferentially removes non-icy material from the inner and outer C ring regions would be required in order to

account for the observed distribution. The possibility of this scenario is discussed in Sec. 5.2.3.

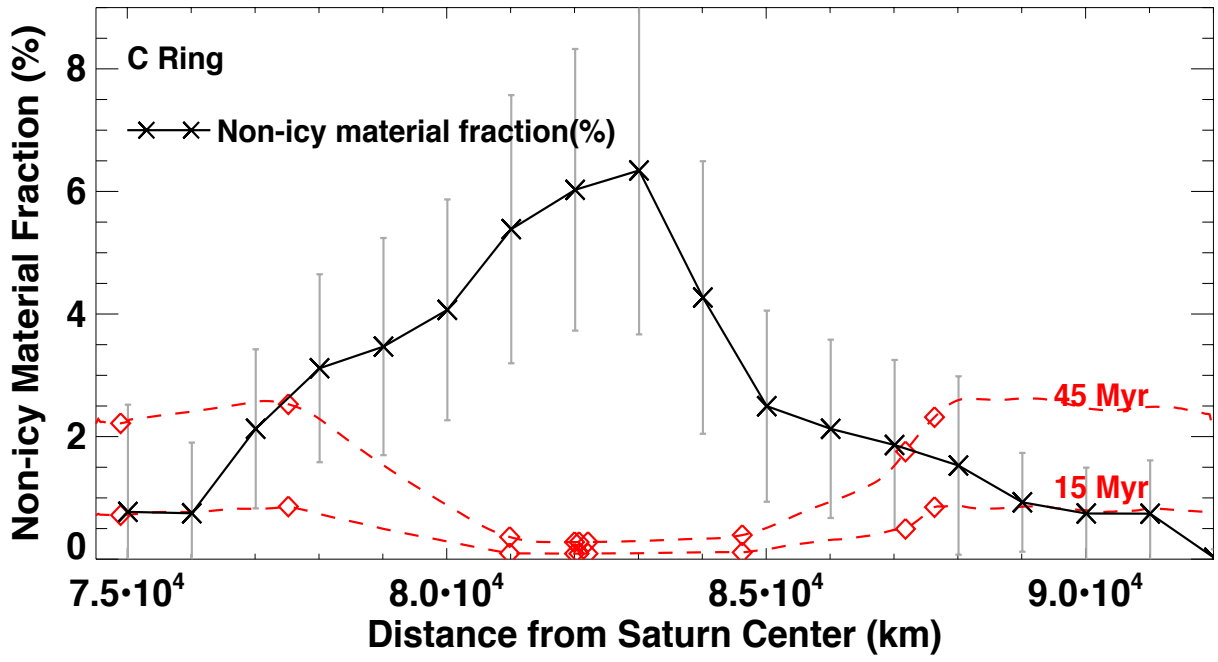

Figure 5.1: Black curve: Derived non-icy material fraction from the observations. Red dashed curve: The non-icy material fraction evolution over 15 and 45 Myr, if meteoroid bombardment is the only source of contamination in a structurally fixed ring, and the flux has remained constant over the past tens of millions of years. Red diamonds demonstrate the positions where opacity measurements (Baillie et al., 2011; Hedman and Nicholson, 2013) have been made through density waves.

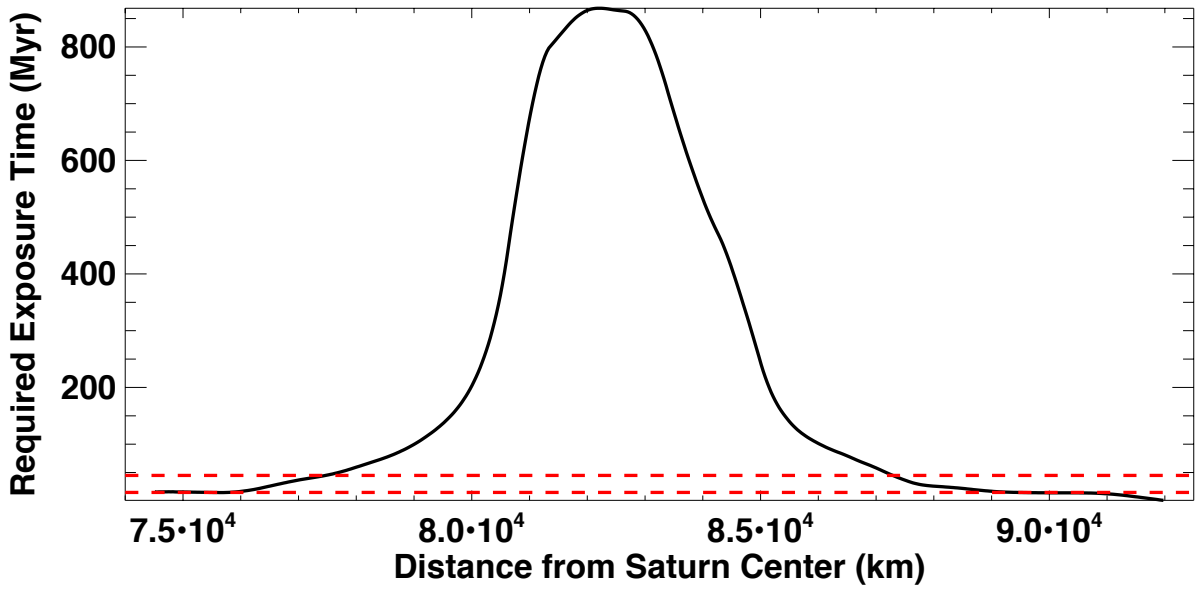

Figure 5.2: Radially varied, required exposure time to accumulate the derived non-icy material fraction from direct deposition due to meteoroid bombardment. The red dashed lines correspond to 15 and 45 million years.

Another alternative is that the C ring did not start out as nearly pure ice. In such a case, if the non-icy material was intramixed within the initial ring composition, any radial variability that may have existed most likely would have already been smoothed out as a result of ballistic transport (Cuzzi and Estrada, 1998; Estrada et al., 2015), given the nominal value for the micrometeoroid flux. That is, ballistic transport, which behaves much like both a diffusive and advective process (Cuzzi and Estrada, 1998; also see Sec 5.2.1), generally works to smooth out any compositional differences that may have existed or that might arise in the rings. Indeed, how material is diffused/advected through ballistic transport in the rings is an effective means by which the age of ring features or the rings themselves can be determined. Therefore, the exceptionally high non-icy material fraction in the middle C ring requires either the recent introduction of a high concentration of non-icy material, or a process that preferentially removes non-icy material from the inner and outer C

ring regions. We argue that the persistence of a non-uniform distribution of silicates within the middle C ring strongly favors the former scenario. In the next sections, we describe several scenarios in more detail that attempt to address this observation.

5.2.1 A Band of Non-icy Material from an Impacting Centaur at C ring center

In the first scenario, we assume that meteoroid bombardment has continuously contaminated the whole of the C ring since it first formed (see the above discussion), and that a higher concentration of non-icy material was injected into the middle C ring at a more recent time. Due to the lack of a complete opacity profile, it is not possible to determine the direct deposition timescale (red dashed curves, Fig. 5.1) that matches the observed non-icy fraction for the low optical depth regions away from the middle C ring peak, but barring any process that might dilute the non-icy fraction (e.g., a by-product of ballistic transport is that icier material spills over from the B ring to C ring; Durisen et al., 1992; Estrada et al., 2015), the implied age of the C ring from this evolution is between 15 and 45 Myr based only on the pollution of the inner and outer C ring for the nominal micrometeoroid flux (see Fig. 5.1). Note that this estimate is inversely proportional to the time-averaged micrometeoroid flux.

Any additional contribution to the effective dielectric constant of material must be attributed to an alternative, more localized source. In order to further examine this source, we investigated a scenario in which the middle C ring was contaminated by a debris cloud derived from a Centaur disrupted by previous encounters with Saturn (Hedman et al., 2011). Centaurs captured into orbit around Saturn might break apart into debris through tidal disruption as they pass close to the planet, or even through direct collision with the rings. This debris will follow the same bound trajectory

and crash into the rings potentially across a range of radii at later periapses (Hedman et al., 2011). Assuming the non-icy material is all silicates, and that this material is now finely ground and intramixed within the ring particles, we find that the total mass of silicates in the debris cloud would need to be between ~4.3×10^{15} − 4.8×10^{15} kg in order to produce the observed non-icy material distribution in the middle C ring, with the mass range depending on the age of the C ring (15− 45 Myr) as determined by our model fit to the low τ regions. Considering that the water ice fraction in Centaurs might range from 0% to 40%, this debris may therefore be produced during the break-up of a Centaur with radius R ~7− 11 km. The capture of the Centaur would likely involve it passing through the ring plane several times leaving little material behind initially, becoming weaker and rubblized until tides break up the object into smaller fragments which could then be captured and integrated into the rings (Hyodo and Ohtsuki, 2014). In such a scenario, it is not clear that the material would initially be concentrated into a narrow annulus of material. However, in the case that a narrow annulus is the initial condition, the spreading timescale of the high concentration of non-icy material through ballistic transport (Cuzzi and Estrada, 1998) could help constrain the earliest possible time the initial contamination occurred.

A conservative estimate of the lower bound on the spreading time scale for a concentration of non-icy material may be obtained by considering that ballistic transport can be approximated as an advective process in which the "bulk flow" is in the direction of ejecta material transport (Cuzzi and Estrada, 1998). Under this assumption, the time $t_{\rm lim}$ it would take for the intramixed pollutant that initially occupies an annulus at ~ 83,000 km to spread into the observed distribution then is given by:

$$t_{lim} \sim \frac{\Delta r}{\delta} t_{BT} \sim 150 t_g \quad . \tag{5.3}$$

Here, $\Delta r = 9000$ km and the throw distance of impact ejecta $\delta = 4rv_{ej}/v_k \sim 10^{-3} r_s \sim 60$ km, where we have taken the velocity of the bulk of ejecta to be $v_{ej} \sim 4$ m s^{-1}. The ballistic transport time scale $t_{BT} \sim t_g . t_g$ (the gross erosion time), is defined as the time a reference ring annulus of surface density σ would disappear due to ejected material if nothing returned:

$$t_g(r_0) = \frac{\sigma(r_0)}{\dot{\sigma}_{ej}(r_0)} \approx 6.22 \times 10^4 years \quad . \tag{5.4}$$

where the ring surface density is $\sigma(r_0) = 5.3$ g cm^{-2} at $r_0 = 83{,}000$ km (Hedman and Nicholson, 2013). The ejected mass flux $\dot{\sigma}_{ej}$ is proportional to the impacting micrometeoroid flux times the ejecta yield Y_0, and is given by $\dot{\sigma}_{ej}(r) \approx 2\dot{\sigma}_\infty \varsigma F(r) Y_0$. We take the mass ejecta yield $Y_0 = 10^4$ and thus have $\dot{\sigma}_{ej}(r_0) \sim 5 \times 10^{-14}$ gcm^{-2}s^{-1}. For an initially narrow annulus of pollutant at 83,000 km, the time to spread to the observed width $\Delta r \sim 9{,}000\ km$ is ~9.3 Myr. Therefore the non-uniform radial peak in our intramixed, non-icy material fraction profile would be a relatively new structure, with an age on the order of ~10 Myr, though the absolute time scale depends on the meteoroid flux rate at infinity and how gravitationally focused the micrometeoroids are by Saturn (Sec. 5.1).

Such Centaur crossing events are fairly likely to occur over this time period. According to numerical simulations (Horner et al., 2004), there is on average one centaur ($R > 1$ km) that impacts Saturn every 2.8×10^4 years, and thus based on this work we estimate that more than 350 Centaurs have had the opportunity to impact Saturn in the past ~10 Myr (though there is some evidence this may be an underestimate, see Hedman et al., 2011; Marouf et al., 2011). In order to find the fraction of Centaurs with radius R larger than 7 km among them, we investigate the absolute magnitude H distribution of observed Centaurs, which is related to their radius as:

$$R = \frac{1329km}{2\sqrt{p}} 10^{-0.2H} \quad . \tag{5.5}$$

where p is the typical Centaur geometric albedo (e.g., Chesley et al. 2002). For this calculation, we adopted the median value for the measured Centaur albedo of $p = 0.07$ (Johnston, 2015). The observed Centaurs have H between 6 and 14.3, with the absolute magnitude H distribution law $N(< H) \sim 10^{0.54H}$ (Larsen et al. 2001, Di Sisto and Brunini 2007). The fraction of Centaurs with radii greater than the required impacting radius ($R > 7$ km) is ~15%. Therefore, on average, ~52 Centaurs larger than 7 km in radius may have hit Saturn within the last ~10 Myrs. Even if we extend the range of Centaur absolute magnitude to $5 < H < 16.2$ (Di Sisto and Brunini, 2007), there would still be ~5 Centaurs larger than 7 km impacting Saturn within the given time frame.

This estimate only considers those objects that impact with Saturn. We expect that an even larger number of them may have passed close enough to the planet to be significantly affected by the planet's gravitational well and might have been broken up into debris. Once the Centaur is disrupted into debris by Saturn's gravity, the debris is likely to be absorbed by the rings after several orbits. The observational evidence would suggest, however, that successful disruption and capture events of such large Centaurs have not happened so frequently otherwise we might expect to see relatively large peaks in non-icy material concentration in other C ring regions rather than the single, well-defined peak we observe in the middle C ring.

5.2.2 Ring Opacity Favors Large Rocky Chunks

In Sec. 5.2.1, we have discussed the case where non-icy material brought in by the incoming Centaur is intramixed within the ring particles as envisioned in the Effective Medium Theory (EMT) model. However, it seems unlikely that an incoming Centaur, basically a rocky object

which may have substantial internal strength, torn apart gently by tides and ultimately broken into pieces that reside in the C ring, could be ground to powder this way, especially if it were done fairly recently. It seems more likely that there would still be many chunks of solid silicates in the centimeter-decimeter-meter size range left, which have now been coated by the icy ring material. This would require more total non-icy material in the middle C ring since non-icy material affects emission most efficiently when finely divided as in the EMT intramixed assumption versus a "salt and pepper", or intramixing type model (e.g., Cuzzi and Estrada, 1998; Poulet and Cuzzi, 2002; Cuzzi et al., 2014).

Moreover, 75% porous ring particles containing less than 7% intramixed non-icy material implies a ring layer opacity of ~0.07 − 0.08 cm^2 g^{-1} (see solid black curve, Fig. 5.3, also see Fig. 5.6) using our nominal particle size distribution, which is inconsistent with the density wave measurements. Surface density measurements have been made at several locations in the C ring where density waves are present (Baillie et al., 2011; Hedman and Nicholson, 2013). The opacity κ can be derived from these measurements (see black diamonds and circles, Fig. 5.3) using

$$\kappa = \frac{\tau_{geometry}}{\sigma} = \frac{\int_{a_{min}}^{a_{max}} n(a)\cdot\pi a^2 da}{\int_{a_{min}}^{a_{max}} \overline{\rho}\cdot n(a)\cdot\frac{4\pi}{3}a^3 da} = \frac{3(4-q)}{4(3-q)}\cdot\frac{a_{max}^{3-q}-a_{min}^{3-q}}{a_{max}^{4-q}-a_{min}^{4-q}}\cdot\frac{1}{\overline{\rho}} \quad . \tag{5.6}$$

Recall that the derived radial opacity profile from density wave measurements is notably non-uniform, with a value in the middle C ring of ~0.022 cm^2 g^{-1}, which is much lower than in the inner and outer C ring. According to Eq. (5.6), in order to have a radially-varying opacity profile, the C ring particles must have a radially-varying particle size distribution or a radially-varying mean particle density $\bar{\rho}$.

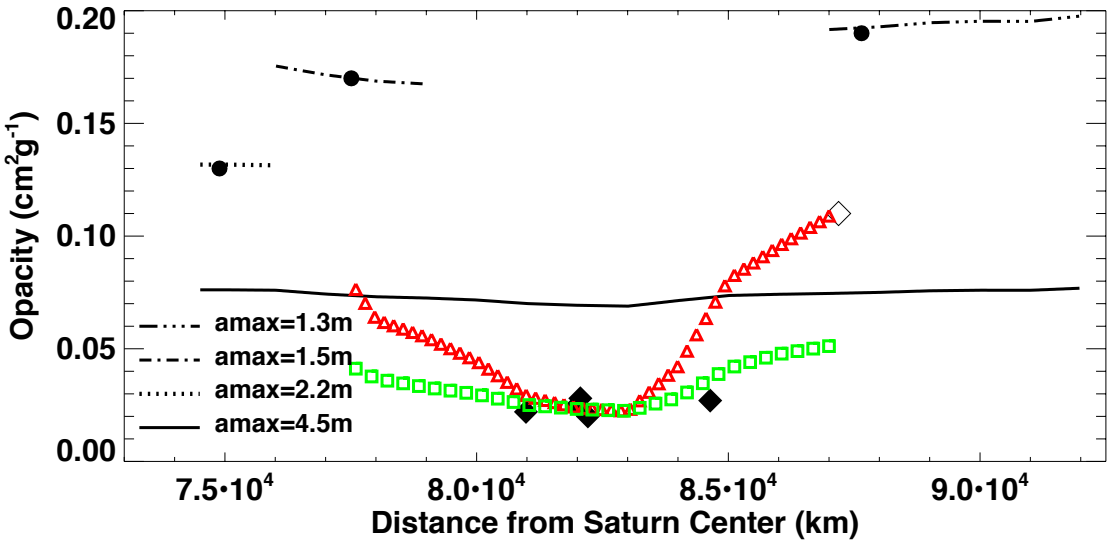

Figure 5.3: Measured opacity using density waves. Circles are from Baillie et al. (2011) and diamonds are from Hedman and Nicholson (2013). Filled symbols are measurements outside the plateaus while the unfilled points are measured inside the plateaus. Opacities calculated with different maximum particle size are presented by different line types. In all these calculations, the same minimum size of 0.4 cm and power law index q = 3.15 is applied. The suggested 75% porosity and the derived radially-varying fraction of silicates are also applied to the four cases with different maximum size. Also plotted are the opacity profiles in the middle C ring using the silicate-core, porous-icy-mantle model (described later in this section, refer to Fig. 5.6). Green squares: opacity profile for radially-varying percentage of large particles containing a silicate core. Red triangles: opacity profile for a radially-varying maximum particle size in the silicate-core, porous-icy-mantle model.

Using the same particle size distribution throughout the C ring for the EMT model of Sec. 3.2, the calculated opacity curve is fairly flat, since less than 7% non-icy material has little effect on the mean particle density. At the inner and outer C ring, the measured opacity is higher than our calculated value, possibly suggesting fewer large particles in those regions. We are able to match the measured opacity by decreasing the maximum particle size from 4.5 m to 1.5m - 2.2 m in the

inner C ring and 1.3 m in the outer C ring (see Fig. 5.3). These changes would not much affect our previously simulated scattered light component for the occultation and non-occultation data, since surface density and opacity mainly depend on the large particles, while small particles dominate the scattering properties. However, by merely increasing the maximum particle size it is still not possible to lower the opacity in the middle C ring to the measured value, because it would require the maximum size to be ~25 m, incompatible with Voyager RSS estimates of the particle size distribution by Zebker et al. (1985). Thus, we conclude that the exceptionally low opacity in the middle C ring suggests a potentially considerable amount of extra mass hidden in the ring particles, just where the finely distributed non-icy material also is.

To address the scattering behavior of particles containing large chunks of silicates, we expect to do more detailed modeling with a discrete dipole approximation (DDA) code in a future paper. For now, we consider a uniform core-mantle model using a silicate-rich core and dirty-ice mantle in order to gauge its effectiveness in matching the observations. In this simplified model, we assume that the composition of the background C ring is primarily water ice, but with a fraction of ~1% non-icy material (as in Fig. 4.20) which is assumed to be intramixed within ring particles that have 75% porosity. We also assume a critical size a_{crit} for the population that includes the Centaur fragments such that particles smaller than this critical size have a composition similar to the background, while particles larger than this contain a silicate core covered with a porous dirty icy mantle that has the same non-icy fraction and porosity as the background C ring particles. To further simplify the model, we also assume that the ratio of silicate core radius to particle radius f_{r} is fixed for all core-containing particles.

We can estimate the best value of the critical particle size and the core radius ratio to match our

observations by considering the two main characteristics in our data that we need to match: high brightness temperature in the occultation data and large thermal emission in the middle C ring. The large occultation brightness is determined by the integrated phase function, which must scatter more light into small scattering angles. The effective anisotropy factor is given by

$$g_{eff} = \frac{\int_{a_{min}}^{a_{max}} \left(\int_0^{\pi} P(\theta,\phi) cos\theta sin\theta d\theta \right) Q_{sca}(a) \pi a^2 n(a) da}{\int_{a_{min}}^{a_{max}} Q_{sca}(a) \pi a^2 n(a) da} \quad . \tag{5.7}$$

where $P(\theta, a)$ is the phase function at scattering angle θ, for a particle of radius a. A larger value of g_{eff} implies a more forward-directed phase function. As discussed in Sec. 4.1.1, we are able to match the low-resolution occultation observation by adding 75% porosity. For this value of the porosity, the effective anisotropy factor increases from ~0.6 (when assuming zero porosity) to above 0.838. Therefore, the larger the anisotropy factor, the higher the brightness of our occultation observation would be. On the other hand, the integrated absorption coefficient

$$\alpha = \frac{\int_{a_{min}}^{a_{max}} Q_{abs}(a) \pi a^2 n(a) da}{\int_{a_{min}}^{a_{max}} Q_{ext}(a) \pi a^2 n(a) da} \quad . \tag{5.8}$$

determines the amount of thermal emission emitted per particle on average. A ring layer with normal optical depth τ, can generate a total amount of intrinsic thermal emission of ~$\tau_{abs} \cdot T_{ring\_physical} (\tau_{abs} \ll 1)$, where $\tau_{abs} = \alpha \cdot \tau$ is the absorption optical depth and $T_{ring\_physical}$ is the physical temperature of the ring layer. At the peak of the middle C ring non-icy material fraction hump (see Fig. 4.20), for particles with 75% porosity and ~6.3% non-icy material, Eqns. (5.7) and (5.8) imply that $g_{eff} = 0.838$ and $\alpha = 0.0626$.

Our core-mantle model is simulated with a layered sphere Mie scattering code. We find that we

obtain a similar effective anisotropy factor $g_{eff} = 0.832$ and absorption rate $\alpha = 0.0620$ when a_{crit} = 60 cm, and the core radius ratio equals $f_r \sim 0.65$. These parameters give the observed value of the opacity at ~83,000 km in the middle C ring of ~0.022 cm^2 g^{-1}. Similarly to Fig. 4.4, we investigate the integrated single scattering phase function of this silicate-core/icy-mantle model (see **Figure 5.4**). The phase function of this model is very close to the intramixed model with 75% porosity, so it will not change the scatter component for the occultation and non-occultation data we simulated before.

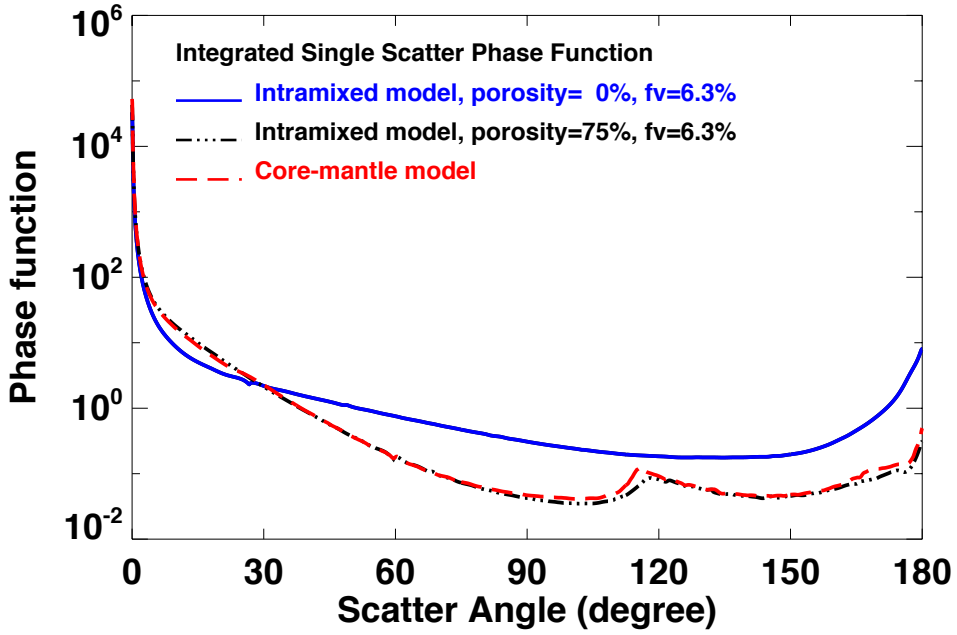

Figure 5.4: Single scattering phase function integrated over the C ring particle size distribution for three models. Nominal particle size distribution is applied to all three cases. Model 1 (blue) silicate intramixed with water ice; zero porosity. Model 2 (black): silicate intramixed with water ice; 75% porosity. Model 3 (red): silicate-core icy-mantle model with a_{crit} = 60 cm, and the core radius ratio equals $f_r \sim 0.65$.

In **Figure 5.5** we provide a quantitative fit to the radial variation of the non-icy fraction in the middle C ring hump between 78000 km – 87000 km, using our determined values for a_{crit} and f_r.

In the left panel, we show a fit under the assumption that among all particles larger than the critical particle size, only a percentage of them contain a silicate core, and the percentage that contains a core is radially dependent on the distance from the peak. At the peak of the middle C ring non-icy material fraction hump (~83,000 km), the percentage is 100%. The percentage drops to ~45% at 78,000 km, and ~20% at 87,000 km (see green squares in Fig. 5.3 for the resulting opacity profile). In the right panel, we show a fit in which all particles larger than the critical size contain a silicate core, but adopt a radially-varying maximum particle size (see red triangles in Fig. 5.3 for the resulting opacity profile). In both of these fits for the core-mantle model, we determine that the pollution source would need to contain a mass of silicate material of ~9.8×10^{16} - 1.07×10^{17} kg, which corresponds to an object radius of R ~ 20-21 km (for a silicate density of 2.7 g cm^{-3}) in order to account for the amount of non-icy material the observations imply in the middle C ring hump. There would be ~3 Centaurs larger than 20km impacting Saturn within the past ~10 Myr (see Sec. 5.2.1 for detailed calculation).

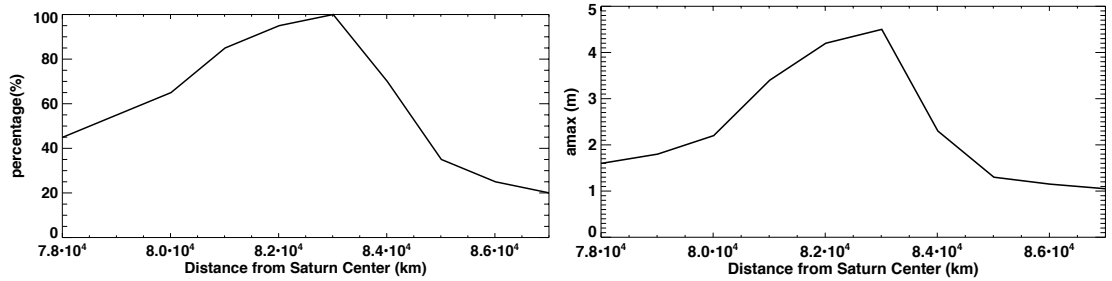

Figure 5.5: Left panel: The radially-varying percentage of large particles (larger than the critical size a_{crit}) that contain silicate cores necessary to match the observed anisotropy factor and absorption rate (Eqns. [22] and [23]). Right panel: The radially-varying maximum size.

Viscous Spreading of an Initially High Surface Density Annulus

Although ballistic transport can explain the radial distribution of the non-icy material fraction in the middle C ring through the spreading of an initially high concentration of finely ground pollutant

that is intramixed within the ring particles (Sec. 5.2.1), it does not do well to explain the observed opacity in the middle C ring, whereas the core-mantle model can. This is because the latter ring particles are much denser than the former for any given particle size since most of the non-icy material is hidden within their interiors. Moreover, if the Centaur debris is initially in a narrow annulus in the form of chunks, then the bulk material must spread viscously in order to account for the observed opacity distribution.

The fits to the radial structure seen in Fig. 5.5 suggests that the Centaur debris was initially in a high surface density annulus centered at ~83,000 km, which later viscously spread radially to a width Δr over time. A rough estimate of this viscous timescale is:

$$t_{visc} \sim \frac{\Delta r^2}{3\nu} \sim 2\times10^7 \left(\frac{\Delta r}{9000km}\right)^2 \left(\frac{300cm^2s^{-1}}{\nu}\right) yrs \quad . \tag{5.9}$$

where the estimate of the viscosity comes from the initial surface density contained in the annulus (see below). However, this estimate becomes increasingly unreliable as a predictor of the actual timescale because the viscosity ν can drop sharply over time as the annulus spreads. Thus we consider a more detailed calculation to estimate the spreading time.

Under the assumption that the Centaur material is initially contained in a dense, narrow annulus, its evolution under the influence of viscosity can be modeled using (Pringle, 1981)

$$\frac{\partial\sigma}{\partial t} = \frac{3}{r}\frac{\partial}{\partial r}\left\{r^{1/2}\frac{\partial}{\partial r}\left(r^{1/2}\nu\sigma\right)\right\} \quad . \tag{5.10}$$

In a Keplerian, pressureless disk such as the rings, the viscosity responsible for angular momentum transport arises as a result of particle interactions and can be divided into contributions from

particle random motions ν_L (the "local" shear stress component, Goldreich and Tremaine, 1978), the momentum transferred from physical collisions ν_{NL} (the "non-local" component, e.g., Araki and Tremaine, 1986) and for dense rings, gravitational scattering due to the presence of self-gravity wakes ν_{grav} (e.g., Salo, 1992; Daisaka and Ida, 1999).

A simple prescription for the viscosity that can be applied to Eq. (5.10) that depends on whether the ring is gravitationally stable or not is given by (e.g., Salmon et al., 2010; also see Schmidt et al., 2009, for a detailed discussion)

$$\nu = \nu_L + \nu_{NL} + \nu_{grav} = \begin{cases} \frac{c^2}{2\Omega}\frac{0.46\tau}{1+\tau^2} + a^2\Omega\tau & Q_T > 2; \\ 26(r_h^*)^5 \cdot \frac{G^2\sigma^2}{\Omega^3} + a^2\Omega\tau & Q_T \leq 2; \end{cases} \tag{5.11}$$

where $Q_T = \Omega c/3.36G\sigma$ is the Toomre parameter which distinguishes between the gravitating ($Q_T \leq 2$) and non-self gravitating ($Q_T > 2$) regimes. The nondimensional factor $r_h^* = r(\pi\rho/9M_s)^{1/3}$ is the ratio of a particle's Hill sphere to its physical radius a, where M_S is the mass of Saturn, and the velocity dispersion $c = 2a\Omega$ for $r_h^* \leq 0.5$, and $c = \sqrt{Gm/a}$ for $r_h^* > 0.5$ where m is the particle mass (see, e.g., Daisaka et al., 2001).

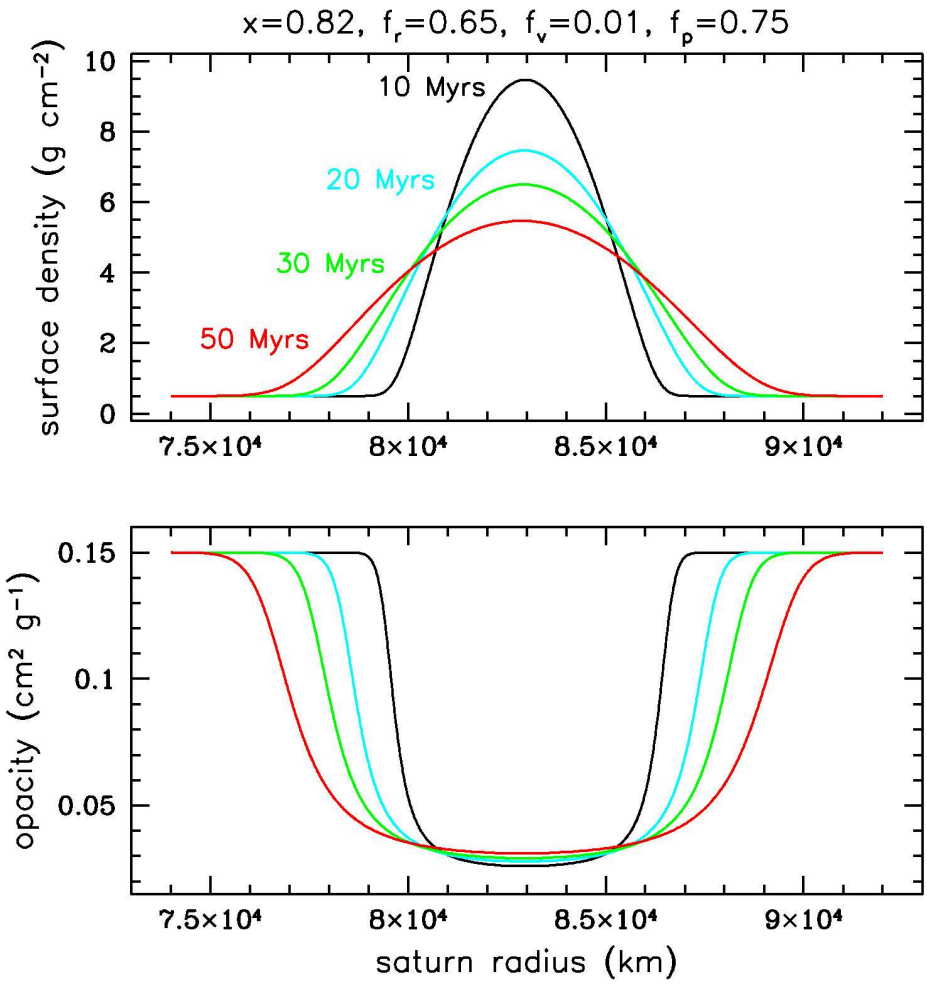

Figure 5.6: Viscous spreading of an initially narrow annulus (50 km) over time. Upper panel: Surface density after 10 (black), 20 (cyan), 30 (green) and 50 Myrs (red solid curves). Lower panel: Corresponding opacity profiles. These simulations indicate that the surface density and width of the middle C ring bump can be achieved in as little as ~20 – 30 Myrs.

In **Figure 5.6** we show a simulation of the spreading of an initial annulus of width Δr = 50 km derived from a $R \simeq 26$ km Centaur composed of rock and ice with a silicate mass fraction of 82%, giving it a density of 1.43 g cm^{-3} and mass $\simeq 1.1 \times 10^{17}$ kg, respectively. The rocky chunks are assumed to be relatively large so the size distribution within the annulus is taken to have a

minimum size (rock+ice) of a_{crit} = 60 cm, and a maximum size of 450 cm. The mass of additional ice brought in by the Centaur is chosen so as to be consistent with particles that have a core-to-particle radius ratio of f_r = 0.65, with porous, dirty icy mantles that have a porosity of f_p = 0.75 and an intramixed fraction of silicates of f_v = 0.01 (see above)[2]. The background C ring is assumed to be made up of icy, porous particles with our nominal choice of parameters for the size distribution (see Sec. 3.2) except that the maximum particle size has been reduced to 2.2 m as described earlier in this section in order to match the opacity in the inner C ring. In determining the viscosity in Eq. (26), we calculate the relevant quantities by finding mass average weighted means integrated over the size distribution[3]. This gives, for example, a more conservative estimate of the velocity dispersion c than assuming it were determined by the largest particle size a_{max}.

In the upper panel we show the evolution of the surface density. The initial surface density in the annulus is $\sigma \approx 420$ g cm^{-2}, which for our parameter choices gives an initial value for $Q_T < 2$. However, this is short lived as the annulus spreads quickly and the local and non-local contributions to the viscosity dominate the evolution. We find that we can roughly match the observed width (~78,000 km - 87,000 km) and peak surface mass density of the middle C ring feature within ~ 20 - 30 Myrs. In the bottom panel, we show the associated ring opacity which is characterized by a broadening, deep dip in opacity similar to what is seen in the observations. As

[2] We note that the ice for the mantles could have come from the C ring itself. In such a case, we could consider a Centaur of pure rock that would be 20 km in radius.

[3] Note that the model of Daisaka et al. (2001) only treats a single particle size a which does not actually appear in the expression for ν_{grav}. Thus in this term the viscosity is determined through the surface density only.

pointed out earlier, the opacity in the middle C ring is satisfied in this model for the choices of the core fraction f_r and critical particle size a_{crit}. Although our simulation is idealized, this relatively simple model indicates that a captured object such as a disrupted Centaur that is initially contained within a narrow annulus in the middle C ring could account for the observed dynamical ring profile, with the Centaur capture occurring as little as ~20 - 30 Myrs ago.

5.2.3 Alternate Scenarios

Tidal or Catastrophic Breakup of Fragments of Saturnian Origin

An alternative source for the high silicate fraction in the middle C ring may be from a rocky fragment that originated from the breakup of one or more of the Saturnian moons. This could occur from either tidal disruption, a catastrophic impact with a heliocentric interloper or possibly even a collision between mid-sized (or larger, see Asphaug and Reufer, 2013) satellites. For example, Canup (2010) suggested that the rings could have formed from the tidally stripped mantle of a Titan-sized differentiated satellite at the tail end of satellite formation. On the other hand, Charnoz et al. (2009b) have argued that the most likely time in which a moon near the Roche limit of the planet could be disrupted would be at the Late Heavy Bombardment (LHB). A Rhea-sized moon could serve as the progenitor for the rings, while also spinning off several mid-sized satellites we see today (Crida and Charnoz, 2010, 2012). A critique of these models is the whereabouts of the rocky content of these moons, in particular the core. However, given the compositions of the mid-sized satellites, the ring progenitor could have been predominantly icy, though it then becomes difficult to explain the rocky fractions of the current satellites in this picture. Charnoz et al. (2011) explained the silicate fractions of the satellites *and* predominantly icy rings with their models and argued that any remaining silicates would be isolated within the rings in larger chunks coated with

ice.

As a consequence of tidal or catastrophic disruption, it may not be unreasonable to consider that there could have been large fragments with high non-icy material fraction that found their way into the C ring, especially if the moon was internally non-uniform (e.g., itself the product of a previous breakup and reaccretion event). On the other hand, a mostly rocky fragment may have been deposited in the already existing rings as a result of the subsequent evolution of debris from a catastrophic collision between mid-sized moons. Depending on the internal strength of the object (*i.e.*, a rubble pile versus a solid fragment), the fragment may itself eventually be tidally disrupted or broken up catastrophically due to an impact with an object of heliocentric origin. In either case, a necessary requirement is that the object must be broken down completely to sizes in the decimeter-to-meter range.

The main difficulty with this scenario is that in order to introduce the extra amount of non-icy material we observe at the C ring center, the object would need to be at least $R \sim 20$ km (assuming the object is pure silicate, see Sec. 5.2.1). Such an object is almost certainly stronger than just self-gravitating and thus if embedded intact within the ring would require a hypervelocity impact with a sufficiently large interloper to completely disrupt. An estimate of the size needed can be ascertained by equating the object mass M times the fragmentation energy per unit mass (in the gravity regime), Q^*_D, needed to disrupt an icy body (Leinhardt and Stewart, 2009)

$$Q_D^* \approx 26 \left(\frac{R}{1km}\right)^{1/3} \left(\frac{v}{1km \cdot s^{-1}}\right)^{0.7} J \cdot kg^{-1} \quad . \tag{5.12}$$

to the kinetic energy of impact. This gives $R_{im} = R(2Q^*_D/v^2)^{1/3}$. A reasonable choice for the impact velocity is $v \sim \sqrt{3}\, v_{orb} \sim 37$ km s^{-1}, where v_{orb} is the orbital velocity at a distance of 83,000 km from

Saturn. This yields the requirement that the impactor size be ≳ 0.58 km. Zahnle et al. (2003) have calculated impact rates onto Saturn and the known moons outside the rings. A similar calculation for the C ring fragment gives a time scale for which one would expect such a disruption on the order of ~ 3.8 Gyr. This is longer than what can be inferred from Zahnle et al. for moons outside the rings in part because for a very flat impactor size distribution, the probability of disruption decreases for decreasing moon size since the number of projectiles large enough to disrupt them increases more slowly than the surface area of the moon decreases (Dones, priv comm).

The problem then is that it becomes very difficult to explain the observed distribution of non-icy material in the middle C ring over these long time scales. If the material is in large chunks, any compositional (and concentrated surface density) features would likely have been smoothed out due to viscosity, whereas if the material were well mixed within the ring particles, ballistic transport would have largely smeared out compositional differences. Thus, a satellite disruption event would probably have needed to happen within the last ~ 100 Myr in order to be a viable alternative. However, this significantly decreases the probability of such a disruptive impact happening to ≲ 3 % in that time frame.

One possibility for such a recent event may come as a consequence of a tidal dissipation factor of Saturn that is an order of magnitude smaller than originally thought as suggested by Lainey et al. (2010, 2012). Though quite controversial, such a low value implies that the entire mid-sized satellite system may evolve rather quickly, and that it is an even more collisional (stochastic) system than previously thought. Several workers have already considered the ramifications of such a low tidal dissipation factor (e.g., Charnoz et al., 2011; Cuk et al., 2016). Cuk et al. (2016; also Cuk 2014) have investigated the evolution of the current mid-sized satellites numerically back in

time and have concluded that as a result of the more rapid evolution of the system, a relatively recent breakup and re-accretion event of some of Saturn's mid-sized moons (inside the orbit of Rhea) may have likely occurred on the order of ~100 Myr ago. Interestingly, the collision of these moons could potentially push a close-in, inner (perhaps Mimas-sized) satellite into Saturn's Roche zone via tidal interaction with the resultant debris disk, where it could subsequently be disrupted leading to the formation of the rings. The age of the rings we see then would be consistent with this breakup event timescale, while their mass could also be consistent with a recent estimate for the rings' mass through density waves in the B ring (Hedman and Nicholson, 2016). Although this presents an intriguing scenario, the remaining uncertainty with the value of Saturn's tidal dissipation factor as well as the relatively low probability of disruption of an embedded moon makes the Centaur capture model more likely.

Removing non-icy material from the inner and outer C ring

As an alternative to introducing an additional external non-icy source into middle C ring, we consider a process that preferentially removes non-icy material from the inner and outer C ring regions. If we imagine a scenario in which the C ring originally had a constant optical depth and surface density across its radial extent similar (or even initially larger) to what is currently observed in the middle C ring, then because meteoroid bombardment is nearly radially uniform, we would expect a roughly constant non-icy material fraction everywhere within the ring. As suggested by Fig.5.2, it would take ~900Myr to accumulate a radially-uniform 6% non-icy material from meteoroid bombardment using the current accepted flux value. On the other hand, if we use the current optical depth and surface density profile, the non-icy fractions would actually be even *higher* in the lower optical depth inner and outer C ring, relative to the middle C ring. In either case, in order to match the observed distribution, there would need to be mechanisms at work that

either acted to preferentially remove the non-icy material from the inner and outer edges, or diluted the pollutant in those regions through the introduction of icy material.

The outer parts of the C ring may be more straightforward to explain. A by-product of the ballistic transport process across the inner B ring edge is that icier material spills over from the B ring into the C ring. For example, the ramp that connects the inner B ring to the C ring comes about due to advective effects (Durisen et al., 1992; Estrada et al., 2015). It has been shown that the ramp has a color and albedo similar to the B ring (Cooke, 1991; Cuzzi and Estrada, 1998). Therefore, as a result of this material exchange process, the C ring may ``lose'' polluting material faster than it gains it, and the relatively sharp drop off in non-icy material fraction seen outside of ~83000 km (see Fig. 5.1) may be due to a steady stream of icy material drifting radially inward.

On the other hand, the inner C ring is more problematic. As shown in Fig. 5.1, the non-icy material fraction drops off much more gradually inside of ~83000 km than outside, and then noticeably flattens out inside of ~76,000 km. This cannot be explained by the dilution mechanism described above. It so happens that this is around the location where part of the radar main beam starts to fall on the outer D ring while at the same time the optical depth becomes very small and uncertain at the C/D boundary, which may incur some error in our analysis. Moreover, in our Monte Carlo simulations we assume that the C and D ring particles are exactly the same, which might be inaccurate. Since the flux at the C/D boundary is very low, these errors might cause a high uncertainty as to whether the magnitude of the non-icy material at the inner edge of the C ring is correct. If this were indeed an artifact, then it is possible that the radial non-icy material fraction profile does not drop off as significantly at the inner edge; however, one would still require some as-of-yet unknown mechanism to explain the lower fraction interior to the middle C ring.

Finally, a mechanism that may work by itself, or in conjunction with the dilution process in the outer C ring concerns the recent discovery of ring rain onto Saturn's ionosphere (Donoghue et al., 2009) which may possibly verify the previously suggested planet-to-ring magnetic connection (Connerney et al., 1984; Connerney et al., 1986; Wilson et al., 1989; Northrop et al., 1987). Small, highly charged debris grains can escape the ring plane to Saturn along magnetic field lines from the C ring (Jontof-Hutter and Hamilton 2012a, 2012b). The critical stability limit for small ionized water ice particles lies in the outermost C ring. As the ionized water ice within the critical stability limit becomes unstable and erodes away, the non-icy material fraction in the inner and mibuddle C ring would increase, potentially providing another means by which the observed distribution can be explained. Furthermore, the critical stability limit would become closer to the rings' inner edge for particles with smaller charge to mass ratio. If the non-icy material has relatively smaller charge to mass ratio than water ice, only non-icy material at small ring radius could be possibly removed. Such a process would need to be investigated in more detail.

5.2.4 Other Non-icy Materials Suggested By Observations At Other Wavelengths

Observations at visible and near-IR wavelengths have revealed a dark reddish C ring, indicating the existence of other non-icy reddening materials like tholins (Cuzzi and Estrada, 1998), or hematite (Stillman and Olhoeft, 2008; Clark et al., 2012) that presumably have been further polluted over time by some extrinsic darkening material. In the case of tholins, for example, the darkening agents were spectrally neutral such as amorphous carbon (Cuzzi and Estrada, 1998). But other extrinsic materials are possible, and can even be reddish themselves in nature (Cuzzi et al., 2009) indicating that the issue of ring composition still remains unsettled. Indeed, some

silicates may likely have been present in the rings from their beginning (e.g., originating from a progenitor moon), but the idea of different materials like silicates, which we consider in this paper as the source of the rings' intrinsic thermal emission, also as extrinsic pollutants has been bolstered by the recent results of the Cassini CDA which determined that the micrometeoroid flux at Saturn is consistent with an Edgeworth-Kuiper belt origin (Altobelli et al., 2015; also see Sec. 5), and not cometary as has been previously assumed.

Regardless, considering the very small amounts of non-icy materials required to give the rings the right color in the visible and near-IR assuming it is intramixed within the ring particles (e.g., 0.35wt% of tholins, Cuzzi and Estrada, 1998; or 0.25wt% of nanohematite, Cuzzi et al., 2009; Clark et al., 2012), their contribution to the effective dielectric constant in the middle C ring can be considered insignificant with regards to the thermal emission. In addition, while using nanohematite as the reddening material, Clark et al. (2012) and Cuzzi et al. (2009) suggested using a small amount of un-oxidized, fine-grained iron instead of darkening material like silicates. As an example, in **Figure 5.7** we plot the magnitude of our derived imaginary part of the effective dielectric constant, which is required for the ring particles to generate the amount of the observed intrinsic thermal emission, as a function of ring radius (compare with Fig. 5.1). By adding 75% porosity to the ring particles, the real part of the effective dielectric constant becomes about 1.45, using Eq. (3.1). However, if we assume un-oxidized iron as the non-icy material and plug its dielectric constant ($\varepsilon_{iron} = 0 - i \cdot 2{\times}10^6$, Cuzzi and Pollack, 1978) into Eq. (3.1) (see Sec. 3.2), we cannot obtain the required imaginary part of the effective dielectric constant for the middle C ring even with as much as 80wt% iron, which is much larger than the amount of fine-grained iron suggested by these authors.

One can always determine the required fraction of any non-icy material by plugging its dielectric constant into Eq. (3.1), assuming that the non-icy material is intramixed within water ice. Then one can derive a radially varying non-icy material fraction profile and appropriate ring particle porosity by matching the imaginary part of the effective dielectric constant profile (Fig. 5.7) while keeping the real part near a value ~1.45. However, larger fractions of these candidate materials in the ring particles (e.g., tholins) needed to match the intrinsic thermal emission would be inconsistent with previously derived non-icy material fractions in the visible and near-IR. Therefore it is certain that even if the ring particles contain some of these other candidate materials which may dominate at shorter wavelengths (see below), there must be some other materials in the C ring such as silicates that primarily accounts for not only the thermal emission, but that can explain the anomalously low opacity in the middle C ring as well. We further point out that this is independent of, say, any uncertainty in the dielectric constant of silicates (of which naturally there are a whole range of "silicates" to choose from). Rather, any uncertainty in the fraction of non-icy material depends much more significantly on the choice of the non-icy constituent. Our analyses alone cannot determine the exact composition of the non-icy material; however, silicates represent a very reasonable candidate material, especially within the context of the newly determined micrometeoroid flux, and the Centaur capture scenario we have advanced.

Finally, we note that past analyses of visible and near-IR observations of the C ring have not indicated the presence of silicates in the fractions we derive in this work, mainly because even the very small amounts of spectrally red absorber (e.g., tholins) required to give the rings their apparent color would overwhelm these unless the silicates were present in much larger amounts (see Cuzzi and Estrada, 1998), even more than the enhanced values we find in the middle C ring. In any case, given the fact that the visible and near-IR can only penetrate through a very thin surface layer of

the ring particles, the bulk of the larger fraction of silicates we find in the middle C ring are very likely to be hidden in the interior of the larger ring particles and not on their surfaces, as described by our silicate-core and porous-dirty ice mantle model.

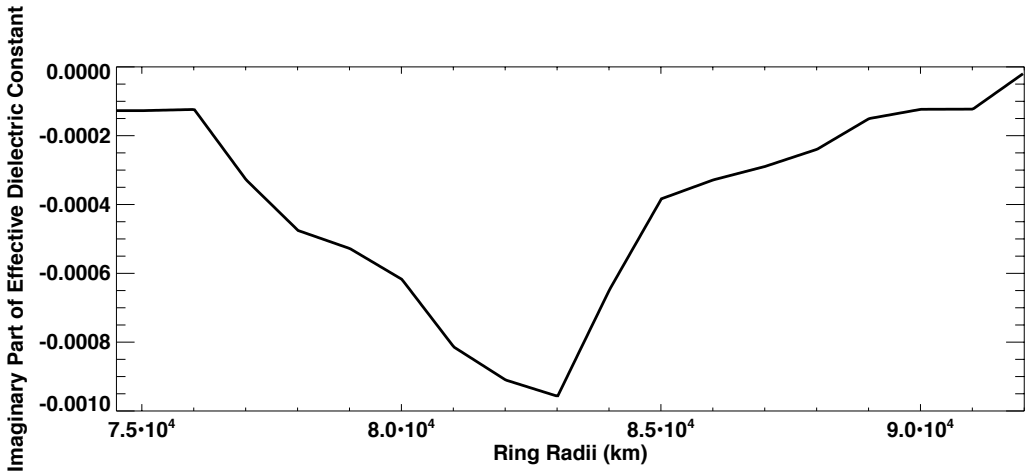

Figure 5.7: Plot of the imaginary part of the effective dielectric constant required to match the thermal emission observed.

5.2.5 Discussion on Composite Ring Particle Mixing Rules

The high particle porosity derived in Sec. 4.1.1 is a surprising result. Initially we expected the ring particles to be mostly solid water ice with a small fraction of voids and non-icy material as inclusions. Thus, we used the Maxwell-Garnett mixing rule of the Effective Medium Theory (EMT) to calculate the ring particle's averaged (effective) dielectric constant taking water ice as the host medium. This mixing rule treats one material as the matrix (host material) in which other materials (guest materials) are embedded in the form of small inclusions. However, this model is not symmetric as the host and guest materials do not contribute on an equal basis to the effective dielectric constant. Therefore, it makes a difference what one chooses as the host material. For example, Cuzzi and Estrada (1998) used a vacuum as the host medium. Here, we investigate how

significant the differences are when choosing different media and compare the results with the symmetric Bruggeman (1935) mixing rule.

To match the high brightness in the occultation data, we have increased the forward-scattered light by decreasing the real part of the ring particle dielectric constant to ~1.45. By using the Maxwell-Garnett mixing rule with water ice as the host material, we are able to match the required real part of the dielectric constant after making the ring particles 75% porous. In **Figure 5.8**, we show the calculated real part of the effective ring particle dielectric constant as a function of the porosity for three different mixing rules: the Bruggeman mixing rule (green curve), the Maxwell-Garnett mixing rule with water ice (black curve), or vacuum (red curve) as the host medium. We find a slight difference of less than 0.2 in the real part of the effective dielectric constant when using water ice or vacuum as the host material in the Maxwell-Garnett mixing rule. The result of the Bruggeman mixing rule lies in between them. Furthermore, we find that the small non-icy material fraction (less than 7%) doesn't affect the real part of the effective dielectric constant by very much. With only a slight difference in these mixing rules, the required porosity needed in order to decrease the real part of the dielectric constant to 1.45 would only be ~ 5% smaller if using the Maxwell-Garnett rule with a vacuum as the host medium or using the Bruggeman mixing rule. Therefore, we would still require the ring particles to have ~70% porosity when using those two rules.

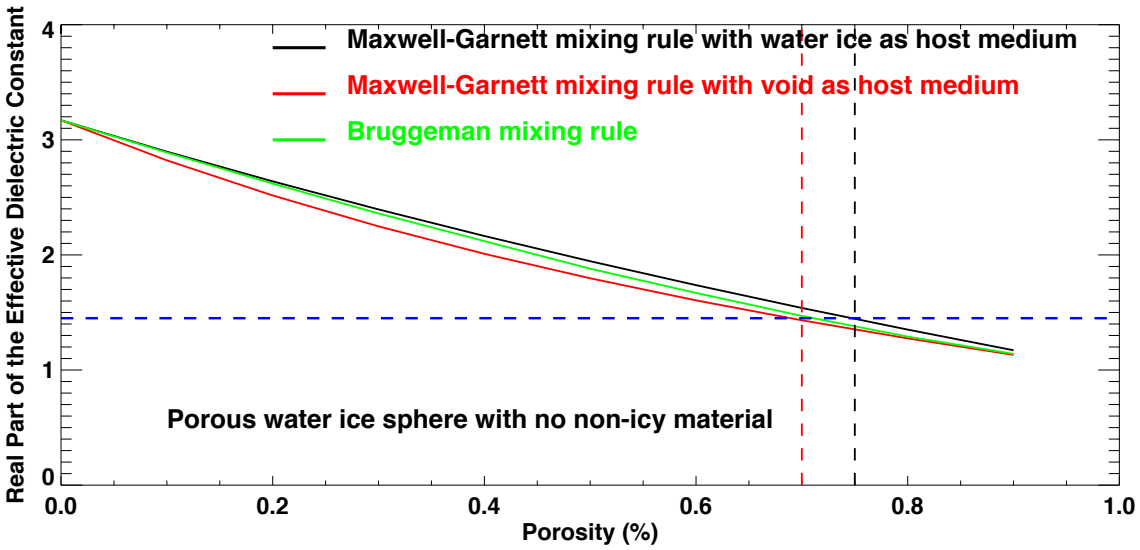

Figure 5.8: The real part of the ring particle effective dielectric constant as a function of porosity using three different mixing rules: Bruggeman mixing rule (green), Maxwell-Garnett mixing rule with water ice (black) or vacuum as the host medium (red).

After obtaining the required real part of the ring particle effective dielectric constant and its corresponding porosity, we are able to derive the radially varying non-icy material fraction merely from the required imaginary part of the effective dielectric constant. Here we compare three cases all of which match the required real part of the effective dielectric constant: (1) the particles are 75% porous and the effective dielectric constant is determined using the Maxwell-Garnett mixing rule with water ice as host medium; (2) the particles are 70% porous and the effective dielectric constant is determined using the Maxwell-Garnett mixing rule with vacuum as host medium; and (3) the particles are 70% porous and the effective dielectric constant is determined using the Bruggeman mixing rule.

In Figure 5.9, upper panel, we show that in all three cases, the real part of the dielectric constant remains relatively unchanged with a value of ~1.45 as we add more non-icy material. In the lower

panel, we investigate how the imaginary part of the effective dielectric constant, which determines the amount of intrinsic thermal emission, varies with the non-icy material fraction mixed within water ice for these same three cases. We find that when using the Maxwell-Garnett mixing rule, taking water ice or vacuum as the host medium actually makes a factor of ~1.5 difference in the required non-icy material fraction. The Bruggeman mixing rule consistently always gives a value in between these two cases. Thus, in order to reach the imaginary dielectric constant required to generate the amount of observed thermal emission, we would require about 50% more non-icy material if using the Maxwell-Garnett mixing rule with vacuum as the host medium (see **Figure 5.10**). These two cases set the upper and lower limit of the non-icy material fraction in the ring particles. The fraction will lie somewhere in between these limits depending on which mixing rule is used. Taking the non-icy material upper limit, the estimated age of the C ring in, for example, the injected Centaur (diffuse debris clouds) model increases from our previous estimate to ~ 30 −90 Myr. The mass of the silicates contained in the injected Centaur becomes $2.7\times10^{16} \sim 3.0\times10^{16}$ kg, and the size of the Centaur also increases slightly to ~13−20 km, while all other estimates remain similar to their previous values.

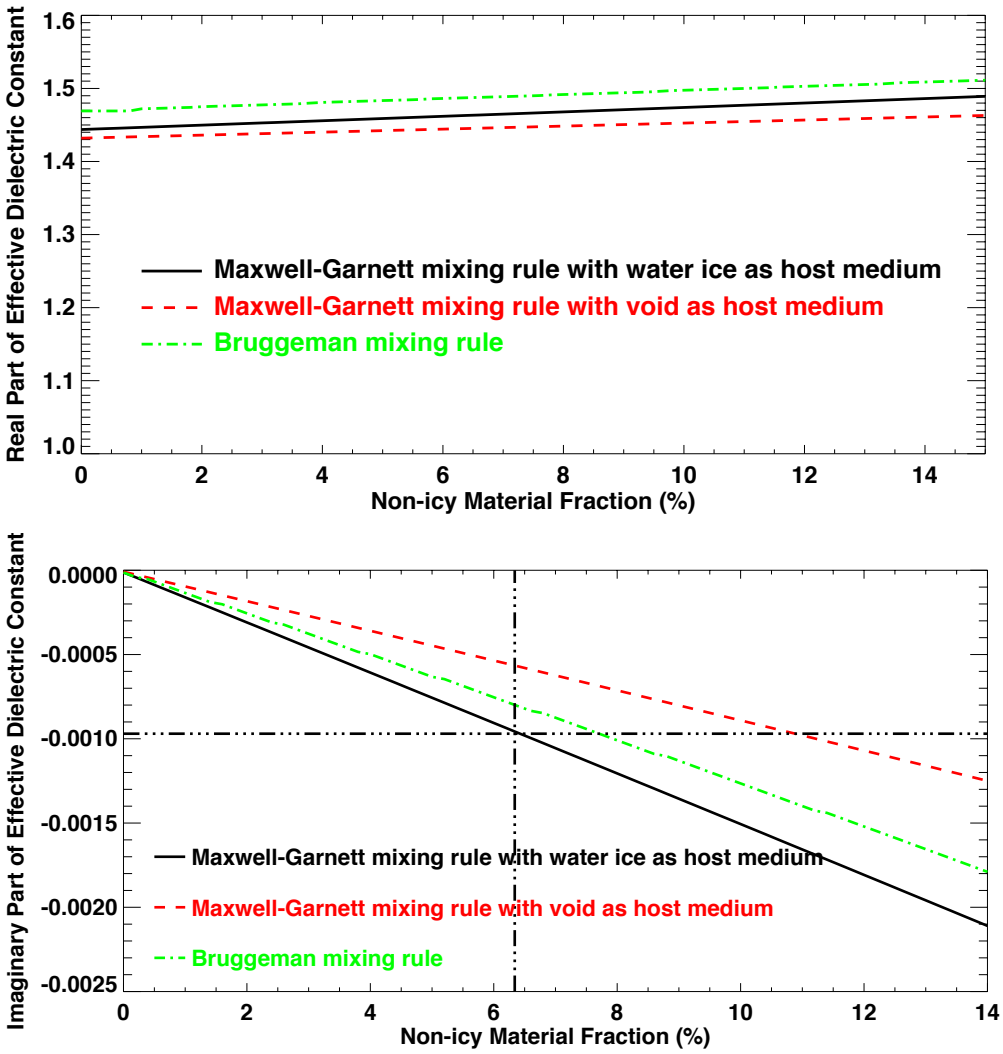

Figure 5.9: Black curve: Maxwell-Garnett mixing rule with water ice as the host material, and 75% porous C ring particles. Red curve: Maxwell-Garnett mixing rule with vacuum as the host medium, and 70% porous C ring particles. Green curve: Bruggeman mixing rule with 70% porous C ring particles.

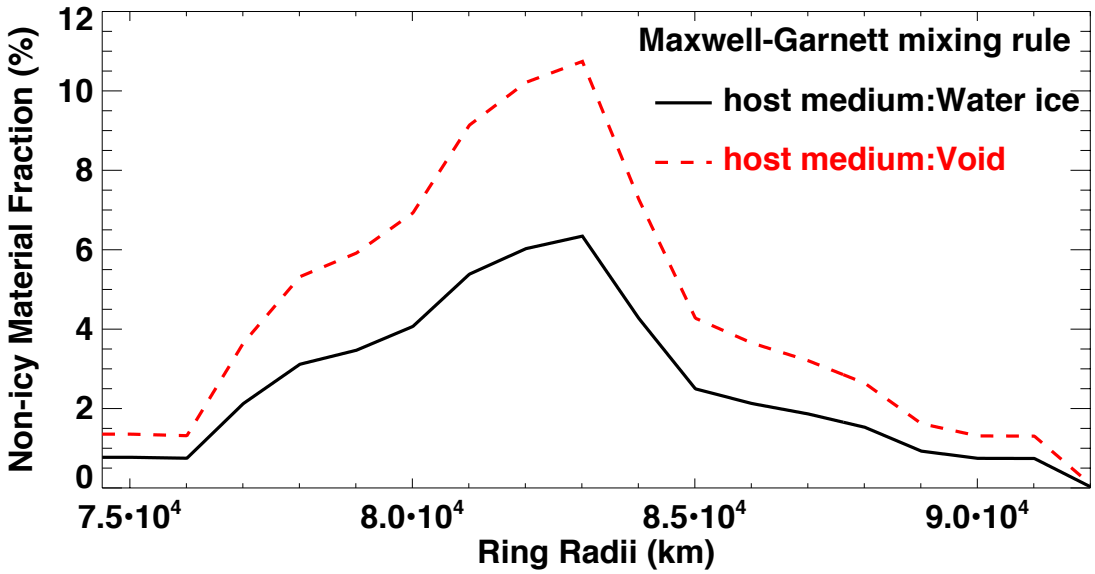

Figure 5.10: Black curve: Maxwell-Garnett mixing rule with water ice as the host material, and 75% porous C ring particles. Red curve: Maxwell-Garnett mixing rule with vacuum as the host medium, and 70% porous C ring particles.

5.3 Other Main Rings

5.3.1 Exposure Time

B Ring

In **Figure 5.11**, we show the required exposure time as a function of ring radius in order to accumulate the observed non-icy material fraction (see Fig. 4.8) from meteoroid bombardment alone. The required exposure time increases with particle porosity, varying from ~10-20 Myr for particles with 55% porosity to ~60-100 Myr for particles with 90% porosity. However, if the B ring particles are well characterized by a power law distribution with a maximum size $\gtrsim$ 5m, minimum size ~ 30cm and power law index q = 2.75 (see Sec. 3.2), the opacity ~ 0.03 - 0.05 cm^2 g^{-1} measured from density waves (Hedman and Nicholson, 2016) suggest that B ring particles have porosities in excess of 85%. This would imply that the age of the B ring is likely to be in the range

of ~40-100 Myr.

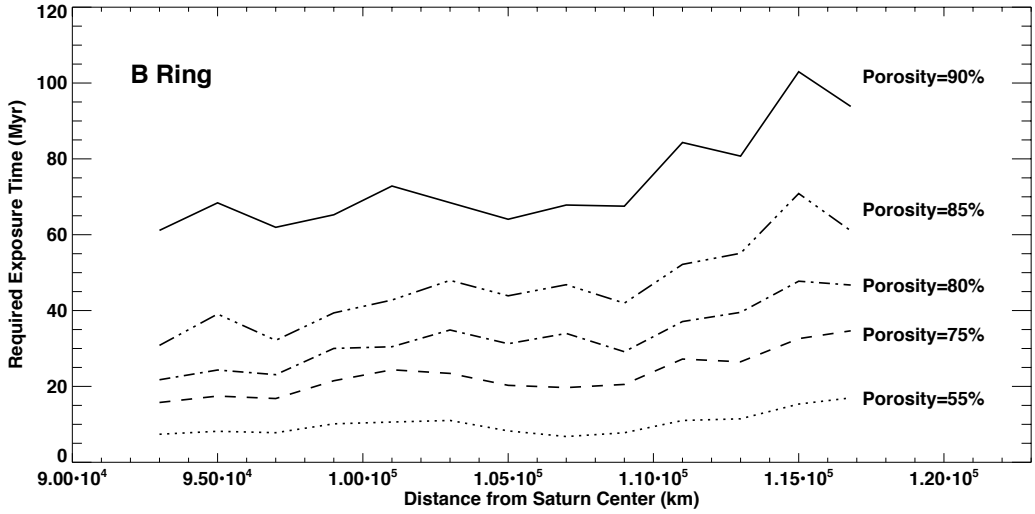

Figure 5.11: Derived exposure time to accumulate the amount of observed non-icy material (see also Fig. 4.8) from meteoroid bombardment, for five different porosity cases.

A Ring

Since we lack specific knowledge about the properties inside the wake regions in the A ring, we have employed the measured opacity to derive the wake optical depth and therefore are not able to constrain the porosity value in the A ring. According to the occultation observations in the low-resolution map scans (see Sec. 4.3.1), for the A0, A1 and A2 regions, the ring particles can be either 55% porous (scatter light with an isotropic scattering phase function) or 90% porous (30% Mie/70% isotropic hybrid scattering phase function). The upper panels of **Figure 5.12** shows that the required exposure times, to accumulate the non-icy material fraction shown in the upper panel of Fig. 4.18 for different porosity values are very close. Even as we vary the scattering phase function between a half-Mie-half-isotropic and a pure isotropic one, the results do not change significantly. The required exposure time for both porosity values are about ~100-150 Myr, while being a little bit longer for particles with 55% porosity. On the other hand, for the A3 region,

according to the occultation observations (see Figs. 4.10 and 4.11), the porosity value is more likely to be ~90%, especially for particle size distribution A3-Case 1. However, if we assume that the A3 region should have a similar exposure time as the A0-A2 regions, the porosity is more likely to be 55% (all three particle size cases) or 90% (particle size distribution 3). We currently cannot provide an explanation for this.

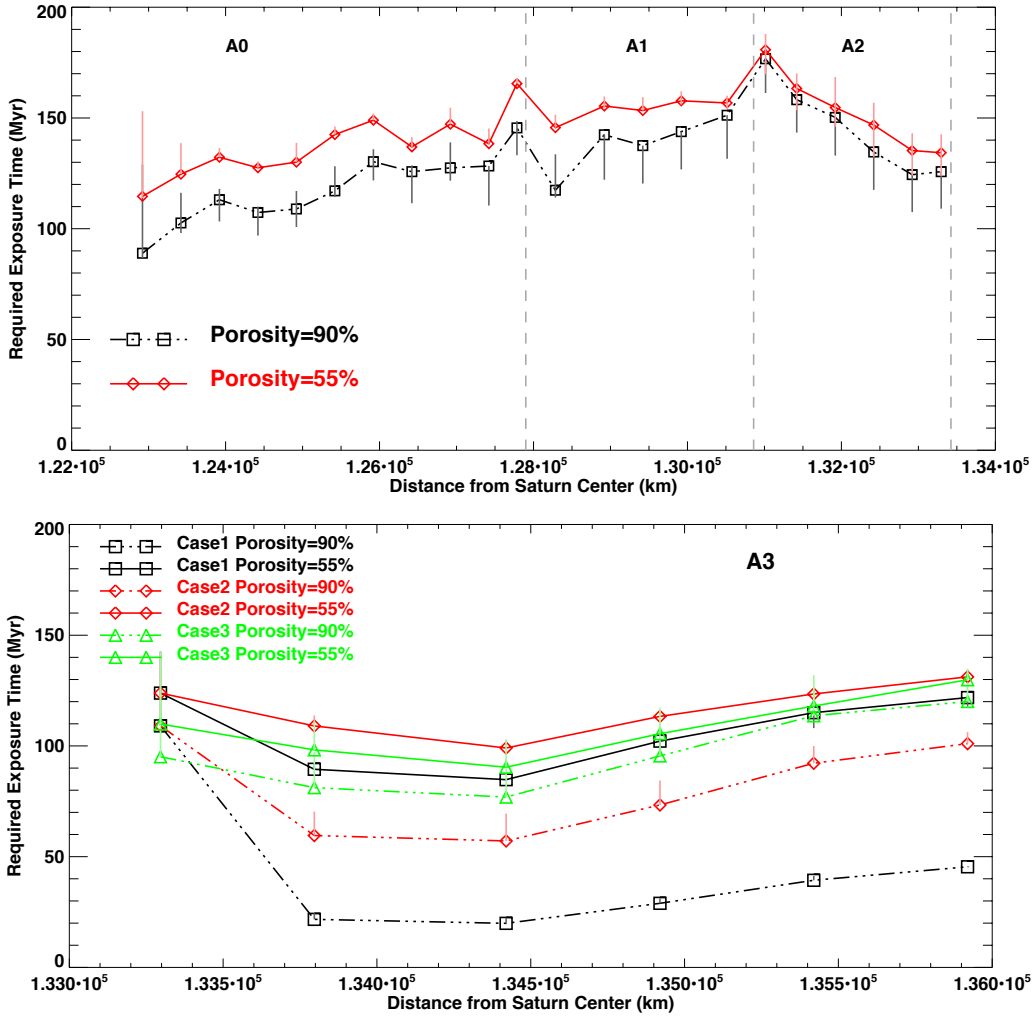

Figure 5.12: Required exposure time across the A ring to accumulate the observed non-icy material fraction from meteoroid bombardment. Upper panel (interior to the Encke gap): Results are derived using the best-fit phase function for a porosity of 55% (red diamonds), and 90% porosity (black squares). Lower panel (exterior to the Encke gap): Derived results for particle size distributions A3-Case 1 (black squares), A3-Case 2 (red diamonds) and A3-Case 3 (green

triangles). The solid curves correspond to 55% porosity, and the dashed curves to 90% porosity. The error bars indicate the range of the exposure times using phase functions between half-Mie-half-isotropic and purely isotropic.

Cassini Division

Finally, we also determine the required exposure time in order to accumulate the observed non-icy material fraction in the Cassini Division in **Figure 5.13** where for these calculations we have assumed a constant opacity of ~0.06 cm^2 g^{-1}. We see that for the range of porosities that we model, the exposure time for the Cassini Division to be polluted to its observed state can be as long as ~90 Myr.

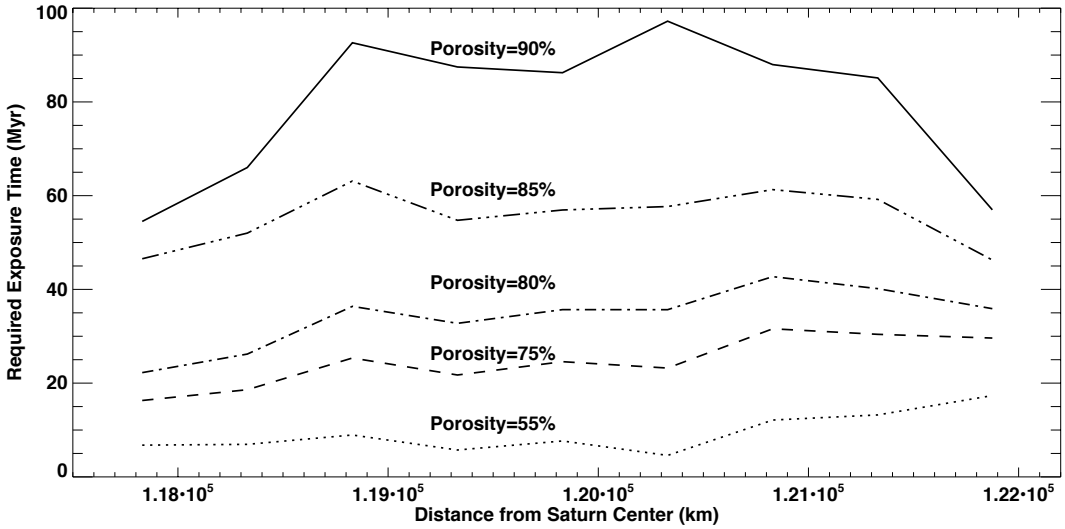

Figure 5.13: Exposure time across the Cassini Division for a range of porosities.

5.3.2 Interpretation

We first compare the derived non-icy material fraction and required exposure time in the B ring,

Cassini Division and A ring with those in the C ring (see Sec. 5.2) in which we determined the non-icy material fraction as a function of radius in the C ring, and found that the non-icy component reaches a maximum of 6%-11% by volume in the center of the C ring near 83,000 km, and that the fraction decreases gradually to 1%-2% inward and rapidly outward from this radial location. To explain this trend, we proposed a possible scenario in which a passing Centaur provides the necessary material for post-formation enhancement of the C ring non-icy material in addition to the micrometeoroid infall component. That is to say, the non-icy material fraction in the inner and outer C ring, which is about 1%-2%, is due to meteoroid bombardment and indicates an exposure time of 15-90 Myr for the nominal value of the micrometeoroid flux at infinity given in Sec. 5.1. Furthermore, we also considered a scenario in which meteoroid bombardment is the only pollution source, which can account for the mid-C-ring non-icy fraction, provided the rings formed ~900 Myr ago, again assuming the nominal bombardment rate. However, the nearly flat radial distribution of the flux would mean that mechanisms would then need to be identified that would act to somehow decrease the non-icy material in the inner and outer C ring. Ballistic transport in the outer C ring may act to dilute the non-icy fraction as icy material spills over from the inner B ring over time. However, the inner C ring remains problematic. No matter which is the case, its exposure time should be comparable to those derived in this work for the B ring, A ring and Cassini Division, if they all formed around same time and their optical depth and surface density have not changed considerably since the rings first formed.

In the B ring, the exposure time increases with increasing porosity from ~10 Myr (assuming 55% porous particles) to ~80 Myr (assuming 90% porous particles). According to the measured opacity, the B ring particles are more likely to contain porosities as high as 85%-90%. In the Cassini Division, the exposure time increases with increasing porosity as well, from ~10 Myr (55%

porosity) to ~90 Myr (90% porosity). The Cassini Division particles are also more likely to be highly porous, as much as 90%, due to the high opacity measured by density waves and also after comparing the shapes of the simulated and observed scattering profiles. In the A ring, the required exposure time in regions interior to the Encke gap is about ~80-150 Myr independent of the porosity we have chosen (from 55% to 90%). In the region exterior to the Encke gap, the required exposure time can vary from ~10 Myr to ~120 Myr depending on the ring particle porosity and particle size distribution assumed. As compared with the exposure time in the C ring, our results taken together would seem to suggest that the main rings formed $\lesssim$ 150 Myr ago. The high contamination rate in the middle C ring which we have explained as being due to the breakup and deposition of a Centaur occurs within this time frame.

It should be emphasized that our Centaur capture scenario is independent of any proposed model for the origin of the main rings (see Charnoz et al., 2009a, for a more complete discussion of ring origin scenarios). Our derived results for the radial distribution of the mass fraction of non-icy material due to direct micrometeoroid bombardment in general imply an exposure age for the rings that would be consistent with young rings, possibly suggesting an origin scenario in which a ring progenitor of Mimas, or several Mimas masses was broken up and formed the rings in a time scale consistent with what we have determined here. However, no model for the origin of the rings in which they form within the indicated time scale has thus far been proposed. It might be argued that such a ring progenitor may have had a rocky core which could still in one form or another remain hidden within the rings (Charnoz et al., 2009b) which might then account for the anomalous fraction in the C ring. However, how that rocky material ends up solely in the C ring but apparently not elsewhere, combined with the fact that the radial distribution of non-icy material and observed opacity in the middle C ring can be simulated through viscous diffusion of an initially

high density annulus of rocky chunks embedded within icy mantles (core-mantle model) suggests that the Centaur capture scenario can readily account for the observations.

6 VLA Multi-wavelength Observations on the C and B rings

In 2015, we obtained multi-wavelength Very Large Array (VLA) microwave interferometer observations on Saturn and its rings. We applied the particle properties (i.e. particle porosity, non-icy material fraction, scattering profile) in the C and B rings derived from Cassini 2.2 cm observation and compare the simulated results with the VLA observation in order to verify our previous findings and investigate ring particles properties at various microwave wavelengths.

6.1 Data overview

The Very Large Array (VLA) has recently been upgraded in the Expanded VLA (EVLA) project obtaining higher sensitivity and wider frequency coverage. We observed Saturn with the upgraded VLA at six wavelength bands ranging from Q band (~ 0.69 cm) to S band (~ 14.1 cm) over four days in 2015: January 24-25 using the CnB configuration; and on May 28-29 in the BnA configuration. During configuration A, the telescopes extend over the 21 km length of each arm, which results in the most magnification and greatest detail during observations. The size of the array gradually decreases with configurations B and C, while larger structure of the source can be observed with shorter baselines. Configurations CnB and BnA are hybrid configurations in which the antennas on the east and west arms are moved in for the next configuration, but those on the north arm remain extended. We have observations in the X and U bands in both CnB and BnA configurations. By combining them, we can gather a great deal more information in both small and

large scales. In CnB configuration the VLA baseline lengths range from 0.065 km to 7.7 km and cover more larger spatial scales. In BnA configuration the VLA baseline lengths range from 0. 4 km to 24 km and cover more smaller spatial scales. A brief summary of all observations can be found in Table 1. All 28 antennas were used in the observation.

Table 6.1: Details of the VLA observations

Freq. band	Wavelength (cm)	Observation Date (UT)	R.A. (J2000)	Dec (J2000)	Dist (AU)	Ring inc. (°)	VLA config	Pole Ang. (°)
S	13.33-15.04	2015.May.28 05:56:37 – 07:49:42	15:57:23.007	-18:13:36.11	8.97	-24.34	BnA	2.201
C	7.08 – 7.53	2015.May.28 03:59:00 – 05:49:59	15:57:24.534	-18:13:40.23	8.97	-24.34	BnA	2.202
X	2.50 – 3.76	2015.Jan.25 12:58:58 – 14:51:59	16:04:45.301	-18:47:24.20	10.38	-24.82	CnB	2.422
		2015.May.29 06:51:11 – 08:44:16	15:57:03.971	-18:12:44.78	8.97	-24.32	BnA	2.192
U	1.66 – 2.50	2015.Jan.24 13:35:40 – 15:24:13	16:04:26.934	-18:46:40.67	10.39	-24.81	CnB	2.413
		2015.May.29 04:55:55 – 06:44:33	15:57:05.494	-18:12:48.88	8.97	-24.33	BnA	2.192
K	1.15 – 1.67	2015.Jan.25 15:03:15 – 16:51:48	16:04:46.914	-18:47:28.00	10.38	-24.82	CnB	2.423
Q	0.62 – 0.75	2015.Jan.24 15:35:23 – 17:23:56	16:04:28.513	-18:46:44.43	10.39	-24.81	CnB	2.414

6.2 Mapping Procedure

After the observation data were calibrated using the NRAO pipeline developed by Bryan Butler,

we looked up the Saturn's pole position angle at each observation time and rotated the *UV* data accordingly to align the north–south pole axis as projected on the sky during the planet's rotation; i.e., the final projection of Saturn's equator on the sky was oriented east–west for each individual scan. We divided all the UV data channels in each frequency band into 2 S band, 2 C band, 32 X band (Jan), 32 X band (May), 48 U band (Jan), 40 U band (May), 64 K band and 64 Q band spectral windows, respectively. Each spectrum window contains 8 channels with a bandwidth of 0.128 GHz, and each window was processed independently. Within each spectral window, all *UV* data from 8 channels were combined before self-calibration and Fourier transformation into the map plane. This increased the signal-to-noise both because of a lengthening of the integration time and due to a better coverage of the *UV* plane.

As a final step, all images were corrected for the primary beam effect, which for extensive sources like Saturn and its rings, becomes noticeable. We modeled and subtracted Saturn's thermal radiation and the rings' brightness temperature in the UV plane. Removal of the model disk before cleaning deletes more than 95% of the image flux, allowing the clean algorithm, which performs poorly on extended emission, to work more efficiently. However, this does not bias the result of cleaning in any way regarding the structures of interest to us: the ring ansae and the latitudinal variation on the planet (Dunn et al. 2002).

In our model we represent the brightness temperature of the unocculted portion of the disk as $T_0 + T_1\langle\mu_p\rangle$, where T_0 and T_1 are model parameters of the uniform and limb-darkened disk, respectively. The variable μ_P is the cosine of the angle between the line of sight and the local normal viewed from the planet atmosphere. Since the geometric size of the planet is known a priori, the value of T_0 and T_1 are obtained by computing a least-squares fit to the UV-data (Dunn

et al., 2002). In addition, given appropriate ring properties parameters, we model the brightness of all the main rings (C, B and A rings) and Cassini Division using a Monte Carlo code that is capable of dealing with the multiple-scattering process within the ring plane (see Sec. 3 for more details). The ring properties parameters (*i.e.*, optical depth, particle size distribution, particle scattering properties, particle composition, etc.) were first obtained from previous work (Cuzzi et al., 2009; Colwell et al., 2007, 2010; Dunn et al., 2002) and progressively modified to minimize the difference between the observations and the models. This "planet + ring" model was also used to self-calibrate the phases of the uv-data (Dunn et al., 2002). Due to the wake structure in the A and B rings, the rings' brightness temperature has been found to be asymmetric. However, as the self-calibration does not remove subtle asymmetric features, our simulated model for the calibration process doesn't take into account this wake structure. Furthermore, we also carefully examined the zones and belts as produced by the subtraction of a homogeneous limb-darkened disk model. We note that since this model consists of a homogeneous limb-darkened disk with rings that are symmetric about the polar axis, the subtraction of this model (not the process of self-calibrating the phases of the uv-data) accentuates the subtle structures of scientific interest (ring brightness in the ansae, any east–west asymmetries, and latitudinal variations on the planet surface). Since we focus our efforts on the rings and their structure, we modeled the thermal radiation from Saturn's disk, including latitudinal variations, as accurately as possible to remove these emissions from the data.

Mapping and cleaning are done with the standard MIRIAD tasks (invert, clean, and restore), using a modified uniform weighting and setting of the robustness parameter to zero. We also apply the appropriate primary beam corrections. Maps were made into square arrays of 2048 on a side with

pixel sizes of 0.05″. To further improve the signal-to-noise ratio, we combined spectral windows in each frequency band, eight as one group and average the data in each group. We average the eight self-calibrated residual UV maps in each group before doing an invert, clean and restore. We then add an average "Saturn + rings" model map back to the cleaned residual map to obtain the final brightness temperature map. Since both the S band and C band observations only have two spectral windows, for each of them we combine all of the data to generate one final map. On the other hand, we noticed especially large noise and obvious artifacts in the final map in the K and Q band data, which might be due to some antenna break down, bad observation time or radio frequency interference. We had attempted to flag out bad observation data but were still not able to remove the artifacts. At high frequencies, especially the Q band, there might be insufficient sampling of large scale structures, which might also cause larger noise. For now, to get a better signal-to-noise ratio in this case, we divided all 64 K-band spectrum windows into two groups and generated two final maps, while in the Q band, we averaged all 64 spectrum windows into one final map.

For the X and U bands, we have data from two different configurations (see Table 7.1). While the observations made with the CnB configuration (Jan 2015) cover the shorter UV distances, the observations made with the BnA configuration (May 2015) cover the much longer UV distances which resolve finer structures on Saturn and its rings. Moreover, the Saturnian system was closer to Earth during the May 2015 observation period. Therefore, we combined corresponding spectral window groups of data in the same frequency range in two configurations to generate the final map.

6.3 Final Maps

Measurements made with an interferometer are only sensitive to brightness contrasts with respect to the empty sky, since VLA is blind to structures on angular scales larger than the fringe spacing formed by the shortest baseline. Therefore, we are unable to sample large structures such as the cosmic microwave background coming from all directions in the empty sky.s Hence in the calibrated final map, the empty sky is at 0 K. Thus the rings and the Saturn disk are 2.7 K lower than their actual brightness temperature. This 2.7 K term, which is the cosmic microwave background (CMB), is not present in the data. In **Figure 6.1** we plot one of the final maps at one spectrum window group set for each frequency band. As mentioned in Sec. 6.2, when we invert the UV data, the maps are set to be 2048×2048 with pixel sizes of $0.05''$ to avoid edge effects in the cleaning process. In Fig. 6.1, we only show the center part focusing on Saturn and its rings. Because of the wide dynamic range between the disk and the rings, we set the color range for -2 K to 20 K on the left column of the figures to show the structure of the rings and color range for 160 K to 240 K (S band), 140 K to 200 K (C band), 100 K to 160 K (X, U and Q band), and 110 K to 140 K (K band) on the right column to show the latitudinal variation of Saturn's thermal radiation. The yellow ellipses on the lower left of each panel indicate the synthesized beam sizes and corresponding position angles (see Tabel.6.2 for the beam sizes). In the left column, X, U, K and Q bands show a hot band in the middle C ring, consistent with the Cassini passive radiometry observations at 2.2 cm. According to Zhang et al., this hot band cannot simply be attributed to the optical depth increase in the middle C ring alone. Instead it is likely to come as a result of the presence of an extra amount of non-icy material concentrated there, which generates more thermal emission. We will investigate this region in more detail and compare it with the results obtained from Cassini observations in Sec. 6.5.1. The resolution in S and C band is not high enough to

resolve the C ring.

In the K band spectrum window set 1 final map, we notice an asymmetry in the C ring region: the east side is brighter than the west which is not expected at all. Due to the low optical depth in the C ring, wake structures which might cause observed asymmetries (e.g., as in the A ring) are not likely to be present here. Indeed, no previous work has ever reported any asymmetry in the C ring. Therefore it is likely that this asymmetry is an uncertainty brought about through the observations or calibration process. The significant brightness change on the edge of Saturn's disk near the C ring together with the large beam size in the K band could generate large uncertainties in the observed C ring brightness, especially since the C ring is an order of magnitude fainter than Saturn. As we have no reference from which to determine which side is better calibrated, we average the data on both sides, which will at the same time result in a larger uncertainty. Similar asymmetry is also observed in the Q band data. However, we find the low brightness on the west side was likely to be an artifact. As shown in **Figure 6.2** where we show a larger 1024×1024 map, we rescale the color axis from -3 K to 3 K to investigate the calibrated brightness on the empty sky, which is supposed to be close to 0 K. In Fig. 6.2, we find a large blue stripe spanning from about (0", 25") to (20", -25"), which crosses through the C ring on the west side. We have attempted to flag out bad data in our investigation of the UV data, but we find we are still not able to remove this artifact. Due to the low brightness temperature in the C ring, this artifact has a significant effect on the west side C ring data, greatly decreasing the observed brightness temperature. Therefore, for the Q band observation in the C ring, we only use the data on the east side. Table. 6.2 summarizes the averaged wavelength and beam size about all the final maps.

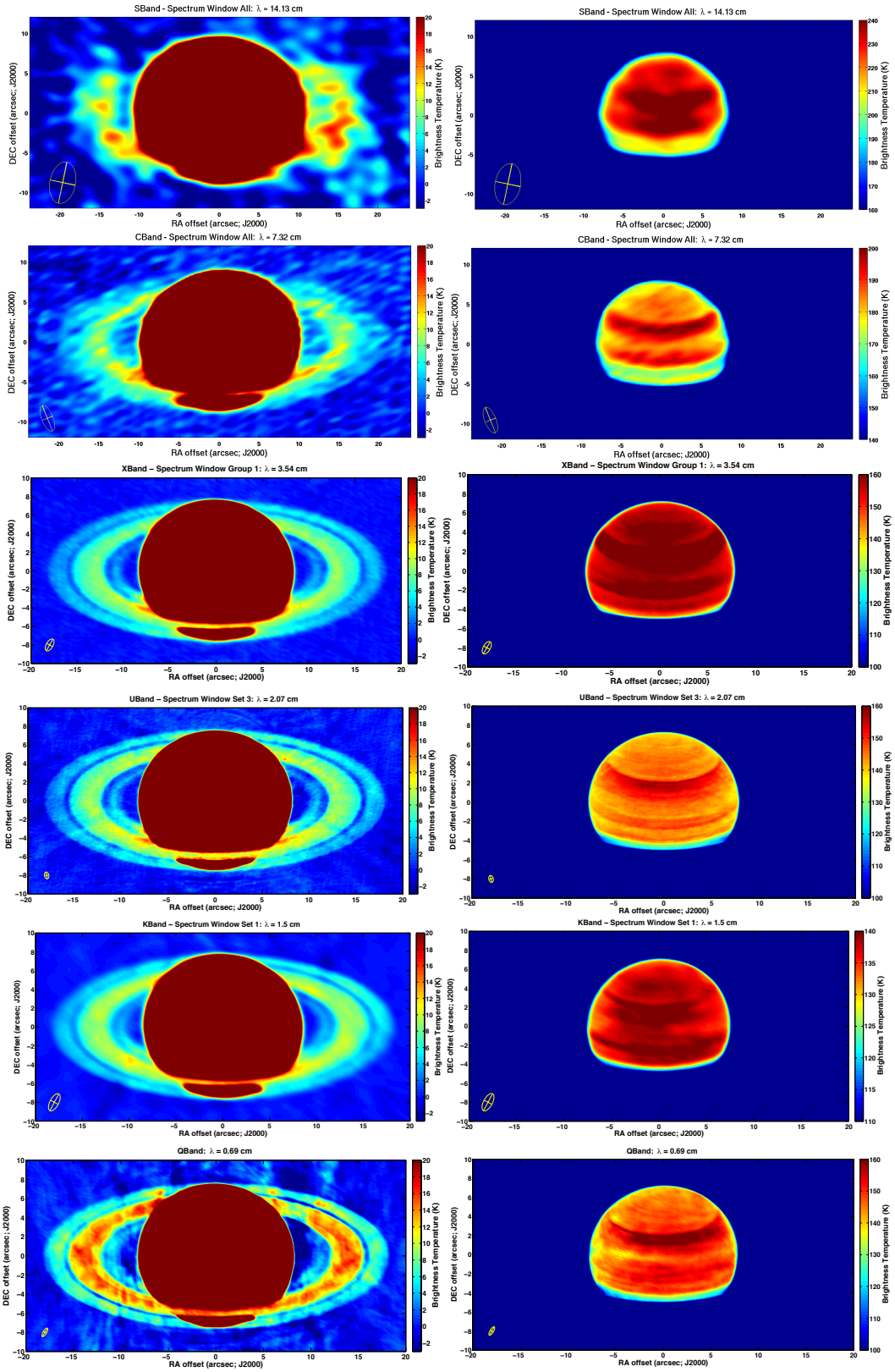

Figure 6.1: Final maps after calibration at four frequency bands (from top to bottom: S, C, X, U,

K and Q band). The color range for the panels on the left column is set from -2 K to 20 K to show the structure of the rings. The color range on the right column are set from 160 K to 240 K (S band), 140 K to 200 K (C band), 100 K to 160 K (X, U and Q band), and 110 K to 140 K (K band) to show the latitudinal variation of Saturn's thermal radiation. The yellow ellipses on the lower left of each panel indicate the synthesized beam sizes and corresponding position angles.

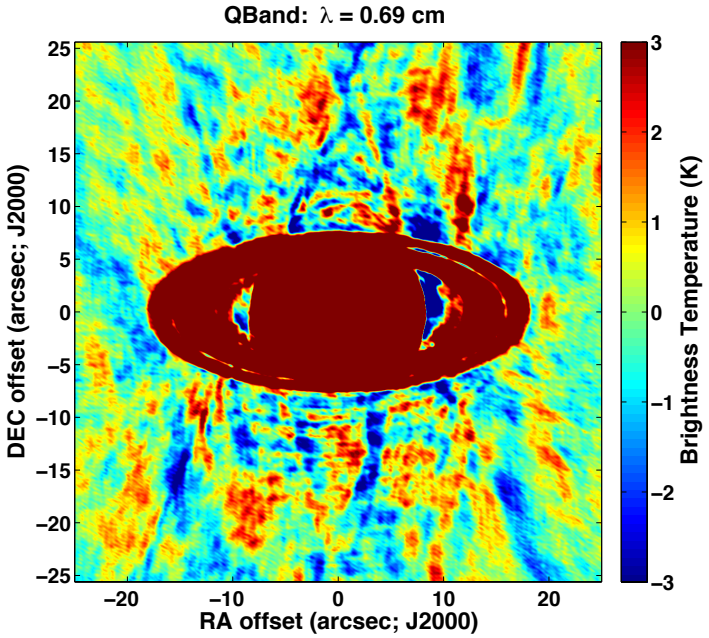

Figure 6.2: A larger 1024×1024 final map after calibration for the Q band observation. The color range is set from -3 K to 3 K to investigate the calibrated brightness on the empty sky, which is supposed to be close to 0 K. There is a large blue stripe spanning from about (0", 25") to (20", -25"), which crosses through the C ring on the west side.

Table 6.2: Beam size and position angle at all spectrum window sets.

		$\lambda\,(cm)$	$f\,(GHz)$	f_{whmx}(")	f_{whmy}(")	***Position angle*** ***(°)***
S Band	SPWS all	14.13	2.12	2.638	1.595	78.5
C Band	SPWS all	7.32	4.10	1.719	0.714	-68.0
X Band	SPWS1	3.54	8.47	0.717	0.364	60.1
	SPWS2	3.15	9.51	0.635	0.328	60.2
	SPWS3	2.86	10.50	0.572	0.297	60.3
	SPWS4	2.65	11.30	0.521	0.265	61.5
U Band	SPWS1	2.40	12.49	0.409	0.223	-79.2
	SPWS2	2.22	13.49	0.407	0.254	-76.7
	SPWS3	2.07	14.49	0.372	0.232	-76.7
	SPWS4	1.93	15.51	0.354	0.201	-80.0
	SPWS5	1.82	16.49	0.335	0.171	-83.3
K Band	SPWS1	1.50	20.00	1.009	0.464	61.8
	SPWS2	1.25	23.98	0.835	0.373	62.9
Q Band	SPWS all	0.69	43.70	0.508	0.187	59.1

Saturn Radiation

Despite the latitudinal stripes on Saturn's disk, the Saturn thermal radiation is best represented by $T_{Saturn} = T_0 + T_1 <\mu_p>$, which is 2.7 K lower than the real Saturn radiation. In **Figure 6.3,** we compare our best-fit frequency-dependent values of $T_{Saturn}(0°)$ (solid line), T_0 (dashed line) and T_1 (dash-dot line) with the limb-darkened Saturn thermal emission calculated assuming a saturated atmosphere model (Li, priv. comm.) and the value suggested by previous VLA observations (Dunn et al., 2002). In Fig. 6.3 left panel, the best-fit values from our observations are represented by the black line with crosses at the observed frequency, while the model values are shown with the red line. The values from Dunn et al. (2002) are shown by the green line with green diamonds. The total Saturn radiation in the normal direction $T_{Saturn}(0°)$ is indicated by the solid lines, uniform disk brightness T_0 by dashed lines and the limb darkening factor T_1 by dash-dot lines. According to

NRAO reports, the absolute accuracy of the flux density scale is estimated to be about 2% at all bands except in the Q band, where pointing errors limit the accuracy to perhaps 3%. The uncertainties in the VLA flux density scale can be brought in by the system error (i.e. receiver noise, atmospheric emission etc.). In addition, there might also be uncertainties brought in through the calibration process (i.e. phase calibration process, cleaning process, etc.) (see Section 6.5 for more discussion on uncertainty calculations). In Fig. 6.3, we have indicated the overall uncertainty with the vertical lines in the observed total Saturn radiation in the normal direction. The y-axis scale for $T_{Saturn}(0°)$ and T_0 is shown on the left and that for T_1 is shown on the right. The limb-darkening factors obtained from the observations are mostly higher than the model, but lower than the values from Dunn et al. (2002). The observed total Saturn radiation in the normal direction is fairly close to the model in most bands with the exception of the S and C bands, where the observed value is much higher than the model. In the right panel of Fig. 6.3, we show the ratio of the limb-darkened component to that of the constant disk T_1 / T_0 from our observations, the calculated model and two data sets from Dunn et al. (2002). The trends of increasing limb-darkened component fraction towards longer wavelengths are in good agreement.

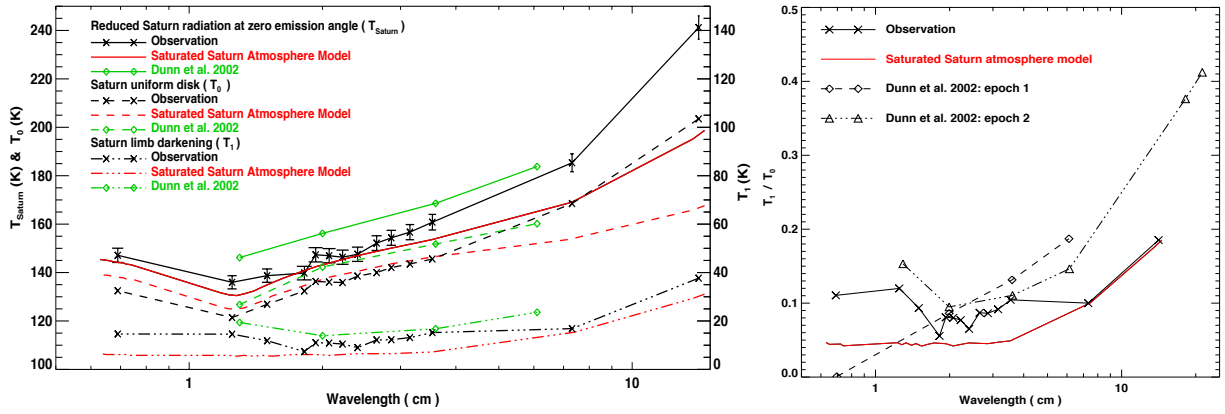

Figure 6.3: Left panel: frequency-dependent values of $T_{Saturn}(0°)$ (solid line), T_0 (dashed line) and T_1 (dash-dot line) from our observations (black line + crosses), saturated Saturn atmosphere model (red) and previous VLA observations in Dunn et al., 2002 (green line+diamonds). The overall

uncertainties are indicated with the vertical lines in the observed values of $T_{Saturn}(0°)$. The y-axis scale for $T_{Saturn}(0°)$ and T_0 is shown on the left and that for T_1 is shown on the right. Right panel: comparison of the ratio of the limb-darkened component to that of the constant disk T_1 / T_0.

6.4 Generation of a synthetic map of Saturn and its rings from simulations.

To construct a synthetic map to compare with the observed map we need to first generate a brightness map of Saturn and its rings projected onto the sky as seen from the VLA, and then convolve it with the observing beam. Our Monte Carlo code package (Dunn et al., 2002) is able to simulate the radiative transfer and internal thermal emission within the ring layer, infer the brightness temperature of the rings as a function of radius and azimuth, and convert the brightness temperature of the rings and the limb-darkened Saturn disk to a map of right ascension and declination. This final map is then convolved with the instrumental response using MIRIAD and can be directly compared to the observations.

6.4.1 Saturn Radiation and the Cosmic Microwave Background

As we have discussed in Sec. 3.1, we reasonably assume that no matter in which direction one observes the rings from, one will always receive a CMB contribution of 2.7 K if Saturn were not there. To limit computational complexity in our simulations, we approximate the CMB contribution by removing 2.7 K from the Saturn's thermal radiation and then combine the reduced Saturn radiation with fully isotropic CMB radiation. This leaves us with an isotropic radiation of 2.7 K coming in from all directions, which will result in a ~2.7 K contribution to the rings brightness temperature. We therefore use an effective Saturn thermal radiation which is 2.7 K less

than the true Saturn thermal radiation to calculate the directly transmitted and scattered component in our Monte-Carlo code. The 2.7 K contribution itself is a significant quantity but, as we mentioned previously measurements made with an interferometer are only sensitive to brightness contrasts, hence this 2.7 K term is not present in the data and we do not include it in our model maps. Therefore we represent the observed planet brightness by $T_0 + T_1\mu_P$, which is 2.7 K lower than the actual planet brightness, and we use this value in our model when simulating the scattered and directly transmitted component for the rings' brightness. In the end, the total simulated brightness temperature to be compared to the observations is the sum of directly transmitted reduced Saturn radiation, the scattered reduced Saturn radiation and intrinsic thermal emission from the rings, which is 2.7 K lower than the actual brightness.

Finally, due to Saturn's large solid angle as seen from the rings, a resolved Saturn thermal emission model is required. In this section, we simulate the results with; 1) the Saturn radiation model derived from previous RADAR observations at 2.2 cm by Janssen et al. (2013) and calculated for the saturated Saturn atmosphere model (Cheng, priv. comm.); and 2) the limb-darkened disk derived from our observations. We also take into account the latitude-dependent stripes (from our observations) on top of the limb-darkened disk. Although Saturn radiation is not the focus of this work, its values are important as we simulate the rings' brightness and have especially significant effects on the rings that cross the planet. To that end, we apply the values from our observations and the saturated Saturn model, and treat the difference in the results as the uncertainty (see Sec. 6.5).

6.4.2 Ring brightness temperature simulation

To generate the ring brightness temperature model, we divide the C and B ring, the Cassini Division and A ring into 47, 68, 12 and 39 ring annuli, respectively. All ring annuli are defined to have the same width. We assume that the ring properties within each ring annulus remains the same. To simulate the azimuthal distribution of the brightness as seen from the VLA, our Monte Carlo code requires knowledge of the ring particle size distribution, composition, scattering properties and the local optical depth. As for the A ring, we applied the best-fit ring particle parameters found in Sec. 4.3. However, considering that the A ring is not the focus of this work, we do not discuss the parameters we use for the A ring wake structures here. A follow-up effort will investigate the A ring features in more detail.

6.4.2.1 Ring particle model 1 "Intramixed" model -- Particle composition and dielectric constant

We applied the two ring particle models proposed in Sec. 5.2 in our simulation. In the first "intramixture" model, we assume that the ring particles are made of porous water ice with non-icy material embedded in the form of small inclusions. The ring particle composition is used to determine the material's effective dielectric constant based on the Maxwell Garnett mixing rule of Effective Medium Theory (EMT; see Bohren and Huffman, 1983). Assuming the inclusions are spherical, the complex effective dielectric constant of a porous mixture of water ice and intramixed non-icy material can be expressed as

$$\varepsilon_{eff} = \varepsilon_{ice}\left[1 + \frac{3(f_v(1-f_p)\frac{\varepsilon_{non\text{-}ice}-\varepsilon_{ice}}{\varepsilon_{non\text{-}ice}+2\varepsilon_{ice}}+f_p\frac{1-\varepsilon_{ice}}{1+2\varepsilon_{ice}})}{1-(f_v(1-f_p)\frac{\varepsilon_{non\text{-}ice}-\varepsilon_{ice}}{\varepsilon_{non\text{-}ice}+2\varepsilon_{ice}}+f_p\frac{1-\varepsilon_{ice}}{1+2\varepsilon_{ice}})}\right] . \quad (6.1)$$

where $\varepsilon_{non\text{-}ice}$ and ε_{ice} are the complex dielectric constants of the non-icy mixture and pure ice,

respectively, f_p is the particle porosity and f_v is the volume fraction of non-icy material mixed within the ice. All A/B ring and Cassini Division particles are assumed to be of ring particle model 1 -- "intramixed" particles. We primarily use silicates as the candidate for the intramixed non-icy material (Cuzzi et al., 1980). The dielectric constant of water ice and silicates are discussed in Sec. 3.2. With the ring particles' effective dielectric constant, Mie theory is then applied for their scattering/extinction efficiency and the phase function in the intramixure model.

6.4.2.2 Ring particle model 2 Core-mantle Model

Due to the anomalously low opacity $\kappa = \tau_{geometry}/\sigma$ observed in the middle C ring (e.g., Hedman and Nicholson, 2013) we were led to consider a silicate-core, porous icy-mantle model as opposed to a purely intramixed model, to address the likelihood that silicates may be present in large chunks instead of fine powder in the ring particles (based on our hypothesis of the disruption of a large silicate object, see Sec. 5.2.2). Such a model fits both the low opacity, by hiding more silicate mass inside the larger ring particles, as well as the thermal emission, but we acknowledged that in order to address the scattering behavior of particles containing large chunks of silicates more rigorously, we expect to do more detailed modeling with a discrete dipole approximation (DDA) code. Here we continue to consider a uniform core-mantle model using a silicate-rich core and porous dirty-ice mantle in order to gauge its effectiveness in matching the observations.

We started with the simplified model derived from Cassini observations, that the composition of the background C ring is primarily water ice, but with a fraction of ~1% non-icy material which is assumed to be intramixed within ring particles that have 75% porosity. We also assume a critical minimum size a_{crit}=60 cm for the population that includes the rocky fragments such that particles

smaller than this critical size have a composition similar to the background C ring, while particles larger than this contain a silicate core covered with a porous dirty icy mantle with the same porosity and non-icy material fraction as the background C ring particles. To further simplify the model, we also assume that the ratio of silicate core radius to particle radius f_r=0.65 is fixed for all core-containing particles. To account for the radially varied non-icy material contamination, we proposed two models. In the first model (Case A), all particles larger than the critical size contain a silicate core, but adopt a radially-varying maximum particle size. The second model (Case B) is under the assumption that among all particles larger than the critical particle size, only a percentage of them contain a silicate core, and the percentage that contains a core is radially dependent on the distance from the peak. The radially-varying maximum particle size and the radially-varying percentage of particles larger than a_{crit} that contains a core is shown in Fig. 5.5 covering the radius range of 78,000 km – 87,000 km. For the C ring particles outside this radius range, they are all assumed to have the same composition as the C ring background material. All the parameters in this model are determined in Sec. 5.2.2 to match our observations by considering the low opacity in middle C ring and the two main characteristics in our data that we need to match: high brightness temperature in the occultation (near-zero azimuths) data and radially varying thermal emission in the C ring.

We simulate our core-mantle model with a layered sphere Mie scattering code (Wiscombe, 1980). In our code, for all particles smaller than $a_{crit} = 60\ cm$ within 78,000 km – 87,000 km and all particles outside this range, Mie theory is applied for their scattering/extinction efficiency and the phase function, as described in ring particle model 1 ("intramixture" model). In Case A, for all particles larger than this critical size a layered Mie scattering code is applied for the scattering/extinction efficiency and the phase function. In Case B, the layered Mie scattering code

is applied to a certain percentage (as shown in Fig. 5.5 right panel) of the particles larger than the critical size and uniform Mie scattering code is applied to the rest of the large particles. We applied both Case A and Case B in our Monte Carlo code and we find that their results are very similar. Therefore in Sec. 6.5.1 we show the core-mantle model simulation results for Case B only unless otherwise noted.

6.4.2.3 Azimuthally uniform C/B rings and Cassini Division - Local optical depth

We employ the normal optical depth profile measured by the Cassini Radio Science Subsystem (RSS) at λ_0 = 3.557 cm (Cuzzi et al., 2009) and then convert this to the value at the observed wavelength λ. The ratio of the optical depth at different wavelengths is obtained by integrating the ring particles' extinction cross-section with the extinction efficiency calculated as described above in Sec. 6.4.2.1 and Sec. 6.4.2.2 (for intramixure and core-mantle model), using Eqn. (3.5). The extinction coefficient for particles of size a at wavelength λ calculated from either Mie scattering theory if particles do not contain a silicate core, or from a layered Mie scattering code if particles contain a silicate core. **Figure 6.4** shows the averaged optical depth for all ring annuli used in the simulation at a wavelength of 0.69 cm, 1.25 cm, 2.07 cm and 3.557 cm.

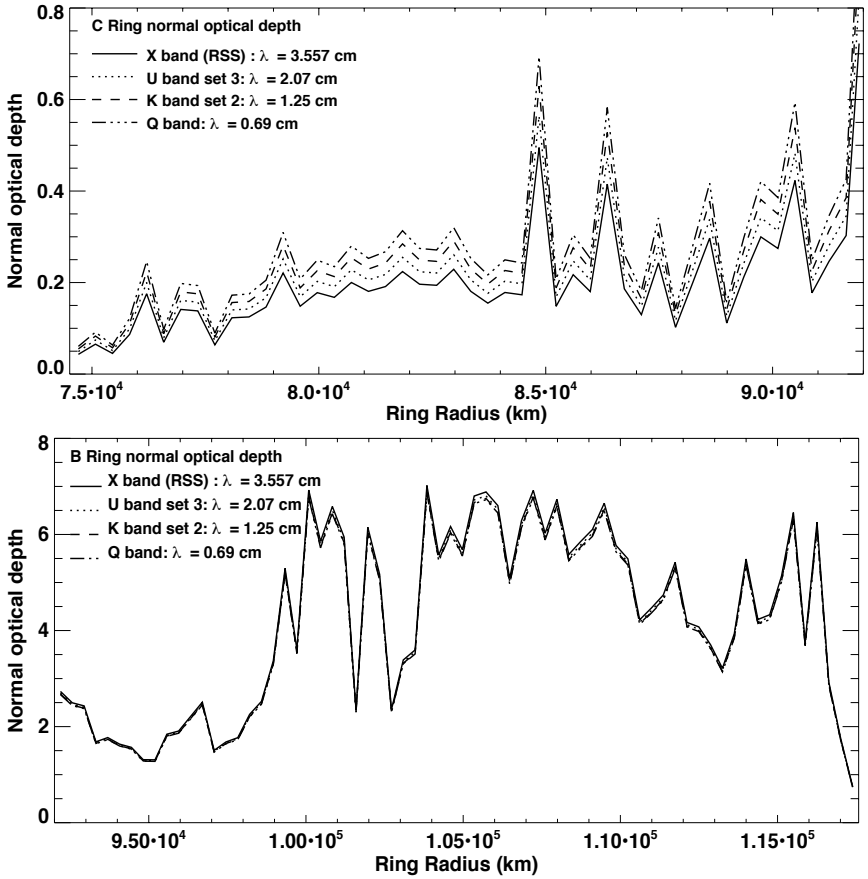

Figure 6.4: Averaged optical depth for all ring annuli used in the simulation at a wavelength of 0.69 cm, 1.25 cm, 2.07 cm and 3.557 cm.

6.4.2.4 Scattering phase function

As described above, for the scattering and extinction cross-sections of individual ring particles, which vary with particle size and dielectric constant, we use either Mie or layered Mie theory. When the ring particle size parameter $x = 2\pi a/\lambda$, which is the ratio of particle circumference to wavelength λ, is more than an upper bound of $x \sim 10$ (Cuzzi and Pollack, 1978), a Mie phase function, which is derived from spherical particles, is inadequate to describe each single scattering, and non-sphericity effects (see Sec. 3.7.1) start to become important. In Saturn's B and A rings, particles are mostly larger than 30 cm and thus the size parameter for these particles is $\gtrsim 85$ at a wavelength of 2.2 cm (U band) and even larger at higher frequencies. As a result, the phase function deviates from being simply Mie scattering. Although the C ring and Cassini division also

contain some large particles, previous Cassini and VLA (Dunn et al 2002) observations have shown that a Mie scattering phase function is a good approximation at 2.2cm due to the large power law index *q*. Thus for our simulations of the C ring and Cassini Division, we initially characterize the ring particles there with a pure Mie phase function. At higher frequencies though, as the size parameter increases, the nonsphericity effect might become important. Under these circumstances, we employ a phase function correction using a semi-empirical phase function for large particles (see Sec. 6.5.1). This semi-empirical phase function was originally proposed by Pollack and Cuzzi (1980) accounting for the scattering properties of large nonspherical particles at far field. However, this semi-empirical phase function alone cannot deal with the scattering behavior within the B ring and A ring wakes due to the larger number density found there leading to the close packing of ring particles that can also cause the phase function to be more isotropic (see Sec. 3.7.2). Furthermore, taking into account the semi-empirical phase function in the near field is computationally expensive.

To that end, we continue using the hybrid phase function that is a linear combination of Mie and isotropic scattering phase functions for the B and A ring particles (see Sec. 3.6, Eqn (3.14)). As shown in Eqn. (3.14), f_{iso} is the fraction of isotropic scattering, and we consider f_{iso} for the B and A ring particles as a variable to be determined in our analyses to best fit the observed scattering profile. This phase function has been shown to be a good approximation for the A and B ring particles' scattering properties in the Cassini data.

With the ring particle properties within each piece of the ring in hand, we simulate the multiple-scattering process of the incident reduced Saturn radiation by ring particles for the scattering component T_{scat}, intrinsic thermal emission from the ring plane T_{th} and directly transmitted light

T_{dir} (which only exists for the rings across the disk of the planet) as a function of ring radial distance r and azimuth. We then map these onto a grid with coordinates north and west of Saturn as viewed from Earth, using Saturn's rotational axis to define the northern direction. Taking into account Saturn's disk brightness distribution and the geometry of the observation in order to combine everything into a single map as viewed from Earth, we finally generate a synthetic map of the brightness of Saturn and its rings as viewed from Earth. We convolve these maps with the observation beam at each frequency (see Table. 6.2) and the final map is now ready to be compared with the calibrated observation map.

6.5 Results

To better compare the simulations with the observations, we divided the C ring (B ring) into 18 (13) ring annuli (the same radius binning we used when analyzing Cassini data, for easier comparison) with a width of ~1,000 km (2,000 km). In the X, U and Q bands, within each ring annulus, we further divided the pixels into 45 azimuthal bins (from -180° to 180°) with each bin having a width of 8°. In the K band, as we have mentioned before, we combined data on the west and east side of the rings and divided each ring annulus into 30 azimuthal bins (from 0° to 180°) with each bin having a width of 6°. We then average the observed/simulated brightness in all pixels within each azimuthal bin in each ring annulus and calculate the corresponding uncertainty in observed brightness in each bin with:

$$\sigma = \sqrt{\sigma_{obs}^2 + \left(\overline{T}_{obs} \cdot \eta_{flux}\right)^2} \quad . \tag{6.2}$$

where σ_{obs} is the standard deviation of the observed brightness temperature for all the pixels

within the bin, which reflects the errors brought in through phase calibration, imperfect cleaning process and initial visibility sampling. $\bar{T}_{obs}$ is the averaged observed brightness of all the pixels within the bin, and η_{flux} is the NRAO reported uncertainty in flux measurements. For all bands, $\eta_{flux} = 2\%$, with the exception of Q band where $\eta_{flux} = 3\%$. The uncertainties in the VLA flux density measurements were determined from the scatter in the individual observations of each source, which accounts for the potential systematic error. Due to the low resolution in both the S and C band, we are not able to resolve the C ring in those wavelengths. On the other hand, we investigate the frequency-dependence of the non-icy material dielectric constant in the B ring and compare it with the C ring results in order to determine whether the large non-icy material fraction in the C ring is mostly intramixed within the ring particles as powder, or buried inside the ring particles as large chunks. Therefore, we focus on the X, U, K and Q band observations in this work.

6.5.1 C Ring

6.5.1.1 Lower frequencies (U and X Band)

For the C ring brightness simulation, we first tried to verify our previously derived results of the high ring particle porosity f_p = 75%, the radially varying volume fraction of silicate in the "intramixing" model (see Sec. 4.1.2, Fig. 4.6) and the core-mantle model we obtained using Cassini passive radiometry data at 2.2cm. We investigated the observations in the X band and U band. In **Figure 6.5** we choose three ring annuli each with a width of ~1000 km and plot the simulated/observed brightness temperature with respect to azimuthal angle. Due to the C ring's low optical depth, the brightness temperature of the rings occulting Saturn is much brighter than

that on the ring ansae. Therefore, we plot the brightness temperature of the occulting rings and ring ansae on two different scales. The brightness temperatures on the ring ansae (larger absolute value of azimuthal angle located on the left and right portions in each panel) are determined from the y-axis scale on the left, while the brightness temperature of the occulting rings (near-zero azimuthal angles located in the middle part in each panel) are determined from the y-axis scale on the right. The observations are plotted in black crosses and the error bars are shown with the black vertical lines. Four different simulation results are also shown for solid pure water ice (blue), 75% porous pure water ice (purple), the fraction of non-icy material derived from the Cassini 2.2 cm observations (see Fig. 4.6) which is intramixed within the 75% porous ring particles (red), and the core-mantle model as described in Sec 3.2.3 (green). On the left column in Fig. 6.5, we show the results at X band spectrum window set 1 (SPWS1) at 3.54 cm, which is the largest wavelength that we are able to resolve the C ring at. On the right column, we show results at U band spectrum window set 3 (SPWS3) at 2.07 cm, which is very close to the Cassini observation wavelength. The results for U band SPWS2 show similar results as SPWS3, but U band SPWS2 is not as well calibrated that it has larger uncertainties in the C ring and shows asymmetry in the west and east C ring ansa which is a calibration artifact. We first look at the portion of the rings being occulting by Saturn in each panel (azimuthal angles that lie approximately between -40^{o} and 40^{o}). The error bars overlying the simulation results there are due to the uncertainty in the Saturn radiation. In all simulation cases, we applied the Saturn radiation derived from our observations as well as the one calculated from the saturated Saturn atmosphere model. We averaged the simulation results from these two cases and indicate the range as given by the error bar. The observed Saturn radiation tends to be higher than the model, and the simulated brightness temperature of the occulting C ring is especially sensitive to the value of the Saturn radiation. For a C ring annulus with optical depth

0.1 and ring inclination angle 24° (which is the same as the value during our observations), a 5 K difference in the Saturn radiation will result in an almost 4 K change in the brightness temperature. As shown in all ring annuli in both X and U bands, the simulation results when assuming zero porosity is much lower than observed while the results assuming 75% porosity in the intramixed model, or 75% porous background material in the core-mantle model fits the observations within the error. An important point to notice here is that adding the required amount of non-icy material doesn't change the simulated brightness of the portion of the rings that are being occulted significantly. These results thus justify the high porosity of the C ring particles derived from the Cassini observations (see Sec. 4.1.1).

The simulated brightness variation on the ansa is negligible for the range of Saturn radiation we used and thus is not shown in the figure for clearer comparison. As for the ring ansae at the X band (left column) and inner (upper right panel) and outer C ring (lower right panel) at U band, solid ring particles that are devoid of any non-icy material predict brightness temperatures larger than observed, which further justifies the necessity for introducing particle porosity. By adding porosity, we see that, at inner and outer C ring in both X and U band (first and second rows), the brightness temperature predicted by purely icy, 75% porous particles is much lower than observed; however, after adding the amount of non-icy material derived from Cassini radiometry data, or assuming the core-mantle model, the simulation fits the observations very well in all panels, though we do notice a discrepancy at around absolute azimuthal angles of 40° - 60° where the simulated brightness is higher than observed. The discrepancy is more obvious in the U band than X band. We discuss this discrepancy in more detail in Sec. 4.1.3. In spite of this discrepancy, both the simulated brightness (addition of scattering component and intrinsic thermal emission) using

the intramixed model and the core-mantle model fit the observations in the X band SPWS1 at ~3.54 cm and U band SPWS3 at ~2.07 cm. The observations at other spectral window sets in the X and U band show similar results that justify the choice of 75% porosity, the radially varying non-icy material fraction in the intramixed model and the core mantle model.

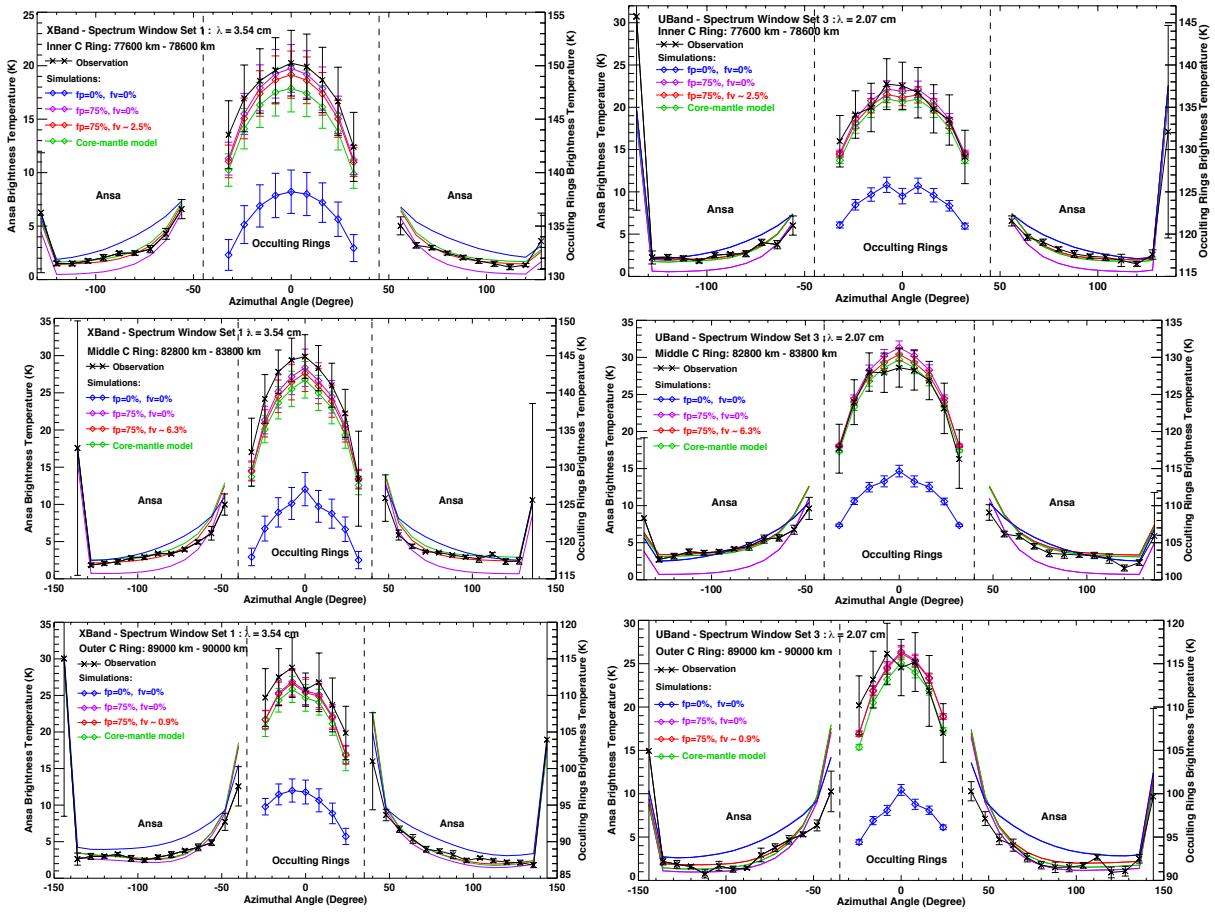

Figure 6.5: Scattering profile (brightness temperature vs. azimuthal angle) in the inner (first row), middle (second row) and outer (bottom row) C ring for X band spectrum window set 1 (left column) and U band spectrum window set 3 (right column). The observations are plotted with black crosses and the black vertical lines indicate the observational uncertainty in each bin. Four different simulation results are also shown for solid pure water ice (blue), 75% porous pure water ice (purple), the fraction of non-icy material derived from the Cassini 2.2 cm observations (see Fig. 4.6) which is intramixed within the 75% porous ring particles (red), and the core-mantle model (green). The brightness temperatures on the ring ansae (on the left and right portions in each panel)

are determined from the y-axis scale on the left, while the brightness temperature of the occulting rings (in the middle part in each panel) are determined from the y-axis scale on the right.

6.5.1.2 Higher frequencies (K and Q Band)

We performed the same simulations for the K band observations where, due to the large uncertainties, we combined the observations on the east and west sides of the C ring to increase the signal-to-noise ratio, since the C ring is azimuthally uniform. In **Figure 6.6** left column (K band SPWS1) and right column (K band SPWS2), the temperatures for the portion of the rings that are occulted are indicated on the y-axis scale on the left side in each panel, while the ring ansa temperatures are indicated on the y-axis scale on the right. As for the occultation data, similar to what we found in the X and U band data, the simulated brightness temperatures when using solid pure water ice particles are much lower than observed, while either after adding 75% porosity to the ring particles or introducing the core mantle model (75% porous background material), the observations are fairly well matched by the simulations. However, regarding the ring ansa, when using the intramixed model and assuming 75% porous particles that contain the same amount of non-icy material derived from the Cassini observations (Fig. 4.6) and furthermore assuming that the dielectric constant of the non-icy material has the same value as that in the U band, the simulated brightness temperature is higher than observed (see red solid lines for the ring ansa). This discrepancy becomes more and more obvious as the wavelengths become smaller and smaller (from the K band SPWS1 to K band SPWS2 and to the Q band). In **Figure 6.7** we show the same simulations for the Q band at the inner, middle and outer C ring. Note though that we only use the observations on the east side for the Q band (on the left in each panel) due to the large RFI crossing the west side. That is to say, if the intramixed model is the case, there must be some frequency-dependent factor that we have neglected.

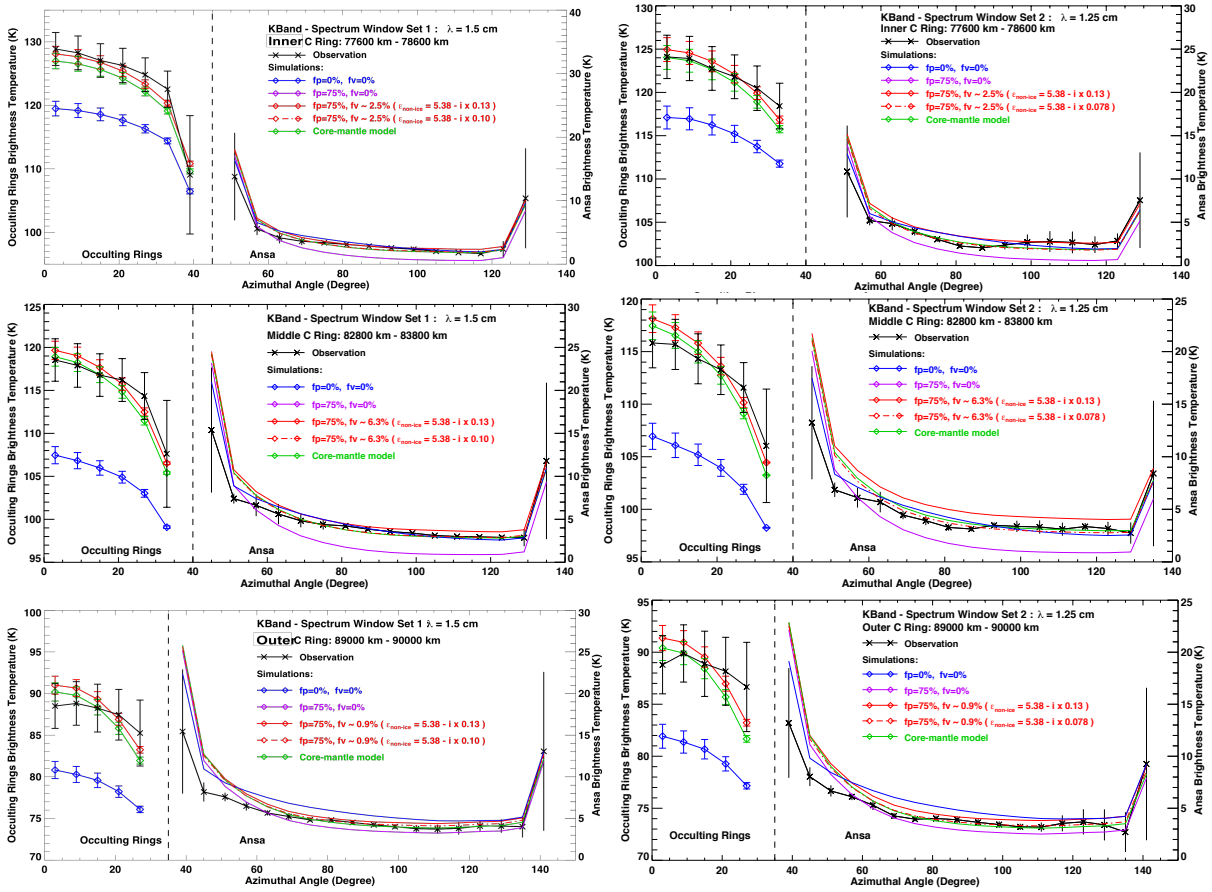

Figure 6.6: Scattering profile (brightness temperature vs. azimuthal angle) in the inner (first row), middle (second row) and outer (bottom row) C ring at K band SPWS1 ($\lambda = 1.5\ cm$, left column) and SPWS2 ($\lambda = 1.25\ cm$, right column). The observations are plotted with black crosses and the black vertical lines indicate the observational uncertainty in each bin. Five different simulation results are also shown for solid pure water ice (blue), 75% porous pure water ice (purple only in ansa data), the fraction of non-icy material derived from the Cassini 2.2 cm observations (see Fig. 4.6) which is intramixed within the 75% porous ring particles (red), and the core-mantle model (green). The simulated brightness using the reduced $\varepsilon_i^{non-ice}(\lambda = 1.5) = 75\% \cdot \varepsilon_i^{non-ice}(\lambda = 2.2)$ and $\varepsilon_i^{non-ice}(\lambda = 1.25) = 60\% \cdot \varepsilon_i^{non-ice}(\lambda = 2.2)$ are shown by the red dashed line.

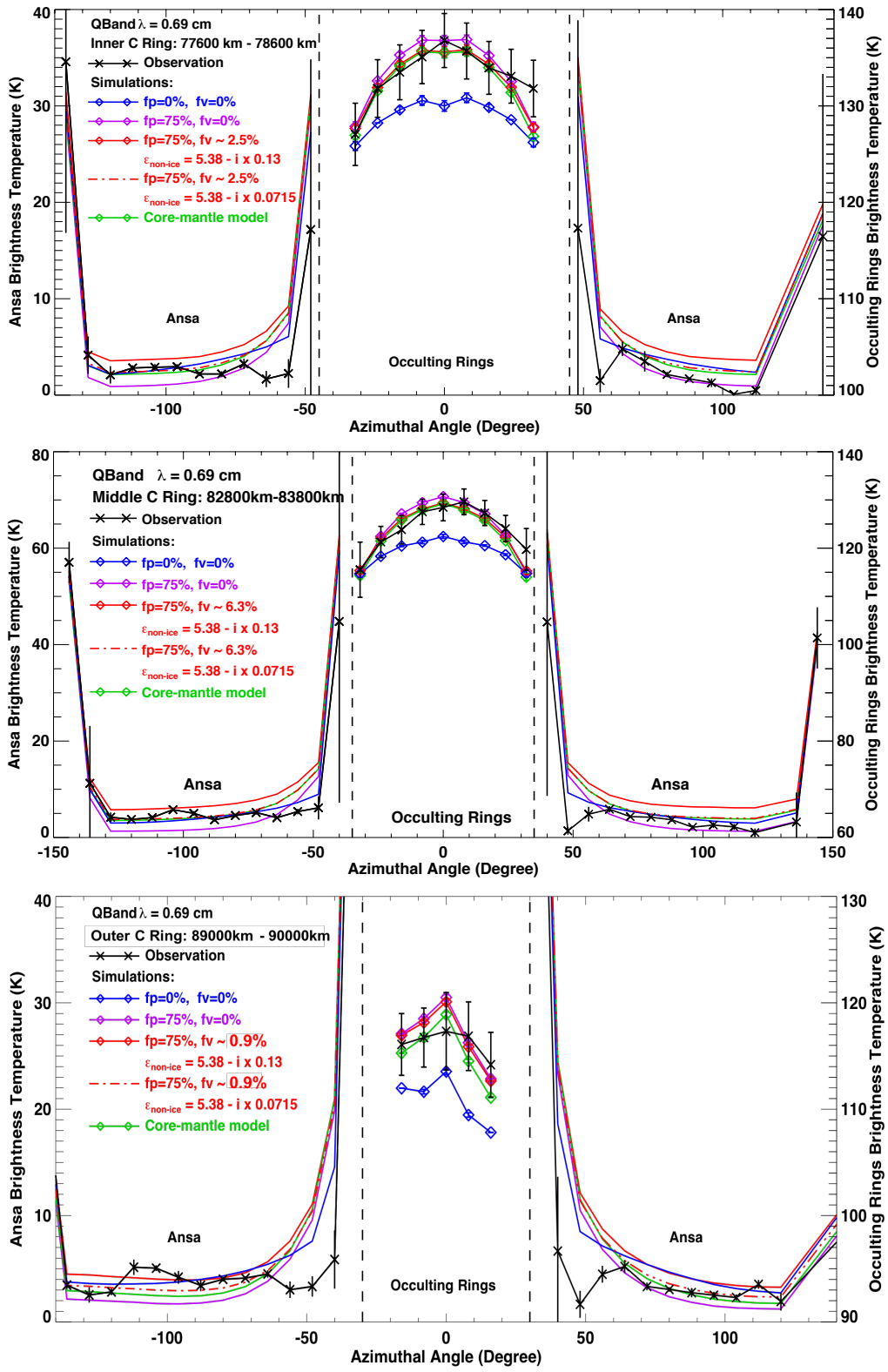

Figure 6.7: Scattering profile (brightness temperature vs. azimuthal angle) in the inner (upper panel), middle (middle panel) and outer (lower panel) C ring for the Q band ($\lambda = 0.69\ cm$). Note

that we only use the ansa observations on the east side (left and middle portion of each panel). The observations are plotted with black crosses and the black vertical lines indicate the observational uncertainty in each bin. Five different simulation results are also shown for solid pure water ice (blue, only in occultation data), 75% porous pure water ice (purple only in ansa data), the fraction of non-icy material derived from the Cassini 2.2 cm observations (see Fig. 4.6) which is intramixed within the 75% porous ring particles (red), and the core-mantle model (green). The simulated brightness using the reduced $\varepsilon_i^{non-ice}(\lambda = 0.69) = 55\% \cdot \varepsilon_i^{non-ice}(\lambda = 2.2)$ is shown by the red dashed line.

The simulated brightness temperature on the ansa is composed of a scattering component and intrinsic thermal emission. The amount of the scattering component is mainly determined by the particle size distribution, local optical depth and the real part of the effective dielectric constant of the ring particle. We have already taken into account the frequency-dependence of the optical depth using Eq. (3.5). On the other hand, the real part of the effective dielectric constant depends mostly on the dielectric constant of water ice and the particle porosity. The small amount of non-icy material doesn't affect the real part of the dielectric constant significantly. We have applied the water ice dielectric constant value at the appropriate frequency using Eq. (3.2). The particle porosity should not have any frequency dependence and has already been shown to be 75% in order to match the near-zero azimuth occultation observation. That is to say, in the intramixed model, there aren't any other frequency-dependent factors that would change the amount of the scattering component. Therefore, the only possibility is that the intrinsic thermal emission has been over estimated at small wavelengths. Considering that the intrinsic thermal emission $T_{thermal} \sim \alpha_{abs} \cdot \tau \cdot T_{physical}$, where α_{abs} is the absorption rate which is approximately proportional to $f_v \cdot \varepsilon_i^{non-ice}$, since f_v shouldn't have any frequency-dependence, the only possible reason for this discrepancy is that the imaginary part of the non-icy material dielectric

constant $\varepsilon_i^{non-ice}$ drops at smaller wavelengths. We find that if $\varepsilon_i^{non-ice}(\lambda = 1.5\ cm) = 75\% \cdot \varepsilon_i^{non-ice}(\lambda = 2.2\ cm)$, $\varepsilon_i^{non-ice}(\lambda = 1.25\ cm) = 60\% \cdot \varepsilon_i^{non-ice}(\lambda = 2.2\ cm)$ and $\varepsilon_i^{non-ice}(\lambda = 0.69\ cm) = 55\% \cdot \varepsilon_i^{non-ice}(\lambda = 2.2\ cm)$, the simulated brightness matches the observation well at most azimuthal angles with the exception of around 40° to 60° (the fit of the simulated brightness using the reduced $\varepsilon_i^{non-ice}$ is indicated by the red dashed lines in Figs. 6.6-6.7). On the other hand, we also note that the core-mantle model naturally matches the observations at both high and low frequencies (again with the exception of around 40° to 60°). This is because in the core-mantle model, most of the non-icy material is buried inside the ring particle core. As the wavelengths become smaller, the observation penetration also becomes shallower and therefore less intrinsic thermal emission escapes the particle and arrives the observer.

6.5.1.3 Phase function correction – "Intramixed" model

As shown in Sec. 6.5.1.1 and Sec. 6.5.1.2, our simulated model fits the observations at most azimuthal angles, but as we pointed out the simulation predicts higher brightness than observed at azimuths with absolute value ~ 40° - 60°. The observed scattering profile at these angles seems to be flatter and doesn't increase towards smaller azimuthal angles as quickly as predicted by a Mie phase function which we have generally applied when simulating the scattering process for the C ring particles. According to Pollack and Cuzzi (1980), the scattering phase function of particles with size parameters smaller than x_0 (x_0 varies with the roughness of a particle) can be approximated with a pure Mie phase function, while larger particles begin to scatter light more isotropically. Although most of the C ring particles are smaller than, or comparable to the microwave wavelengths, especially in the U and X band, there are some larger particles whose scattering phase function cannot be adequately described by a Mie phase function. We also notice

that the discrepancy between the simulations and the observations at absolute azimuths between ~40° - 60° is more obvious at higher frequencies (K and Q band). Considering that due to the decrease in wavelength, there should be even more particles with size parameters larger than x_0 in the K and Q band, this discrepancy at absolute azimuths of ~40° - 60° is even more likely to be caused by the scattering properties of large particles in the C ring.

With this in mind, we first update our simulated intramixture model by using different phase functions for particles of different sizes. For particles with size parameters smaller than x_0, we use a Mie phase function, while for particles with size parameters larger than x_0, we apply a semi-empirical phase function for non-spherical particles developed by Pollack and Cuzzi (1980; also see Sec. 3.7.2). As one can imagine, by introducing a more isotropic phase function for large particles, the simulated brightness temperature at near-zero azimuthal angles where the rings occult Saturn would become smaller, so to compensate for that decrease we need to increase porosity values to be higher than 75%. To obtain a best-fit model for the C ring particles at both low and high frequencies, we choose U band as the low frequency and K band as the high frequency. The choice of U band as the low frequency example provides us with a way to compare the results with our previous Cassini radiometry observations, while using K band as the high frequency example allows us to avoid the large uncertainties in the Q band observations. We first scanned all possible models in the U band and derived the required non-icy material fraction for each new model. We then repeated this in the K band, applying the non-icy material fraction derived in the U band. Finally, we computed a reduced χ^2_{red} goodness fit in both the U and K bands in order to find the best-fit model.

As shown in Sec. 3.7.1, the semi-empirical phase function has three free parameters: M, x_0 and

f_p. *M*, as described in Sec. 3.7.1, determines how isotropic the semi-empirical phase function is and depends on the particle shape and roughness. We test two *M* value cases (*M=1.5* and *M=4*), which are the maximum and minimum derived in lab for nonspherical particles (Pollack and Cuzzi, 1980). The parameter x_0 is the critical size parameter, determining where the particle nonsphericity starts to cause the particle scattering phase function to deviate from a Mie phase function. According to Pollack and Cuzzi (1980), x_0 also depends on the particle shape and roughness, varying from 2 to 10 for cubes, octahedrals, convex-concave particles and flakes. In this section, we vary x_0 among the set of values 5, 10, 20, 30, 50, 100 and 150. The parameter f_p is the ring particle porosity, which we vary over four values (70%, 75%, 80% and 90%). The results of the reduced χ^2_{red} goodness fits in the U and K band are shown in **Figure 6.8**. The green horizontal line shows the χ^2_{red} value when applying a Mie phase function to all C ring particles, assuming 75% porosity and the derived non-icy material fraction from the Cassini observations. When assuming *M* = 1.5, we find that the minimum χ^2_{red} is reached when $f_p = 80\%$ and $x_0 = 150\ cm$ (case 1) for the U band data, and when $f_p = 80\%$ and $x_0 = 100\ cm$ (case 2) for the K band data. The fitting of case 1 in the K band and the fitting of case 2 in the U band are also close to the minimum χ^2_{red} value, so the difference in between the fitting of these cases is not very significant. Therefore, we consider both case 1 and case 2 as possible models for *M* = 1.5. On the other hand, when assuming *M* = 4.0, the minimum χ^2_{red} is reached when $f_p = 90\%$ and $x_0 = 100\ cm$ for the U band data, and when $f_p = 90\%$ and $x_0 = 50\ cm$ for the K band data. We note, however, that the fitting of $f_p = 90\%$ and $x_0 = 100\ cm$ in the K band is much worse and predicts a brightness temperature that is much too high near zero azimuth where the rings occult Saturn. Therefore, we consider $f_p = 90\%$ and $x_0 = 50\ cm$ (case 3) as the only possible model for *M* = 4.0. In **Table 6.3**, we list all three possible cases. As we mentioned previously, x_0 is in

the range of 2 to 10 based on lab results. However, when applying such small x_0 values, the integrated scattering phase function becomes so flat that the simulated brightness at near-zero azimuthal angles is much lower than observed, even for the 90% porosity case. We cannot adequately explain at this time why the best-fit x_0 value is much higher than the lab results, though it may be an indication that the C ring particles are not very nonspherical.

Table 6.3: Three best-fit cases when introducing semi-empirical phase function for large particles in the C ring.

	M	f_p	x_0
Case 1	**1.5**	**80%**	**150**
Case 2	**1.5**	**80%**	**100**
Case 3	**4**	**90%**	**50**

In **Figure 6.9** and **Figure 6.10**, we compare the new simulated scattering profile with the observations in the U and K bands. The fitting for Case 1 and Case 2 is very similar as we indicated above, so we only show the fits for Case 2 and Case 3. In the U band (Fig. 6.9), the simulated brightness for both Case 2 (left column) and Case 3 (right column) effectively matches the occultation data at near-zero azimuthal angles where the rings occult Saturn. As for the ring ansae, in the inner C ring Case 2 fits the observations better while Case 3 predicts too low a brightness around 50 to 60 degree on the west ansa (Fig. 6.9, upper panel). Case 3 matches the observations better especially around 40 to 60 degree in both the middle (Fig. 6.9, middle panel) and outer (Fig. 6.9, lower panel) C ring, while Case 2 still matches the observations within the error bars. However, in the outer C ring, the simulated brightness around 80 to 100 degrees is higher than observed in Case 3 which may be due to the averaged phase function in Case 3 being too flat.

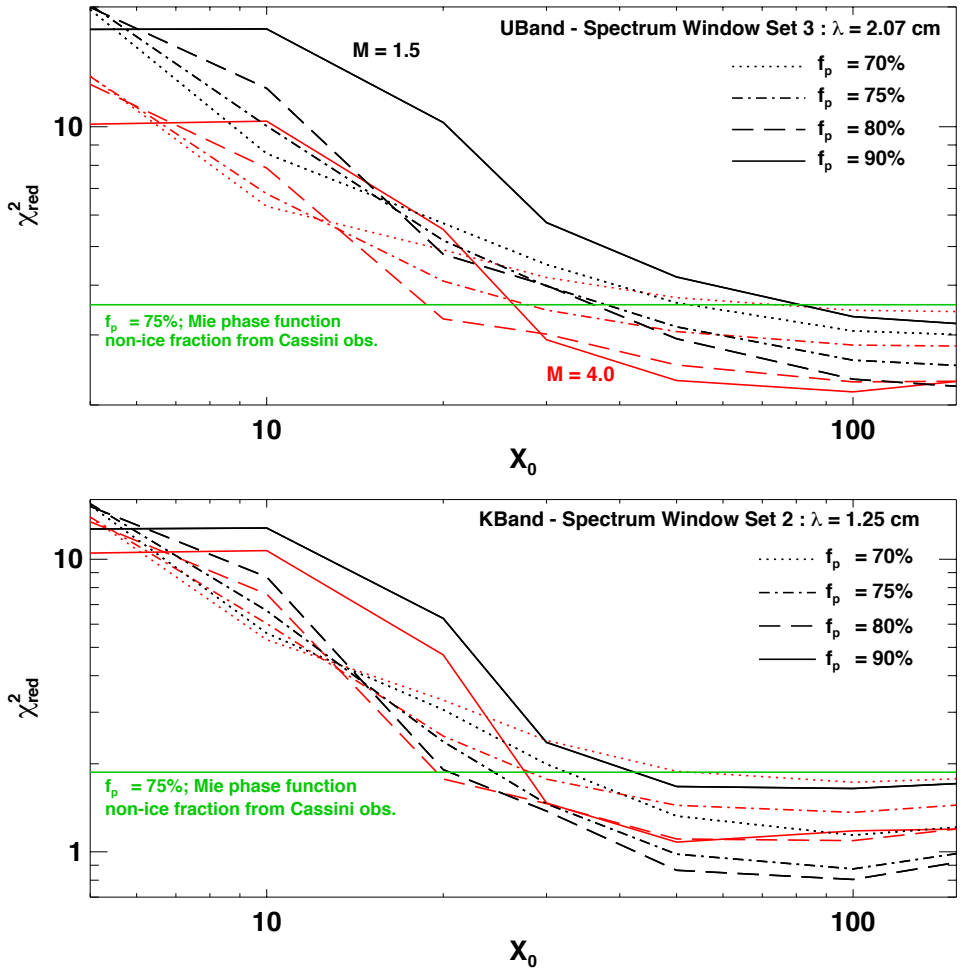

Figure 6.8: The value of the reduced χ^2_{red} for all possible cases we scanned in the U band SPWS3 (upper panel) and K band SPWS2 (lower panel). In the upper panel the reduced χ^2_{red} is the value with the best-fit non-icy material fraction for each case derived using the U band data. In the lower panel, the reduced χ^2_{red} is the value when applying the best-fit non-icy material fraction for each case, derived using the U band data, to the K band simulation. Different line types indicate different ring particle porosity values as indicated. Red curves show the results with M = 4.0 while black curves are the results when M = 1.5. The green horizontal line shows the χ^2_{red} value when applying a Mie phase function to all C ring particles and assuming a 75% porosity for the ring particles that contain the non-icy material fraction derived from the Cassini observations.

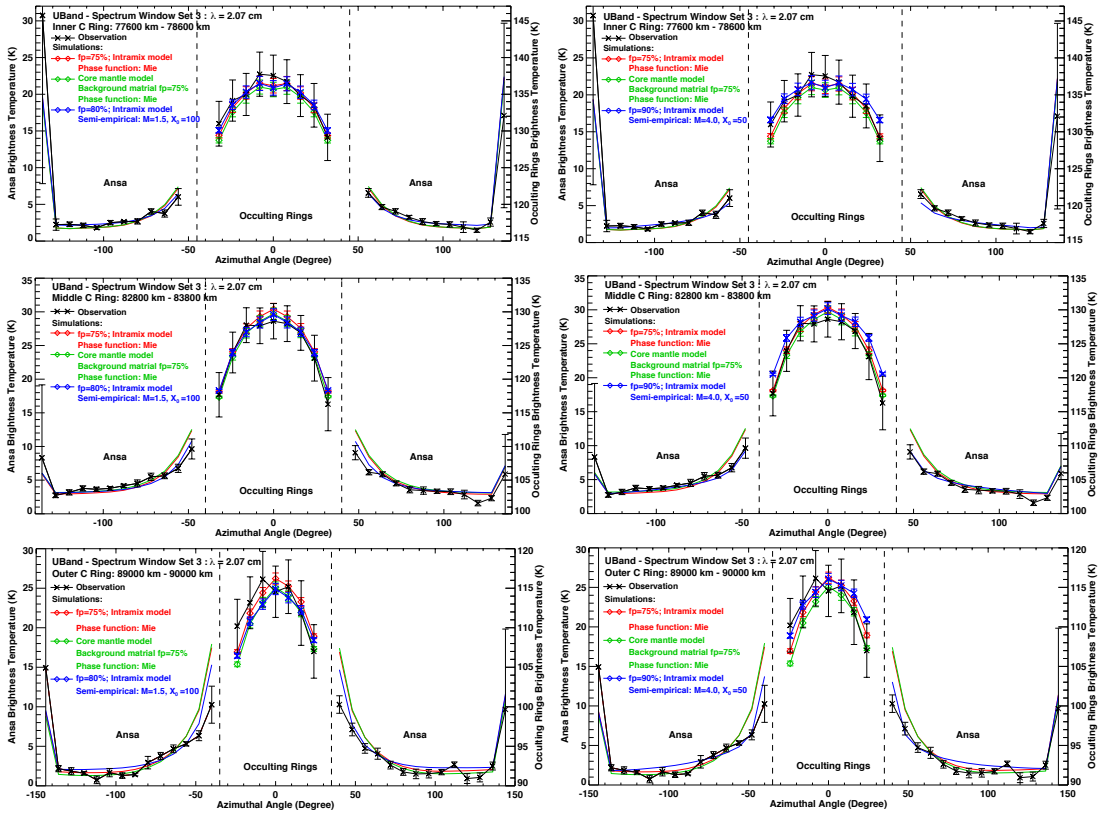

Figure 6.9: Scattering profile (brightness temperature vs. azimuthal angle) in the inner (upper panel), middle (middle panel) and outer (lower panel) C ring for U band spectrum window set 3. The observations are plotted with black crosses and the black vertical lines indicate the observational uncertainty in each bin. The left column shows the results when assuming $M = 1.5$, $f_p = 80\%$, and $x_0 = 100$cm (Case 2). The right column shows the results when assuming $M = 4.0$, $f_p = 90\%$, and $x_0 = 50$cm (Case 3). In each panel, three different simulation results are shown for: the fraction of non-icy material derived from the Cassini 2.2 cm observations (see Fig. 4.6) which is intramixed within the 75% porous ring particles, and particle scattering is characterized by a Mie phase function (red); the core-mantle model derived from Cassini observations with particles scattering using a Mie phase function (green); and the new best-fit model where small particles scattering is characterized by a Mie phase function and large particle scattering by a semi-empirical phase function (blue).

We further investigate the simulated scatting profile for the K band spectrum window set 2 in **Figure 6.10**. For the same reason as mentioned in Sec. 4.1.2, if we assume that the non-icy material has the same dielectric constant in the U and K bands and apply the amount of non-icy material fraction derived from the U band data to the K band in the intramixed model, the simulated intrinsic thermal emission becomes too high for the observations in the K band. Therefore, when we perform the χ^2 fit in the K band, we allow the imaginary part of the non-icy material dielectric constant to vary. We find that $\varepsilon_i^{non-ice}$ in the K band (at 1.25 cm) becomes 42% (Case 1), 35% (Case 2) and 23% (Case 3) of its value in the U band around 2.07 cm. As shown in Fig. 6.10, both Case 2 and Case 3 fit the observations well, especially at azimuthal angles of 40 to 60 degrees, but it is difficult to discern which case fits the observations better. **In Figure 6.11**, we summarize the drop in the imaginary part of the non-icy material fraction with decreasing wavelength when assuming intramixed model for all three cases discussed here using the semi-empirical phase function and the original case when applying Mie scattering phase function to all C ring particles and assuming 75% porosity in the particles. This wavelength-dependent dielectric variation may be able to serve as the non-icy material microwave spectrum curve and help us determine its composition.

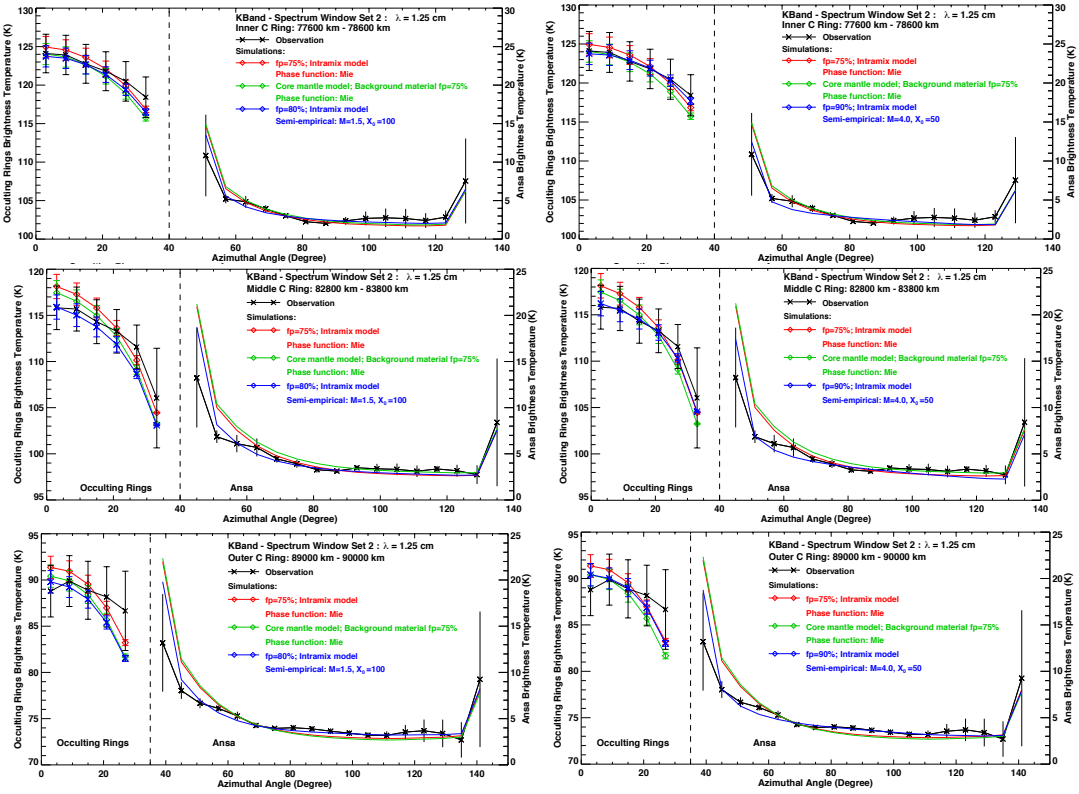

Figure 6.10: Scattering profile (brightness temperature vs. azimuthal angle) in the inner (upper panel), middle (middle panel) and outer (lower panel) C ring for K band spectrum window set 2 (at 1.25 cm). The observations are plotted with black crosses and the black vertical lines indicate the observational uncertainty in each bin. The left column shows the results when assuming M = 1.5, f_p = 80%, and x_0=100 cm (Case 2). The right column shows the results when assuming M = 4.0, f_p = 90%, and x_0=50 cm (Case 3). In each panel, three different simulation results are shown for: the fraction of non-icy material derived from the Cassini 2.2 cm observations (see Fig. 4.6) which is intramixed within the 75% porous ring particles, and particle scattering is characterized by a Mie phase function (red); the core-mantle model derived from Cassini observations with particles scattering using a Mie phase function (green); and the new best-fit model where small particles scattering is characterized by a Mie phase function and large particle scattering by a semi-empirical phase function (blue). For the red and blue curves, we have already taken into account the decrease in the imaginary part of the non-icy material dielectric constant.

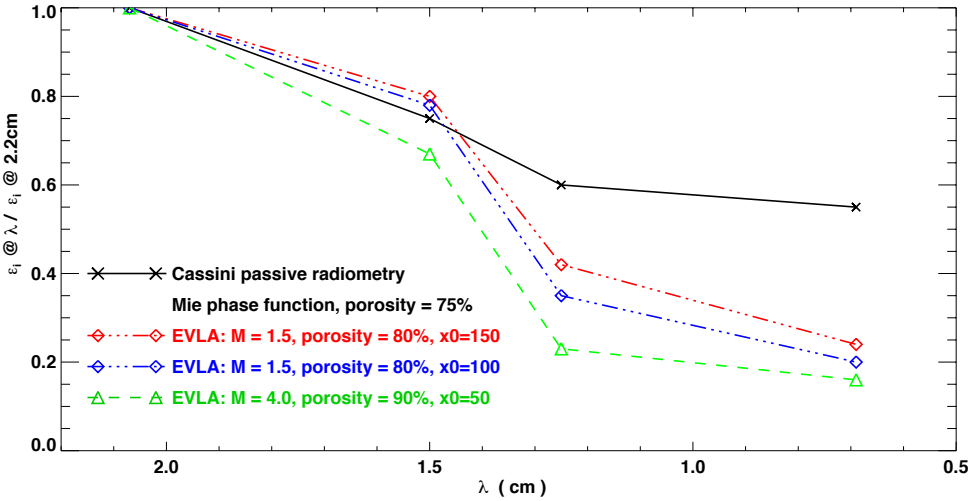

Figure 6.11: The frequency-dependence of the imaginary part of the non-icy material fraction with decreasing wavelengths for four different cases in the intramixed model: 1) 75% particle porosity, Mie phase function (black crosses); 2) case 1: M=1.5, 80% particle porosity, X_0=150 (red diamonds); 3) case 2: M=1.5, 80% particle porosity, X_0=100 (blue diamonds); 3) case 1: M=4.0, 90% particle porosity, X_0=50 (green triangles).

In **Figure 6.12** we also plot the derived non-icy material fraction in the U band for all three possible cases and compare them with the non-icy material fraction profile we derived from the Cassini radiometry observations in the U band. It can be seen that the non-icy material fraction peak in the middle C ring derived from EVLA observations is shifted to the left by ~2,000 km as compared to the one we previously obtained from the Cassini radiometry data (see Sec. 4.1.2). Although the profiles in case 1 and case 2 are still within the error bars of the Cassini results, the profile in case 3 is much higher around a radius of 79,000km – 81,000km. To investigate this difference in the profiles, we applied the non-icy material fraction derived from EVLA observations to our Cassini high resolution observations of the rings in **Figure 6.13** where we compare the simulated and observed reduced (2.7K lower than the rings brightness temperature observed by Cassini radiometer) scattering profiles (brightness temperature vs. azimuthal angle) at four radii in the C

ring, and compare the results in these three cases using semi-empirical phase function with our original case derived from Cassini observations (75% porosity; Mie phase function for all C ring particles). We chose four ring radii for which the difference in the non-icy material fractions is the most significant: 78,500 km – 79,000 km (annulus 1, first column), 80,500 km – 81,500 km (annulus 2, second column), 82,500 km – 83,500 km (annulus 3, third column) and 87,500 km – 88,500 km (annulus 4, fourth column). The simulated brightness in Cases 1 and 2 match the observations as well as the original case in annulus 1 and 2, and fit the observation even better in annulus 4. However, the simulated brightness is slightly smaller than the observation in annulus 3 The simulated brightness in Case 3 is lower than the observed brightness near 45 degrees in annulus 1~3, but does fit the observations in annulus 4. As a further comparison, in **Figure 6.14** we also applied the new models to the Cassini low-resolution observations of the rings that occult Saturn and we found all three models fit the observations well.

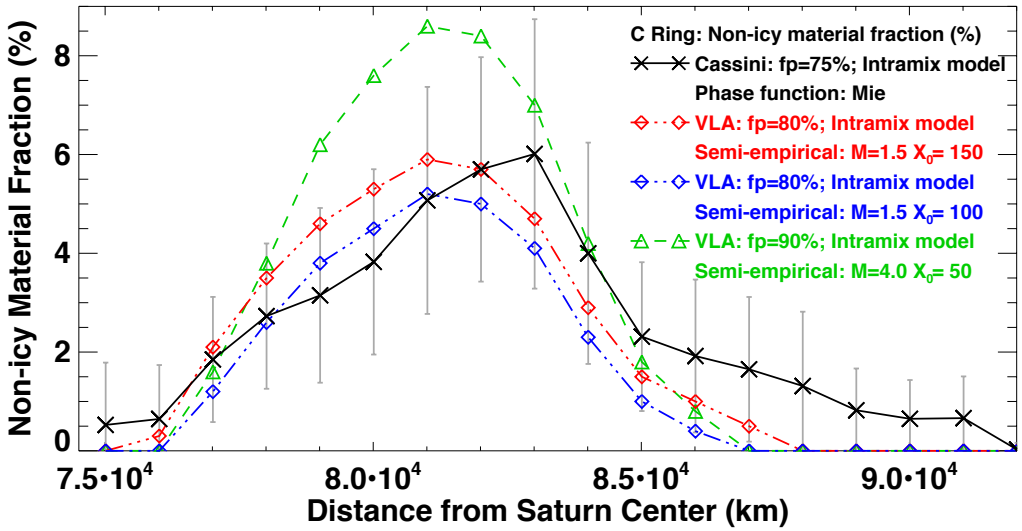

Figure 6.12: The non-icy material fraction derived from the U band VLA observation for all three possible cases compared with the non-icy material fraction profile we derived from the Cassini radiometry (black). The vertical grey lines indicate the error bars of the results derived from the Cassini observations.

Figure 6.13: Comparison of the simulated and observed reduced scattering profiles at three different radii in the C ring. Black crosses: observations. Green crosses: original fitting when using a Mie phase function (75% porous particles and the non-icy material fraction shown in Fig. 6). Red crosses: new fitting including this semi-empirical phase function.

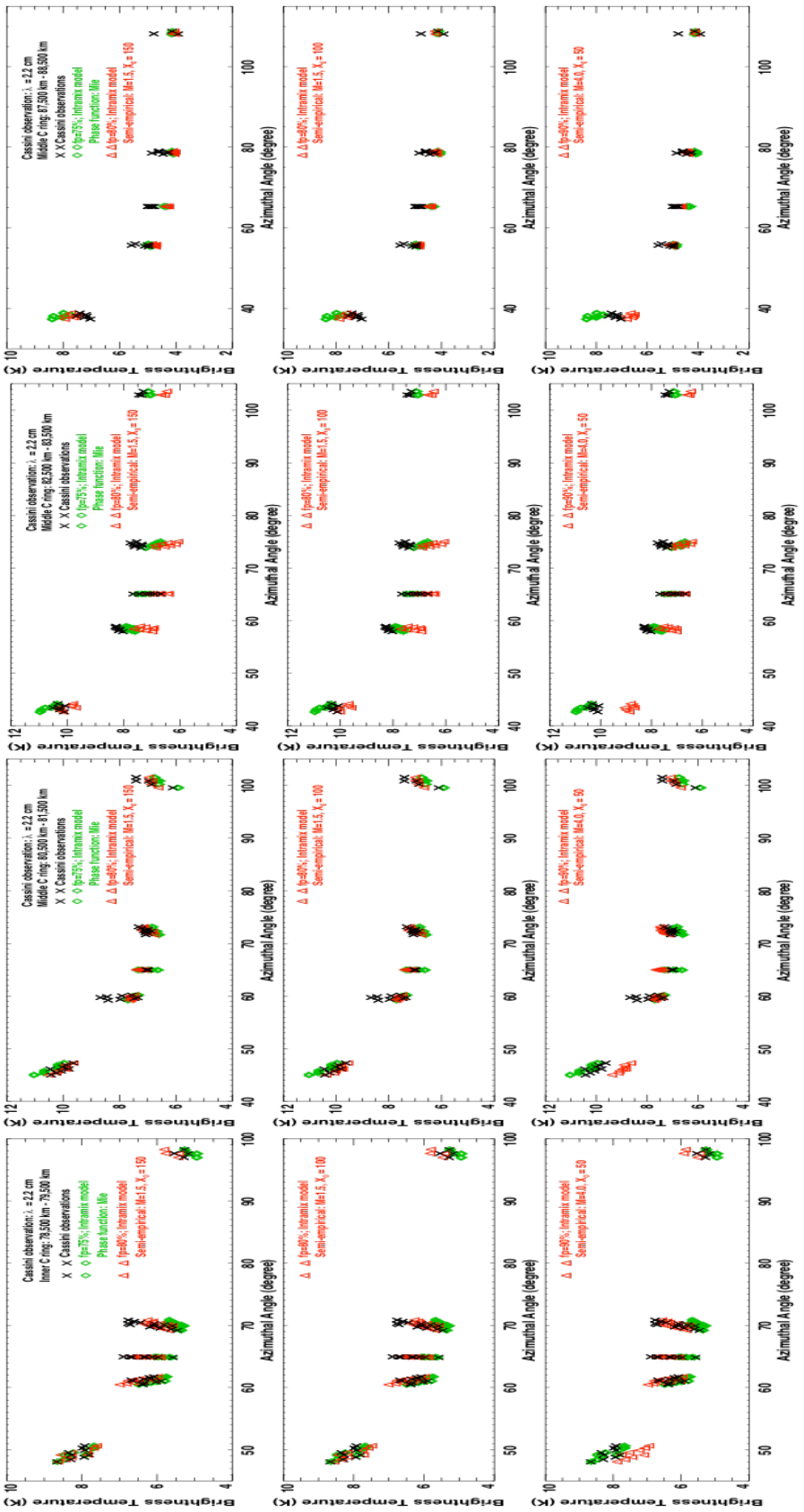
Cassini observation: λ = 2.2 cm
Inner C ring: 79,500 km - 79,500 km
Middle C ring: 80,500 km - 81,500 km
Middle C ring: 82,500 km - 83,500 km
Middle C ring: 87,500 km - 88,500 km
X X Cassini observations
◇ ◇ fp=75%; Intramix model
Phase function: Mie
Δ Δ fp=90%; Intramix model
Semi-empirical: Me=1.5, X_c = 150
Semi-empirical: Me=1.5, X_c = 100
Semi-empirical: Me=4.0, X_c = 50
Brightness Temperature (K)
Azimuthal Angle (degree)

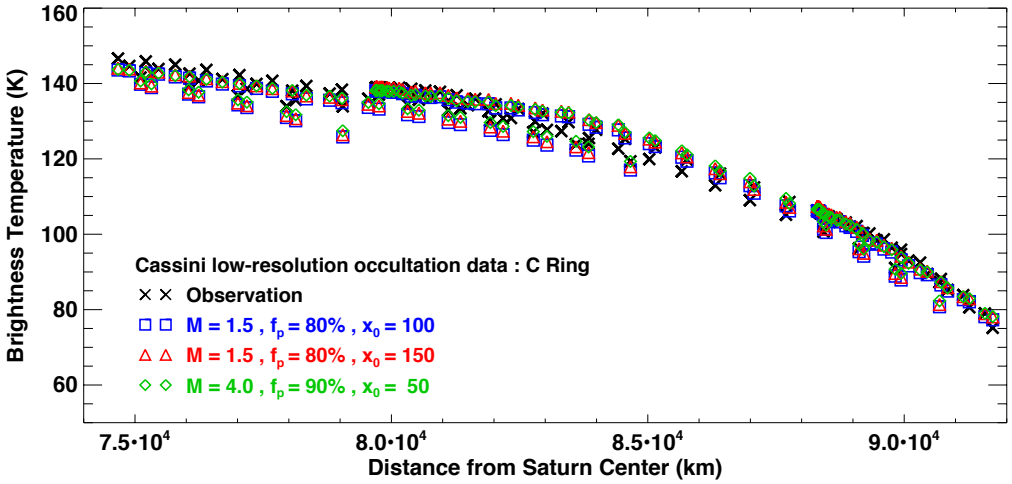

Figure 6.14: Three new models as applied to the Cassini low-resolution observations of the rings that occult Saturn. The observations are indicated by the black crosses. All three models fit the observations well.

6.5.1.4 Phase function correction – core-mantle model

Finally, we apply the new semi-empirical phase function to the core-mantle ring particle model. In these newly updated core-mantle models, the background C ring is primarily water ice with high porosity f_p. As shown in Fig. 6.12, in the inner and outer C ring where particles do not contain a silicate core, nearly zero non-icy material is observed. Therefore, we assume that the background C ring material is pure water ice. In between 75,500 km 88,000 km, the observed non-icy material is assumed to be in the form of silicate cores hidden within ring particles larger than a_{crit}. In this simplified model we have also assumed that the ratio of silicate core radius to particle radius f_r is fixed for all core-containing particles. As we proposed in Sec. 5.2.2, we introduce either a radially varying maximum particle size (case A) or a radially varying percentage of particles larger than a_{crit} that contain a silicate core (case B).

Starting in the U band, we find three sets of core mantle model parameters that generate similar

scattering profiles as the simulation results given in Cases 1, 2 and 3, respectively (see Sec. 6.5.1.3). The simulated scattering profiles are determined by two main factors: 1) the phase function which determines the scattering components; and 2) the absorption rate which determines the intrinsic thermal emission. As we have shown in Sec. 5.2.2, for our original core-mantle model, if only particles larger than 60 cm contain a silicate core, the integrated phase function is similar to that when all particles are composed of the background C ring material. That is to say, the silicate cores have little effect on the scattering phase function since the particle size distribution drops quickly towards large particles and only a small fraction of the particles contain a silicate core. Therefore the integrated scattering phase function depends mostly on the background material porosity and the ring particle nonsphericity (through scattering phase function). Therefore, to bring in the nonsphericity effect of large particles to the core mantle model, we assume that the background material contains ring particles with the same porosity as found in the "intramixed" model and the particles scatter with the same phase function (the scattering for particles smaller than x_0 are characterized by a Mie phase function, while particles larger than x_0 by a semi-empirical phase function with value M) for each case in Sec. 6.5.1.3.

Another important factor is the averaged absorption rate which is approximately proportional to the amount of intrinsic thermal emission. We determine the parameters in the core-mantle model in order to match the simulated thermal emission required in each case. In **Figure 6.15** we first calculate the radially varying averaged absorption rate in each semi-empirical phase function case, under the intramixture model using:

$$\alpha_{abs} = \frac{\int_{a_{min}}^{a_{max}} Q_{abs(a)} \cdot a^{2-q} \cdot da}{\int_{a_{min}}^{a_{max}} Q_{ext(a)} \cdot a^{2-q} \cdot da}, \tag{6.3}$$

where $q=3.15$ is the power law index of the C ring particle size distribution. From Fig. 6.15 we see that the absorption rate is the highest in the middle C ring around 81,500 km. Assuming that at this ring radius the maximum particle size is 4.5 m and 100% of the particles larger than a_{crit} contain a silicate core, we find the appropriate value of a_{crit} and f_r in order to simultaneously match the absorption rate in each case as well the measured opacity (0.022 cm^2/g) as determined by density waves (see **Table 6.4**). We then derive the radially varying maximum particle size (case A) or radially varying percentage of particles larger than a_{crit} that contain a silicate core (case B) in order to match the simulated radially varying thermal emission in each case, the results of which are plotted in **Figure 6.16**.

Table 6.4: Core mantle model parameters for the three best-fit semi-empirical phase function cases.

	Phase Function		**Core-mantle model**				
	M	x_0	f_p	a_{crit}	f_r	a_{abs}	$\kappa = \tau/\sigma$ (cm^2/g)
Case 1	1.5	150	80%	60 cm	0.65	0.0541	0.023
Case 2	1.5	100	80%	85 cm	0.70	0.0504	0.021
Case 3	4.0	50	90%	90 cm	0.65	0.0432	0.028

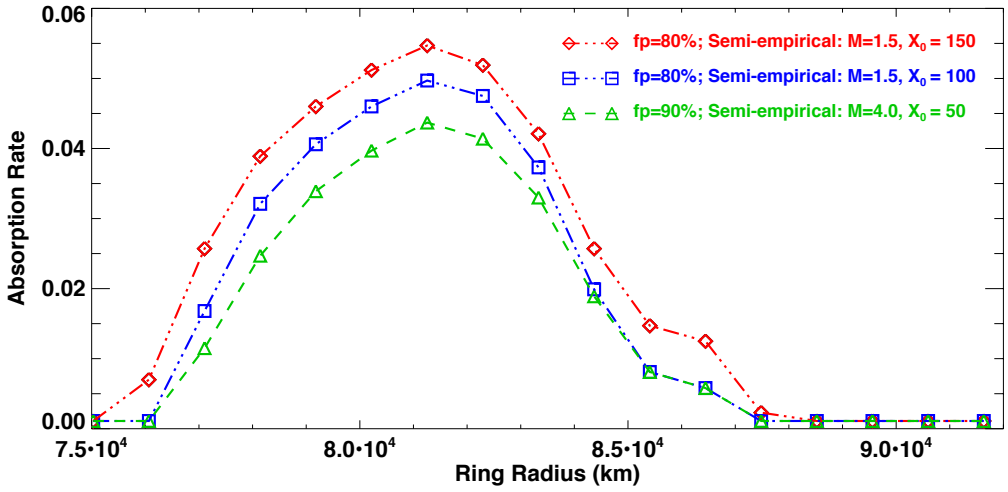

Figure 6.15: Radially varying absorption rate for three intramixture model cases. Case 1: red dash-

dot line/red diamonds; Case 2: blue dash-dot line/blue diamonds; Case 3: green dashed line/green triangles.

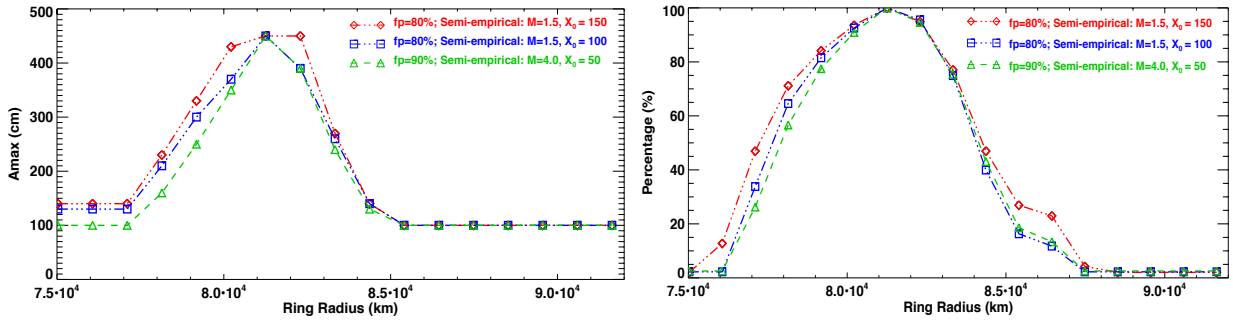

Figure 6.16: Left panel: The radially-varying maximum ring particle size (case A). Right panel: The radially-varying percentage of large ring particles (larger than the critical size a_{crit}) that contain silicate cores necessary to match the absorption rate shown in Fig. 6.15 (case B).

We applied the semi-empirical phase function in Cases 1, 2 and 3 to the corresponding newly derived core-mantle model and investigated how these new models match the observations in the U, K and Q bands. In Cases 1 and 2, the simulation results are very similar and thus we only show Cases 2 and 3 as examples here. On the other hand, in the core-mantle model, the radially varying maximum size case (Case A) and radially varying percentage of particles larger than the critical size that contains a silicate core case (Case B) show similar results, though Case B fits the low observed brightness temperature at absolute azimuths around 40-60 degree slightly better. This is because in Case A, as we decrease the maximum particle size at ring radii away from the non-icy material fraction peak, the effect of the semi-empirical phase function for large particles is reduced as less large particles are present. Thus we continue here by focusing on the simulation results of Case B. As shown in **Figure 6.17** left column, in the U band (left column), the new core-mantle model cases 2-B (blue) and 3-B (purple) fit the observations (black) better than both the original intramixed model (red) and the original core mantle model (green) assuming a Mie scattering phase

function for all particle sizes. Case 3-B fits the observation even better in the middle and outer C ring around azimuthal angles of 40 – 60 degrees. However, the scattering profile for case 3-B is somewhat too flat so that it predicts a slightly higher brightness than observed around absolute azimuthal angles in the range around 80 -120 degrees in the inner and outer C ring. The effect of the semi-empirical phase function is more obvious in the K band (middle column) where Case 2-B and Case 3-B fit the observations well, especially Case 3-B. The core-mantle ring particle model also naturally explains the lower than expected intrinsic thermal emission at higher frequency so that we don't need to assume a frequency-dependent non-icy material dielectric constant. However, the fitting in the Q band (right column) for cases 2-B and 3-B is only slightly better, while case 3-B predicts a slightly lower brightness than observed from the occultation observations. Furthermore, the core-mantle model nicely explains the lower than expected thermal emission in the Q band. Considering the large artifacts present in the Q band data, we cannot tell whether the very low observed brightness around -50 ~ -70 azimuths is a real effect or not. We notice that in all core mantle cases, the frequency-dependent amount of thermal emission is naturally explained so that we don't need to assume a frequency-dependent non-icy material dielectric constant. In Figure 6.18, we show the radially varying integrated absorption rate in the C ring at different wavelengths. The black curves show the values in the intramixure model when assuming 75% porous particles containing the non-icy material fraction profile derived from the Cassini observations and also assuming that the dielectric of the non-icy material remains constant at all wavelengths. Although the imaginary part of the water ice dielectric constant increases slightly at smaller wavelengths, the imaginary part of the ring particles effective dielectric constant in the intramixure model doesn't change much since it is mainly determined by the non-icy material. Therefore the increasing absorption rate is due to the fact that particles with larger size

parameters (the ratio of particle circumstance to wavelength) tend to have larger absorption rate. On the other hand, the red curves in Fig. 6.18 show the radially varying absorption rate in the original core mantle model derived from Cassini observations, which doesn't change much at smaller wavelengths. Note that although the absorption rate at inner and outer C ring edge increases at small wavelengths since there is 1% non-icy material intramixed in the background material, the thermal emission at inner and outer C ring edge is pretty small and won't be affected much.

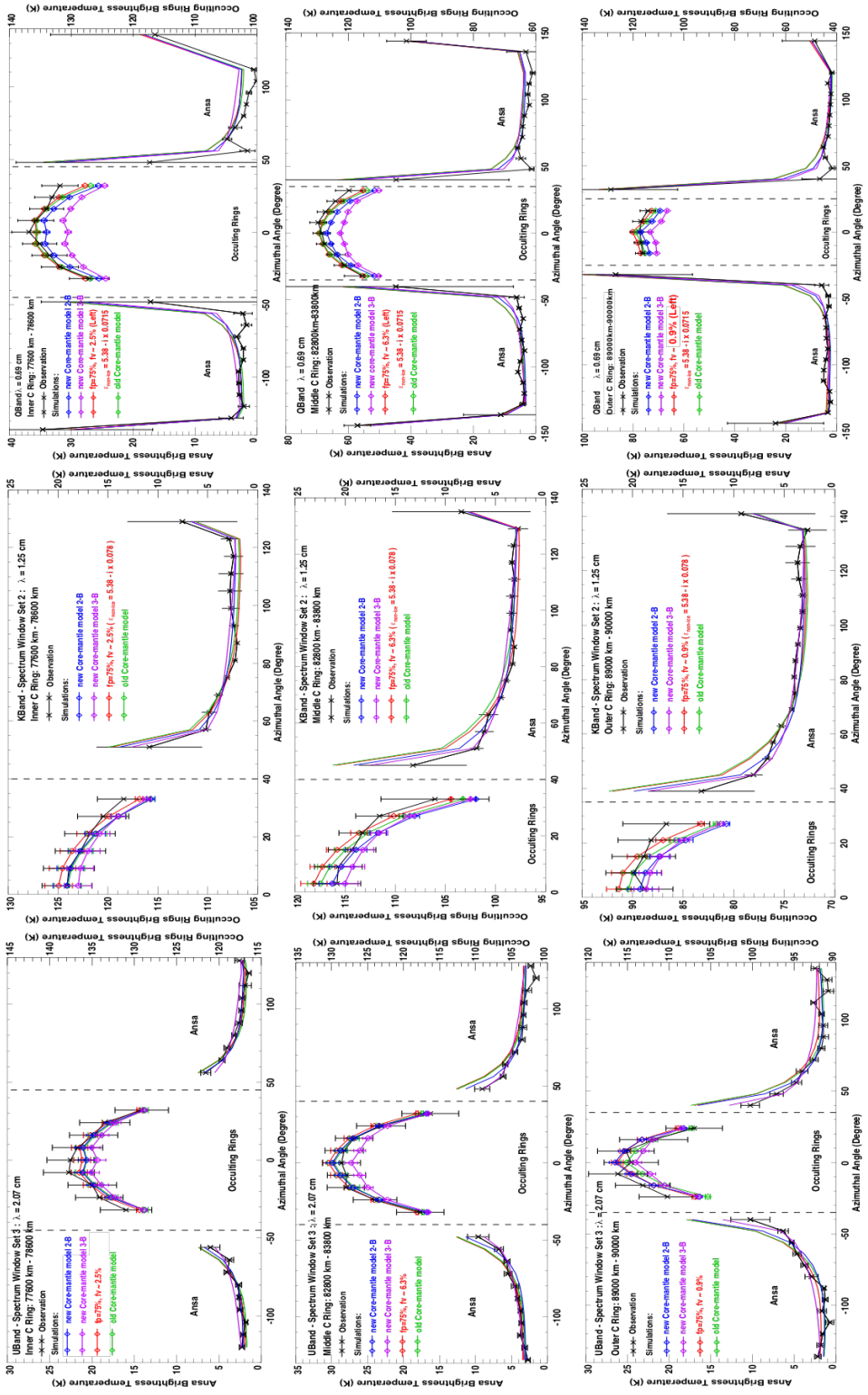

Figure 6.17: Simulated brightness temperature at inner (first row), middle (second row) and outer (bottom row) C ring using the newly derived core-mantle models, old core mantle model and intramixure model in the U band (left column), K band (middle column) and Q band (right

column). New core-mantle model cases: 1) case 2-B (blue): 80% porous pure water ice background material; semi-empirical phase function M=1.5, X_0=100; radially varying percentage of particles larger than the critical size that contains a silicate core case. 2) case 3-B (purple): 90% porous pure water ice background material; semi-empirical phase function M=4.0, X_0=50; radially varying percentage of particles larger than the critical size that contains a silicate core case. 3) intramixure model (red): 75% porous particles with radially varying non-icy material fraction derived from Cassini observations. 4) old core mantle model (green): 75% porous water ice with 1% non-icy material background material; Mie phase function for all sizes of particles; radially varying percentage of particles larger than the critical size that contains a silicate core case.

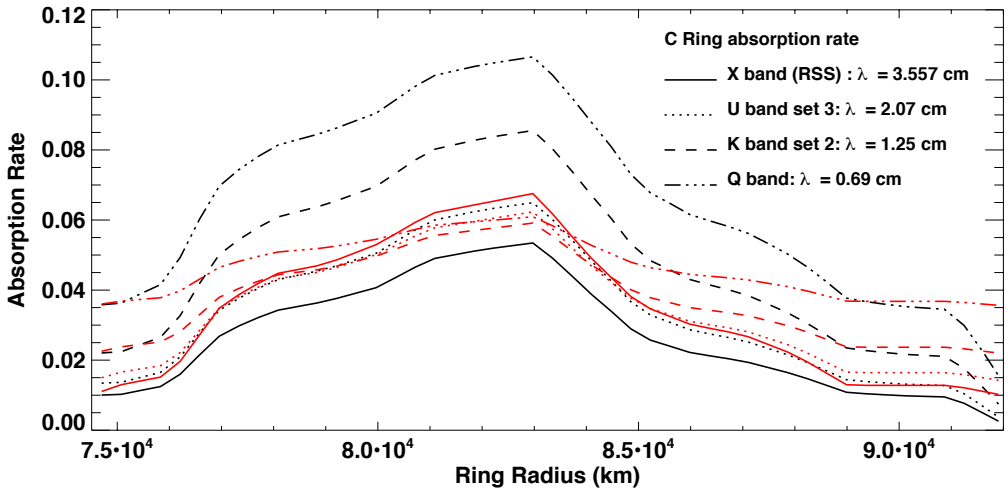

Figure 6.18: Radially varying absorption rate in the C ring at different wavelength bands. Black curves: intramixure model with 75% porous particles containing the non-icy material fraction profile derived from Cassini observations, while assuming that the imaginary part of the non-icy material dielectric constant remains constant. Red curves: original core-mantle model derived from Cassini observations; background material: 75% porous water ice with 1% non-icy material intramixed.

6.5.2 B Ring

Because the non-icy material fraction radial profile is fairly flat in the B ring (see Sec. 4.2.1), we derive the required non-icy material fraction independently in each wavelength band and then compare them with the results from the Cassini observations. We simulated the B ring brightness at porosity values of 55%, 80% and 90% (see Sec. 4.2), and applied a hybrid phase function for the B ring particles assuming that the scattering phase function is radially varying as suggested by Sec. 4.2. We set f_{iso} (Eq. [3.14]) as a free parameter and attempt to find the minimum χ^2 value when fitting the observed scattering profile.

In **Figure 6.19** we show the best-fit simulated brightness temperature in the inner (first row), middle (second row) and outer (third row) B ring for the U (left panels), K (middle panels) and Q (right panels) bands. Three different porosity cases are assumed, 55% (blue rectangles), 80% (green triangles) and 90% (red diamonds). We scanned all possible values of f_{iso} and f_v for each ring annulus in each porosity case in order to find the least χ^2 fit. For most ring annulus, the best-fit result matches the observation pretty well both in the brightness magnitude and the shape of scattering profile. However, we note that the 55% porosity case cannot match the observations in the Q band, which therefore indicates that the B ring particles are likely to be more porous than 80%. This result is consistent with the density wave measurements that the high opacity in the B ring indicates that the ring particles are 85% - 90% porous. In **Figure 6.20**, we show the derived non-icy material fraction for the X, U, K and Q bands only for the 80% (upper panel) and 90% (lower panel) porosity cases and compare them with the results we derived from the Cassini observations. Here we have assumed that the non-icy material dielectric constant doesn't change with frequency in any of the bands. Since the intrinsic thermal emission is approximately

proportional to the product of the imaginary part of the non-icy material dielectric constant and the non-icy material fraction, while the non-icy material fraction should be constant at all wavelengths, any change in the independently derived non-icy material fraction can later be attributed to changes in the imaginary part of the non-icy material dielectric constant. The black curves show the results derived from Cassini passive radiometry observations, while the non-icy material fractions in the X (purple), U (red), K (blue) and Q (green) bands are independently derived using the VLA observations. Due to the lower resolution of the VLA data, the derived non-icy material fraction profiles are considerably flat and lack the radial variation as seen in the Cassini observations. In the 90% porosity case (upper panel), the profiles for the X, U, K and Q bands all roughly have the same magnitude as the radiometer data. The blue (green) dashed line shows the expected non-icy material fraction in K (Q) band, if the imaginary part of the non-icy material dielectric constant shows same decreasing trend as found in the C ring intramixure model (see Fig. 6.11). Considering that when applying different phase functions (Mie and three other different cases involving semi-empirical phase function) the decreasing trend is different as shown in Fig. 6.11, we indicate the range of the expected non-icy material fraction profile for different phase function cases as the error bars. We can conclude that no obvious decrease in the non-icy material fraction with higher frequency. The non-icy material fractions for the 80% porosity case (lower panel) in the X, U and K band data are also roughly at the same level as the 80% porosity Cassini result. However, the Q band derived fraction is much lower (roughly at the same level of the expected value, green dashed line). We will show later in more details that this decrease in the derived non-icy material fraction in the B ring at Q band is not caused by the decrease in the imaginary component of the non-icy material dielectric constant, since there does not appear to be any obvious decrease seen between the U and K bands. Finally since the 55% porosity case always

predicts brightness temperature higher than observations in the Q band even with pure water ice, we rule out this value. The independently derived non-icy material fraction at K band for the 55% porosity case is also mostly zero within the B ring radius range.

Figure 6.19: The best-fit simulated brightness temperature in the inner (first row), middle (second row) and outer (third row) B ring for the U (left panels), K (middle panels) and Q (right panels) bands. Three different porosity values are considered: 55% (blue), 80% (green) and 90% (red)

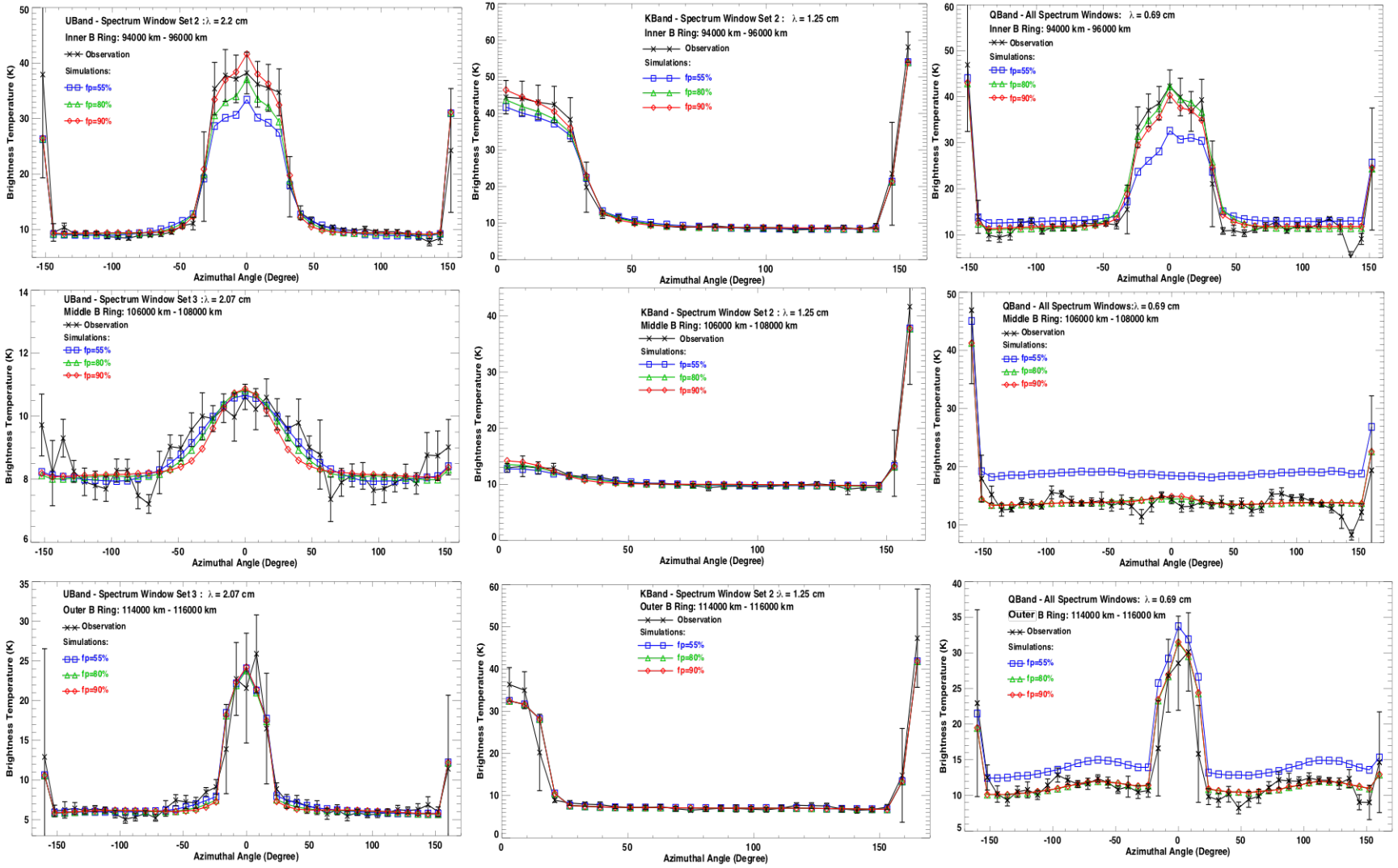
UBand - Spectrum Window Set 2 :λ = 2.2 cm
Inner B Ring: 94000 km - 96000 km
KBand - Spectrum Window Set 2 : λ = 1.25 cm
Inner B Ring: 94000 km - 96000 km
QBand - All Spectrum Windows: λ = 0.69 cm
Inner B Ring: 94000 km - 96000 km
UBand - Spectrum Window Set 3 :λ = 2.07 cm
Middle B Ring: 106000 km - 108000 km
KBand - Spectrum Window Set 2 : λ = 1.25 cm
Middle B Ring: 106000 km - 108000 km
QBand - All Spectrum Windows:λ = 0.69 cm
Middle B Ring: 106000 km - 108000 km
UBand - Spectrum Window Set 3 : λ = 2.07 cm
Outer B Ring: 114000 km - 116000 km
KBand - Spectrum Window Set 2 λ = 1.25 cm
Outer B Ring: 114000 km - 116000 km
QBand - All Spectrum Windows: λ = 0.69 cm
Outer B Ring: 114000 km - 116000 km
Observation
Simulations:
fp=55%
fp=80%
fp=90%
Brightness Temperature (K)
Azimuthal Angle (Degree)

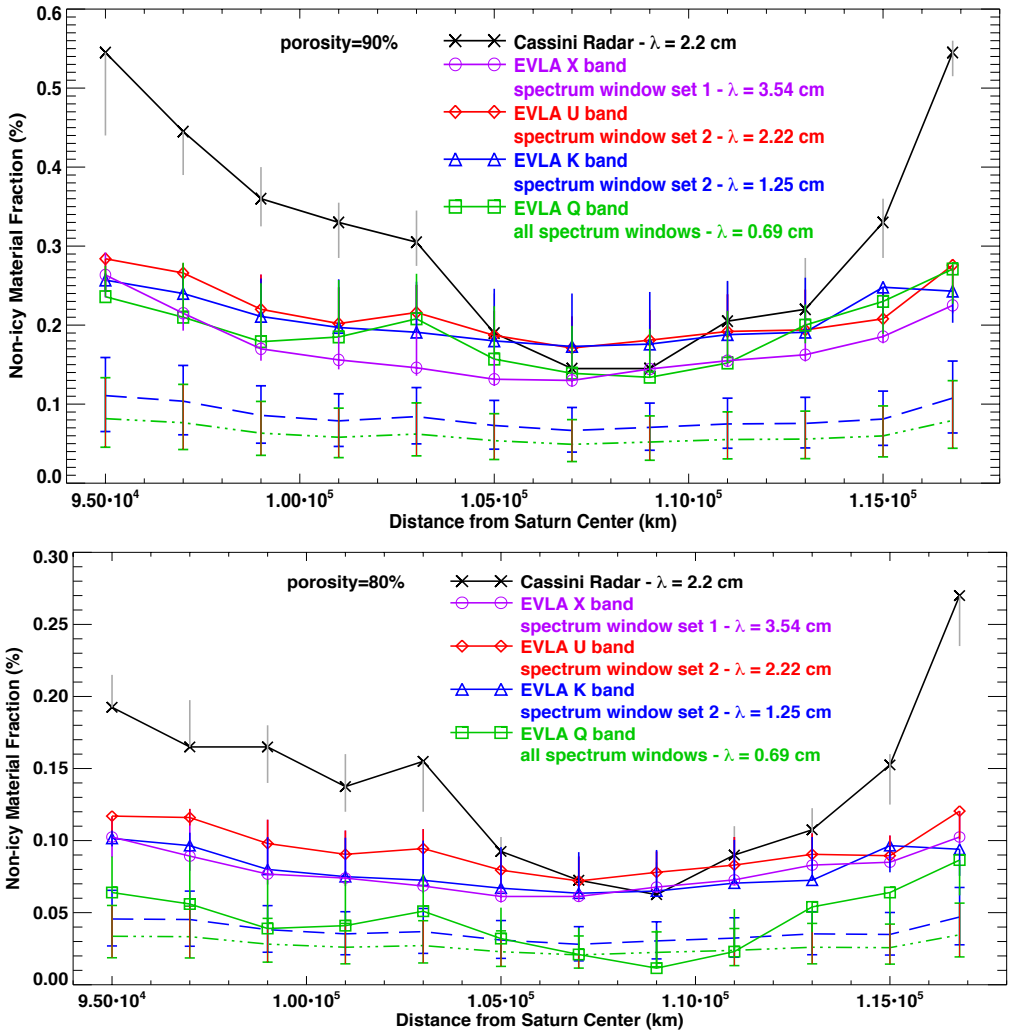

Figure 6.20: Derived non-icy material fraction derived independently using the VLA observations in X (purple), U (red), K (blue) and Q (green) bands. The porosity is assumed to be either 90% (upper panel) or 80% (lower panel). The non-icy material dielectric constant has been assumed to remain constant in any of the wavelength band. The black curves show the results derived from Cassini passive radiometry observations. The blue (green) dashed line shows the expected non-icy material fraction in K (Q) band, if the imaginary part of the non-icy material dielectric constant shows same decreasing trend as found in the C ring intramixure model (see Fig. 6.11). Considering that when applying different phase functions (Mie and three other different cases involving semi-empirical phase function) the decreasing trend is different as shown in Fig. 6.11, the range of the expected non-icy material fraction profile for different phase function cases are indicated as the

error bars.

In **Figure 6.21**, we investigated the frequency-dependence of the amount of observed intrinsic thermal emission from a ring annulus in middle B ring (black crosses and solid line), the amount contributed by water icy (green diamonds and solid line), the required amount contributed by non-icy material to match the observation (which equals the observed amount subtracted by the contribution from water ice, red triangles and solid line) and the amount predicted by our simulation when using the non-icy material fraction derived from Cassini 2.2 cm observation (red dashed line). From top to bottom panels in Fig. 6.21, we show the results for 90%, 80% and 55% porosity cases. We can see that the observed thermal emission from ring particles increase with higher frequencies. For a single particle, its absorption rate is linearly proportional to frequency and the imaginary component of dielectric constant (if $\varepsilon_i \ll \varepsilon_r$, i.e. water ice and silicates). Considering that the imaginary component of water ice dielectric constant increase slight from U band to Q band, the thermal emission contributed by water ice increases with frequencies slightly faster than linear increasing. On the other hand, since the less porous the particles are the more water ice material presents in the B ring, the increased amount of thermal emission from water ice is greatest in the 55% case (bottom panel in Fig. 6.21). In the 55% porosity case, the thermal emission from water ice becomes so high at Q band that it is already higher than the total observed amount of thermal emission. This is why the best-fit model in the 55% porosity case always predicts brightness higher than observed and hardly any non-icy material is required to match the observation at K and Q band. As for the non-icy material, their thermal emission contribution also increases with frequencies if assuming the fraction derived from Cassini observation at 2.2 cm (see red dashed lines in Fig. 6.21). However, only the required amount of thermal emission contributed

by non-icy material in the 90% porosity case coincides with this increasing trend (see top panel in Fig. 6.21, the red solid and dashed lines coincide with each other at all frequencies). This is why the independently derived non-icy material fractions at all frequencies in the 90% porosity case coincide with each other. In the 80% porosity case (middle panel in Fig. 6.21), at Q band, the thermal emission contribution from water ice has become too high and thus requires much less contribution from non-icy material than predicted when assuming the non-icy material fraction derived from Cassini observation, which therefore results in a much lower independently derived non-icy material fraction from Q band observations. This is very different from the C ring case (see **Figure 6.22**), where the observed amount of thermal emission has almost remain constant (black crosses and solid line) while the thermal emission contribution from non-icy material predicted in the intramixure model using the fraction derived from Cassini observation 2.2cm increases significantly at higher frequencies (red triangles and solid lines). Fig. 6.22 indicates that the main reason we require a decrease in the imaginary component of non-icy material dielectric constant in the C ring to match the observation when assuming intramixure model is not only because of the increasing thermal emission from water ice as the case in the B ring but also mainly because of the greatly increased thermal emission contribution from non-icy material at high frequencies. To conclude, when assuming the intramixing model in the B ring, we find that the non-icy material fraction in the B ring at different wavelengths is more likely to remain constant as suggested in the 90% porosity case. Therefore, the imaginary part of the non-icy material dielectric constant in the B ring particles doesn't change at different microwave wavelengths. If they have the same origin as the non-icy material in the C ring particles, the dielectric constant of non-icy material in the C ring should also remain the same from U band to Q band. Therefore these non-icy materials in the C ring are more likely to present in large chunks as described by the core-

mantle model. On the other hand, the excessive amount of thermal emission contributed by water ice at Q band in the 80% and 55% porosity cases suggests that the B ring particles are more likely to be highly porous ~90%, which will result in a low surface mass density, consistent with the value measured by density waves.

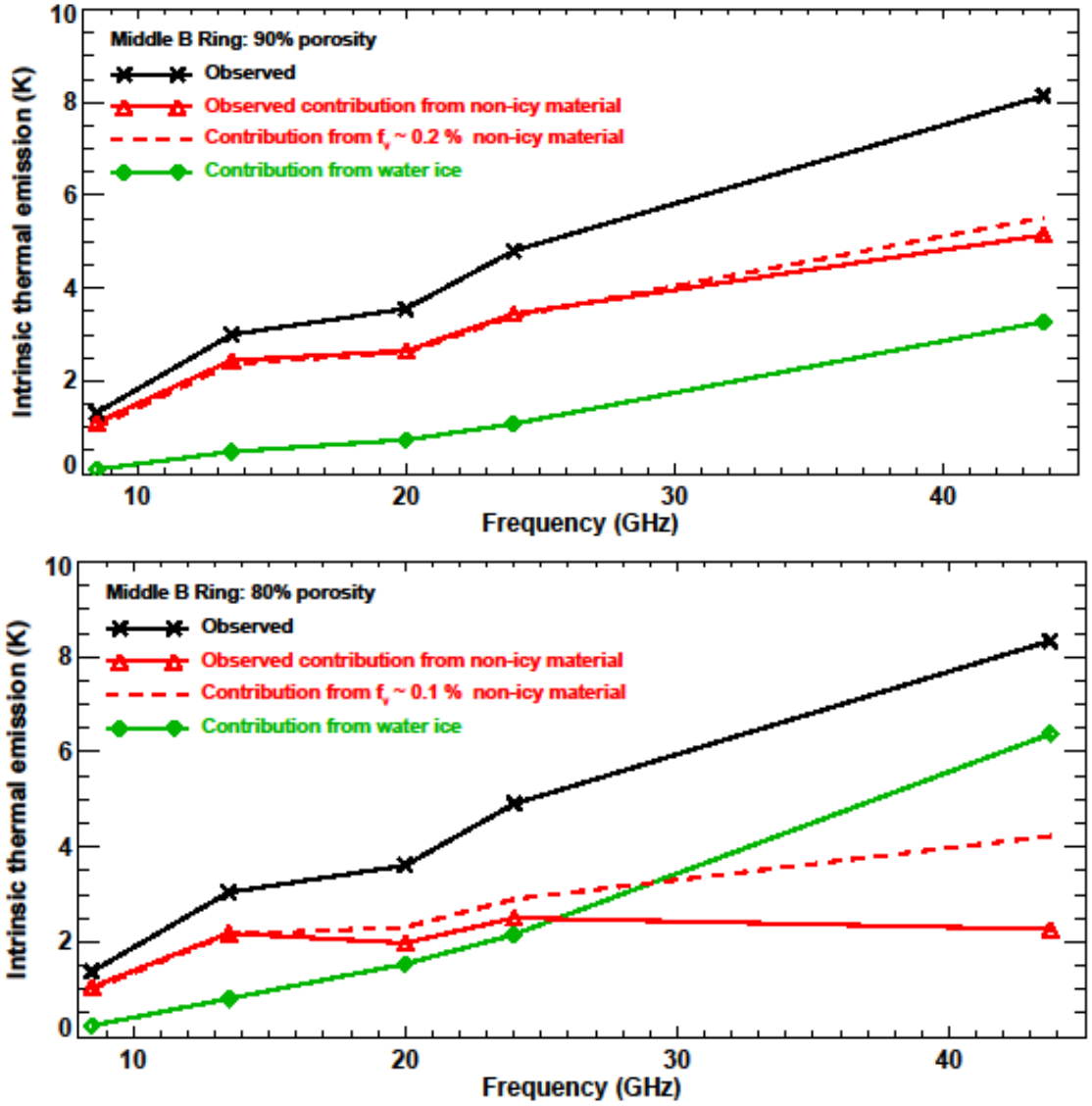

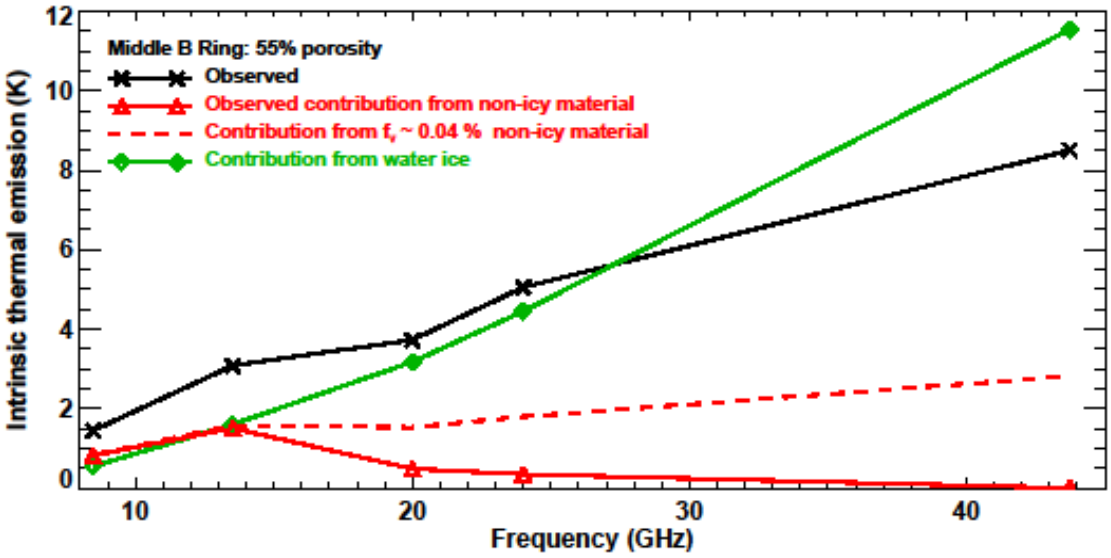

Figure 6.21: The frequency-dependence of the amount of observed intrinsic thermal emission from a ring annulus in middle B ring (black crosses and solid line), the amount contributed by water icy (green diamonds and solid line), the required amount contributed by non-icy material to match the observation (which equals the observed amount subtracted by the contribution from water ice, red triangles and solid line) and the amount predicted by our simulation when using the non-icy material fraction derived from Cassini 2.2cm observation (red dashed line). From top to bottom panels, we show the results for 90%, 80% and 55% porosity cases.

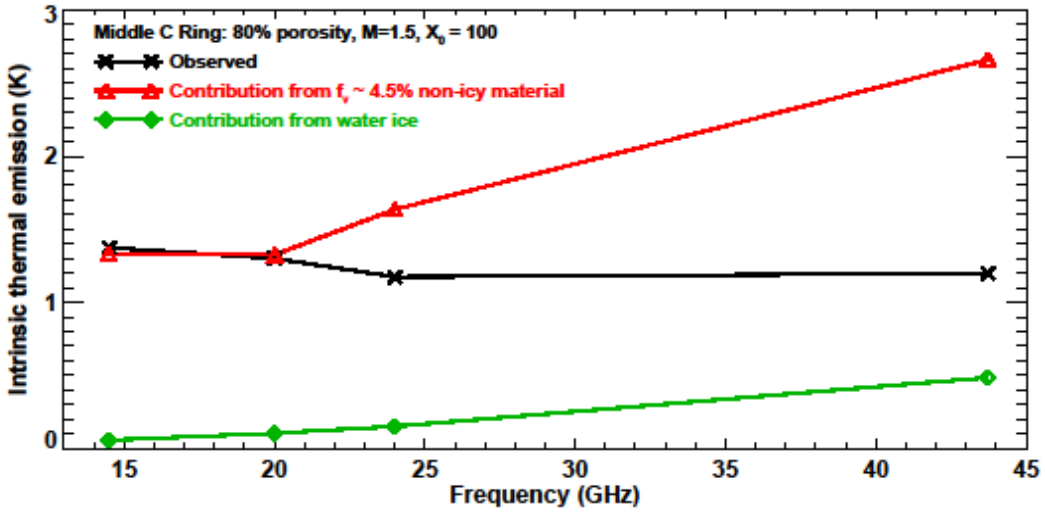

Figure 6.22: The frequency-dependence of the amount of observed intrinsic thermal emission from a ring annulus in the C ring (black crosses and solid line), the amount contributed by water icy (green diamonds and solid line), the thermal emission contribution from non-icy material predicted in the intramixure model using the fraction derived from Cassini observation 2.2cm(red triangles and solid lines).

7 Conclusions

We have calibrated and analyzed the Cassini Radiometry observations at 2.2cm and VLA multi-wavelength microwave observations of Saturn's rings. In the C ring, the high brightness temperature as seen where the ring obscures the planet suggests a scattering phase function that is much more forward-directed than a Mie phase function. We find that we can obtain a consistent scattering phase function by adding 70% - 75% porosity to the C ring particles. As a consistency check, we have simulated back scattering in the C ring with these highly porous particles and we find a very low, normalized backscatter cross-section of about 3% in agreement with stringent upper limits reported from Arecibo observations for the C ring (Nicholson et al., 2005). We speculate that it may be possible that ring particles achieve a quasi-equilibrium porous regolith as

a result of a balance between impact gardening due to micrometeoroid bombardment and ballistic transport and inter-particle collisions.

In addition, because the VLA covers a more complete azimuthal angle range than the Cassini high-resolution radiometry observations, we are able to obtain a complete scattering profile in the C ring. When we applied a pure Mie scattering phase function to all C ring particles, we found that the predicted scattering profile increases too steeply towards smaller angles in this range of azimuthal angles. This problem is resolved after we introduce a semi-empirical phase function for the large particles. Assuming the intramixture model, we derived new non-icy material fractions for all three new possible cases (see Table 6.3) and find that all of them show a similar non-icy material fraction trend, though the non-icy material fraction in one case (case 3, 90% porosity) is higher than the other cases (cases 1 and 2), as well as those results derived from the Cassini observations. However, as we apply case 3 to our Cassini observations, it predicts lower brightness temperature than observed around 40 to 50 degrees. We further derived the corresponding core mantle model for each case involving the semi-empirical phase function. After introducing the semi-empirical phase function for large particles and the newly updated core mantle model, we are able to both fit the scattering profile well, and are able to match the U and K band data without assuming that the dielectric constant of the non-icy material is wavelength dependent in the microwave. Although we can match the observations at most azimuthal angles in the Q band, the observed brightness in between -50 to -70 degrees is still lower than our simulation results. Considering the large uncertainty in the Q band data, we cannot conclude at this time whether this discrepancy is physical or not.

The amount of non-icy material in Saturn's rings is the key to understanding their origin and age.

The Cassini RADAR and the EVLA has provided us with the chance to measure the non-icy material fraction within the bulk of the ring mass in the microwave, which is much more sensitive to the embedded pollutants than visible or near-IR observations and have much higher resolutions than previous observations. From our analyses of observations around 2.2cm, we have determined the non-icy material fraction as a function of radius in the C ring, and find that the non-icy component reaches a maximum of 6%-11% by volume in the center of the C ring (when assuming the non-icy material is intramixed with water ice), and the fraction decreases gradually inward and rapidly outward from this radial location. The radial variation of the non-icy material, the concentration of which reaches a maximum near 83,000 km, cannot be explained by direct meteoroid deposition alone.

We have proposed a possible scenario in which a passing Centaur provides the necessary material for post-formation enhancement of the C ring non-icy material in addition to a smaller meteoroid infall component. We have considered two variations of this scenario. First, we suggested that diffuse debris clouds derived from the incoming Centaur, disrupted from previous encounters with the planet or rings, are absorbed and become intramixed with the rings' icy particles. In this case, the currently observed non-icy material distribution of the C ring would have taken some 15-90 Myr to accumulate given the currently accepted value of the micrometeoroid flux at infinity of $\sim 4.5\times10^{-17}$g cm^{-2} s^{-1}, with the variation in time scale depending on specifics of the treatment of the EMT model, and the non-icy material fraction in the inner and outer C ring as determined by the local opacity. This scenario can explain the high non-icy material fraction, but not the low opacity there. Specifically, we have found that 70% - 75% porous particles using our nominal particle size distribution for the C ring results in a ring opacity of $\sim 0.07 - 0.08$ cm^2 g^{-1} (see solid curve, Fig. 5.3), which is a factor of ~4 higher than yielded by the density wave measurements in the middle

C ring.

As a variant on the Centaur disruption model, we have considered the likelihood that a recently-captured Centaur would not have been ground down to powder, but in fact most of its mass would remain in larger chunks in the cm-m range, which have since acquired porous, icy mantles over time. As a result, we proposed a silicate-core and porous-dirty-icy-mantle model in which the mass of the Centaur is initially contained in a narrow annulus located at the peak of the current non-icy material fraction bump in the C ring center (83,000 km). We have shown that this annulus can viscously spread to the feature's current width and surface density in as little as ~20 - 30 Myr, though this depends on model parameters. It is possible that a combination of viscous spreading and ballistic transport acting together could shorten this time further. We find this variant more compelling because it successfully fulfills the requirements for a strong forward-directed scattering phase function, while explaining both our derived radially-variable thermal emission *and* the low opacity in the middle C ring, without requiring the Centaur to be ground to powder.

We applied the radially varying non-icy material fraction profile derived at 2.2cm, when assuming that the non-icy material is intramixed within the ring particles, to VLA high frequency observations in the K and Q band. We found that they predict an intrinsic thermal emission that is higher than observed, which requires that the imaginary part of the non-icy material dielectric constant decrease with increasing frequency. On the other hand, we find that the core-mantle model, which accounts for the possibility that the bulk of the non-icy material (silicates) are present in large chunks embedded within the ring particles, naturally fits the observations at both low and high frequencies. We are also aware that for most silicates, their imaginary components of the dielectric constant actually increase at higher frequencies rather than decrease. Therefore, the extra

amount of non-icy material in middle C ring is more likely to be in the form of large chunks coated with dirty water ice instead of intramixed within the ring particle, since it naturally explains the lower than expected intrinsic thermal emission at higher frequencies.

We have examined other possible scenarios that might account for the observations, and identified the difficulties with them. We considered the possibility that the silicates in the C ring came from an object that originated from within the Saturnian system. This could have occurred from the breakup of one or more of the Saturnian moons, either from tidal disruption, catastrophic impact by a heliocentric interloper or even a collision between mid-sized satellites. However, such a scenario faces several hurdles, not least of which is that the event must have occurred within the last ~100 Myrs. This time scale becomes realizable if the tidal dissipation parameter for Saturn is much lower than previously thought, which remains controversial. Even so, an embedded rocky fragment of the required size that originated from one of these moons would almost certainly have significant strength, and would need to be totally broken up into small chunks via a catastrophic impact with an object of heliocentric origin. In such a case, then it is possible that its evolution could be similar to the Centaur model. However, we have investigated the probability of such a catastrophic impact occurring within the last ~ 100 Myr and have found an optimistic estimate to be on the order of ~ 2 - 3%.

We have also considered a scenario in which meteoroid bombardment is the only pollution source, which provides the mid-C-ring non-icy fraction only if the rings formed ~900Myr ago, again assuming a micrometeoroid flux at infinity of $\sim 4.5\times10^{-17}$g cm^{-2} s^{-1}. But the nearly flat radial distribution of the flux would mean that mechanisms would then need to be identified that would act to dilute or decrease the non-icy material in the inner and outer C ring. Ballistic transport in

the outer C ring may act to dilute the non-icy fraction as icy material spills over from the inner B ring over time. However, the inner C ring remains problematic. As a final consideration, we postulate that ring rain erosion would tend to make the non-icy material fraction in the inner and middle C ring higher than the fraction in the outer C ring. That is, the non-icy material fraction in the inner and middle regions would have been increased as ice was preferentially eroded away along magnetic field lines. Given that there are more uncertainties inherent in this scenario, we find the Centaur capture model more preferable.

Although we have not specifically addressed the possibility in this work, it has been proposed that the rings could have been initially much more massive in the past, having formed from the breakup of a large moon (e.g., Charnoz et al., 2009a; Canup, 2010). Such a massive disk would then evolve viscously over time to its current lower-mass state. A difficulty with this scenario is that much of the material may evolve inwards into the C ring region increasing its surface density considerably relative to the B ring (see Salmon et al., 2010; Charnoz et al., 2011) which is inconsistent with the rings' current configuration, unless some mechanism can act to prevent or limit inward spreading. If it were the case though, the age of the C ring would likely be older than our estimation, since massive rings would be less vulnerable to pollution by meteoroid impacts and it would take a longer time to reach the non-icy material fraction we observe today. However, given that the low optical depth C ring would take ~700 Gyr to double its width by viscous spreading alone (Charnoz et al., 2009b), it would seem unlikely that the rings have achieved their current configuration this way, if they were indeed initially very massive. Therefore additional mechanism(s) would have to be identified that can explain the C ring's current low mass density and optical depth relative to the B ring. Despite this apparent puzzle, an initially massive ring remains an interesting possibility that is worthy of further study.

In the B ring, starting from 2.2cm Cassini observations, we determined the scattering phase function and for a range of ring particle porosity, we derived the non-icy material fraction and the corresponding exposure time required to accumulate it. We find that the brightness temperature in the B ring as seen where the rings obscure the planet does not depend significantly on the particle porosity; however, it suggests a scattering phase function that varies in between a half-Mie-half-isotropic and a purely isotropic one. The radially varying best-fit phase function transitions from a half-Mie-half-isotropic phase function in the optically thinner, inner and outer B ring to a purely isotropic one in the opaque, optically thick middle B ring. The variation of the best-fit phase function follows the variation of the optical depth in that the larger the optical depth, the more isotropically the particles scatter. The amount of derived non-icy material fraction varies significantly with different porosity values, but follows the same radial trend being higher in the inner and outer B ring while being lowest in the middle B ring. This is because for optical depths larger than unity, as is the case in the entire B ring, almost all the incident meteoroid flux is absorbed. In such a case, the more optically thick the region is, presumably the larger the surface mass density it would contain, and thus the relative amount of pollution will be less for the same amount of exposure time.

We further derived the non-icy material fraction independently from VLA observations at other wavelengths (X, K and Q bands). The results are very similar to each other, especially the X, U and K band data, when assuming 80% or 90% porosity, which doesn't show the decrease in the imaginary component of the silicate dielectric constant as we saw in the middle C ring assuming an intramixed model. It either indicates that the non-icy material in the middle C ring has a different origin source than the non-icy material in the B ring which was brought in through meteoroid flux,

or that the core-mantle model in the middle C ring is the more likely case, which naturally explains the lower than expected intrinsic thermal emission at higher frequencies. While deriving the best-fit non-icy material fraction in the B ring, we also notice that when assuming 55% porosity for the B ring particles, the simulation cannot match the observation in the Q band. Therefore, the B ring particles are likely to be more porous than 80%, which is consistent with its high opacity which also suggests porosity higher than 85%. Under the assumption that micrometeoroid bombardment is the primary pollution source, we estimated the required exposure time in order to accumulate the observed non-icy material fraction with the known micrometeoroid flux. We found that for the B ring the exposure time varies depending on the porosity of the ring particles. For particles that have porosities of 85% ~ 90%, the exposure time is 30 ~ 100 Myr.

The situation within the A ring is more complicated due to the presence of self-gravity wake structure, and variation in the particle size distributions across the ring, leading us to model the A ring as four separate regions. To simulate the scattered brightness we required optical depth values for both the wake and gap regions. Stellar occultation measurements usually assume an infinite optical depth inside the wakes. Because we employ the measured opacity from density waves (Spilker et al., 2004; Tiscareno et al., 2007; Colwell et al., 2009) to derive the optical depth in the wakes, we are not able to constrain the porosity for the A ring particles. Therefore, we varied the porosity between values of 55% and 90%. The situation is less complicated interior to the Encke gap. By investigating the occultation observations, the ring particles scatter isotropically if they are 55% porous, while if the ring particles have a porosity of 90%, their phase function is best fit by one that is 30% Mie/70% isotropic. However, independent of the choice of porosity, the derived non-icy material fraction is always ~0.2%-0.3% with a corresponding exposure time of

~80-150Myr. Exterior to the Encke gap, occultation observations suggest that the particles are 90% porous and their scattering phase function is best fit by one that is isotropic. We modeled this region using three different particle size cases (see Sec. 3.2) and found the best match to be that of A3-Case1 (Table 3.2) while all other cases would predict a brightness much higher than observed. However, we are not able to match the scattering profile exactly exterior to the Encke gap using a purely isotropic phase function even for this optimal case. Using an isotropic phase function, we found that the required exposure time varies from ~10-120Myr depending on the ring particle porosity and particle size distribution case assumed.

Since most of the Cassini Division particles are smaller than our wavelength of interest, their scattering properties should be similar to the C ring particles, which can be modeled using a Mie phase function. By comparing the simulated scattering profile using a Mie phase function with the observations, we find that the Mie phase function works well especially when the particles have 90% porosity. Furthermore, the high opacity derived from density wave measurements also indicates porosity values as high as 90% or perhaps even higher. Both the derived non-icy material fraction and the required exposure time increase as the porosity increases. We find the non-icy material fraction to be ~1% - 2%, similar to what we found previously for the inner and outer C ring despite finding that the Cassini Division ring particles are more likely to have 90% porosity, whereas the C ring particles were found to have porosities of ~70%-75%. Finally, the exposure time for the Cassini Division is estimated to be 60 ~ 90 Myr (assuming 90% porosity), which is consistent with the exposure time in A ring interior to the Encke gap.

We conclude that ring particles in all the main rings are likely to be highly porous, especially the

C Ring, B ring and Cassini Division particles, which is in line with each other. The pollution exposure time in the B ring, Cassini Division and A ring all lie between ~10-150Myr, which is also consistent with the exposure time due to micrometeoroid bombardment we derived for the inner and outer C ring. These results taken together support the idea that Saturn's rings are geologically young, $\lesssim$ 150 Myr old, further suggesting a formation scenario in which the rings are derived from the relatively recent breakup of an icy moon, perhaps of Mimas' mass consistent with the post Voyager ring mass estimate (Esposito, 1984), though recently Hedman and Nicholson (2016) suggest that the total mass of the rings may be as little as 0.4 times Mimas' mass. Whichever the case may be, the anomalously high non-icy material fraction which we found in the middle C ring (which can best be explained by the capture and breakup of a Centaur within the last 10 - 30 Myrs) fits well into this picture.

8 Future Observations During Cassini F-Ring and Proximal Orbits

In 2017, the Cassini Mission will end by exploring for the first time the region between the rings and planet, a rich source for discovery. It will begin with 20 orbits with periapse just outside the F Ring before transitioning to 22 Proximal Orbits, with periapse between the rings and planet. The last orbit will take the spacecraft into Saturn on September 15, 2017, where it will be vaporized by the planet's atmosphere. The F-ring and proximal orbits will be so close to the rings that we will be able to look at the rings at unprecedented high resolutions. With the extremely valuable insight gained from the research findings in the prime mission, we have been able to design high-resolution active and passive radar observations for the Cassini F-ring and proximal orbits, which have been allocated with two passive and four active observation times in 2017 (see Table 8.1).

These observations offer the tantalizing prospect of being able to retrieve the entire scattering profile, vertical distribution and address large-scale structures and dynamics in the rings.

Table 8.1 Scheduled passive and active radar observations on the rings in F-ring and Proximal orbits

F Ring Orbit				
Rev	**Name**	**Duration**	**Periapse Passing Time**	**Observation Type**
255	RADAR_255RI_RADSCNOUT001_PIE	2017-002T05:37:00 ~ 2017-002T10:00:00	2017-002T05:47:56	Passive Radiometry
				Active Scatterometry
260	RADAR_260RI_R1DHRSOUT001_PIE	2017-038T01:17:00 ~ 2017-038T03:00:00	2017-038T01:46:32	1-D Range Slicing through rings A through C in F-ring orbit (Passive Radiometry)
	RADAR_260RI_RADSCNOUT001_PRIME	2017-038T05:30:00 ~ 2017-038T08:00:00		Passive Radiometry
Proximal Orbit				
Rev	**Name**	**Duration**	**Periapse Passing Time**	**Observation Type**
276	RADAR_276RI_INBHIRES001_PIE	2017-148T12:17:00 ~ 2017-148T14:19:00	2017-148T14:26:21	1-D Range Slicing through rings A through C in Proximal orbits (Passive Radiometry)
277	RADAR_277RI_OUTBHIRES002_PIE	2017-155T01:42:00 ~ 2017-155T03:42:00	2017-155T01:42:27	
282	RADAR_282RI_OUTBHIRES003_PIE	2017-187T09:35:00 ~ 2017-187T11:41:00	2017-187T09:35:35	

The passive radiometry data will start to be collected right after the spacecraft turns at the periapse in the F-ring orbits. The F-ring orbits dive through the ring plane just outside the F-ring at about 150000 km from Saturn's center, providing us with resolution as high as several hundred kilometers. As we have mentioned before, the ring particle scattering phase function, which can reveal a lot information on single and bulk ring particle properties (i.e. size distribution, porosity, surface roughness, non-sphericity and wake structures), is most sensitive and changes most rapidly at near-zero azimuthal angles (the projection of the spacecraft lies at zero azimuth). Taking

advantage of the high resolution in the F-ring orbit, we are going to scan all the main rings back and forth at several near-zero azimuthal angles right after the spacecraft passes the periapse. In addition, since the geometry of the spacecraft varies quickly near periapse, we will be able to retrieve a complete scattering profile for all the rings at very high resolution. We will also obtain passive radiometry observations on the rings back-scattering by scanning the part of the rings at near 180° azimuthal angles with large ring opening angle. The surprisingly high porosity in the ring particles, especially C ring particles, will be further investigated, since both forward and backward scattering are very sensitive to the particle porosities. Large particles, which have very large back-scattering will also be revealed. Furthermore, while previous passive radiometry data were only collected at two ring opening angles, the proximal observation will observe the rings at continuously changing ring opening angles, which would be very crucial to the study of the wake structures in the rings. We also expect to look into the especially high non-icy material fraction at middle C ring found in the prime mission at various ring opening angles and derive a higher resolution radially-varying non-icy material fraction profile.

Furthermore, we are also awarded four active radar revolution times (one in F-ring orbits and three in Proximal orbits) for 1-D range slicing on the main rings. We will scan RADAR beam 3 along the line connecting the ring plane crossing point with Saturn's center (1-D slicing). The range resolution corresponding to the radial resolution will vary from 3 - 4 km down to 500 m, at best. The F-ring orbit brings us closest to the A ring and provides the best resolution on the A ring. While the proximal orbits bring us closest to the C ring and provide the best resolution on the C ring. These observations will look at the rings' back-scattering as a function of radial distance. Although similar observations have been done at optical wavelengths, Radar will be seeing a different population of ring particles because our measurements will be dominated by cm-scale

and larger particles, while the optical observations are seeing a wider spectrum of particle sizes. Therefore, we would add some constraints on size distributions and the variation of sizes and particle densities as a function of radial position. If there are systematic structures in the rings (like wave structure in the longitudinal direction), these might be observable as systematic Doppler variations. These observations are also highly complementary to previous occultation results because they observe completely different phenomena but at comparable resolution. These observations also offer the best opportunity to address the vertical distribution and dynamics in the rings. We will also obtain more passive radiometry observations interleaved with the 1-D range slicing.

Future observations at the Cassini F-ring and proximal orbits are very likely to provide more insights from both passive and active radiometry data at very high resolution. They will not only verify our previous results from the prime mission, but also offer more valuable insights into our understanding of the origin and dynamics of Saturn's rings. Determination of the ring particle properties is paramount to this understanding for future studies of the rings going forward. As we mentioned in the Introduction, much of the structure in Saturn's rings remains largely misunderstood. For example, in the C ring there is the puzzling observation that the surface density in the higher optical depth plateaus does not differ much from that in the much lower optical depth continuum indicating some very real variation in the particle properties inside and outside the plateaus. The same can be said of our conclusion that the non-icy material fraction across the B ring does not vary significantly, even in the opaque regions which in the Cassini era have been thought to be hiding a great deal of mass. However, a similar non-icy material fraction across the B ring suggests then that these regions are not that massive, despite being opaque. This might imply particle sizes are smaller in the dense wakes than previously thought. Ring particle

properties are also critical for more detailed modeling of ballistic transport across the main rings, because their structural and compositional evolution will depend keenly on the nature of the ring particles themselves. For example, very porous particles might produce much different ejecta velocity distributions and ejecta yields that can vary spatially across the rings. A lack of significant radial variation in the composition of the rings overlying a likely significant radial variation in particle size distribution across the rings will also need to be reconciled. There is still a great deal to be done, but we must acknowledge that these results of the Cassini era will stand firmly as the benchmark until that point in a possibly uncertain future that we may return to observe Saturn and its majestic rings up close once again.

BIBLIOGRAPHY

Altobelli, N. et al., 2015. Dust populations in the outer Solar System: 10 years of monitoring by Cassini-CDA. Proceedings of the EPSC, Nantes, France, id. EPSC 2015-577.

Araki, S. and Tremaine, S. 1986. The dynamics of dense particle disks. Icarus 65, 83-109.

Asphaug, E., and Reufer, A., 2013. Late origin of the Saturn system. Icarus 223, 544-565.

Baillie, K. et al., 2011. Waves in Cassini UVIS stellar occultations. 2. The C ring. Icarus, Volume 216.

Barber, P.W. and Hill, S.C., 1990. Light Scattering By Particles: Computational Methods. Series: Advanced Series in Applied Physics, ISBN: 978-9971-5-0813-5. WORLD SCIENTIFIC.

Bohren, C., and Huffman, D. R. 1983. Absorption and scattering of light by small particles. Wiley, New York.

Brillouin, L., 1949. The Scattering Cross Section of Spheres for Electromagnetic Waves. Journal of Applied Physics, Volume 20, Issue 11, p.1110-1125.

Bruggeman, D.A.G., 1935. Berechnung verschiedener physikalischer Konstanten von heterogenen Substanzen. I. Dielektrizitätskonstanten und Leitfähigkeiten der Mischkörper aus isotropen Substanzen Annalen der Physik, vol. 416.

Canup, R. M., 2010. Origin of Saturn's rings and inner moons by mass removal from a lost Titan-sized satellite. Nature 468,7326,943.

Charnoz, S. et al., 2009a. Did Saturn's rings form during the Late Heavy Bombardment? Icarus, Volume 199, Issue 2, p. 413-428.

Charnoz, S. et al., 2009b. Origin and evolution of Saturn’s ring system. In Saturn After Cassini-Huygens, (Dougherty, M. K., Esposito, L. W., and Krimigis, S. M., eds.), Springer-Verlag Press, pp. 537-576.

Charnoz, S. et al., 2011. Accretion of Saturn’s mid-sized moons during viscous spreading of young massive rings: Solving the paradox of silicate-poor rings versus silicate-rich moons. Icarus 216, 535-550.

Chesley, S.R., et al., 2002. Quantifying the risk posed by potential Earth impacts. Icarus, Volume 159, Issue 2, p. 423-432.

Colwell, J. E. et al., 2007. Self gravity wakes and radial structure in Saturn's B ring. Icarus 190, 127-144.

Clark, R. N. et al., 2008. Compositional mapping of Saturn's satellite Dione with Cassini VIMS and implications of dark material in the Saturn system, Icarus 193, 372–386.

Colwell, J. E. et al., 2010. Cassini UVIS stellar occultation observations of Saturn's rings. Astron. J. 140, 1569-1578.

Clark, R. N. et al., 2012. Nano-Iron on Outer Solar System Satellites, Implications for Space Weathering. Proceedings of the AGU, Fall Meeting, #P53B-05.

Colwell, J.E. et al., 2006. Self-gravity wakes in Saturn's A ring measured by stellar occultation from Cassini. Geophysical Research Letters, Volume 33, Issue 7, CiteID L07201.

Colwell, J. E. et al., 2007. Self gravity wakes and radial structure in Saturn's B ring. Icarus 190, 127-144.

Colwell, J. E. et al., 2009. The structure of Saturn's rings. In: Dougherty, M.K., Esposito, L.W., Krimigis, S.M. (Eds.), Saturn From Cassini-Huygens. Springer-Verlag Press, pp. 375-412

Colwell, J. E. et al., 2010. Cassini UVIS stellar occultation observations of Saturn's rings. Astron. J. 140, 1569-1578.

Cruikshank, D. P. et al., 2005. Tholins as coloring agents on outer Solar System bodies. Adv. Space Res. 36, 178–183.

Cuk, M., 2014. After Imbrium, before Babylon: Solar System's middle years. 46th DPS Meeting, Urey Prize Lecture.

Cuk, M., Dones, L., Nesvorny, D., 2016. Dynamical evidence for a late formation of Saturn's moons. Submitted to Astrophys. J.

Cuzzi, J. N., and Van Blerkom, D., 1974. Microwave brightness of Saturn's rings. Icarus 22, 149-158.

Cuzzi, J. N., and Dent, W. A., 1975. Saturn's rings - The determination of their brightness temperature and opacity at centimeter wavelengths. Astrophys. J. 198, 223-227.

Cuzzi, J. N. and Pollack, J. B., 1978. Saturn's rings: Particle composition and size distribution as constrained by microwave observations. I - Radar observations, Icarus 33, 233-262.

Cuzzi, J. N., Pollack, J. B., Summers, A. L., 1980. Saturn's rings - Particle composition and size distribution as constrained by observations at microwave wavelengths. II - Radio interferometric observations. Icarus 44, 683-705.

Cuzzi J.N. et al., 1984. Saturn's rings: Properties and Processes; in Planetary Rings, R. Greenberg and A. Brahic, eds. University of Arizona Press, Tucson.

Cuzzi, J. N., and Durisen, R. H., 1990. Bombardment of planetary rings by meteoroids: General formulation and effects of Oort cloud projectiles. Icarus 84, 467-501.

Cuzzi, J. N., Estrada, P. R., 1998. Compositional Evolution of Saturn's Rings Due to Meteoroid Bombardment. Icarus 132, 1-35.

Cuzzi et al., 2004. Utilitarian Opacity Model for Aggregate Particles in Protoplanetary Nebulae and Exoplanet Atmospheres. The Astrophysical Journal Supplement, Volume 210, Issue 2, article id. 21.

Cuzzi, J. N. et al., 2009. Ring particle composition and size distribution. In: Dougherty, M.K., Esposito, L.W., Krimigis, S.M. (Eds.), Saturn From Cassini-Huygens. Springer-Verlag Press, pp. 459p. 45.

Daisaka, H., Ida, S., 1999. Spatial structure and coherent motion in dense planetary rings induced by self-gravitational instability. Earth, Planet Space 51, 1195anetar

Daisaka, H., Tanaka, H., Ida, S., 2001. Viscosity in a dense planetary ring with self-gravitating particles. Icarus 154, 2964, 29

de Pater, I. and Dickel, J.R., 1991. Multifrequency radio observations of Saturn at ring inclination angles between 5 and 26 degrees. Icarus, 94, 474.

Di Sisto, R. P. and Brunini, A., 2007. The origin and distribution of the Centaur population. Icarus 190, 224-235.

Dones, L., 1991. A recent cometary origin for Saturn's rings? Icarus 92, 194.

Dones, L. et al., 1993. Voyager photometry of Saturn's A ring. Icarus 105, 184–215.

Dougherty et al., 2009. Saturn from Cassini-Huygens. Springer. ISBN 978-1-4020-9216-9.

Doyle, L. R., Dones, L., Cuzzi, J. N., 1989. Radiative transfer modeling of Saturn's outer B ring. Icarus (ISSN 0019-1035), vol. 80, July 1989, p. 104-135.

Dunn, D.E., et al., 2002. More Microwave Observations of Saturn: Modeling the Ring with a Monte Carlo Radiative Transfer Code. Icarus, 160, 132.

Dunn D.E. et al., 2004. Microwave observations of Saturn's rings: anisotropy in directly transmitted and scattered saturnian thermal emission. Icarus vol 171.

Dunn, D.E., et al., 2005. High-Quality BIMA-OVRO Images of Saturn and its Rings at 1.3 and 3 Millimeters. Astron. J, 129, 1109.

Durisen R.H. et al., 1992. Ballistic transport in planetary ring systems due to particle erosion mechanisms. II - Theoretical models for Saturn's A- and B-ring inner edges. Icarus vol.100.

Elachi, C. et al., 2004. RADAR: The Cassini Titan radar mapper. Space Sci. Rev. 115, 71–110.

Elliot J.P. and Esposito L.W., 2011. Regolith depth growth on an icy body orbiting Saturn and evolution of bidirectional reflectance due to surface composition changes. Icarus, vol 212.

Epstein, E.E. et al, 1980. Saturn's rings – 3-mm observations and derived properties. Icarus, vol. 41, Jan. 1980, p. 103-118.

Epstein, E.E. et al, 1984. Saturn's rings – 3-mm low-inclination observations and derived properties. Icarus (ISSN 0019-1035), vol. 58, June 1984, p. 403-411.

Esposito, L. W. et al., 1984. Saturn's rings: Structure, dynamics, and particle properties; in Saturn, T. Gehrels and M. Matthews, eds. University of Arizona Press, Tucson.

Esposito, L. W., 2008. History of Saturn's rings from UVIS observations. Proceedings of the EPSC, p. 757.

Estrada, P. R. and Cuzzi J.N., 1996. Voyager observations of the color of Saturn's rings; Icarus 122, 251–272.

Estrada, P. R. et al., 2015. Combined structural and compositional evolution of planetary rings due to micrometeoroid impacts and ballistic transport, Icarus 252, 415-439.

Ferrari, C. C. et al, 2009. Structure of self-gravity wakes in Saturn's A ring as measured by Cassini CIRS. Icarus, Volume 199, Issue 1, P. 145-153.

French, R. G. and Nicholson, P. D., 2000. Saturn's Rings II. Particle Sizes Inferred from Stellar Occultation Data, Icarus 145, 502-523.

French, R. G., et al., 2007. HST observations of azimuthal asymmetry in Saturn's rings. Icarus 189, 493-522.

Goldreich, P., Tremaine, S., 1978. The velocity dispersion in Saturnllar Occu Icarus 34, 227,us 3.

Goldreich, P., Tremaine, S., 1982. The dynamics of planetary rings. Ann. Rev. Astron. Astrophys. 20, 249-283.

Goldstein, R. M. and Morris, G. A., 1973. Radar Observations of the Rings of Saturn. Icarus 20, 260-262.

Goldstein, R. M., et al., 1977. The rings of Saturn - Two-frequency radar observations. Icarus 30, 104-110.

Grossman, A. W., 1990. Microwave Imaging of Saturn's Deep Atmosphere and Rings. Unpublished Ph.D. thesis, California Institute of Technology, Pasadena.

Gru¨n, E., H. A. Zook, H. Fechtig, and R. H. Giese 1985. Collisional balance of the meteoroid complex. *Icarus* 62, 244–272.

Hanel, R. et al., 1981. Infrared observations of the saturnian system from Voyager 1. Science 212, 192–200.

Hanel, R. et al., 1982. Infrared observations of the saturnian system from Voyager 2. Science 215, 544–548.

Harbison, R. A. et al., 2013. The smallest particles in Saturn's A and C Rings, Icarus, Volume 226, Issue 2.

Harris, A.W., et al., 1984. The origin and evolution of planetary rings. IN: Planetary rings.

Hedman, M. M. et al., 2011. Saturn's Curiously Corrugated C Ring. Science, Volume 332, Issue 6030.

Hedman M.M. and Nicholson P.D., 2013. Kronoseismology: Using density waves in Saturn's C Ring to probe the planet's interior. The Astronomical Journal, Vol 146.

Hedman, M. M., and Nicholson, P. D., 2016. The B-ring's surface mass density from hidden density waves: Less than meets the eye? In press at Icarus. arxiv: http://arxiv.org/abs/1601.07955

Hodkinson, J.R. and Greenleaves, I., 1963. Computations of light-scattering and extinction by spheres according to diffraction and geometrical optics, and some comparisons with the Mie theory. Journal of the Optical Society of America, vol. 53, issue 5, p. 577

Horner, J. et al., 2004. Simulations of the Population of Centaurs I: The Bulk Statistics. Monthly Notices of the Royal Astronomical Society, Volume 354, Issue 3.

Hyodo, R., and Ohtsuki, K., 2014. Collisional Disruption of Gravitational Aggregates in the Tidal Environment. Astrophys. J., 787(May), 56.

Janssen, M.A., et al., 2009. Titan's surface at 2.2-cm wavelength imaged by the Cassini RADAR radiometer: Calibration and first results. Icarus, Volume 200, Issue 1, titan.

Janssen, M.A., et al. Saturn's thermal emission at 2.2-cm wavelength as imaged by the Cassini RADAR radiometer. Icarus, Volume 226, Issue 1(2013)

Janssen, M.A., et al., 2016. Titan's surface at 2.2-cm wavelength imaged by the Cassini RADAR radiometer: Results and interpretations through the first ten years of observation, Icarus, in press, doi: 10.1016/jicarus.2015.09.027.

Johnston, W.R., 2015. TNO and centaur diameters, albedos, and densities V3.0. EAR-A-COMPIL-5-TNOCENALB-V3.0. NASA Planetary Data System.

Jontof-Hutter, D. and Hamilton, D.P., 2012a. The fate of sub-micron circumplanetary dust grains

I: Aligned dipolar magnetic fields. Icarus, Volume 218, Issue 1.

Jontof-Hutter, D. and Hamilton, D.P., 2012b. The fate of sub-micron circumplanetary dust grains II: Multipolar fields. Icarus, Volume 220, Issue 2.

Johnson, T. V., and Lunine, J. I., 2005. Saturn's moon Phoebe as a captured body from the outer Solar System. Nature, Volume 435, Issue 7038.

Kempf, S., Altobelli, N., Horanyi, M., and Srama, R., 2013. The mass flux of micrometeoroids into the Saturn system. AGU, Fall Meeting, 2013, #P21E-05.

Kofman, W., et al., 2015 Properties of the 67P/Churyumov-Gerasimenko interior revealed by CONSERT radar, Science, Volume 349, Issue 6247, pp.

Kuiper, G. P., Cruikshank, D. P., Fink, U., 1970. The composition of Saturn's rings. Bulletin of the Astronomical Society, Vol. 2, p. 235 - 236

Lainey, V. et al., 2010. Saturn tidal dissipation from astrometric observations. Proceedings of the EPSC, Rome, Italy, p. 123.

Lainey V. et al., 2012. Strong Tidal Dissipation in Saturn and Constraints on Enceladus' Thermal State from Astrometry. The Astrophysical Journal, Volume 752

Larsen, J.A. et al. 2001. The spacewatch wide-area survey for bright Centaurs and trans-neptunian objects. Astron. J. 121, 562-579.

Leinhardt, Z.M. and Stewart S.T., 2009. Full numerical simulations of catastrophic small body collisions. Icarus, Volume 199.

Lebofsky, Larry A., Johnson, Torrence V., McCord, Thomas B., 1970. Saturn's rings: Spectral reflectivity and compositional implications. Icarus, Volume 13, Issue 2, p. 226-230.

Marouf, E.A. et al., 2008. Saturn After Cassini- Huygens, conference, London, #113.

Marouf, E. A. et al., 2011. Uncovering of small-scale quasi-periodic structure in Saturn's C ring and possible origin. EPSC-DPS joint meeting, Oct 2-7, Nantes, France, p. 265.

Mishima, O. et al., 1983. The far-infrared spectrum of ice Ih in the range 8–25 cm^{-1}. Sound waves and difference bands, with application to Saturn's rings. J. Chem. Phys. 78(11), 6399–6404.

Morfill, G. E. et al., 1983. Some consequences of meteoroid bombardment of Saturn's rings. Icarus **55,** 439–447.

Morishima R. et al. 2016. Incomplete cooling down of Saturn's A ring at solar equinox: Implication for seasonal thermal inertia and internal structure of ring particles. Icarus, in press.

Morris, R. V. et al., 1985. Spectral and other physiochemical properties of submicron powders of hematite (-Fe2O3), maghemite (-Fe2O3), maghemite (Fe3O4), goethite (-FeOOH), and lepidochrosite (-FeOOH). J. Geophys. Res. 90, 3126–3144.

Nicholson P.D. et al., 2005. Radar imaging of Saturn's rungs. Icarus, Volume 177, Issue 1.

Nicholson P.D. et al., 2008. A close look at Saturn's rings with Cassini VIMS. Icarus, Volume 193, Issue 1.

Nicholson P.D. and Hedman M.M., 2010. Self-gravity wake parameters in Saturn's A and B rings. Icarus, Volume 206, Issue 2.

Paillou P. et al., 2008. Microwave dielectric constant of Titan-relevant materials. Geophysical Research Letters, Vol 35, L18202.

Pollack, J. B., Summers, A., and Baldwin, B., 1973. Estimates of the sizes of the particles in the rings of Saturn and their cosmogonic implications. Icarus 20, p. 263-278.

Pollack, J. B., 1975. The rings of Saturn. Space Science Reviews, vol. 18, Oct. 1975, p. 3-93.

Pollack, J.B. and Cuzzi, J.N., 1980 Scattering by nonspherical partiles of size comparable to wavelength – A new semi-empirical theory and its application to tropospheric aresols. Journal of the Atmospheric Sciences, vol. 37, p. 868-881.

Pollack J.B. et al., 1994. Composition and radiative properties of grains in molecular clouds and accretion disks. The Astrophysical Journal, 421:615-639.

Porco C.C. et al., 2008. Simulations of the dynamical and light-scattering behavior of Saturn's

rings and the derivation of ring particle and disk properties, The Astronomical Journal, 136:2172-2200.

Poulet, F., and Cuzzi, J. N., 2002. The composition of Saturn's rings. Icarus 160, 350-358.

Poulet F. et al., 2003. Compositions of Saturn's rings A, B, and C from high resolution near-infrared spectroscopic observations, Astronomy and Astrophysics, v.412, p.305-316.

Pringle, J. E., 1981. Accretion discs in astrophysics. Ann. Rev. Astron. Astrophys. 19, 137-162.

Reffet, E. et al., 2015. Thickness of Saturn's B ring as derived from seasonal temperature variations measured by Cassini CIRS. Icarus, Volume 254.

Salmon, J. et al., 2010. Long-term and large-scale viscous evolution of dense planetary rings. Icarus 209, 771-785.

Salo, H., 1992. Gravitational wakes in Saturn's rings. Nature 359, 619-621.

Schmidt, J. et al., 2009. Dynamics of Saturn's dense rings. In: Dougherty, M.K., Esposito, L.W., Krimigis, S.M. (Eds.), Saturn After Cassini-Huygens. Springer-Verlag Press, pp. 413p. 41.

Sierks et al., 2015. On the nucleus structure and activity of comet 67P/Churyumov-Gerasimenko. Science, Vol. 347 no. 6220.

Smith B.A. et al., 1982. A new look at the Saturn system – The Voyager 2 images. Science, vol 215.

Soderblom J.M., 2015. The fractured Moon: Production and saturation of porosity in the lunar highlands from impact cratering. Geophysical Research Letters, Vol 42.

Spilker, L.J. et al., 2004. Saturn A ring surface mass densities from spiral density wave dispersion behavior. Icarus, Volume 171, Issue 2, p. 372-390.

Stillman, D., Olhoeft, G., 2008. Frequency and temperature dependence in electromagnetic properties of Martian analog minerals, Journal of Geophysical Research, Volume 113, Issue E9

Thomas, P.C. et al., 2007. Hyperion's sponge-like appearance. Nature 448, 50-56.

Tiscareno, M. S. et al., 2007. Cassini imaging of Saturn's rings. II. a wavelet technique for analysis of density waves and other radial structure in the rings. Icarus 189, 14-34.

Tsiganis K., et al., 2005. Origin of the orbital architecture of the giant planets of the solar system. Nature 435, 459–461.

van der Tak et al., 1999. Time Variability in the Radio Brightness Distribution of Saturn. Icarus, 142, 125.

Vouk, V., 1948. Projected Area of Convex Bodies. Nature, Volume 162, Issue 4113, pp. 330-331.

Weiss, J. W. et al., 2006. A Near-Arm/Far-Arm asymmetry in Saturn's rings and implications for ring structure. DPS meeting #38, Bulletin of the American Astronomical Society, Vol. 38, p. 552.

Wiscombe, W.J., 1980, Improved Mie scattering algorithms, Applied Optics, vol. 19, May 1, 1980, p. 1505-1509.

Wyatt, P.J., 1962. Scattering of electromagnetic plane waves from inhomogeneous spherically symmetric objects. Physical Review Volume 127, Number 5.

Wisdom, J., Tremaine, S., 1988. Local simulations of planetary rings. Astronom. J. 95, 925–940.

Zahnle K. et al., 2003. Cratering rates in the outer Solar System. Icarus, vol 163.

Zebker, H.A., Marouf, E.A., Tyler, G.L., 1985. Saturn's rings:. Particle size distributions for thin layer model. Icarus 64, 5314, 53.

Zhang Z., et al., 2017a. Cassini microwave observations provide clues to the origin of Saturn's C ring. Icarus, vol 281, p. 297-321.

Zhang Z. et al., 2017b. Exposure age of Saturn's A and B Rings, and the Cassini Division as suggested by their non-icy material content. Submitted to Icarus.